Design, development and use of a deformable breast phantom to assess the relationship between thickness and lesion visibility in full field digital mammography

The Dissertation (or Treatise) Committee for Mary Shahrzad Ossati Certifies that this is the approved version of the following dissertation (or treatise):

Design, development and use of a deformable breast phantom to assess the relationship between thickness and lesion visibility in full field digital mammography

Committee:

Katy Szczepura, Supervisor

Peter Hogg, or Co-Supervisor

Design, development and use of a deformable breast phantom to assess the relationship between thickness and lesion visibility in full field digital mammography

Relationship between breast phantom thickness and lesion visibility in mammographic imaging

by

Mary Shahrzad Ossati

Dissertation

Presented to the Faculty of the Graduate School of

Salford University

in Partial Fulfilment

of the Requirements

for the Degree of

Doctor of Philosophy

Salford University

July 2015

Relationship between breast phantom thickness and lesion visibility in mammographic imaging

Dedication

To my wonderful husband Ricky and my sweet daughter Doreen

Abstract

Design, development and use of a deformable breast phantom to assess the relationship between thickness and lesion visibility in full field digital mammography

Mary Shahrzad Ossati Salford University, 2015

Aim of research:

This research aimed to design and develop a synthetic anthropomorphic breast phantom with cancer mimicking lesions and use this phantom to assess the relationship between lesion visibility and breast thickness in mammography.

Due to the risk of cancer induction associated with the use of ionising radiation on breast tissues, experiments on human breast tissue was not practical. Therefore, a synthetic anthropomorphic breast phantom with cancer mimicking lesions was needed to be designed and developed in order to provide a safe platform to evaluate the relationship between lesion visibility and breast thickness in mammography.

Method:

As part of this research custom Polyvinyl alcohol (PVAL) breast phantoms with embedded PVAL lesions doped with contrast agent were fabricated and utilised. These breast phantoms exhibited mechanical and X-ray properties which were similar to female breast/breast cancer tissues. In order for this research to be useful for human studies, patient safety factors have constrained the extent of this research. These factors include compression force and radiation dose.

After acquiring mammograms of phantoms with varying thicknesses, the image quality of the embedded lesions were evaluated both perceptually and mathematically.

The two-alternative forced choice (2AFC) perceptual method was used to evaluate image quality of the lesions. For mathematical evaluation the following methods were utilised: line profile analysis, contrast-to noise ratio (CNR), signal-to noise ratio (SNR) and figure of merit (FOM).

Results:

The results of the visual perception analysis of the mammograms demonstrate that as breast compressed thickness reduces the image quality increases. Additionally, the results display a correlation in the reduction in the level of noise with the reduction in breast thickness. This noise reduction was also demonstrated in the profile plots of the lesions. The line profile analysis, in agreement with visual perception, shows improvement of sharpness of the lesion edge in relation to the reduction of the phantom thickness. The intraclass correlation coefficient (ICC) has shown a great consistency and agreement among the observers for visibility, sharpness, contrast and noise. The ICC results are not as conclusive for the size criterion.

Mathematical evaluation results also show a correlation of improvement in the image quality with the reduction in breast thickness. The results show that for the measures CNR, SNR, and FOM, the increase in image quality has a threshold after which the image quality ceases to improve and instead begins to reduce. CNR and FOM dropped when the breast phantom thickness was reduced approximately 40% of its initial thickness. This consistently happened at the point where the filter changed from rhodium (Rh) to molybdenum (Mo).

Conclusion:

This breast phantom study successfully designed and developed an anthropomorphic compressible breast phantom with cancer mimicking lesions with mechanical and X-ray properties similar to human breast tissue. This study also

demonstrates that as breast compressed thickness reduces the visibility of the perceived lesion increases. The radiation dose generally decreases up to the point that the filter changes from rhodium to molybdenum. After this point, the radiation dose increases regardless of the phantom thickness. The results from this thesis are likely to have implications for clinical practice, as they support the need for compression/thickness reduction to enhance lesion visibility.

Table of Contents

List of Tables

List of Figures

Acknowledgements

I would love to express my appreciation, gratitude and thanks to my supervisors, Katy Szczepura and Professor Peter Hogg. Thank you for your support, encouragement, and all your constructive feedback throughout my scientific PhD journey.

I would love to thank Catherine Hanna, the fantastic knowledgeable mammographer at Salford royal hospital who has patiently helped me with the mammography part of my research.

I would love to thank Salford University for providing me bursary and for giving me the opportunity to work as a graduate teaching assistant in the radiography department.

Lastly, I would love to express my special thanks to my family. I would love to show my gratitude to my lovely husband, Rick Turpin, who has supported me for years throughout my studies and to my little Doreen who has tried hard not to distract me during my write up period. I would immensely thank my parents Dr. Nassrin Moini and Dr. Hassan Ossati for encouraging me to be in the path of learning.

Chapter 1 Introduction

In order to provide good quality mammograms, breast compression in mammography is required. Compression is needed regardless of patient related factors such as breast density, and mammographic techniques (O'Leary, Grant, & Rainford, 2011). As the compression reduces the thickness of the breast, the breast structures are brought closer to the detector (Chevalier, Leyton, Tavares, Oliveira, da Silva, & Peixoto, 2012). This in turn reduces the distance that radiation must travel through the tissue. Subsequently, the amount of scattered radiation is reduced, and the sharpness of the features in the captured mammograms is increased. This reduction in tissue thickness also has the effect of reducing the required dose of radiation necessary to acquire the mammographic image (Chevalier, Leyton, Tavares, Oliveira, da Silva, & Peixoto, 2012) (Kaabi, Bariki, & Janeczek, 2013).

Compression force also improves the image quality by limiting breast movement and spreading the overlapping breast tissue (O'Leary, Grant, & Rainford, 2011) (Chevalier, Leyton, Tavares, Oliveira, da Silva, & Peixoto, 2012). Immobilizing the breast increases the definition or sharpness of the structures in the image by reducing movement unsharpness. Spreading the overlapping breast structures differentiates the true lesions from summation shadows which are caused by overlapping soft tissues (Brant & Helms, 2012).

The National Health Service Breast Screening Programme (NHSBSP) provides guidelines for the use of compression in mammography (NHS Breast Screening Programme, 2000). These guidelines refer to the gentle and slow use of compression to hold the breast tissue firmly in position, and define an upper limit of compression which should not be exceeded (200 N or 20 kg). The guidelines do not discuss the adequate

range for compression force in order to provide diagnostically acceptable mammograms. Because of this missing link, numerous experiments on compression force in mammography have already been carried out to determine the optimal compression force to enhance image quality, decrease the patient radiation dose, and reduce patient discomfort. These studies are explored in Chapter 3.

Failure to apply adequate compression force increases the possibility of missing the lesions. Whereas, when excessive compression forces are used, the risk of discomfort and possible injury to the patients as a result of the procedure increases. Evidence shows that if the screening clients experience too much discomfort, the may not attend again on future screening occasions. Therefore, finding the relationship between the image visibility and the breast thickness will assist the clinicians to reach an appropriate thickness in order to visualize breast cancer.

1.1 THIS RESEARCH STUDY

This research aims to design and develop a synthetic anthropomorphic breast phantom with cancer mimicking lesions and use this phantom to assess the relationship between lesion visibility and breast thickness in mammography. This demonstrates whether image visibility improves with the decrease of the breast phantom thickness due to an increase of compression force. This helps determine how much the breast must be compressed in order to create adequate mammographic lesion visibility. This study also considers the relationship between the breast phantom thickness and the radiation dose.

Due to the risk of cancer induction associated with the use of ionising radiation on humans, synthetic anthropomorphic (see glossary on page 305) breast phantoms are often utilised in mammography research. In general, phantoms are designed objects that are

used in medical imaging research to replace the real tissue where using the living human is inappropriate (Surry, Austin, Fenster, & Peters, 2004).

In order for the phantoms to be suitable as a human substitute, their mechanical and X-ray properties must be similar to the tissues they mimic. Mechanically the phantoms need to simulate both the stiffness and compressibility of the mimicked human tissue.

Due to the limitations of existing commercial physical and computerised phantoms, development of a physical breast phantom was required in this research. Non-toxic, biodegradable, biocompatible, simple, and low cost water-based poly vinyl alcohol (PVAL) phantoms/lesions with multiple freezing-thawing cycles (FTC) were fabricated and utilised. The lesions were made of PVAL and water-based X-ray contrast media. The mechanical and X-ray properties of the phantoms/lesions were then measured to ensure their mechanical and X-ray properties were similar to breast tissue and cancer lesions. Since the X-ray properties of the PVAL phantoms are dissimilar to human breast tissue, the appropriate amount of contrast agent was measured and added to the PVAL lesions. The contrast agent helped to simulate the right attenuation difference between the cancer mimicking lesions and the surrounding PVAL breast phantom. The compressible phantoms developed in this research can tolerate over 200 N of compression force without being damaged. This allows the application of a wide range of compression forces to the PVAL breast phantoms in order to acquire images of various phantom thicknesses.

In this study, mammography was performed both during the design and development of the phantoms and after finalising the design. Imaging of the phantoms during the design was aimed to improve the phantom/lesion fabrication by assessing the appropriateness of the tissue substitutes. After completing the design, mammography

imaging was utilised to measure the lesion visibility in relation to breast phantom thickness.

After acquiring mammograms of the phantoms at various thicknesses, the image quality of the embedded lesions was evaluated mathematically and perceptually. Mathematical methods employed were contrast-to-noise ratio (CNR), signal-to-noise ratio (SNR), line profile analysis, and figure of merit (FOM). The perceptual method utilised was two-alternative forced choice (2AFC) (Blindell & Hogg, 2012).

1.2 STRUCTURE OF THIS THESIS

This thesis consists of 11 chapters including the introduction. Chapter 2 provides background information around the anatomy of the breast and the abnormalities that can occur within the breast. This is then followed, in Chapter 3, with a brief discussion on previous breast compression studies corresponding to the relation between the compression force, breast thickness, image quality, and patient's discomfort. Chapter 4 and Chapter 5 introduce two different categories of breast phantoms employed in medical imaging research: physical and computerised. As mammography was the main imaging modality in this research, Chapter 6 was dedicated to the physics of mammography unit. Chapter 7 defines the structure and chemical/physical properties of PVAL and the formation of the gel. It also discusses why PVAL is suitable for use in biomedical engineering and in this project. Although this research was not specifically CT based, a CT scanner was used in the initial evaluation of the imaging properties of the PVAL phantoms/lesions. Therefore, Chapter 8 was provided to discuss the physics of the CT scanner and the processes of image acquisitions and image reconstructions. In the next chapter, Chapter 9, the concept of visual perception and perceptual methods such as receiver operating characteristic (ROC) and 2AFC were discussed. Chapter 10 and

Chapter 11, discuss the materials/equipment and experiments that took place, and the analysis of their results. Additional supporting data can be found in the appendices.

Chapter 2 The breast and its abnormalities

In order to design and develop anthropomorphic breast phantoms with cancer mimicking lesions, some knowledge of the anatomy of the breast and its abnormalities is required. This chapter aims to discuss the anatomy and properties of the breast and breast cancer lesions. Considering the anatomy and properties of the breast/lesions will help the breast phantom/lesions to be similar to human breast tissue with cancer lesions.

2.1 BREAST CANCER

Breast cancer is a malignant tumour which can initiate in any tissue of the breast and invade the surrounding area. This cancer, similar to other types of cancers, can be the result of the uncontrolled cell division (proliferation). In normal cell division, two basic classes of genes, referred to as proto-oncogenes and tumour suppressor genes are responsible to regulate the cell divisions. When these genes mutate permanently, the cells divide uncontrollably. Consequently, the uncontrolled cell division results in cancer. This can spread or metastasize to distant organs through the blood stream or lymphatic system. (Clark, Levine, & Snedeker, 1997)

2.2 BREAST CANCER MORTALITY STATISTICS

After lung cancer, breast cancer is the second leading cause of cancer death among women. Breast cancer is a major concern for women. In 2010, over 11,000 people died from breast cancer in the United Kingdom alone with 99% of these being women (Cancer Research UK, 2014). In 2012 in the UK about 11,600 women died because of breast cancer. 1,200 deaths occurred in women younger than 50. Around three-quarters of the deaths from breast cancer occurred in women aged 60 and over (Cancer Research UK, 2014).

Although the incidence rates of breast cancer in the UK have increased by 72% since mid-1970s, the chance of survival at least ten years has also increased. Currently, approximately 2 in 3 women diagnosed with breast cancer can survive beyond 20 years after detection (Cancer Research UK, 2014).

2.3 ANATOMY OF THE BREAST

The female breast (Figure 2.1) is composed of glandular, fibrous and adipose (fatty) tissue (Geddes, 2007). The glandular part of the breast consists of 15-20 lobes separated by fat and is made up of lobules. Each lobe has a major duct connecting to the nipple. Lobules consist of alveoli cells which are clustered around fine tubes called ductules. The ductules join to each other to form a larger canal called a lactiferous duct. The milk produced in alveoli is drained towards the nipple through the lactiferous duct. The breast tissue is supported by fibrous connective tissue referred to as Cooper's ligaments. The Cooper's ligaments maintain the shape of the breast and attach it to the chest muscle (Butler, Mitchell, & Ellis, 2007) (ElSharkawy, 2014). Figure 2.1 illustrates the anatomy of the beast.

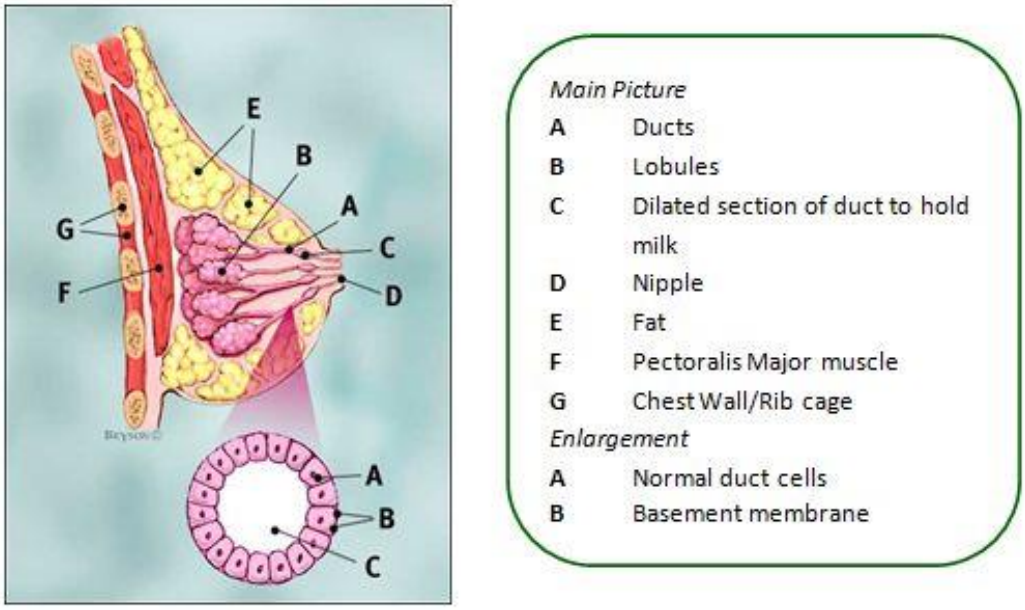

Figure 2.1 Breast anatomy (Marshall University, 2009)

The female breast mostly consists of a group of fat cells referred to as adipose tissue. The adipose tissue ranges from the collarbone to the armpit and to the middle of the ribcage (National Breast Cancer Foundation, 2012). The size of the breast is mainly determined by the amount of the adipose tissue in the breast. Typically, smaller breasts have a higher amount of glandular tissue compared to their adipose tissue (Fritsch & Kuehnel, 2007).

2.4 DETECTION OF BREAST CANCER

Several different imaging modalities are employed for the detection of breast cancer in screening and symptomatic populations. These include mammography, ultrasound, magnetic resonance imaging (MRI), tomosynthesis, cone beam computed tomography (CBCT), and contrast-enhanced Dedicated Breast CT.

Mammography, as an X-ray exam of the breast, is the most common imaging modality utilised (National Cancer Institute, 2014). Mammography is employed as both a screening and a diagnostic tool in order to detect the breast lesions/microcalcifications.

Breast ultrasound examination, as a non-ionising radiation-based imaging technique, helps physicians evaluate suspicious breast abnormalities that have been detected with mammography screening/diagnostic and/or palpation. Due to the availability of real time ultrasonic images, ultrasound imaging is also used in breast biopsy procedures to guide operators during needle insertion (Mayo Clinic, 2015). Subsequently pathology lab analyses determine whether the breast abnormalities are cancerous. In general, breast biopsy is the removal of the breast tissue in order to examine it under microscope by a pathologist for the signs of breast cancer or other abnormalities (Cancer Research UK, 2014).

Breast MRI is a revolutionary diagnostic imaging modality which utilises a magnetic field and radio waves in order to produce the breast images. Although breast MRI is not routinely used for breast screening, it can help detect the breast cancer among the women who are at high risk for developing the breast abnormalities (cancer.net, 2014).

Tomosynthesis is a three-dimensional medical imaging technology that acquires several pictures of each compressed breast at multiple angles during a short scan. In this modality the breasts are immobilized with a slight pressure during the procedure. The X-ray tube moves in an arc around the breast in order to take images. Then a computer is employed to produce three dimensional images from the acquired data. One of the advantages of tomosynthesis over the conventional mammography is the elimination of the tissue overlap problems which occur in two-dimensional mammography. This helps to achieve more confident and accurate readings/diagnosis (Smith, 2008).

Cone beam computed tomography (CBCT) (Lai, et al., 2007) and Contrast-enhanced Dedicated Breast CT (Prionas, et al., 2010) are other imaging techniques that are used to detect breast cancer.

2.4.1 Limitations of mammography

Mammography, as a routine breast imaging procedure, has its own limitations. These limitations can be due to the level of expertise of the operator, the machine related features (for example detectors), the breast structures, or the size and the location of the lesions. These limitations can result in false positive/negative diagnosis. The demographic with the highest likelihood of false positive/negative results is towards the younger women with denser breasts (American Cancer Society, 2014) (Joy, Penhoet, & Petitti, 2005). Dense breasts make the detection of the cancer lesions and microcalcifications harder.

Mammography procedure requires compression force, which can cause pain among some women. The pain might discourage women from attending regularly for screening mammography (NHSBSP, 2006) (O'Leary & Al Maskari, 2013). This limitation of the mammography procedure can be resolved by utilising other modalities such as magnetic resonance imaging (MRI). Although other breast imaging modalities do not employ the compression mechanism which is commonly used in mammography, they might have other limitations such as cost, higher radiation dose to the breast, lower sensitivity and specificity. For example, breast MRI as an advanced imaging modality can detect some cancer lesions which cannot be seen in mammogram, but due to the high cost of the purchase, maintenance and training, not very many hospitals are equipped with breast MRI technology (American Cancer Society, 2014).

2.5 BREAST PROJECTIONS IN MAMMOGRAPHY

As the breast is not uniform in shape or structure, different mammographic projections are needed to visualise the suspected abnormalities. Typically the two main projections which are used during the mammography procedure are the craniocaudal projection (CC) and the mediolateral oblique projection (MLO). In cases where the abnormality is not well visualised by the above projections, supplementary mammographic projections including the lateromedial (LM) projection and the mediolateral projection (ML) can be utilised. The following image (Figure 2.2) shows all these four types of mammographic projections (Imaginis Corporation, 2014).

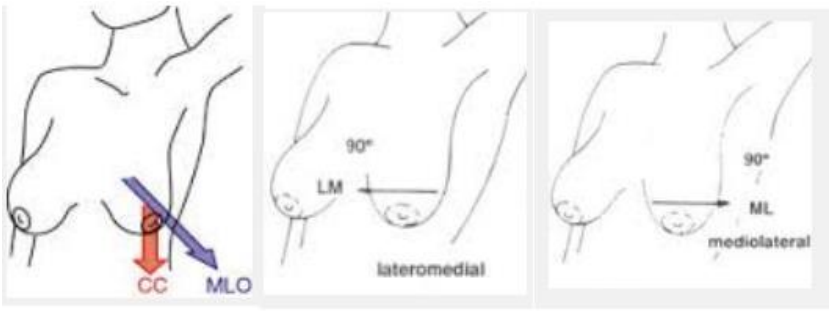

Figure 2.2 Mammographic projections (Imaginis Corporation, 2014)

2.6 TYPES OF BREAST CANCERS

There are many types of breast cancers that originate in different parts of the breast, e.g. milk ducts, lobules, and nipples. Some of these types include carcinoma, adenocarcinoma and sarcoma. Carcinoma is a cancer that starts in the lining layer of an organ such as breast. Adenocarcinomas are cancers that begin in the gland tissue such as breast lobules. Sarcomas are cancers which start from connective tissues (muscle, fat or blood vessels) (American Cancer Society, 2014).

Breast cancers can be invasive or non-invasive. Invasive Ductal Carcinoma (IDC) is an example of invasive breast cancers which includes several subtypes (Papillary

Carcinoma, Medullary Carcinoma, and Tubular Carcinoma) (Danziger & Simonsen, 2011). An example of non-invasive breast cancer is Ductal Carcinoma in Situ (DCIS).

IDC as the most common breast cancer initiates in the cell linings of the breast ducts and invades through the wall of the ducts. IDC is able to metastasize to adjacent lymph nodes, blood stream or other body parts. About 8 out of 10 invasive breast cancers can be classified as IDC (American Cancer Society, 2014). Most commonly, IDC form speculated firm masses with irregular and ill-defines margins. Invasive Lobular Carcinoma (ILC) is the second most common breast cancer which begins in the milk-producing glands or lobules. Normally, the average age of the patients with ILC is a few years older than that of patients with IDC. Due to the formation of ill-defined IDC, detection of this type of cancer is difficult. DCIS is the most common type of non-invasive breast cancer which starts in the milk ducts. There are other types of breast cancer such Lobular Carcinoma in Situ (LCIS), and Paget's disease of the nipple (NHS, 2014) (Winchester & Winchester, 2006).

Breast calcifications are small deposits of calcium salt which in most cases are benign, but they can be early signs of breast cancer (Breast Cancer Care, 2014)**.** Calcifications are viewed in mammograms as bright structures with high signal to noise ratio (SNR). This high SNR is due to the presence of calcium which has a high X-ray attenuation coefficient (see glossary on page 305). Calcifications can be grouped as macrocalcifications and microcalcifications (Figure 2.3). Macrocalcifications are calcifications with a diameter greater than 1 mm and are associated with benign conditions whereas microcalcifications are sized between 0.1-1 mm and can be associated with later breast cancer. A group of microcalcifications, referred to as cluster, can be associated with cancer. The size, shape, and pattern of microcalcifications are related to

the type of microcalcifications (Karahaliou, Arikidis, Skiadopoulos, Panayiotakis, & Costaridou, 2012).

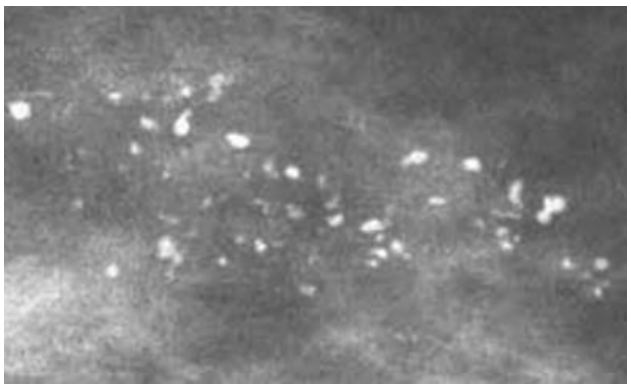

Figure 2.3 Microcalcifications (Halls, 2011)

2.7 BREAST CANCER STAGING

The Tumour lymph Nodes Metastasis (TNM) staging systems describes the size of the tumour (T), evidence of the spread of the cancer to the lymph nodes (N) and evidence of the spread, metastasis (M), to other parts of the body. This classification helps the specialists to determine the type of the treatment based on the stage. For example, T2 N0 M0 means, the size of the tumour is 2.1 to 5 cm, no evidence of spread to any lymph nodes, and there is no evidence of metastasis (Cancer Research UK, 2014). The following table (Table 2.1) illustrates TNM staging.

Facet	Stage	Description
Tumour (T)	TX	no assessment for the size
	Tis	DCIS
	T1	tumour <= 2 cm
	T2	2 cm < tumour <= 5 cm
	T3	tumour > 5 cm
	T4 -subcategories	can be inflammatory carcinoma
Nodes (N)	NX	no assessment for the lymph node
	N0	no cancer cells found in any nearby nodes
	N1	cancer cells in the upper levels of lymph nodes in the armpit but the nodes are not stuck to surrounding tissues
	pN1mi	one or more lymph nodes contain areas of cancer cells
	N2	cancer cells in the lymph nodes in the armpit, stuck to each other and to other structures
	N3	cancer cells in lymph nodes above the collarbone
Metastasis (M)	M0	no sign of cancer spread
	cMo(i+)	no sign of the cancer on physical examination, scans or X-rays but cancer cells are present in blood, bone marrow, or lymph nodes far away from the breast cancer - the cells are found by laboratory tests
	M1	cancer has metastasized to another part of the body

Table 2.1 TNM staging (Cancer Research UK, 2014)

2.8 BREAST QUADRANTS

The occurrence of cancer is not uniform throughout the breast. Different regions of the breast have a higher incidence of cancer than others. By dividing the breast into five regions (upper outer quadrant UOQ, upper inner quadrant UIQ, lower outer quadrant LOQ, lower inner quadrant LIQ, and centre) the relative distribution of cancer within the breast can be seen (Figure 2.4). The following image shows the approximate occurrence of breast cancer by quadrant (Madjar & Mendelson, 2011).

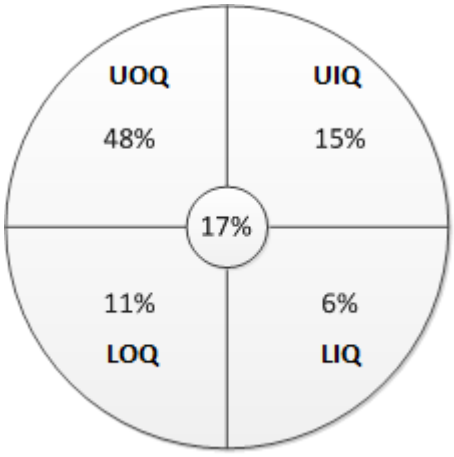

Figure 2.4 Breast Quadrants of a right breast. Upper outer quadrant (UOQ), upper inner quadrant (UIQ), lower outer quadrant (LOQ), lower inner quadrant (LIQ), and centre (Madjar & Mendelson, 2011)

As can be seen in the above figure, the upper outer quadrant (UOQ) shows the highest percentage of occurrence of breast cancer. Although the percentage of the approximate occurrence of breast cancer by quadrant varies between studies (Aljarrah & Miller, 2014), researchers believe that the upper outer quadrant contains a greater amount of breast tissue and a high percentage of ducts. Hence, the chance of cancer occurrence in this quadrant is high (Yu, 2000).

Multifocality and multicentricity are two concepts in breast cancer research which define presence of two or more lesions foci within a single quadrant or different quadrants of the same breast. In multifocality, the tumours are in one single quadrant arisen from the original tumour. Whereas in multicentricity the tumours are formed separately from each other and are located in multiple quadrants of the same breast (Coombs & Boyages, 2005).

2.9 SHAPE AND MARGIN OF THE LESIONS/MASSES

The margin and shape of the masses or lesions indicate if the lesion is benign or malignant. The shape can be round, oval, irregular, or lobulated. The margin can be

circumscribed, spiculated, obscured, indistinct, or microlobulated. Lesions which have an oval or round shape and include a circumscribed margin are usually benign. Whereas lesions with an irregular shape often have a higher likelihood of being malignant. The following image (Figure 2.5) illustrates common shapes and margins of lesions.

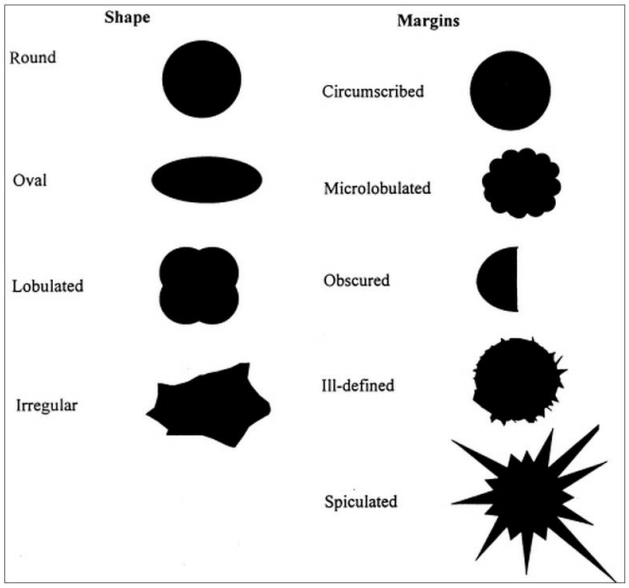

Figure 2.5 Shape and margin of cancer lesions (Bast, Bast, & Holland, 2000)

Some examples of benign circumscribed masses include cysts and fibroadenomas. Although invasive ductal carcinomas (IDC) exemplify cancers with irregular shape and spiculated margins, they can have well-defined margin (Dronkers & Hendriks, 2011). The following mammograms (Figure 2.6 and Figure 2.7) show the benign and malignant masses (Bast, Bast, & Holland, 2000) (Dronkers & Hendriks, 2011).

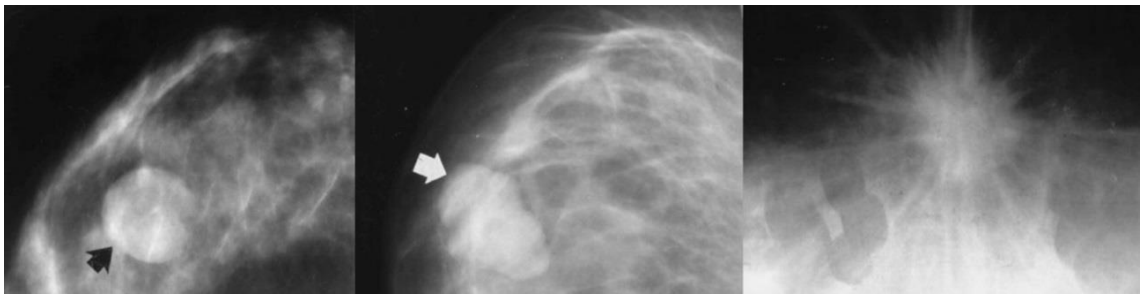

Figure 2.6 Mammograms showing benign and malignant masses Left: Cyst- round circumscribed - Middle: Fibroadenoma - lobular, circumscribed, and low density - Right: Invasive ductal carcinoma (IDC) - irregular shape and spiculated margins (Bast, Bast, & Holland, 2000)

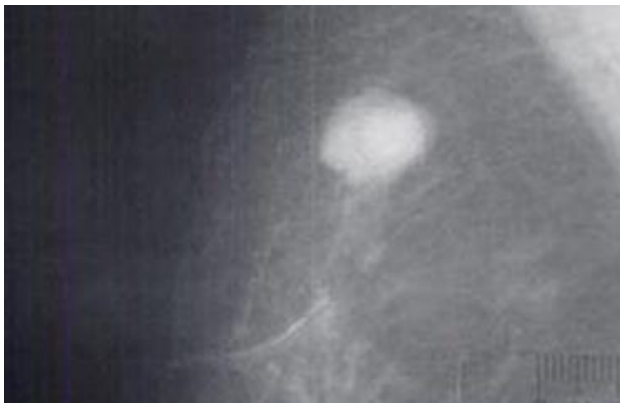

Figure 2.7 A 12 mm round IDC with well-defined margin

2.10 MECHANICAL PROPERTIES OF THE BREAST

For a phantom to be anthropomorphic, it must not only exhibit the imaging properties similar to human tissue, but also requires the mechanical properties to resemble their human counterparts. When relating compression to image visibility in mammography, the key mechanical property of breast tissue is its compressibility. The terminology used to describe this property varies and has also been referred to as elasticity or stiffness.

In determining an acceptable range of compressibility for human breast tissue, the results of various clinical research shows a large variation among these studies. A common conclusion among the studies is that lesions are stiffer than normal breast tissue. Krouskop et al. have found that invasive ductal carcinoma (IDC) can be between 4.8 to

27.9 times stiffer than the fatty tissue. A research by Samani et al. has shown that the stiffness of invasive ductal carcinoma is up to 13 times higher than fatty tissue (Samani, Zubovits, & Plewes, 2007). Sarvazyan's results using 162 breast tissue samples have presented that the breast cancer lesions can have a wide range of stiffness which can be up to seven times higher than normal tissue (Sarvazyan, 1993). The compressibility of the fatty tissue was found by different researchers in the range of 0.5 to 25 kPa (Gefena & Dilmoney, 2007). Interestingly, the range of 20 kPa was found by Krouskop with various pre-compression forces and loading frequencies using an Instron machine (Krouskop, Wheeler, Kallel, Garra, & Timothy, 1998).

It is important to investigate the reasons for variation of the quantitative measurements of the mechanical properties of the breast tissue. Using various methods in order to measure the mechanical properties of the breast can be one of the reasons for the variation of the results between studies. For example the amount of pre-compression force can make a significant difference in the measurement of the compressibility of the samples (Krouskop, Wheeler, Kallel, Garra, & Timothy, 1998).

Temperature can be another factor which can affect the measurement of the stiffness of the breast tissue such as fat (Gefena & Dilmoney, 2007) inside and outside of the breast. Since the body temperature and the temperature of the fat out of the body are different, this might have an effect on the stiffness of the fat. Samples of breast tissue acquired from surgical procedures (fat, glandular, and cancer lesion) could have a different stiffness than live tissue due to lack of metabolic activities and dehydration. The samples used in these types of studies also might not be homogeneous. For example, the lesion might contain other tissues such as fat and glandular. Other factors to consider when measuring breast tissue stiffness include patient age and sample shape and size.

Variation in sample size may affect the results. For example, in Krouskop's study, the numbers of fat and invasive ductal carcinoma samples were 8 and 32 respectively whereas in Samani's research the numbers were 71 and 9 (Krouskop, Wheeler, Kallel, Garra, & Timothy, 1998) (Samani, Zubovits, & Plewes, 2007).

2.11 X-RAY PROPERTIES OF THE BREAST

X-ray properties of body parts, such as the breast, can be measured by Hounsfield unit (HU). Details of HU will be discussed in Chapter 8. According to Boone et al. (Boone, Nelson, Lindfors, & Seibert, 2001), the HU of breast fat, glandular tissue, and cancer lesions are -180, 40, and 80 respectively. As the graph shows (Figure 2.8), the HU of the breast structures change corresponding to the kVp.

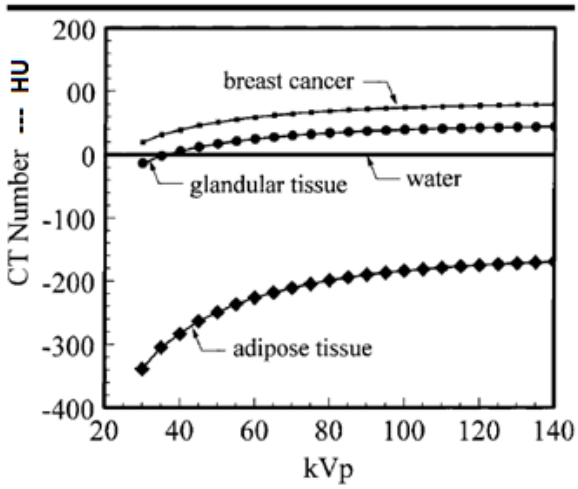

Figure 2.8 HU for breast cancer, glandular tissue, adipose tissue, and water (Boone, Nelson, Lindfors, & Seibert, 2001).

The HU of fat in general has been measured in ranges of (-150,-50), and also (-200,-10) (Kim, Lee, Lee, Park, Pyo, & Cho, 1999). It is important to take into consideration that the location of the measured fat in the body has an influence on its HU. Similarly, the composition of the fat, which can vary from person to person, can be

another factor which may have an impact on the measurement of its HU (Kim, Lee, Lee, Park, Pyo, & Cho, 1999). CT techniques, CT manufacturing variations, X-ray scattering (Yang, Burkett Jr, & Boone, 2014), and selection of the region of interest (ROI) could be other reasons for discrepancies of the HU of fat.

Chapter 3 Mammographic compression studies

This chapter introduces and discusses various breast compression studies in order to show different research approaches regarding finding adequate ways of compressing the breast during mammography.

In a qualitative and quantitative visual perception based research by D O'Leary et al, compression force, radiation dose and image quality data were acquired from 4790 mammograms. In the quantitative part, the image quality was grouped into perfect, good, moderate, and inadequate. This method of evaluation of clinical image quality is referred to as the PGMI system (Perfect, Good, Moderate, and Inadequate) (Goel & Pacifici, 2014). Both craniocaudal and mediolateral oblique projections were considered in this research. In the qualitative part, the pain reported by the patients was taken into consideration.

In data analysis, univariate analysis of variance (ANOVA) statistical test was employed. The results showed that in order to acquire good and perfect images in full-field digital mammography, significantly higher compression force is required. With this higher compression force, the image quality for good and perfect images is noticeably higher than moderate and inadequate images. This research supports the increase of compression force in order to acquire high quality images and suggests the utilisation of 121.34 N and 134.23 N for craniocaudal and mediolateral oblique projections respectively in digital mammography. The results also exhibited the higher compression forces result in lower mean glandular doses. The results of the qualitative part also showed that there were no complaints regarding the pain from the patients when the high compression force was applied on them (perfect and good image categories) (O'Leary, Grant, & Rainford, 2011). A strong point in this research was the utilisation of a big

sample size. The drawback is the definition of the criteria for assessing the images. For example “perfect” is a relative term to assess the entire image. A better definition for the criteria could increase the level of accuracy during the evaluation of the images.

In a different study by Poulos et al. (2003), the relationship between applied compression force, breast thickness, reported discomfort and image quality was determined. In this research the sample was selected from the population of 114 women with a mean age of 60 years attending the mammographic breast screening. The research included two parts: clinical and experimental. The clinical part was the normal mammography and the experimental part was one extra exposure with a reduced level of compression. In the experimental part, the level of compression force reduction started with the range of 10-30 N, then a reduction of 30 N was found to be more appropriate as the research progressed.

After completion of the mammography procedure, the participants were asked to complete a questionnaire regarding the level of discomfort experienced during the mammography procedure.

The image quality of the normal and extra mammograms were then compared as paired set and evaluated by 6 radiologists. The criteria were spatial and contrast resolution for various breast features and the scores were from significantly better to significantly worse. For data analysis, programs such as Pearson’s correlation coefficients, one-way analysis of variance (ANOVA), one-sample t-tests were applied to the collected data.

The visual perception results demonstrated no significant differences between each set for any criterion except contrast resolution within the fatty region of the breast. The results also demonstrated no linear relationship between the applied compression force and the thickness of the compressed breast. There was also no relationship between

the applied compression force and the reported discomfort. The results demonstrated a significant relationship between the breast volumes measured by cup size and compression force, compressed breast thickness and reported discomfort. This means that the larger volume breasts required larger compression force. Larger volume breasts displayed higher mean compressed thickness and higher mean compressed thickness was associated with discomfort among women.

According to this research, compression force should be applied until the minimal thickness is acquired. Increasing the pressure after reaching the minimal thickness does not change the breast thickness. Hence, it does not improve the image quality or reduce the radiation dose. It potentially increases the discomfort for women (Poulos, McLean, Rickard, & Heard, 2003). Although this research is one of the novel studies in breast compression force, it has a few downsides. The term minimal is a relative term which does not provide accurate level of measurement for the compression force and breast thickness during mammography. During the selection of the amount of reduced compression force in the experimental part of this research, the inconsistency to pick a constant compression force could also add inaccuracy to this research. The number of the participants (114 women) can be another limitation of this research (Poulos, McLean, Rickard, & Heard, 2003).

In a study by Korf et al., a comparison of the relationship between compression force, image quality and radiation dose was assessed. The results of this research indicate an improvement in image quality based upon increased compression force. This study was conducted using an Artinis contrast-detailed phantom within a Superflab phantom and focused on the change-in-density point of compression. A computed radiography (CR) mammography unit with automatic exposure control (AEC) was utilised in this research. Image quality was assessed using image quality figure (IQF) scoring (see

glossary on page 305) and visual inspection. The researchers of this study concluded that less compression is acceptable, without a significant decrease in image quality, if the patient is in pain or discomfort during the mammographic procedure. They also concluded that the entrance dose decreases with increased compression force (Korf, Herbst, & Rae, 2009).

In this study (Korf, Herbst, & Rae, 2009), the image quality was assessed using an Artinis contrast-detailed phantom within a Superflab phantom. The contrast-detailed phantom consists of an aluminium base with gold discs (Artinis Medical Systems, 2014). This structure does not simulate the breast properties. For example, the young's modulus of the gold is about 70 GPa while the young's modulus of the breast is about 20 KPa (Wu, Heidelberg, & Boland, 2005) (Fromageau, Gennisson, Schmitt, Maurice, Mongrain, & Cloutier, 2007). Moreover, in the image quality assessment, visual inspection and image quality figure (IQF) scoring were based on visual evaluation. Due to the subjective nature of this image quality assessment technique, the assessment was possibly subjected to human errors (Wang, Wang, Chan, Wang, & Liou, 2011).

Mercer and her research collaborators found out that variation in compression force applied in mammography is highly related to the practitioners rather than the patients. In this study, practitioners have been categorised into three groups by their compression force mean value. These groups apply high (12.6 daN), intermediate (8.9 daN) and low (6.7 daN) compression forces. The mean compression value within each group is not significantly different. Compression force variation among these practitioners affects the radiation dose, image quality consistency and patient experience (Mercer, Hogg, Szczepura, & Denton, 2013).

The results of the study carried out by Chida and his fellow researchers suggested that a reduced compression force is more tolerable for some women. This study appears contrary to the results acquired by D O'Leary et al (O'Leary, Grant, & Rainford, 2011) supporting the employment of higher compression force. The reduction of compression from 120 N to 90 N caused the breast thickness to increase by 3 mm. The mAs was increased by 20% for the increased thickness. However, the image quality was assessed as unchanged from the higher compression force. In this research, the image quality was evaluated objectively using a method suggested by the American College of Radiology. During assessment, an RMI 156 phantom with and without added 3 mm acrylic plate was utilised (Chida, et al., 2009).

The results of a study by Dustler and his fellow researchers have shown an uneven distribution of pressure in the mediolateral oblique projection on the breast tissue components. According to the study a higher pressure is concentrated on the juxtathoracic edge due to the compression of the stiff muscles. The results indicate that repositioning the breast to exclude 1 cm of the juxtathoracic region including the pectoral muscle and anterior axillary fold causes the pressure to be distributed more evenly among the different parts of the breast. The distribution of the pressure was measured employing thin force sensing resistor (FSR) pressure sensors connected to the compression paddle. The results show that the repositioned breasts were thinner and had a larger area over which pressure was affected. Further, the results emphasized a need for the proper positioning of the breast during the mammography procedure (MLO-projection) in order to obtain a balance between compression force and the tissue inclusion (Dustler, Andersson, Förnvik, & Tingberg, 2012).

The breast re-positioning research by Dustler, Sardanelli et al. has focussed on breast biphasic compression to include the tissues that Dustler’s study had excluded. This

study emphasizes on a technique of changing the angle of the compression paddle during the compression of the breast to improve the inclusion and viewing of the pectoral muscles in CC projection. In this method the compression angle starts at 22.5° and is continually reduced until the paddle is parallel with the receptor. The results of this study show an improvement of presenting the pectoral muscles in CC projection from 34% (monophasic) to 54% (biphasic). The following image (Figure 3.1) shows the phases applied in biphasic compression (Sardanelli, Zandrino, Imperiale, Bonaldo, Quartini, & Cogorno, 2000).

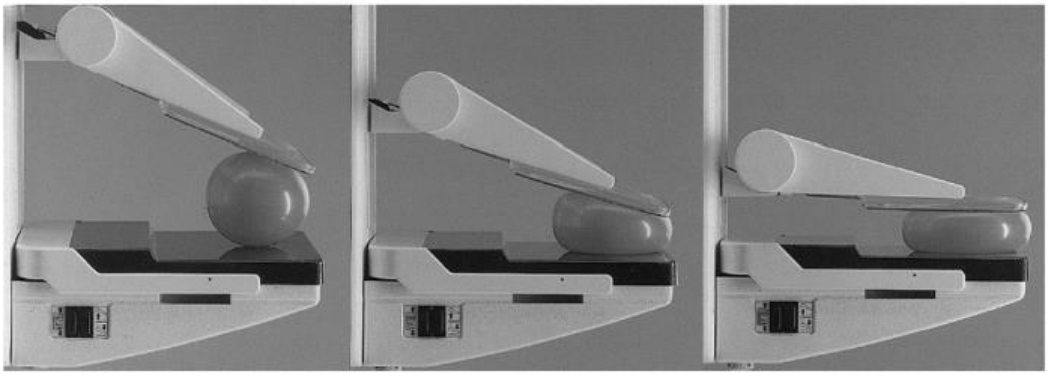

Figure 3.1 Biphasic compression (Sardanelli, Zandrino, Imperiale, Bonaldo, Quartini, & Cogorno, 2000)

A breast positioning system has been suggested to increase the field of view with an additional volume of breast in full-field digital mammography (Varjonen, Pamilo, Hokka, Hokkanen, & Strömmer, 2007). This system consists of two moving transparent sheets (Figure 3.2) that can be placed under and above the compressed breast. The role of these sheets is to pull the breast into the imaging field during compression. Mammograms (Figure 3.3) presented show that this method is able to extend the breast away from the chest wall and increase the breast volume imaged. The pectoral muscle is clearly visible in the right mammogram with enhanced positioning method.

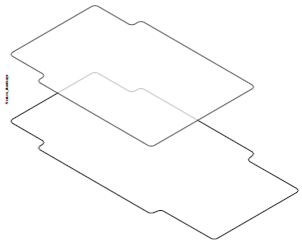

Figure 3.2 Positioning sheets (Varjonen, Pamilo, Hokka, Hokkanen, & Strömmer, 2007)

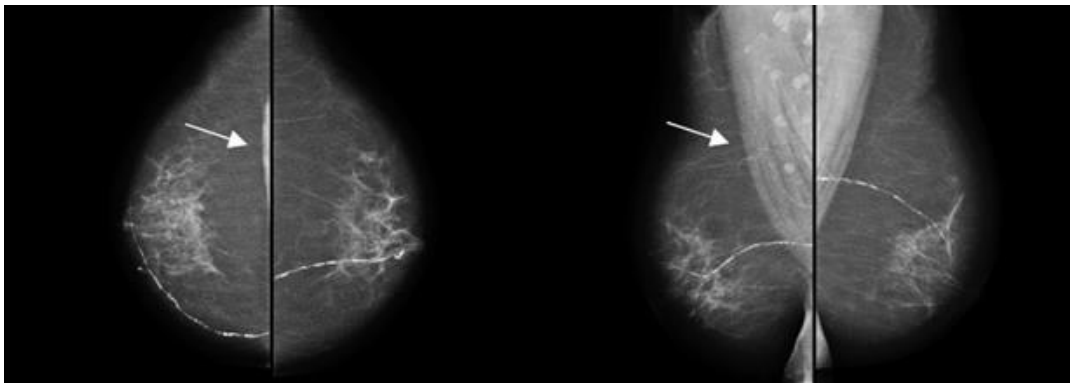

Figure 3.3 Comparison of mammograms with standard compression to mammograms which benefit from the use of the Varjonen et al breast positioning system. Left: standard compression. Right: mammogram with the special positioning system. (Varjonen, Pamilo, Hokka, Hokkanen, & Strömmer, 2007).

Although the proper positioning methods and the use of biphasic compression method (Chapter 3 on page 27) enable a better visualization of the breast structures such as pectoral muscles, there is no need to apply these methods in this research. This is because of the homogeneity of the PVAL breast phantoms. However, it is necessary to see the entire breast phantom/lesion in the mammograms in order to assess the image quality such as contrast, noise, and sharpness.

The compression methods discussed in this chapter use either objective (mathematical) or subjective (visual) methods in order to assess the image quality. This research is aimed to cover the objective and subjective methods for the assessment of the acquired mammographic images.

Chapter 4 Physical breast phantoms

Mammographic breast imaging research requires the use of ionising radiation during the capture of medical images. Due to the risk associated with the use of ionising radiation on living human breasts, synthetic anthropomorphic breast phantoms are utilised in breast related experiments. Phantoms are designed objects in medical imaging research to replace the real tissue when using the living human is inappropriate (Surry, Austin, Fenster, & Peters, 2004)

In breast research, depending on the nature of the study, various types of breast phantoms have been employed. Types of breast phantoms can be classified into two categories: compressible phantoms and non-compressible phantoms. Compressible phantoms resemble human breasts in terms of flexibility and can be used in mammography procedures as well as biopsy training. Whereas non-compressible phantoms have very specific imaging structures and are typically used for quality control procedures and dosimetry.

4.1 Compressible Breast Phantoms

Price et al. (2010) introduced a compressible breast phantom comprising freeze-thawed polyvinyl alcohol (PVAL) in ethanol and water. This solid and elastically compressible gel with the concentration between 5% and 20% has a linear attenuation coefficient ranging from 0.76 cm^{-1} to 0.86 cm^{-1} at 17.5 keV which is similar to the published (Johns & Yaffe, 1987) values of breast tissue at the same energy. In this research, heavy metal salt such as barium chloride was suggested to use in order to increase the attenuation. This increase was to simulate the attenuation coefficient of fibrous or cancer lesions (Price, Gibson, Tan, & Royle, 2010).

Silva et al. (2010) produced a compressible breast phantom. This was obtained from gel paraffin and self-polymerizing acrylic with inserted silicone implant. This phantom was utilised to evaluate the effect of the implant on the visibility of the mammographic findings such as microcalcifications. In this research, Nylon thread, ground porcelain and nylon masses were used to simulate fibres, microcalcifications and cancer lesions (Figure 4.1) (Silva, Souza, Salmon, & Souza, 2010). This research has shown that the insertion of prosthesis into the breast reduces visibility of the breast tissue.

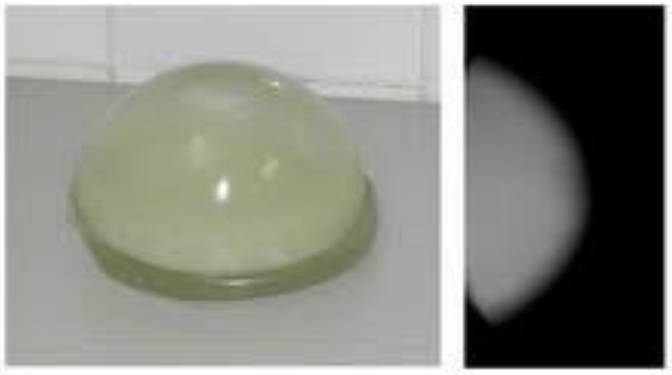

Figure 4.1 Phantom with silicone implants (Silva, Souza, Salmon, & Souza, 2010)

An example of a compressible phantom which is used in ultrasound guided needle biopsy is produced by Kyoto Kagaku Co. As the image in Figure 4.2 shows, the phantom can be used with an ultrasound scanner and biopsy needle simultaneously. The targets, red and yellow simulated lesions, are positioned in three layers. These lesions have different echogenicities (see glossary on page 305).

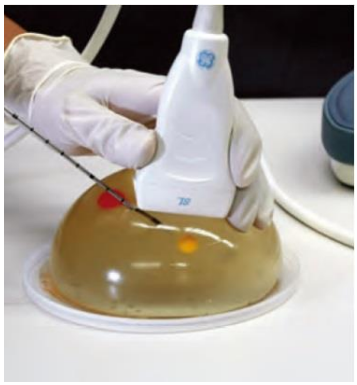

Figure 4.2 Ultrasound guided needle biopsy needle phantom (Kyoto Kagaku).

Another deformable phantom created by Kyoto Kagaku Co. is the breast ultrasound examination phantom (Figure 4.3) known as BREASTFAN. This is designed for use in breast ultrasound examination training. This phantom contains simulated lesions such as benign, malignant and cyst with different echogenicities (Kyoto Kagaku).

Figure 4.3 Breast ultrasound examination phantom (Kyoto Kagaku)

The Stereotactic Breast Biopsy Phantom (Figure 4.4) is another type of biopsy training breast phantom. This phantom contains multiple radiopaque lesions. The phantom is made of clear gel covered in soft skin-like vinyl layer. The stereotactic breast biopsy phantom is compressible with a biopsy instrument.

Figure 4.4 Stereotactic Breast Biopsy Phantom (Gammex Inc., 2014)

4.2 NON-COMPRESSIBLE BREAST PHANTOMS

Gammex Inc. produce a non-compressible anthropomorphic breast phantom referred to as the "Rachel" breast phantom (Figure 4.5). This phantom provides a mammogram with breast feature detail (Gammex Inc., 2014).

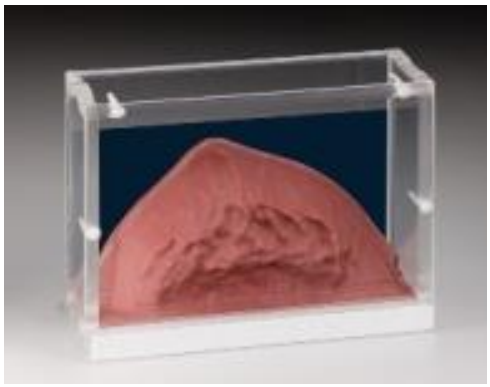

Figure 4.5 Anthropomorphic Rachel breast phantom (Gammex Inc., 2014)

Yip et al. have produced another type of non-compressible phantom in their study: ROC curve analysis of lesion detectability on phantoms. In these phantoms, layers of grapefruit fibre were placed on a slab of Lucite to build the phantom. Egg shells and chalk powder were then used to simulate the high and moderate contrast microcalcifications. Circular pieces of X-ray film and aluminium foil were employed to simulate low contrast lesions (Yip, Pang, Yim, & Kwok, 2001).

Almeida et al. have used non-compressible breast phantoms to study dosimetry. Breast Tissue Equivalent (BTE) is one of the non-compressible phantoms that they have used to measure the air kerma and glandular dose in mammography. These semi-circular phantoms (Figure 4.6) have been found to have both adequate density and attenuation properties similar to fat and glandular tissues of human breasts.

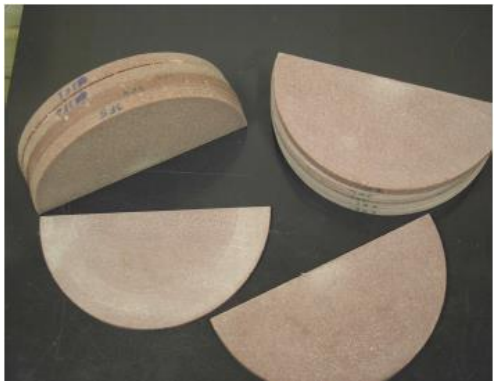

Figure 4.6 BTE Phantoms (Almeida, Coutinho, Peixoto, & Dantas, 2009)

The Contrast Detail Mammography (CDMAM) phantoms (Figure 4.7) are non-compressible phantoms produced by Artinis Medical Systems for use in quality control in mammography. These phantoms are used to detect the low contrast and small details since viewing the low contrast and small findings are necessary in mammography. These phantoms are utilised for quality control of the mammography units at regular time intervals.

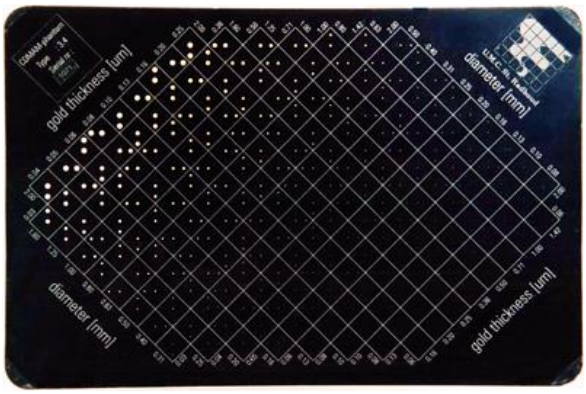

Figure 4.7 CDMAM phantom (Artinis Medical Systems)

4.3 ASSESSMENT OF THE AVAILABLE BREAST PHANTOMS

In this research, a compressible breast phantom with X-ray and mechanical properties similar to human breast tissue is required. Various breast phantoms were discussed in this chapter. These breast phantoms are utilised for specific purposes such as biopsy training, teaching the anatomy of the breast and its abnormalities, and mammographic quality control.

Two categories of breast phantoms were discussed earlier: compressible phantoms (4.1 on page 29) and non-compressible phantoms (4.2 on page 32). As this research focuses on the effect of compression on lesion visibility, non-compressible phantoms such as CDMAM and Rachel are not suitable for the mammography procedure of this research.

Along with having similarity in the compression characteristics of the breast phantom to human breast tissue, this research is looking at the visibility of lesions within the phantom and needs to have X-ray imaging properties that are consistent with human breast tissue. The compressible breast phantoms utilised in ultrasound are not suitable for the mammography part of this research. This is because the imaging principles of the X-ray based mammography and sound wave based ultrasound are different and also the mechanism of compression in mammography is completely different from ultrasound.

The focus of the compressible breast phantom with inserted silicon was on the effect of the silicone prosthesis in mammography images. The mechanical properties of theses phantoms have not been measured. Therefore they cannot be considered as anthropomorphic or tissue-mimicking breast phantoms.

Among the compressible phantoms mentioned above, the polyvinyl alcohol (PVAL) breast phantom designed by Price and his colleagues could be utilised in this research. However, the usage of ethanol and barium chloride presents significant health and safety risks and also creates a need to safely dispose of these hazardous substances (University of Guelph, 2002). Therefore, a water-based phantom was produced in order to pursue the objectives of this research.

Chapter 5 Computerised phantom models

Computerised phantoms have become widely used in medical imaging research (Li, Segars, Lo, Veress, Boone, & Dobbins III, 2008). These phantoms are capable of simulating the human anatomy and physiology. This simulation of real human tissues and their mechanisms can be utilised to improve the medical imaging modalities and techniques (Segars & Tsui, 2009). This chapter aims to discuss computerised phantoms as possible alternative for physical phantoms and explain why these phantoms have not been used in this research.

There are a number of advantages of using computerised phantoms over physical phantoms. Physical phantoms such as PVAL are material-based; therefore they can deteriorate over a period of time while computerised phantoms do not. Computerised phantoms can be transferred nationwide digitally, whereas physical phantoms have to be relocated physically. Replicating physical phantoms is more difficult than generating the computerised replicates. Although these phantoms are beneficial in biomedical research, they have many limitations which are discussed later in this chapter (5.4 on page 50).

Computerised phantoms are classified into three categories: voxelized phantoms, mathematical phantoms, and hybrid phantoms. Voxelized phantoms are realistic phantoms based on actual patient data acquired from CT or MRI images. In these phantoms, the patient's 3D image is segmented and a unique index value is assigned to each segmented area. Since these computerised phantoms are dependent on a particular patient's anatomy, it is hard to implement anatomical variations or patient motions (Ljungberg, Strand, & King, 2013). In order to overcome these disadvantages, numerous models based on various patient datasets have to be assembled. As these models require

individual segmentation, a great amount of modelling and time will be needed in order to simulate anatomical variations and patient motions (Ljungberg, Strand, & King, 2013).

Mathematical phantoms (also known as numerical phantoms) are computer software based methods to implement and display the human tissue and its motions and deformations on the computer screen (Yan, Gu, Huang, Lv, Yu, & Kong, 2007). So far, many mathematical models have been used in simulation of human tissue and its deformation. Two examples of mathematical models are Mass-Spring (Hammer, Sacks, del Nido, & Howe, 2011) and linear elastic FEM (Finite Element Modelling) (Bro-nielsen, 1998). These models all have their own limitation factors when it comes to physically realistic modelling of human tissue and its deformation. The models mentioned above can work well with small strains and local deformations, but they suffer from simulation of large global deformation modelling such as large twisting or bending of the tissue (Yan, Gu, Huang, Lv, Yu, & Kong, 2007). Unlike voxelized phantoms, mathematical phantoms suffer from not being able to adequately represent the real anatomical features of the body. This problem resulted in inventing another classification for the computerised phantoms called hybrid.

Hybrid phantoms are a combination of the patient-based voxelized phantoms and the equation-based mathematical phantoms with the assistance of computer graphics. A hybrid phantom is initially produced from a voxelized model of segmented 3D patient images such as MR or CT images. Then the complex anatomical structures are modelled utilizing Non Uniform Rational B-splines (NURBS) and subdivision surfaces (see glossary on page 305) (Cashman, 2010). Examples of hybrid phantoms are Four dimensional Mathematical Cardiac-Torso (4D MCAT), 4D NURBS-based Cardiac, and 4D extended Cardiac-Torso (XCAT) (Segars & Tsui, 2009).

5.1 VOXELIZED BREAST PHANTOMS

A voxelized breast phantom with anatomical features was introduced by Bliznakova and his colleagues. This phantom consists of the breast surface, the duct system, cooper's ligaments, the pectoral muscle, the background and the breast abnormalities (Figure 5.1). In order to compare the image of the synthetic mathematical phantom with the real breast, the synthetic mammograms from the monoenergetic fan beams were generated. The subjective and objective assessments of the real and synthetic mammograms revealed a good correlation between the phantom/lesion and the real breast/lesion. Although this model contains good anatomical features, it does not provide the breast compressibility (Bliznakova, Bliznakov, Bravou, Kolitsi, & Pallikarakis, 2003).

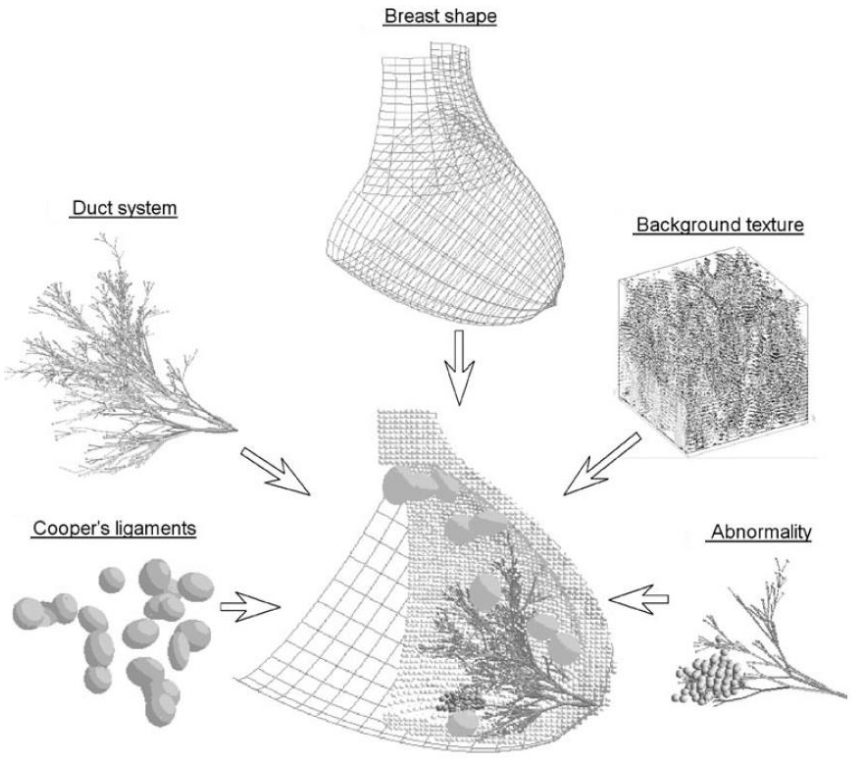

Figure 5.1 Numerical breast compositions (Bliznakova, Bliznakov, Bravou, Kolitsi, & Pallikarakis, 2003)

In this model, an elongated semi-ellipsoid and an elongated semi-hyperboloid has two geometrical primitives composed the breast. The next step was the simulation of the ductal system using a group of cylinders. It is worth mentioning that all the measures such as the radius, height and direction of ductal system were assigned accurately to the breast phantom ductal components. The background texture simulates the fat, fibrous and connective tissues. The background is shown by a 256x256x256 voxel matrix. Each voxel was 1 mm^3. A power spectrum method (Veenland, Grashuis, van der Meer, Beckers, & Gelsema, 1996) was employed to produce the synthetic fractal images (see "Description of 3D background matrix formation" from (Bliznakova, Bliznakov, Bravou, Kolitsi, & Pallikarakis, 2003)). Cooper's ligaments are modelled as ellipsoid shells, located at random positions in the breast model. The abnormalities can be round, oval, elongated and irregular shapes. The user can define size, location, numbers and attenuation coefficient corresponding to the type of the abnormality. This means that, by changing the lesion's parameters, the level of malignancy can be changed. In order to generate the irregular lesions, a 3D random walking algorithm (Kaplan & Glass, 1995) was utilised.

After constructing the breast model, the simulation of the radiographic imaging process was performed using the Lazos method (Lazos, Kolisti, & Pallikarakis, 2000). The following image (Figure 5.2) shows the synthetic mammograms versus real mammograms. The mammograms of real breast and synthetic illustrate three types of breast composition; dense (a), (b), fatty-glandular (c), (d), and fatty (e), (f).

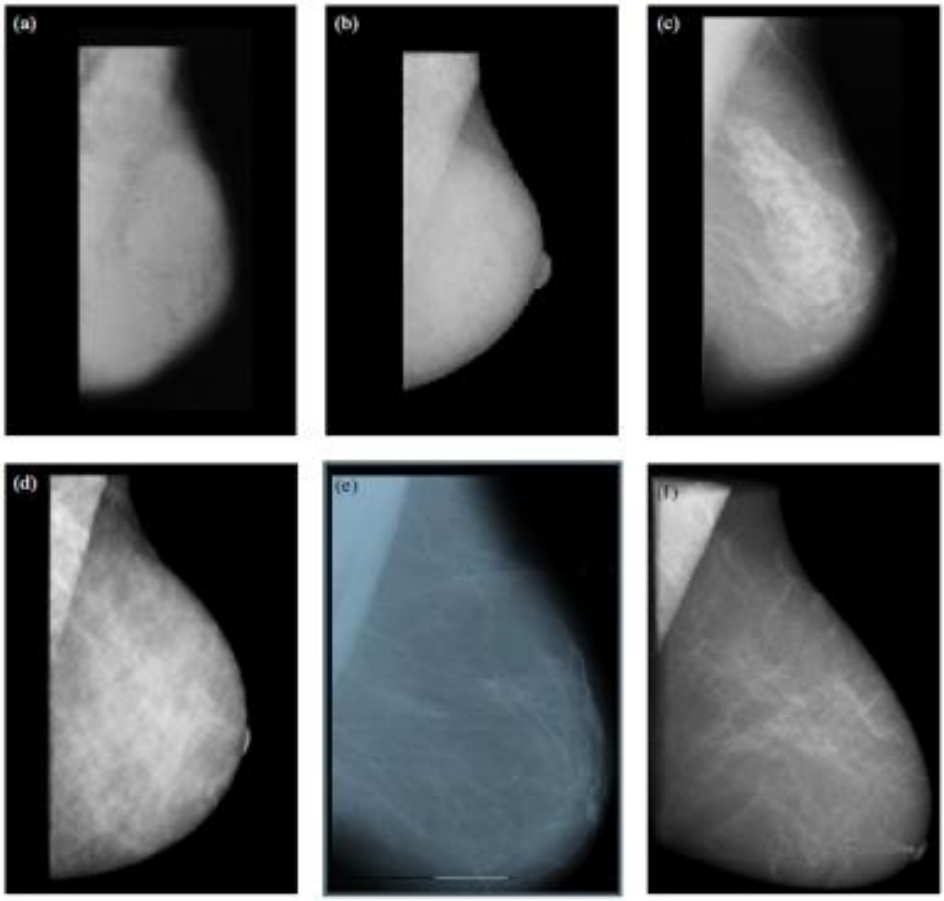

Figure 5.2 Comparison of real mammogram images to synthetic images. (a),(c), and (e) were acquired from the real breast and (b), (d), and (f) were synthetic (Bliznakova, Bliznakov, Bravou, Kolitsi, & Pallikarakis, 2003)

In a study by Saunders and et al., a voxelized breast phantom and compression force followed by X-ray simulated images illustrated how the quality of medical images can be affected by compression force (Saunders & Samei, 2008). The mammography system was simulated using a Monte Carlo algorithm on the Penelope program. A voxelized breast phantom with anatomical structures and breast masses were generated in this system. This model was based on tracking photons through the voxelized breast phantom and following them until they were absorbed by an a-Se based detector. In this study, standard compression and 12.5% reduced compression were simulated. The results

for the reduced compression demonstrated higher scatter fractions as expected. It also showed that the reduced compression reduces the glandular dose for the constant photon flux. According to this study, the breast compression can be reduced by about 12% if the total tube output increases by 10% and signal detector reduces by 10%. The reduction of the compression will produce little effect on the image quality (mass conspicuity) or radiation dose (Saunders & Samei, 2008)

5.2 MATHEMATICAL BREAST PHANTOMS

The breast undergoes deformations due to the forces from medical imaging procedures such as compression in mammography, ultrasound or magnetic resonance (MR) and also surgical procedures such as biopsy (Han, et al., 2012). Hence, simulations of breast and its deformation have been carried out by numerous researchers (Ruiter, Stotzka, Gemmeke, Reichenbach, & Kaiser, 2002) (Samani & Plewes, 2004) (Chung, Rajagopal, Nielsen, & Nash, 2008) (Azar, Metaxas, & Schnall, 2001) .

In general, realistic computerised breast models have the potential to help cancer diagnosis, image guided surgery, image registration, and surgical planning (Han, et al., 2012). Predicting the accurate location of the tissue and the lesions utilizing mathematical models might improve the detection of the cancer lesions (Han, et al., 2012).

Simulated mathematical breast phantoms can be also applied in imaging experimentation and training. The training can be achieved by comprehending and interpreting anatomy on mammograms (Bliznakova, Bliznakov, Bravou, Kolitsi, & Pallikarakis, 2003). These phantoms can be used for image quality and dosimetry research, assessing the new technologies such as tomosynthesis, tomographic mammography, and cone-beam volume CT. These models might be cost effective,

practical, and flexible compared to physical phantoms (Bliznakova, Bliznakov, Bravou, Kolitsi, & Pallikarakis, 2003).

5.2.1 Common Mathematical Methods

Two common mathematical models which simulate the breast tissue and the deformation of it under compression are finite element (FE) and mass spring models.

The finite element model (FEM) is one of the widespread applied methods in mathematical modelling (Unlu, et al., 2005). In this method, small interconnected components known as “finite elements” are employed to simulate real objects. The elements are connected to each other at locations called nodes on the surface of the finite elements (Unlu, et al., 2005). Basically, nodes represent geometric locations and define the element boundary in the model.

One of the first steps in implementing the FE models is generating a geometrical mesh. This mesh is essentially based on patient data from the three dimensional MR or CT images. The acquired mesh represents the structure of interest in the research. Mesh generation is a complicated, time consuming and tedious task (Samani, Bishop, Yaffe, & Plewes, 2001). The following image (Figure 5.3) shows the finite element mash constructed with triangular finite elements (del Palomar, Calvo, Herrero, López, & Doblaré, 2008).

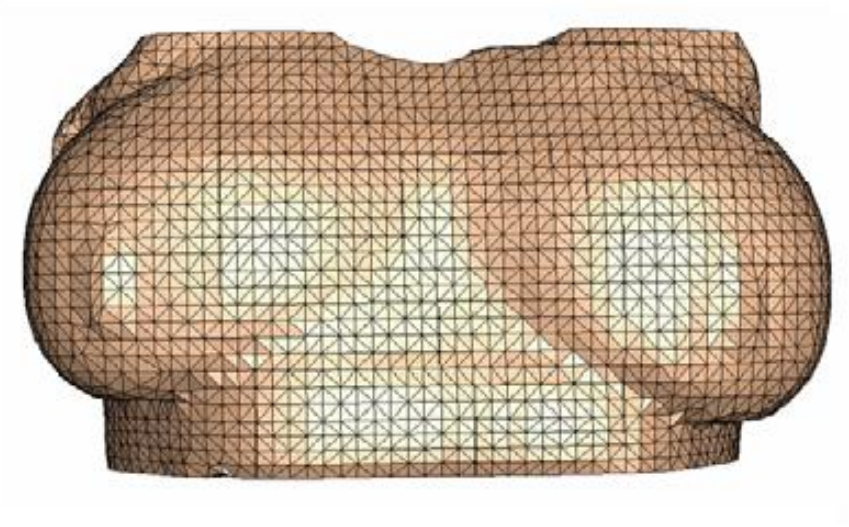

Figure 5.3 Finite element mesh to simulate numerical breast

5.2.1.1 Finite element breast models

Stewart et al. (2011) have used a finite element model to simulate compression during an MR guided biopsy. In this study, a lesion was designed in the breast model. Since, the female breast has nonlinear characteristics; the hyperelastic nonlinear geometry and nonlinear material theory were considered in this modelling (details are out of scope for this research). The linear tetrahedral Herrmann formulated (5-node isoparametric element) finite element (Figure 5.4) was used to discretize the FE breast mesh (Stewart, Smith, & Hall, 2011).

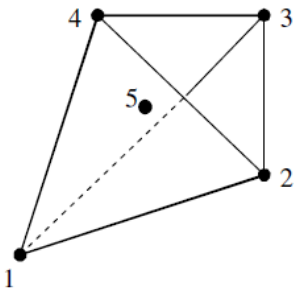

Figure 5.4 Linear tetrahedral Herrmann formulated element (Stewart, Smith, & Hall, 2011)

The FE model suggested in this study starts from the images acquired from the MR imaging. In this model the breast was considered as a combination of fat and glandular tissues. Therefore, other breast features such as blood vessels, cooper's ligaments, and pectoral muscles were not added to this FE model.

First, an MR image of a breast containing a non-invasive lesion was acquired as a reference. The next step was the construction of the mesh which happens in multiple steps. First, displaying the MR image in 3D utilizing a piece of software (ANALYZE) (AnalyzeDirect, 2010) to segment the breast image and the lesion surface separately. After the segmentation process, the surface of the breast/lesion for the FE analyses was generated utilizing the HyperMesh software (Altair Engineering, 2010). The output of these processes was the discretization of the breast and lesion separately constructing 10,915 tetrahedral elements for the breast surface and 1,562 tetrahedral elements for the lesion. The next step was to tie the breast nodes and the lesion nodes together employing a kinematic constraint (Stewart, Smith, & Hall, 2011).

The total breast volume and the fat tissue volume were measured from the MR image in order to be utilised in the material properties calculations. Material properties such as Young's Modulus were assigned to the breast model and the lesion based on the volume fraction rule (Wellman's equation) (Wellman, 1999). The next step was measuring the displacement vector to each surface node in order to use in displacement measurement due to the compression force. The finite element analysis in this model was the comparison between the displacement of the lesion in the MR and the mathematical model. The last step was the modelling of compression force. The following diagram displays the FE breast model construction in this research (Figure 5.5). The readers are referred to the original literature for the details of this model (Stewart, Smith, & Hall, 2011).

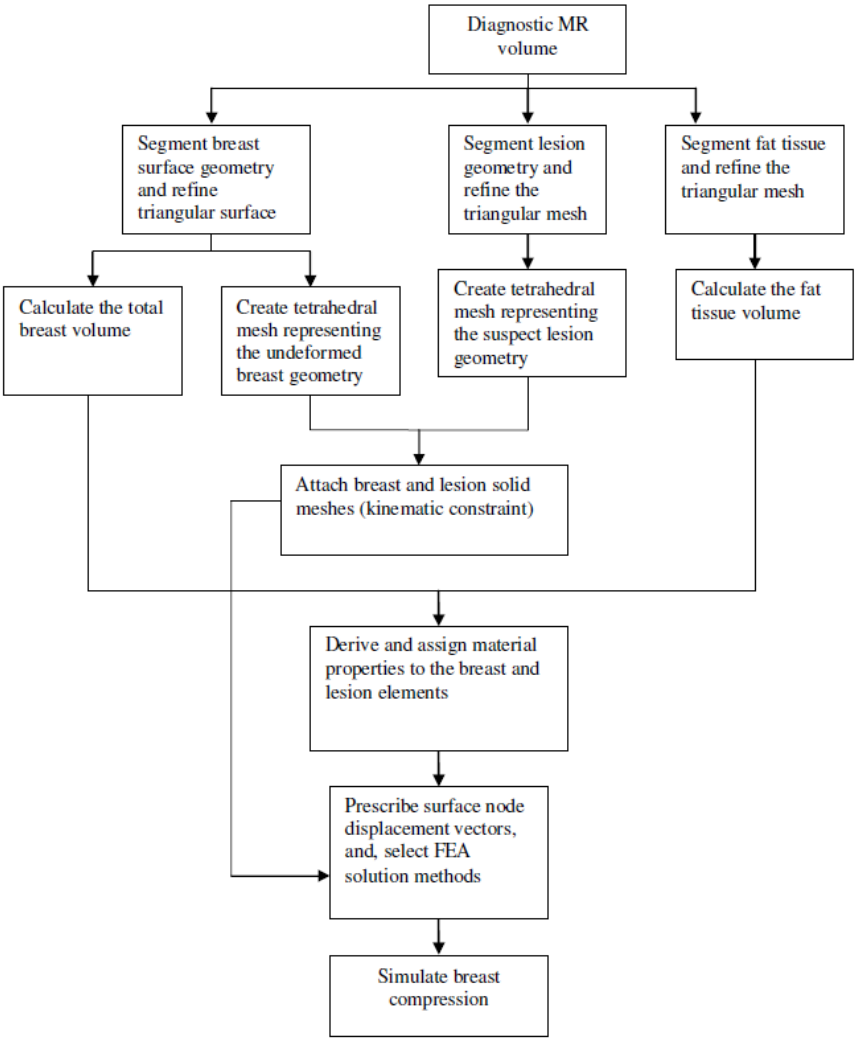

Figure 5.5 Overview of the proposed FE breast model construction

In biomedical engineering, finite elements have been widely used as mathematical models to simulate deformable tissues. Although these models enable the researchers to simulate the tissues with various complex geometrical shapes, they have multiple drawbacks. Drawbacks include the complexity of mesh generation, and time consuming processes to solve the deformation of the model (large deformations). Errors introduced from the selection of the material properties and boundary conditions are other issues

with these models (Tanner, Hipwell, & Hawkes, 2008) (Samani, Bishop, Yaffe, & Plewes, 2001).

5.2.1.2 Mass spring system

Among all the deformable mathematical models, mass spring is the simplest and most computationally efficient (Jarrousse, 2011). This modeling is suitable for simulating the dynamic character of complex single or multi-organ tissues. Although this model compared to the FE model is more practical to implement and more effective in computation, it has remarkably lower accuracy (Wang, Xiong, & Xu, 2006). Non-realistic mechanical properties for the simulated tissues were one of the reasons for low accuracy of this model. Complex calculations regarding the spring forces and non-constant stiffness spring are required to address the problems with the mechanical properties of the tissues (Patete, et al., 2013).

This model has been used by Patete and his colleagues for computer assisted breast surgery (Patete, et al., 2013). Similar to the FE breast models, this model uses a computer mesh (Figure 5.6) based on the MR images before and after compression to simulate the human breast. The segmentation of the MR images was based on the Fuzzy C-Means (FCM) algorithm followed by a Gaussian Hidden Markov Random Field (GHMRF) model-based procedure (Patete, et al., 2013). A tetrahedral mesh generation algorithm was applied to produce a volumetric 3D mesh of the volume of interest representing skin, fat and mammary glands. The algorithm for the deformation of the model was based on a mass-spring model. In this model, each tetrahedron edge was represented by a pure elastic spring. The dynamic behaviour of the each tetrahedron edge was defined by Hook's law and the calculation of the displacement of each vertex was measured through the Verlet numerical integration (Verlet, 1967). Similar to other

numerical breast models, this model requires further robust investigation to predict breast deformations accurately (Patete, et al., 2013).

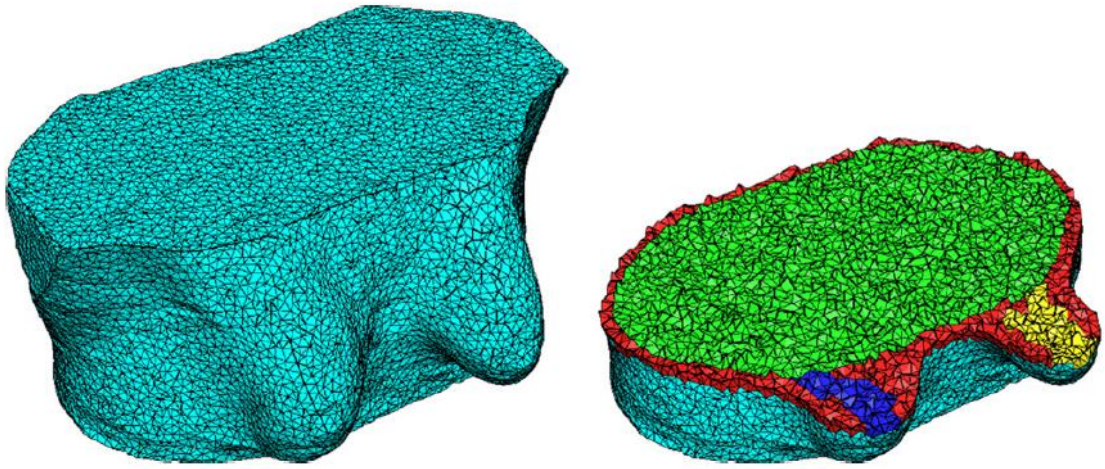

Figure 5.6 MR-based tetrahedral mesh - Left: complete mesh - Right: internal structure (Patete, et al., 2013)

5.2.2 Material properties in mathematical models

Researchers have given wide range of values for the material properties of various types of the tissues mainly from ex-vivo experimental data. According to various studies, fibroglandular and fat tissues as main constituents of the breast follow the exponential, hyperelastic (Neo-Hookean, Mooney-Rivlin, Ogden, Arruda-Boyce, and polynomial models) (Han, et al., 2012), or linear elastic stress-strain relationships. Therefore, various material models have been employed in different research such as hyperelastic and exponential models (del Palomar, Calvo, Herrero, López, & Doblaré, 2008)

5.2.3 Software packages used in mathematical modelling

ABAQUS, HyperWorks, LS-DYNA (Exponent Inc., 2010) and ANSYS (Tanner, Schnabel, Smith, Sonoda, Hill, & Hawkes, 2002) are all commercial software packages which are capable of FE modelling. Segmentation and displacement measuring can be

carried out utilizing Scion Image (Azar, Metaxas, & Schnall, 2000). Borland C, C and other programming languages have been used in some of the studies in order to simulate human anatomy such as breast tissue (Bliznakova, Bliznakov, Bravou, Kolitsi, & Pallikarakis, 2003).

5.3 HYBRID BREAST PHANTOMS

In a research by Li et al. a mathematical breast phantom was created by generating a polygon mesh from the segmented CT data (Li, Segars, Lo, Veress, Boone, & Dobbins III, 2008). A marching cubes algorithm was utilised to generate the mesh. Then the mesh underwent a subdivision surface model in order to join into the NURBS-based cardiac-torso (NCAT) phantom (Figure 5.7).

A simple compression model was designed and implemented in order to display the deformation of the breast phantom. The mechanical properties of various features of the breast were not considered in the breast compression algorithm (Li, Segars, Lo, Veress, Boone, & Dobbins III, 2008).

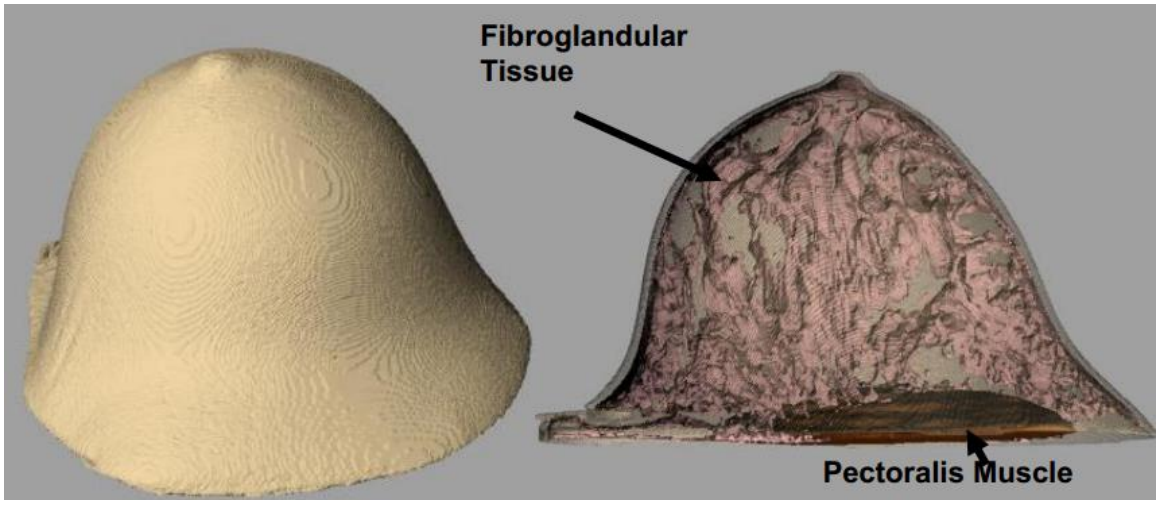

Figure 5.7 Three-Dimensional Computer Generated Breast Phantom Left: Skin surface- Right: inner structure surfaces (Li, Segars, Lo, Veress, Boone, & Dobbins III, 2008)

In order to verify the appearance of the simulated phantom before and after compression, a noise free X-ray imaging simulator was utilised to produce the synthetic images. The following image (Figure 5.8) illustrates the simulated craniocaudal (CC) projection of a synthetic breast versus a real breast mammogram (Li, Segars, Lo, Veress, Boone, & Dobbins III, 2008).

Although this model displays the breast structures and the deformation of the breast, a more accurate delineation of the internal breast features is required in this phantom in order to properly simulate a human breast. Similarly, the simulation of breast compression needs to be improved (Li, Segars, Lo, Veress, Boone, & Dobbins III, 2008).

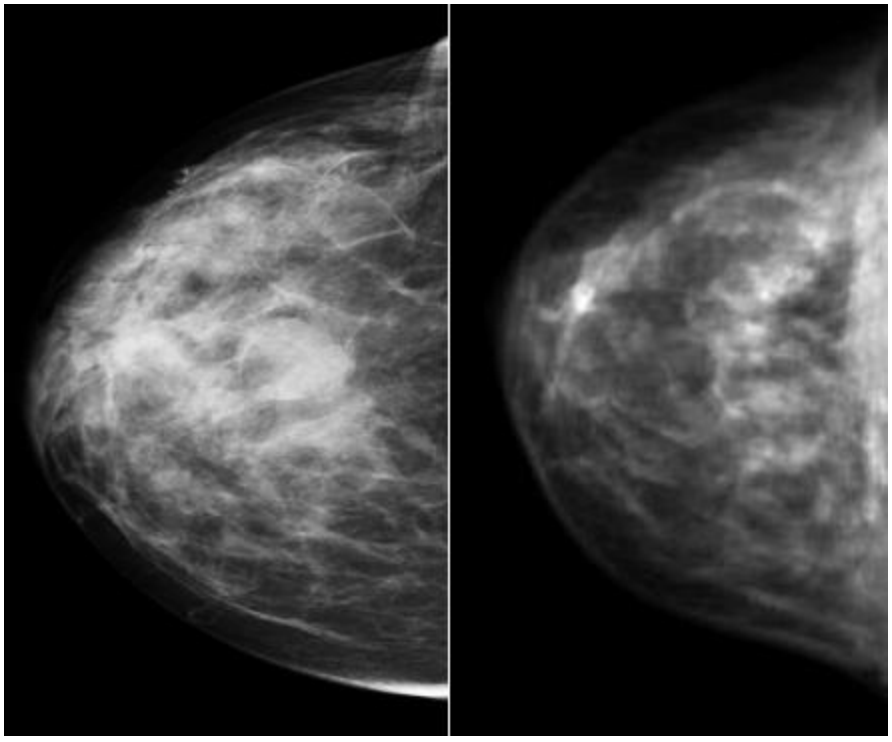

Figure 5.8 Simulated craniocaudal (CC) projection of a synthetic breast versus a real breast mammogram. Left: real mammogram - Right: synthetic (Li, Segars, Lo, Veress, Boone, & Dobbins III, 2008)

5.4 CHALLENGES WITH USING COMPUTERISED PHANTOMS

In real mammograms, a good contrast is essential in order to detect abnormalities, especially microcalcifications. Therefore, simulating an adequate contrast in computerised phantoms is required. One of the drawbacks of the computerised phantoms compared to the real mammograms is generating a good background contrast (Bliznakova, Bliznakov, Bravou, Kolitsi, & Pallikarakis, 2003). Insufficient contrast can hide the simulated breast texture in mammograms. Therefore, this is one issue that has to be addressed in computerised models.

In mathematical models, the evaluation of the performance of an imaging modality is dependent upon the level of accuracy of the imaging hardware being simulated. However, in the employment of physical phantoms, the real hardware (mammography equipment) can be utilised and configured during the imaging procedure (Markey, 2013). Utilizing the Monte Carlo algorithm on the Penelope program by Saunders et al. is an example of simulating the mammography system rather than direct use of it (Saunders & Samei, 2008).

Constructing heterogeneous models containing breast tissues are additional challenges to address in mathematical modelling. These tissues include adipose, fibroglandular, pectoral muscles, Cooper's ligament and skin. Unlike other body parts, each breast has its own specific structural map, and each component of this structure has its own mechanical properties which can change over time. These variations make the computation of computerised phantoms difficult and might not let researchers take all the parameters into consideration.

There are also numerical challenges associated with the simulation of mechanical friction generated from the contact of the breast phantom and the paddle which have to be taken into consideration (Chung, Rajagopal, Nielsen, & Nash, 2008).

Complex algorithms (Azar, Metaxas, & Schnall, 2002) and time consuming computation (Han, et al., 2012) are other reasons that physical phantoms are still constructed and applied in studies such as image quality and dosimetry.

One of the main differences between the computerised modelling and the physical phantoms is the requirement of the human MR or CT images before and after tissue deformation (for example breast compression) in order to simulate the models. The real human images are necessary to validate the models by measuring the amount of displacement of the tissue/lesion in the image versus the predicted displacement using the mathematical model. This requires a time consuming imaging procedure which can be eliminated by fabricating physical phantoms (del Palomar, Calvo, Herrero, López, & Doblaré, 2008) (Samani, Bishop, Yaffe, & Plewes, 2001).

Chapter 6 Mammography

6.1 MAMMOGRAPHY

Mammography is a well-established process which employs low-energy X-rays to examine the breast tissue and detect cancer tumors at early stages. This imaging modality can be used as both a diagnostic tool and a screening tool. Mammography, as a screening tool, has reduced breast cancer mortality due to the early detection of breast tumors and microcalcifications. Research shows that breast screening decreases the number of deaths from breast cancer by about 1,300 a year in the UK (Cancer Research UK, 2014). Although sensitivity of the mammography procedure varies with age and breast density (Kolb, Lichy, & Newhouse, 2002), it is still has the highest demand of the medical imaging modalities (Robson, 2010). The X-ray risks associated with this imaging procedure is far below the risk of breast cancer. Therefore it should not stop women opting for the procedure (Heywang-Köbrunner, Hacker, & Sedlacek, 2011) (Yaffe & Mainprize, 2011).

Research shows the invention of full field digital mammography (FFDM) has improved the accuracy of imaging of denser breasts for women younger than 50 years compared to screen-film systems (Pisano, et al., 2008). Interestingly, this research could not show the significance of the performance improvement of FFDM for women aged 65 years or older with fatty breasts. Although the entire sample size in this research was over 4000 participants utilising various types of mammography units, the subgroup for this particular age range (65+) may not have been large enough for the analysis. Another reason for this disagreement between the results could be the low number of observers which was two radiologists, one for digital and one for screen-film mammography.

In England, the NHS offers FFDM from the age of 47 to 73. Women older than 73 can opt to be screened every 3 years by their local breast screening centre (Cancer Research UK, 2014).

Before the development of the mammography imaging technique, breast imaging was performed employing conventional X-ray systems. The use of conventional X-ray systems resulted in higher radiation doses and lower image quality. The invention of the mammography unit with improved target/filters, focal spots, Automatic Exposure Control (AEC) systems, tube voltage, and high dynamic range made this modality desirable in breast imaging. Another benefit was in the elimination of the screen film imaging technique. This allowed for the separation of the image acquisition from the display of the acquired image (Robson, 2010) and the capability of reading the acquired images in near real time.

The advantages of FFDM over the screen film (SF) have made this imaging modality popular worldwide over the last decade. One advantage of FFDM over SD is the elimination of film processing including the storage and retrieval of the films. FFDM also allows for the ability to post-process the captured images rather than having to capture an additional image in conventional X-ray systems. As the images are digital, telemammography can be achieved and the mammograms can be shared digitally. FFDM also creates the ability to change the contrast and brightness of the images after the images have been acquired. Compared to a conventional X-ray, FFDM patients receive a lower radiation dose (Hambly, McNicholas, Phelan, Hargaden, O'Doherty, & Flanagan, 2009).

Despite all the advantages of utilizing the mammographic imaging and all the technical improvements over time, mammography still suffers from some drawbacks. One of the problems present in mammography is that this imaging modality uses a two-

dimensional image to represent a three-dimensional object. In the two-dimensional radiograph, the resulting image is the summation (line integral) of the attenuation present along a certain path. Therefore, a low-contrast object can be fully masked by dense tissue above or below the low-contrast object (superimposition). This problem can have a bigger effect on denser breasts due to the close attenuation of the lesions and dense breast tissue. The problem with superimposition and masking in mammography can increase the number of false-positive and false-negative cases (Robson, 2010).

Digital breast tomosynthesis (DBT) is a three dimensional mammography procedure which minimizes the effect of overlapping breast tissue during imaging. In this breast imaging technique a reconstructed image is created from the data acquired at a limited number of views over a limited number of arc angles. In this modality, specific reconstruction techniques such as shift-and-add and filtered back projection are employed in order to form three dimensional images from two dimensional projections. At a workstation, similar to CT, a series of images (for example 0.5 mm thickness) are presented to the radiographers. These individual image slices allow better visualization of the lesions and lesion margins. One of the disadvantages of this imaging modality is that different manufacturers apply various techniques to develop and perform tomosynthesis. These variations can produce different clinical results (Helvie, 2010).

One of the initial concerns regarding digital radiography in general was that FFDM has a lower spatial resolution compared with SF systems. It was thought that the lower spatial resolution could lead to missing subtle features in the radiographic imaging. However, according to research by Suryanarayanan et al, digital imaging systems have higher dynamic range and detective quantum efficiency (DQE), leading to high contrast resolution (Suryanarayanan, Karellas, Vedantham, Ved, Baker, & D'Orsi, 2002). The results of studies by Fischer et al and by Fischmann et al have also shown an

improvement in image quality. This then leads to better detection of subtle features such as microcalcifications in the breast (Fischer, et al., 2002) (Fischmann, Siegmann, Wersebe, Claussen, & Müller-Schimpfle, 2005).

The results of the Digital Mammographic Imaging Screening Trial (DMIST) as well as numerous results from recent European studies indicate that FFDM has a significantly higher cancer detection rate compared to SF mammography (Pisano, et al., 2008) (Skaane, Hofvind, & Skjennald, 2007) (Vigeland, Klaasen, Klingen, Hofvind, & Skaane, 2008) (del Turco, et al., 2007) (Heddson, Rönnow, Olsson, & Miller, 2007).

6.2 PHYSICS OF MAMMOGRAPHY

In order to accomplish the objectives of this research, the use of a mammography unit was necessary. Therefore, in order to understand the results of utilising the mammography machine appropriately, it was important to know the underlying physics and mechanism of the system. The mammography procedure is an X-ray based modality, therefore, the first step in this scientific journey was to discuss the production and spectrum of the radiation applied to the breast phantoms. The X-ray spectrum has an important effect on image quality and absorbed radiation dose. For more information, Appendix I includes details of the production of X-rays.

Since this research was simulating the real clinical procedures, and in clinical use automatic exposure controls (AEC) are routinely utilised, knowing about the mechanism of AEC was recommended. The main factors that AEC circuits are associated with are kVp, mAs, anode/filter, detectors, SNR, compression force, breast thickness, and breast density. Hence, it was preferred in this research to discuss these subjects briefly.

The following areas are covered in this section: X-ray spectrum, X-rays incident on the detector, low energy in mammography, mammography density, and digital

mammography. Digital mammography is categorized into digital (DR) and computed (CR). Both classifications are briefly discussed in this chapter.

6.2.1 X-ray spectrum

The X-ray spectrum, specified by the tube energy and the anode/filter combination, has a significant role in image quality and absorbed radiation dose (Boone, Fewel, & Jennings, 1997). In mammography a low energy X-ray beam is required in order to visualize subtle density differences between normal and abnormal tissues. A mammography unit is equipped with special anode/filter configurations to operate in the appropriate kVp range. The suggested typical range for kVp varies among multiple studies. For example, 24-32 kVp as a typical range was suggested by the International Atomic Energy Agency (IAEA) while 18-42 kVp was considered a range for traditional mammography by Zhang et al. (Zhang, Li, & Liua, 2012). The kilovoltage settings of 23–35 kVp were mentioned by Ranger et al. (Ranger, Lo, & Samei, 2010). Variations in kilovoltage settings among different studies might be because of the use of various models of mammography units from different manufacturers.

In a typical mammography unit, the anode/filter combinations are typically, molybdenum/molybdenum (Mo/Mo) or molybdenum/rhodium (Mo/Rh). Some of the mammographic units are equipped with a dual-track anode which allows the mammographer or the mammography unit using AEC to select either molybdenum or rhodium (Sprawls, 1995). Additionally, because of advances in new digital detectors, other types of anode/filter combinations such as rhodium/rhodium (Rh/Rh), and tungsten/rhodium (W/Rh) can be utilised in the mammographic systems (Chevalier, Leyton, Tavares, Oliveira, da Silva, & Peixoto, 2012). Although Mo/Mo or Mo/Rh are commonly used in mammography (for example, Hologic Selenia), research shows that

the W/Rh target/filter is the best choice in terms of image quality at a lower dose. This target/filter combination is capable of working as the best choice for all breast thicknesses and breast compositions to detect lesions and microcalcifications (Baldelli, Phelan, & Egan, 2010).

In mammography, the molybdenum energy spectrum consists of characteristic and a Bremsstrahlung continuum energies (Figure 6.1). Molybdenum anode produces two characteristic X-ray energies. These X-ray energies are at 17.9 keV and 19.5 keV respectively. These produce high contrast mammograms for breasts with average thickness. A molybdenum filter removes the beam energies higher than 20 keV and the resulting mammogram is produced with low-energy photons. In other words, most Bremsstrahlung spectrum X-rays above the K-edge energy or the binding energy of the K-shell electrons of 20 keV are cut off utilizing a Mo filter (Figure 6.1). The removal of high energy X-ray radiation above 20 keV improves the subject contrast (Huda & Slone, 2007) (Sprawls, 1995).

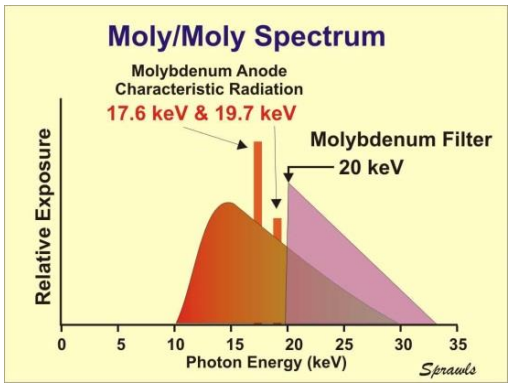

Figure 6.1 Mo/Mo spectrum (Sprawls, 1995)

A rhodium filter which is either selected by the mammographer or the mammography unit using AEC is an alternative filter. This is typically included in mammographic units with double filters. The k-edge boundary is moved to a higher

energy (23.22 keV) compared to Mo filter (20 keV) (Figure 6.2). Shifting to a higher energy means that the Bremsstrahlung radiation between 20 keV and 23.22 keV is included in the X-ray beam. This additional radiation has a higher penetrating energy and can be used for denser or thicker breasts (Sprawls, 1995). For most patients, the Mo/Mo setting is utilised. However, for thicker/denser breasts, a Mo/Rh filter with a higher kVp is automatically selected (Paredes, 2007).

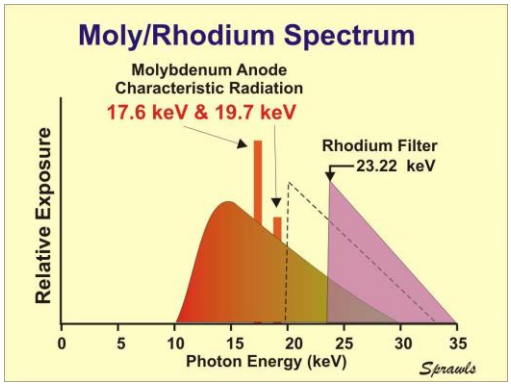

Figure 6.2 Mo/Rh spectrum (Sprawls, 1995)

6.2.2 X-ray interactions in the detectors

X-ray interaction is common among different types of detectors. There are three main atomic reactions between the X-ray photons and the mammographic detectors. These X-ray interactions include: elastic scattering, Compton (inelastic) scattering, and the photoelectric effect (Yaffe, 2010).

In elastic scattering, the emitted photon from the matter has the same energy as the incoming photon. In other words, the energy of the emitted scattered photon does not dissipate after interaction with the matter. In Compton scattering (Figure 6.3), part of the energy of the photon is absorbed when the photon liberates a recoil electron which is a low binding electron. The rest of the energy remains in the scattered photon. This

interaction causes loss of spatial resolution, increase of the noise and decrease of the contrast (Toennies, 2012).

The amount of Compton scattering increases with the increase of photon energy. The scattered photon can be scattered in any direction and also can be hazardous for the radiographers (Fosbinder & Orth, 2011).

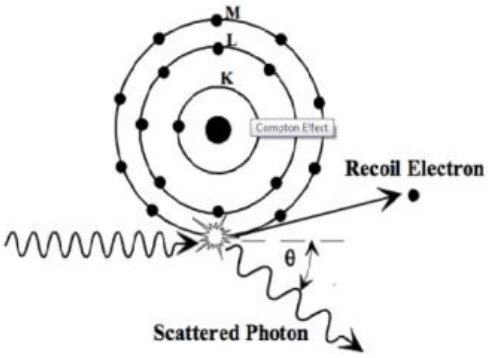

Figure 6.3 X-ray interaction via Compton scatter (Stangl, 2013)

In photoelectric interaction or photoelectric effect (Figure 6.4), the incoming X-ray photon with an energy higher than the electron's binding energy liberates the electron from one of the inner atom shells (K-shell or L-shell). Much of the energy of the photon transfers to this photoelectron. The vacancy of the electron is then refilled by a more loosely bound orbital electron from a higher atomic shell and the rest of the energy is either transferred to a second auger electron or the low-energy fluorescent X-ray (Yaffe, 2010).

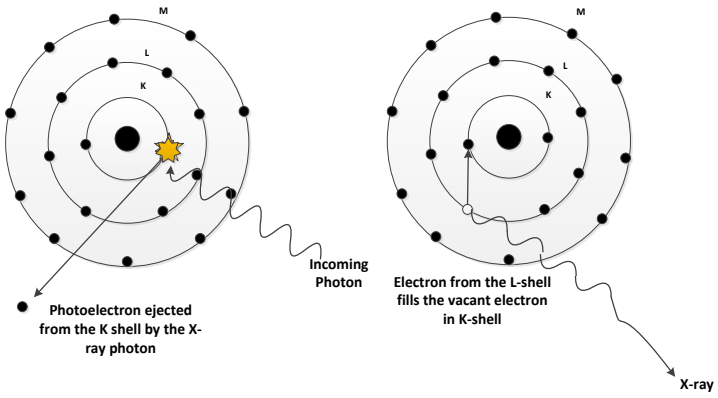

Figure 6.4 X-ray interaction via photoelectric effect. Left: Incoming photon ejects an electron from the inner shell. Most of the energy of the incoming electron transfers to a photoelectron. Right: the vacancy of the electron in the inner shell is filled by an electron from the outer shell

The probability of photoelectric absorption per unit mass is related to the following equation.

$$\frac{Z^3}{E^3}$$

In this equation Z represents the atomic number of the object and E represents the X-ray energy (Bushberg, Seibert, Leidholdt, & Boone, 2012). This equation shows the inverse relationship between the photoelectric interaction and the increase of energy. At low kVp levels, the photoelectric interaction predominates over Compton scattering, whereas at higher kVp levels, Compton interaction occurs mainly. Therefore, since mammography is a low energy procedure, the photoelectric effect is the main X-ray interaction in the detector (Saha, 2013).

The type of material used as detectors has a significant influence on the increase of the photoelectric effect. Suitable detector materials are those with relatively high atomic numbers such as iodine and selenium. At 20 keV, 94% of X-ray interactions will be by photoelectric interaction for iodine and 96% for selenium (Yaffe, 2010). Since photoelectric absorption requires low photon energy and low photon energy is desirable

in mammography in order to produce images with good visibility these detector materials are suitable for mammography.

6.2.2.1 Application of iodine-based contrast agent in mammography

"Attenuation" as a key concept in medical imaging is the removal of photons from a beam of X-rays as it passes through an object. X-ray beams can be attenuated by interaction mechanisms such as scattering and absorption. The photoelectric effect described in (6.2.2 on page 58) can cause the attenuation in soft tissue when the photon energy is low. The occurrence of photoelectric absorption depends on the atomic number of the matter (absorber) and the photon energy

The following graph (Figure 6.5) illustrates the mass attenuation coefficient for tissue and iodine as a function of X-ray energy. The curves show decrease in the attenuation coefficient with the increase of energy. The sudden increase in the attenuation coefficient referred to as "absorption edges" happens because of the increase in the probability of photoelectric absorption. This occurs when the energy of photon exceeds the binding energy of inner-shell electrons such as K shell. One of the reasons that the non-toxic high atomic number element such as iodine can be used to increase the photoelectric interactions is that the range of the energy that is used to start photoelectric interactions is in the diagnostic energy range (Bushberg, Seibert, Leidholdt, & Boone, 2012) (Sprawls, 1995).

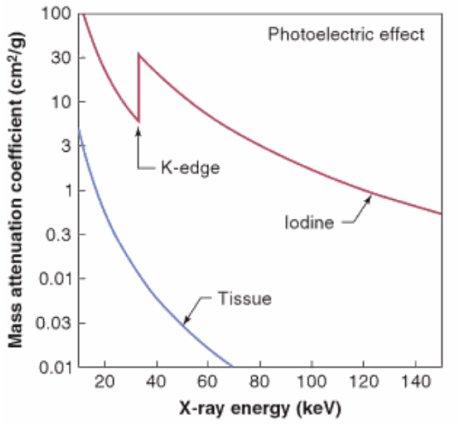

Figure 6.5 Mass attenuation coefficient in relation to X-ray energy (Bushberg, Seibert, Leidholdt, & Boone, 2012)

In this research, a non-ionic iodinated contrast agent called Optiray 320 (DailyMed, 2012) was used to increase the attenuation of the phantom lesions as it was readily available. The contrast agent increases the density and atomic number of the phantom region of interest (University of the West of England, 2010) leading to increase of attenuation coefficient and consequently increase of the Hounsfield unit (HU).

6.2.3 X-rays incident on the detector

As Figure 6.1 and Figure 6.2 illustrate, mammographic systems work based on low-energy photons. In order to explain the reason for using low-energy photons to produce mammograms, the relationship between the thickness of the object of interest in the breast, the attenuation coefficient of the object and the detector are discussed.

As an X-ray photon travels through breast tissue, it reacts differently with the different densities of tissues within the breast. The following schematic diagram of the breast (Figure 6.6) shows two sample paths that an incident photon (X-ray) can travel, A and B. In path A, the X-ray passes through the normal tissue. While in path B, there is a structure such as a lesion with the thickness ‘a’.

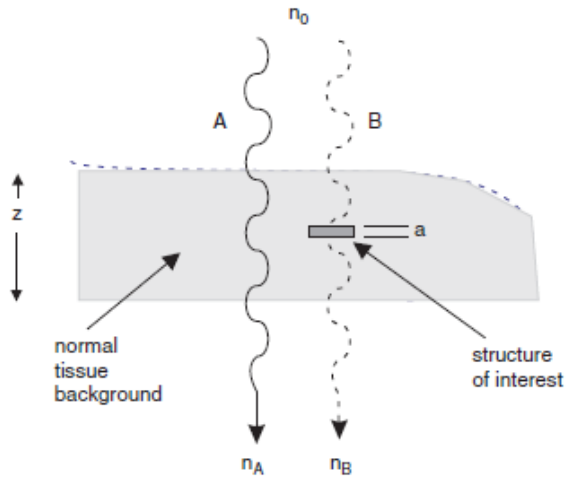

Figure 6.6 X-ray transmission path A: through normal breast tissue B: through sructure of interest (Yaffe, 2010)

In path A, the mean number (n_A) of the X-rays transmitted through the breast tissue with monoenergetic X-ray beam is represented by the following equation.

$$n_A = n_0\, e^{-\mu z}$$

In this equation, n_0 is the mean number of transmitted X-ray beam to the breast, μ is the X-ray attenuation coefficient (see glossary on page 305) of the normal tissue (background) and z is the thickness of the breast.

In path B, the mean number (n_B) of X-rays transmitted through the structure of interest with the thickness of 'a' is represented by the following equation.

$$n_B = n_0\, e^{-\mu(z-a)-\mu' a}$$

In this equation μ′ represents the X-ray attenuation coefficient of the structure of interest. The signal difference between n_A and n_B is calculated with the following equation

$$SD = n_A - n_B$$

The contrast can be defined using the following equation.

$$\frac{n_A - n_B}{n_A + n_B}$$

This contrast is related to the X-ray attenuation coefficient between the background tissue and the structure of interest such as a lesion and the thickness of the structure. This contrast however is not related to the thickness of the breast.

The actual number of X-rays on the detectors is related to the quantum detection efficiency (η). This parameter describes the fraction of X-rays incident on the detector and is related to the attenuation coefficient of the detector based on the X-ray energy and the thickness of the detector. In actuality, the amount of X-rays detected for paths A and B are represented as ηn_A and ηn_B respectively (Yaffe, 2010).

Using the radiation contrast equation $\frac{n_A - n_B}{n_A + n_B}$ after replacing n_A and n_B with $n_0\, e^{-\mu z}$ and $n_0\, e^{-\mu(z-a)-\mu' a}$ respectively, the following equation is acquired for the contrast.

$$\frac{1 - e^{a(\mu-\mu')}}{1 + e^{a(\mu-\mu')}}$$

The above equation is dependent upon the X-ray attenuation coefficient between the background tissue and the structure of interest such as lesion and the thickness of the lesion. The radiation contrast is not dependent upon the thickness of the breast or the number of transmitted X-ray beams to the breast. This is a simplified model in order to demonstrate the reason of using low energy X-ray beams in mammography. In practice, with the polyenergetic X-ray spectrum, the contrast shows dependence on the breast thickness (z), the mean number of transmitted X-ray beam to the breast (n_0), and the X-ray attenuation coefficient (μ).

Research shows that the linear attenuation coefficient of the breast features such as fat, fibroglandular tissue and lesions is decreased with the increase of the X-ray energy (Figure 6.7) (Yaffe, 2010). Attenuation is produced by the absorption and scattering of the incoming photons to the tissue. At low energy this is dominant by the photoelectric absorption. Since the probability of the photoelectric absorption is related to the photon energy, and the atomic number of the absorber (6.2.2 on page 58), Hence the increase of the photon energy decreases the attenuation coefficient of the X-rayed tissue.

Likewise, the difference between the linear attenuation coefficient of the breast tissue such as fat/glandular and the lesion is decreased (Figure 6.7) with the increase of the X-ray energy. These reductions applied in the latter radiation contrast equation above display the decrease of contrast between the breast tissue and the structure such as a lesion with the increase of the X-ray energy. Therefore, in order to produce adequate contrast mammograms, lower energy is required in mammography (Yaffe, 2010).

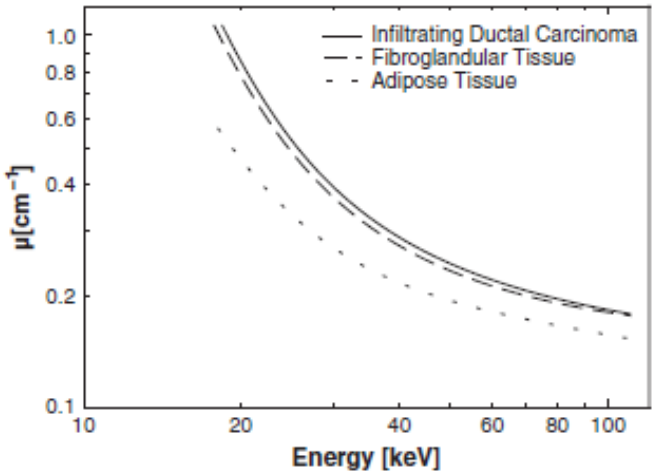

Figure 6.7 linear X-ray attenuation coefficients of fat, fibroglandular tissue, and cancer lesion in the breast (Yaffe, 2010)

The following graph (Figure 6.8) displays the relation between the radiation contrast and the X-ray energy for fat, fibroglandular tissue and an infiltrating ductal carcinoma (Yaffe, 2010).

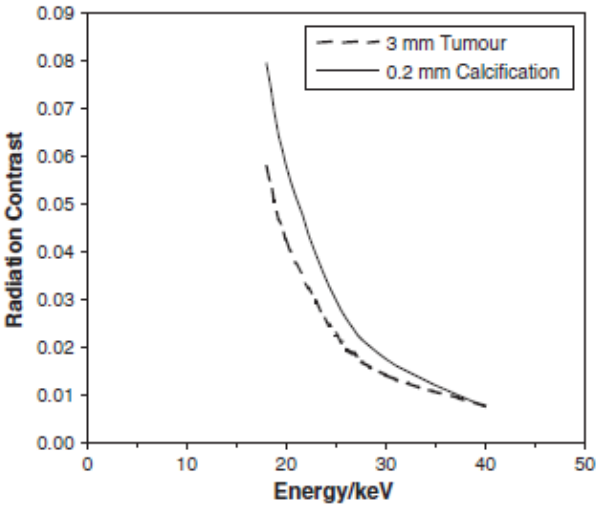

Figure 6.8 Contrast of the breast tumour and calcification in relation to X-ray energy (Yaffe, 2010)

6.3 DIGITAL MAMMOGRAPHY

Modern mammography is categorized into digital radiography (DR) and computed radiography (CR). Both of these categories are subsets of digital mammography. Digital mammography was implemented progressively in Canada in 2006 and has been widely used in recent years (Brooks & Morley, 2013). In 2000, the first full-field digital mammography (FFDM) was approved by the U.S. Food and Drug Administration (FDA) for clinical purposes (Hendrick, et al., 2010). In 2010, the Department of Health Advisory Committee on Breast Cancer Screening in the UK decided to adopt direct digital radiography (DDR) based mammography rather than computed radiography (CR) into the NHS Breast Screening Programme. As of October

2013, 99% of the breast screening departments in the UK were equipped with at least one direct digital mammography unit (Public Health England, 2014).

Computed mammography is a cassette based system which is less effective in detecting cancer lesions but is also less costly compared to digital mammography. Research shows that CR systems are about 21% less effective than direct digital mammography. This lower effectiveness may be due to loss of spatial resolution, or sharpness, and image noise (Chiarelli, et al., 2013) (Brooks & Morley, 2013).

Due to the use of advanced technology in digital detectors such as flat-panel detectors with integrated thin-film transistor (TFT), charge-coupled device (CCD), or complementary metal oxide semiconductor (CMOS) image sensor, the time consuming processes of manipulating the cassettes, and photostimulable phosphor (PSP) read-out has been eliminated. Unlike the CR systems, DR provides almost instant display of the mammograms on the monitor (Herrmann, 2008). The following diagrams (Figure 6.9) show different classifications of digital X-ray technologies in general (Lança & Silva, 2013).

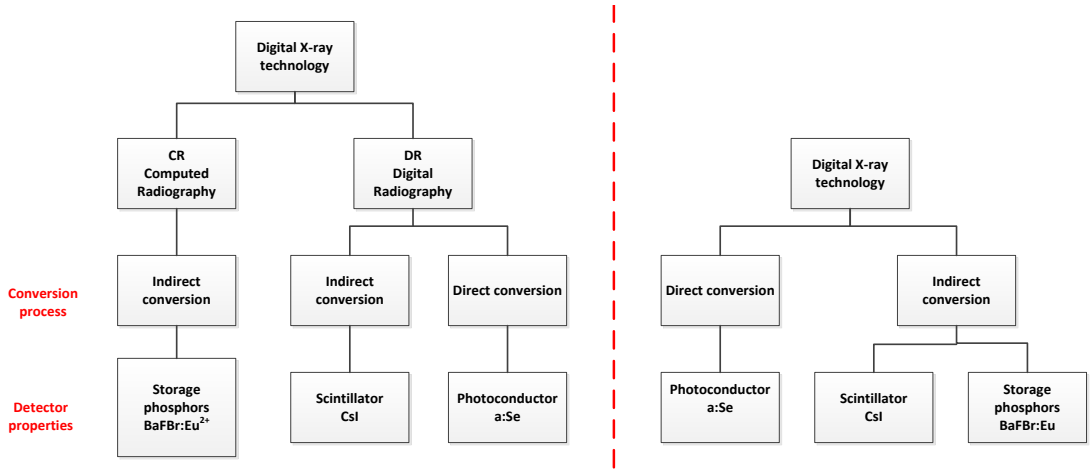

Figure 6.9 Digital X-ray technology (Lança & Silva, 2013)

6.3.1 Direct and Indirect detectors

In digital mammography, the detector is a core feature which creates electronic signals to represent the spatial pattern of the transmitted X-ray beams by the breast. The energy of the transmitted X-ray radiation which has passed through the breast is absorbed by the detector. This absorbed energy is then converted to light or electric charge. The signal is collected and, if the light was the output of the conversion phase, the signal will convert to electronic charge. After the production of the electronic signals, the process of reading the charge is followed by amplification and digitization (Yaffe, 2010).

Mammographic digital detectors can be categorized as direct and indirect. As the following image (Figure 6.10) shows, both types of detectors include X-ray photon absorption, conversion to electric charge, readout, and analogue/digital layers.

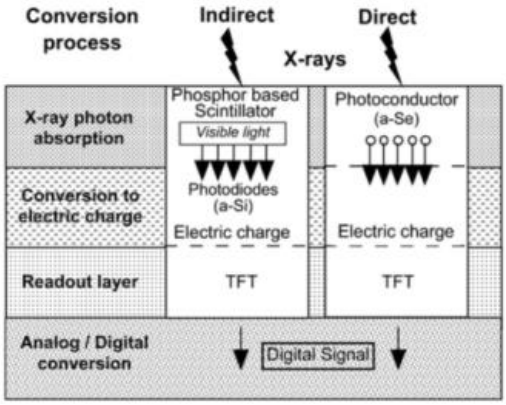

Figure 6.10 Indirect and direct conversion in digital mammography (Noel & Thibault, 2004)

Direct digital detectors convert the X-ray photons directly to electric charge, whereas, with indirect systems, the X-ray photons are converted to light first before converting to electric signal. In indirect detectors, X-ray photons are absorbed on a scintillator (see glossary on page 305) such a phosphor based (or Thallium-activated caesium iodide (ScI:Tl)). The light generated in the scintillator is detected by an array of photodiodes. The electric charges created in the conversion to electric charge layer drift

towards the arrays of thin-film transistors (TFT) in the readout layer. The TFT array collects the electric signal and stores it in detector element capacitors. The array is then read immediately by the TFT in order to produce the image (Bushberg, Seibert, Leidholdt, & Boone, 2012). The last layer shows the conversion of the analogue signals to digital (Noel & Thibault, 2004).

Due to the light spread in the scintillator, the spatial resolution of indirect systems is lower than in direct detectors. The following image (Figure 6.11) illustrates the line spread function (see glossary on page 305) in indirect detectors versus direct detectors. Because of the scattering of light in the scintillator, indirect detectors generate broad line spread functions while direct detectors have narrower line spread functions.

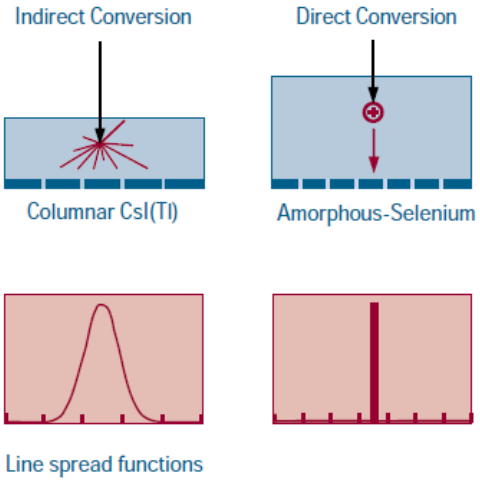

Figure 6.11 Line spread function for indirect and direct conversion (Smith, 2003)

In direct conversion digital detectors, the X-rays are absorbed by the detector and the electrical signal is generated directly due to the presence of an external electric field. The electrons (or holes based on the polarity of the electric filed) move towards a pixel electrode and are collected on a pixel capacitor. The movement of the electrons/holes are

along the direction of the electric filed lines. This un-scattered drift results in a narrow point spread response about one micron (Figure 6.11) (Markey, 2013).

Amorphous selenium (a-Se) flat panel detectors are ideal for direct digital mammography. These detectors offer high X-ray absorption efficiency, high inherent resolution, and low noise. They are also suitable for radiation dose efficiency (Markey, 2013) (Smith, 2003).

6.3.2 Computed radiography

Similar to screen film (see glossary on page 305), computed radiography (CR) systems are based on the photostimulable luminescence principle. CR is known as a cassette-based technology. In these systems, X-ray photons are absorbed on a photostimulable phosphor (PSP) plate within the imaging cassette. This modality then utilises a laser scanning mechanism to extract the data trapped on the cassette.

6.3.3 Digital detector types

Various types of detectors are used in mammographic systems. Some common digital mammographic detector types include phosphor-flat panel, selenium flat panel, and phosphor-CCD. Since a selenium flat panel detector was employed in the mammography unit of this research, therefore, only this detector is discussed in the next section.

6.3.3.1 Selenium flat panel

Another type of digital detector is the selenium flat panel detector which uses amorphous selenium (a-Se) (100-200 mm) as an X-ray absorber. The X-rays hit the a-Se and produces photoelectrons. The interaction between the electrons of the selenium atoms and the X-rays creates an electron-hole pair. This electron-hole pair is the source of the generation of the electric signals. The selenium is encompassed between two electrodes

(Figure 6.12). The electrodes generate an electrical field. The lower electrodes formed as a large matrix of detector elements (dels). The dels store the charge as capacitors. There is a TFT switch at the corner of each TFT. The charges then move to the readout circuit when the TFT switches are on. The TFT switches get command from control lines to open sequentially (row by row). The signals from the activated dels are transmitted along readout lines to be amplified and digitized (Yaffe, 2010).

Selenium flat panel detectors offer very high DQE and high resolution, resulting improved image quality and the potential for lower radiation dose (Smith, 2003).

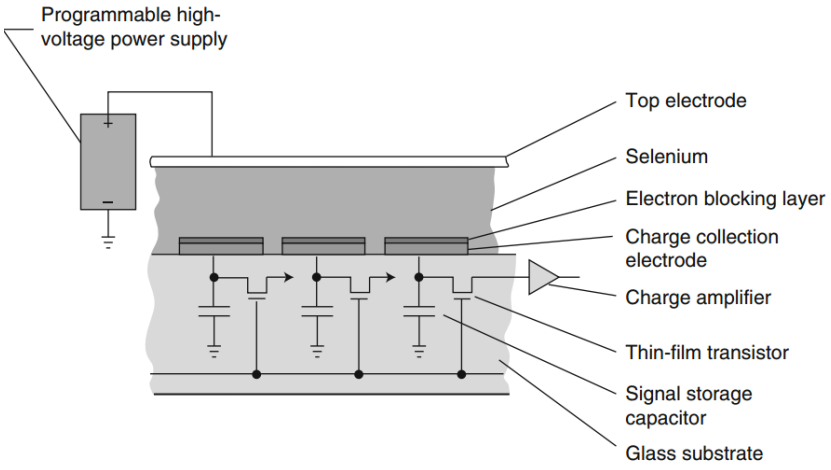

Figure 6.12 Selenium system (Yaffe, 2010)

6.3.4 Detector Elements (del)

A detector element (del) or aperture, as a smallest detector component (Hashimoto, 2008), is considered as the heart of detectors. In image acquisition, dels provide X-ray discrete measurement to construct the image. In other words, the information displayed by every single pixel is originated in each del. Generally, the resolution of the detectors is related to the size of the del (Hashimoto, 2008).

The centre to centre distance between two adjacent dels in the array of dels is called pitch (p) and the size of each del is 'd' which is referred to as aperture size (Figure 6.13). Fill factor is one of the measures which indicates the fraction of the area that is sensitive to X-rays and is represented by the following equation.

$$\text{Fill factor} = \frac{d^2}{p^2}$$

For example, if d is smaller than p, then the fill factor depending on the geometry of the del can be less than 1. The amount of fill factor can affect the sensitivity and efficiency of the detector. The loss of X-rays because of the geometry will reduce the efficiency and sensitivity of the detector (Yaffe, 2010).

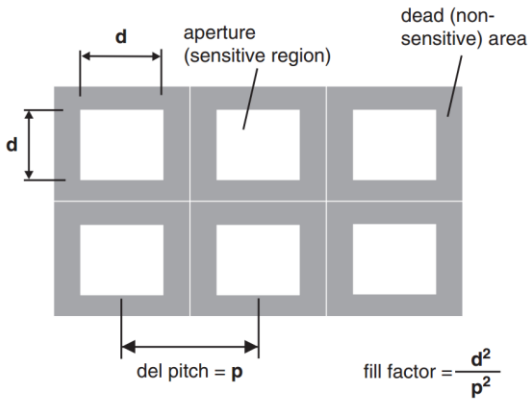

Figure 6.13 Detector element (dels) (Yaffe, 2010)

6.3.5 Digitization

Typically analogue data is the output of the medical imaging detectors. The digital data is required in order to process the data by computer, transfer it to other work stations and store it digitally. Therefore, the detectors utilise specific electronic circuits called analogue-to-digital convertors (ADCs) in order to digitize the input signals. This

process is called digitization of the signals. Digitization has two steps: sampling and quantization.

An analogue signal is typically continuous in time. This means that the signal has value at each point in time. In the sampling technique, instead of selecting all the points in the analogue signal, some certain points in time are selected in order to form the digital signal. In the quantization technique each analogue sample converts to digital signal (Bushberg, Seibert, Leidholdt, & Boone, 2012).

6.3.6 Dynamic range in DR

Dynamic range is the range of intensity from minimum to maximum that can be shown as differences in signal intensity (Schaefer-Prokop & Prokop, 1997). Dynamic range in digital mammography is related to grey-scale shades in the image. The grey-scale shades are defined as bits and the content of the bits (0/1) defines the grey shade. A mammography system that offers at least 12 bits of dynamic range will not deteriorate the fundamental information (Smith, 2003). The large dynamic range in digital mammography improves the visualization of various parts of the breast in the image and offers wide exposure latitude (see glossary on page 305) (Markey, 2013). The dynamic range should be enough to be able to cover the entire range of intensities for all the tissue types such as adipose, glandular, and fibrous and abnormalities such as microcalcifications.

The high contrast resolution resulting from the high dynamic range in digital mammography improves image acquisition, especially for dense breast tissue (Medical Services Advisory Committee , 2008).

6.3.7 Pixel size in mammography

In digital mammography, spatial resolution of an image is affected by the pixel size and the spacing between the pixels. However, a higher number of pixels do not always provide a higher spatial resolution. Image blurring can result from a number of factors including X-ray scatter, light scatter, and a combination of both in the detector (Chotas, Dobbins III, & Ravin, 1999). For example, in scintillator based systems, even with pixel sizes smaller than 100 μm, the spatial resolution is not as good as the direct selenium based systems with a pixel size of 70 μm (see 6.3.1 on page 68) (Smith, 2003). Typically, the size of the pixel element on currently available mammographic detectors is between 50 μm and 100 μm (Freitas, Kemp, Louveira, Fujiwara, & Campos, 2006).

6.4 PERFORMANCE OF DIGITAL DETECTORS

Measuring the performance of digital radiographic detectors is essential in order to generate good quality radiographs. Good image quality leads to accurate diagnosis. Hence, there are numerous research studies regarding the measurement and improvement of image quality in digital radiography. Since the evaluation of image quality in relation to breast phantom thickness is one of the objectives of this research, knowing the effects of the performance of the detectors on the images is essential. Furthermore, the parameters which are used to measure the performance of detectors such as sharpness, noise and contrast can be used to evaluate the image quality of the mammograms in the visual perception part of this research.

The performance of the system can be described by number of performance parameters. Contrast, sharpness, and noise are important characteristics to determine the performance of image quality. Characteristics such as sharpness and noise can be defined in terms of the modulation transfer function (MTF) and noise power spectrum (NPS) or

Wiener spectra (WS). Noise can also be used in the measurement of signal to noise ratio (SNR) and detective quantum efficiency (DQE).

6.4.1 Contrast

Contrast is the relative signal difference between two adjacent objects in the image. It is especially important when describing the difference between the image of the object and the background. In other words, contrast can be defined as the relative brightness difference between two locations in an image (Cunningham, 2000).

In DR systems, the contrast and brightness can be adjusted by the display system (Pisano & Yaffe, 2005). It is important to mention that post-processing can only improve the contrast and brightness of what exists in the image. It cannot recover information that has not been obtained due poor acquisition.

In digital mammography, the characteristic response curve represents the contrast of an imaging system. As Figure 6.14 displays, the characteristic curve of a digital mammography is linear. This means that the produced signal is linearly proportional to the intensity of X-rays transmitted through the breast. Due to the large dynamic range of the digital detectors, ranges of tissue can be viewed in the image. Since the contrast is an important parameter in image quality, digital mammography offers the ability to adjust the brightness and contrast of the image after image acquisition and during image viewing (Yaffe, 2010).

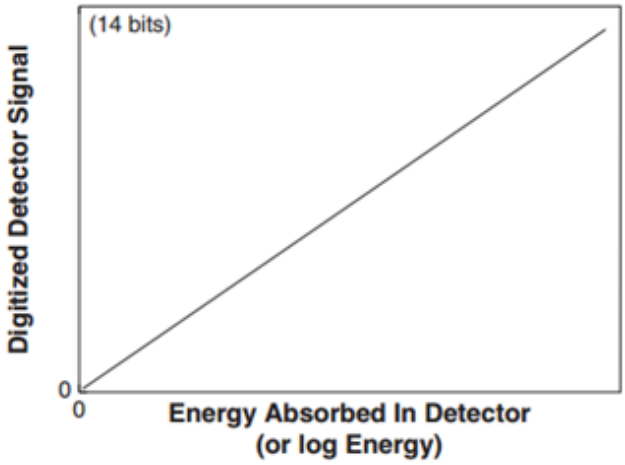

Figure 6.14 Characteristic response of a detector designed for digital mammography (Yaffe, 2010)

6.4.2 Sharpness

Sharpness in medical imaging shows the ability of the system to distinguish the anatomic features of the imaged object. Degradation of sharpness in the radiographs can increase the chance of missing the detection of abnormalities (e.g. lesions) in the breast. Sharpness is directly related to the spatial resolution of the imaging system (Samei, 2003).

Spatial resolution is a concept in medical imaging which allows two adjacent structures or objects to be visualized separately. The spatial resolution in digital mammography is 5-10 line-pairs/mm (a dark line next to a light line), whereas, the spatial resolution in SF mammography is 20 line-pairs/mm (Whitman & Haygood, 2013).

The modulation transfer function (MTF) is defined as a measure of signal transfer (modulation) over a range of spatial frequencies. MTF is used to measure image sharpness (Smith, 2003). In digital mammography, the value of MTF is affected by the focal spot size, detector's active area, the spread of the signal in the detector, and the laser in CR-based detectors (Whitman & Haygood, 2013).

The following image (Figure 6.15) illustrates the concept of MTF. Three sinusoidal pulses (left) are the input signals on a detector. Each signal has its own frequency. The output signals are measured by the imaging system (right). As the image shows the frequency of input and output signal are the same, but the amplitude of the output signals dropped in comparison with the input signals. The reduction of the amplitude is more noticeable in input signals with higher frequencies. This reduction results in the loss of resolution in the imaging system. The following MTF plot demonstrates the drop in amplitude (87%, 56%, and 13%) as a function of spatial frequency (1 cy/mm, 2 cy/mm, and 4 cy/mm). In other words, the plot shows the spatial resolution of the imaging modality as a function of spatial frequency of the input pulse to the detector (Bushberg, Seibert, Leidholdt, & Boone, 2011).

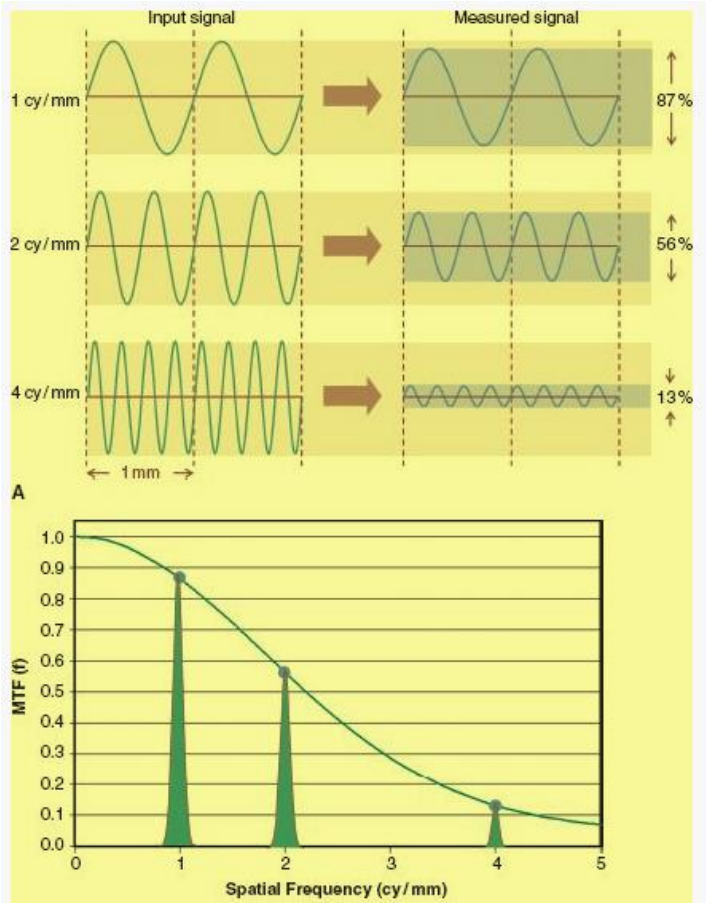

Figure 6.15 MTF for input signals with various spatial frequencies

The following image (Figure 6.16) illustrates MTF for the SF, indirect and direct detectors. As the graph shows, the direct a-Se detectors generate the highest MTF compared to SF and indirect detectors. Due to generation of light scattering in scintillator-based detectors using indirect technology, scintillator-based detectors produce lower MTF values.

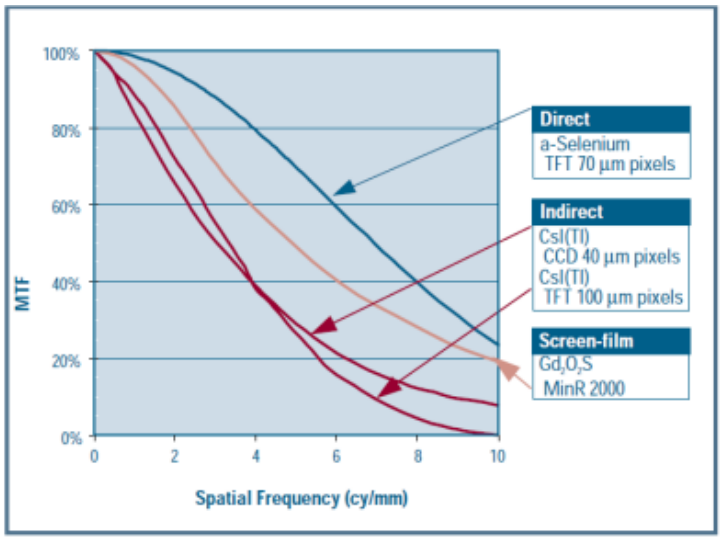

Figure 6.16 MTF for direct, indirect and screen-film mammography systems (Smith, 2003)

6.4.3 Noise and Signal to Noise Ratio

Generally, in medical imaging, noise is the unwanted image detail which interferes with the visualization of the areas of interest (Samei, 2003). The main sources of noise are classified into the following categories: anatomical noise, electronic noise, scattered radiation noise, and quantum noise.

Electronic noise is a random noise which can be generated from the electronic components of the imaging modality such as analogue to digital convertors (Williams, et al., 2007). Anatomical noise is the image of anatomical organ which always presents, but might not be important for diagnosis. The anatomical noise can block the area of interest in the image (Bushberg, Seibert, Leidholdt, & Boone, 2012). Scatter radiation is another source of noise in the image. Because of the scattering of the X-ray by the anatomical tissues, the intensity of the X-ray on the exit side of the patient reduces. This reduction of X-ray intensity reduces the signal to noise ratio (SNR) (Williams, et al., 2007).

Both the production of X-rays and the interaction of photons with the detectors and also in the tissue are in a random manner. In other words, there is no even

distribution of photons on the detector. One area of a detector can receive more photons than other areas. The random pattern or uneven distribution of photons is the main reasons of generation of noise within the image. This noise is known as quantum noise and is related to the quantum structure of an X-ray beam (Sprawls, 1995).

Signal to noise ratio (SNR) as a measure of image quality, is the ratio of signal to noise in the detectors. It can be defined as the ratio of the number of X-rays used to form the image (n_d) to the square root of the number of X-rays (n_d) (Yaffe, 2010).

$$SNR = \frac{n_d}{\sqrt{n_d}} = \sqrt{n_d}$$

In order to visualise the small features in the breast such as microcalcifications, it is necessary to reduce the noise and increase the SNR. This can happen either by increasing the mAs or by utilizing a detector with high quantum detection efficiency (η) (Yaffe, 2010).

6.4.4 Detective Quantum Efficiency

Detective Quantum Efficiency (DQE) is one of the main measures to evaluate the performance of the digital X-ray system. As mentioned above, the higher SNR results in better quality mammogram. SNR decreases when other sources of noise other than quantum noise affecting the image quality. The signal directly transmitted from the breast to the detector produces SNR_{in} which is defined in the following formula.

$$SNR_{in} = \frac{n_0}{\sqrt{n_0}} = \sqrt{n_0}$$

In this formula n_0 is the number of photons in a specified area. In a perfect system $\sqrt{n_0}$ would be the only source of the noise, but in reality not all the photons get absorbed by the detectors, therefore the noise will be affected by quantum detection efficiency or η

resulting $\eta.n_0$ as signal and $\sqrt{\eta.n_0}$ as noise. Signal to noise ratio (SNR_{out}) is defined in the following equation.

$$SNR_{out} = \frac{\eta.n_0}{\sqrt{\eta.n_0}} = \sqrt{\eta.n_0}$$

The performance of the imaging system can be determined by the ratio of the SNR_{out} to SNR_{in}. This ratio is referred to as Detective Quantum Efficiency (DQE) and indicates how well the system transfers the input SNR (Yaffe, 2010).

$$DQE = \frac{{SNR_{out}}^2}{{SNR_{in}}^2} = \frac{\eta.n_0}{n_0} = \eta$$

6.4.5 Noise Power Spectrum

The presence of the noise in the images is unavoidable. If the noise level compared to the image intensity of the anatomical tissue is high, the important information on the image can be lost due to the presence of the noise. Therefore, utilizing mathematical methods to measure the level of the noise in the medical imaging is essential.

Generally speaking, variance or σ^2 is a metric which is employed in order to quantify the noise in the image. This metric does not measure the noise texture. For example, the following image (Figure 6.17) depicts two CT images of a test object. Both images have the same standard deviation in the specified ROI. As the image shows the appearance of the noise in those images is not identical. The difference between the frequency dependence of the noise causes this perceptual difference in the noise of both images. This frequency dependence of the noise variance is measured by the noise power spectrum (NPS) (Bushberg, Seibert, Leidholdt, & Boone, 2012).

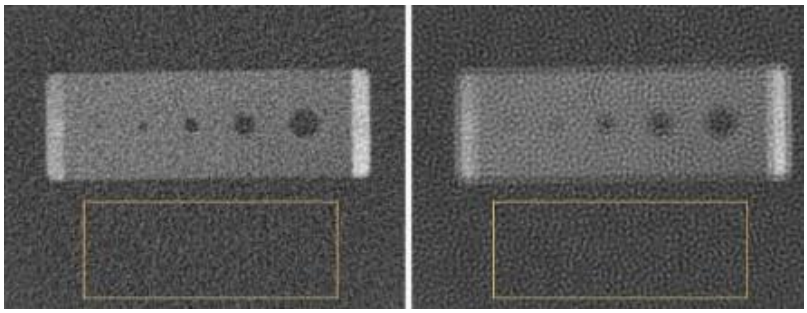

Figure 6.17 Two CT images of a test object with identical standard deviation and different noise appearance (Bushberg, Seibert, Leidholdt, & Boone, 2012).

6.4.6 The relationship between image quality parameters

The following image (Figure 6.18) shows the relationships between image quality parameters. SNR represents the relationship between noise and contrast. The ratio between signals to noise represents the most significant indicator in image quality. The research by Dobbins shows that a ratio of 5:1 is adequate for observers (Dobbins III, 2000). As the level of noise decreases, the SNR increases. An increase in the SNR directly results in an increase in the image quality and therefore the possibility of object detection (Lança & Silva, 2009).

Wiener spectrum (WS) or NPS (Noise Power Spectrum) represents the relationship between noise and spatial resolution. This is an important tool to evaluate the noise power in the spatial frequency domain. MTF is affected by contrast and resolution. All the parameters have influence on the DQE as the main system performance measure.

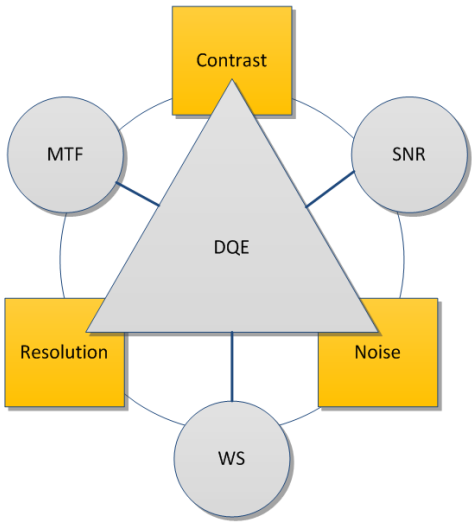

Figure 6.18 Relationship between image quality parameters (Oliveira & Lança, 2011)

6.5 MAMMOGRAPHY UNIT

A mammography unit is comprised of many different components including focal spots, collimator, field of view, grid, mammographic monitors, compression device, paddles, and automatic exposure control (AEC). This section is aimed to discuss the role of the parts of a mammography unit which have been directly used in this research. These parts include: compression device, paddles, and automatic exposure control (AEC). Appendix I covers some other key components of a mammography unit such as focal spots, collimator, field of view, grid, and mammographic monitors.

6.5.1 Compression device

The breast compression can be operated manually or motorized. In the motorized compression, a foot pedal assists the operator to be hands free, so she can use her hands to position the breast. The foot pedals operate the up/down motion for the compression paddle. Manual compression can be achieved by a compression knob.

Generally, the initial breast compression starts with the motorized device. The foot pedal is programmed to a sufficient amount of compression to hold the breast in

position without over-compressing it. Then final compression is applied manually by the mammographer in order to compress the breast sufficiently for the imaging procedure (Andolina & Lillé, 2011). The following image (Figure 6.19) shows the compression pedals and knobs in both sides of mammography unit.

Figure 6.19 Mammography unit (Hologic Inc., 2014)

A mammography unit is also equipped with a feature called Automatic compression release. This feature allows the breast to be released automatically after the X-ray exposure. It also releases the breast when the power to the machine is cut off (Andolina & Lillé, 2010). The automatic compression unit can be set on/off from the control panel.

6.5.2 Paddles

Paddles are plastic trays in a mammography unit which are utilised to compress and immobilize the breast during the imaging. The compression of the breast is carried out between the compression paddle and the support table. Paddles come in a variety of sizes and shapes based on the breast size and the purpose of mammography. Selecting the proper size of paddle has effect on image quality. Using too small of a paddle on a large breast can cause uneven and insufficient compression and might miss some areas to compress. Likewise, choosing large paddles for small breast might prevent access to the breast (Defreitas, Pellegrino, Farbizio, Janer, & Hitzke, 2008).

Depending on the mammographic procedure, different types of paddles can be used for screening and diagnostic purposes (Figure 6.20). In the diagnostic mammography technique of spot (cone) compression, the focus of compression is on a specific area of the breast. Therefore, a small compression paddle is used to obtain the mammogram. Spot compression can also be used to detect microcalcifications (Canadian Cancer Society, 2014). Magnification, biopsy, and male breast paddles are other types of mammography paddles utilised for various mammographic purposes (AR Custom Medical Products, 2007).

Figure 6.20 Different mammographic compression paddles

Typically, the 18x24 cm and 24x30 cm paddles are required for breast screening(Bassett, Jackson, Fu, & Fu, 2004). These flat and parallel paddles match the size of the image detector. Flex paddles as an alternative for flat rigid compression paddles can also be utilised in mammography. The tilting mechanism of these spring loaded paddles provides more uniform compression from the chest wall to the nipple (Bushberg, Seibert, Leidholdt, & Boone, 2012). Although the flex paddles are recommended by mammography unit manufacturers in order to decrease the pain and discomfort for women, there is no comprehensive study regarding the relationship between these two types of the paddles and the pain experience. On the contrary, due to the better contrast using the rigid paddle, this paddle was recommended for standard mediolateral oblique and craniocaudal projections (Broeders, et al., 2015).

Since the conventional paddles are rigid and might cause pain and discomfort among the women, especially on the thicker parts of the breast, ergonomic paddles have been taken into consideration. One of the recent ergonomic paddles that has been introduced by Fujifilm Corporate is the FS (Fit Sweet) Compression Paddle. This flexible paddle (Figure 6.21) bends along the breast when it is in contact with the breast. The flexibility and shape of this paddle makes the positioning of the breast easier and reduces the pressure on the breast during compression (Otani, 2013).

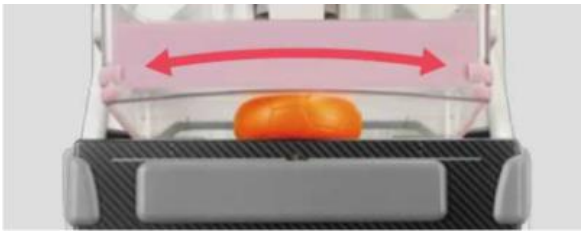

Figure 6.21 FS (Fit Sweet) Compression Paddle (Otani, 2013)

6.5.3 Automatic Exposure control (AEC)

Automatic exposure control (AEC) as a key component in mammography has a crucial role in FFDM. It facilitates consistent optimal image exposure despite differences in the breast size, density and operator's skill level (Benchimol, Näsström, & Shi, 2009).

The main role of AEC in these systems is to set the radiation level to determine the signal difference to noise ratio (SDNR) and in some designs, it ensures the intensity of the X-ray does not exceed the limit of the detector or digitizer (Pisano & Yaffe, 2005).

Although the presence of an AEC is important in specifying the exposure level to the breast and detector, its main roles are to help perform the predetermined SNR and provide an acceptable radiation dose to the breast rather than specifying the brightness or contrast of the image (Yaffe, 2010).

In CR systems, the AEC circuit is an electronic X-ray sensor placed beneath the image receptor. AEC terminates the X-ray exposure when it senses the predetermined radiation level. However, in DR systems based on flat-panel detectors, the AEC is integrated into the detector. This multi-element sensor design allows the entire detector (the information from the entire breast and the air around the breast) to be utilised to sense the radiation transmitted through the breast. There are many algorithms to use the information on the digital detectors efficiently.

Typically, the AEC systems are based on test exposure (pre-exposure). In these systems, a small amount of radiation with a very short exposure time approximately 4 ms is used to make a test image. The data acquired from the test image is then employed to calculate the optimum exposure parameters (kVp and mAs) for the main image (Benchimol, Näsström, & Shi, 2009) (Pisano & Yaffe, 2005).

6.6 MAMMOGRAPHY DENSITY

Breast mammograms demonstrate different appearances of the breast components. The variation in X-ray brightness of different features of the breast is directly associated with the X-ray attenuation of those breast features. As the following graph (Figure 6.22) demonstrates, the attenuation coefficient of the breast features drops with an increase in the X-ray energy. A breast mammogram demonstrates darker areas for the fat (radiolucent) and bright regions for fibroglandular tissue (radiopaque). In other words, the regions with higher X-ray attenuation seem brighter on the radiograph. Mammographic breast density is known as regions of brightness related to fibroglandular tissue (Yaffe, 2008).

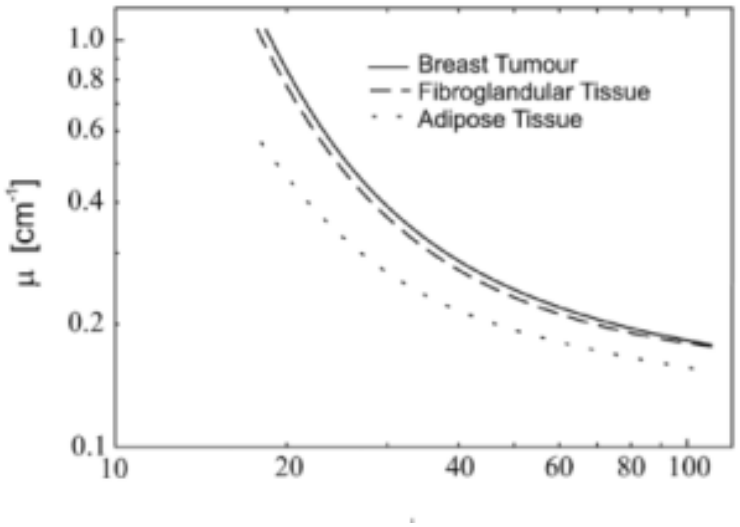

Figure 6.22 Linear X-ray attenuation coefficients of fat and fibroglandular tissue in the breast in relation to X-ray energy (Yaffe, 2008)

Breast density is one the main risk factors associated with development of breast cancer (McCormack & dos Santos, 2006) (Wolfe, 1976). Research shows women with the mammographically denser breast have higher chance of developing breast cancer (Qureshi & Samera, 2009).

6.6.1 Breast Imaging Reporting and Data System (BIRADS)

There are numerous methods of measuring mammographic density (Yaffe, 2008). These assessments can be either qualitative or quantitative. Breast Imaging Reporting and Data System (BIRADS) (Geller, et al., 2002) is a breast qualitative density classification system which is widely used in mammography. This system has 4 main categories: BIRADS-1 specifies fatty breast; BIRADS-2 dispersed fibroglandular tissue; BIRADS-3 is heterogeneous dense breast; and BIRADS-4 for the highest density breast. Since the sensitivity of the mammography decreases for the denser breasts, this system assists the clinicians to focus on other imaging procedures which are less affected by density (Buist, Porter, Lehman, Taplin, & White, 2004) (Bird, Wallace, & Yankaskas, 1992).

In order to make the BIRADS system more quantitative, the mammograms have been classified to 4 density categories defined as <25, 25%-50%, 51%-75%, and >75%. The category of <25% indicates that the breast is almost entirely fat and glandular tissue is less than 25% of the breast. 25%-50% shows the presence of scattered fibroglandular tissues, ranging from 25% to 50%. 51%-75% indicates that the breast is heterogeneously dense, ranging from 51% to 75%, and >75% means that the breast contains glandular tissues greater than 75% (Nicholson, LoRusso, Smolkin, Bovbjerg, Petroni, & Harvey, 2006).

Although the worldwide BIRADS system is a common language between radiologists to report mammographic breast densities, the image features are determined subjectively. Therefore this system may be prone to visual errors and can be affected by the expertise level of the image readers. Hence, computerised methods have been developed to measure the breast density more quantitatively (Yaffe, 2008).

Chapter 7 Polyvinyl alcohol

The breast phantoms/lesions in this research are created from polyvinyl alcohol. Polyvinyl alcohol is a biocompatible, tissue mimicking, biodegradable and non-toxic polymer. The hydrophilic characteristic of PVAL makes this polymer desirable and widely used in biomedical and pharmaceutical applications (Hassan & Peppas, 2000).

PVAL brain, vessel and breast biopsy phantoms are examples of water-based PVAL phantoms utilised in MR and ultrasound studies (Surry, Austin, Fenster, & Peters, 2004) (Surry & Peters, 2001). Other applications of PVAL are in artificial cartilage, contact lenses (Ru-yin & Dang-sheng, 2008), vascular cell culturing and vascular implanting (Jiang, Liu, & Feng, 2011).

PVAL gel has mechanical, optical and acoustic similarity to living human breast tissue (Kharine, et al., 2006) (Fromageau, Gennisson, Schmitt, Maurice, Mongrain, & Cloutier, 2007). The mechanical properties of PVAL gel make it a suitable material for the creation of tissue-mimicking phantoms in mammography. Optical and acoustic characteristics also make the gel appropriate for studies using other medical imaging modalities such as ultrasound.

The X-ray properties of PVAL gel are not similar to the human breast, but the similarity between the X-ray properties of the PVAL gel and human breast can be simulated by utilizing substances such as ethanol (Price, Gibson, Tan, & Royle, 2010) or contrast agents.

The PVAL has to be crosslinked to be able to produce gel (Figure 7.1). A crosslink is a bond that links the polymer chains together. The crosslinked gel is a hydrophilic (see glossary on page 305), three-dimensional polymeric network which swells in water yet remains insoluble. Aqueous solutions of PVAL can be solidified to

produce a gel by either chemical or physical crosslinking. In chemical crosslinking, agents such as glutaraldehyde, acetaldehyde, and formaldehyde have been used. Chemical crosslinking is undesirable due to the presence of chemical residue and the time-consuming effort required for extracting the toxic residual components. Physical crosslinking, in contrast, is a mechanism to produce gel without the usage of crosslinking agents (Hassan & Peppas, 2000). Physically crosslinked gels (Figure 7.1) exhibit a higher mechanical strength and stability than chemically crosslinked gels (Hassan & Peppas, 2000). The mechanical strength is derived from the distribution of the mechanical load among the crystallites of the three-dimensional (network) structure of the gel.

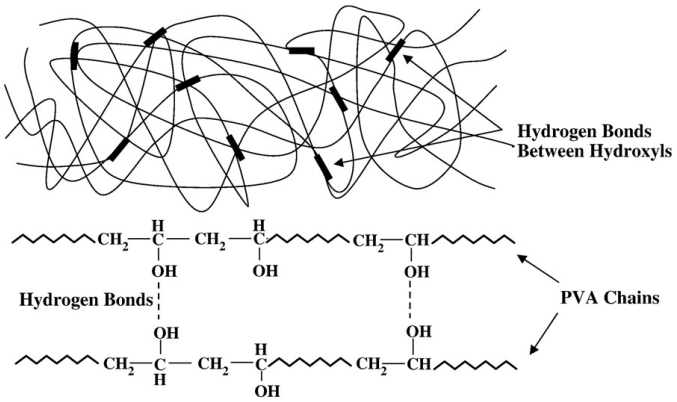

Figure 7.1 Crosslinking of PVAL by freezing-thawing cycle and hydrogen bonding production (Bonakdar, Emami, Shokrgozar, Farhadi, Ahmadi, & Amanzadeh, 2010)

7.1 FORMATION OF PVAL GELS THROUGH FREEZE-THAWING

The formation of PVAL gel from the aqueous solution can be explained by three models: hydrogen bonding, crystallite formation, and liquid-liquid phase separation (Peppas & Stauffer, 1991). In a heated aqueous PVAL solution (dissolved PVAL crystals in deionised water) mobile molecular chains come in contact with each other for a short time but do not develop bond with each other. After reducing the temperature below 0 °C, the chains stay in contact with each other for a longer period of time and result in

intermolecular interactions of the PVAL chains including hydroxyl bonds (Ru-yin & Dang-sheng, 2008). Hydrogen bonding between hydroxyl groups of PVAL is thought to be the source of the crosslink (tie point) between the molecules of PVAL polymer. The hydrogen bonding creates a network of hydrogen bonded PVAL crystallites which is hypothesized as the cause of the gel formation. This formation of crystallites initiates from a double layer of PVAL molecules held together by hydroxyl bonds and the presence of weak van der Waal forces. The crystallites originate from a folded chain structure of PVAL and are scattered in an amorphous polymeric network. Figure 7.2 below shows a typical crystallite consisting of folded polymer (PVAL) chains of lamellar thickness l, width w, and distance b between the rows of chains (Hassan, Ward, & Peppas, 2000).

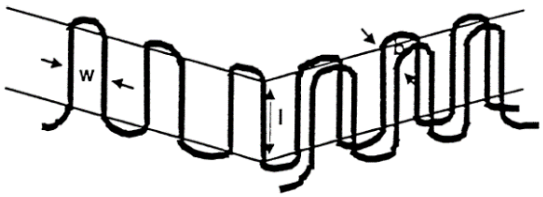

Figure 7.2 Typical crystallite of folded polymer (PVAL) chains (Hassan, Ward, & Peppas, 2000)

Liquid-liquid phase separation results in polymer-rich and polymer-poor regions. During the freezing cycle, the water freezes and it expels the PVAL as impurity of the water to the surrounding area (polymer-rich region). When the ice melts, it leaves a porous region whereas the PVAL crystallites form a network around the pores (junction points in a porous network) (Ricchiardi, Auriemma, & de Rosa, 2005) (Peppas & Stauffer, 1991).

Each freezing thawing cycle makes the polymer-rich region richer and the polymer-poor region poorer. Consequently, the PVAL network becomes more rigid after

each freezing thawing cycle due to the expulsion of PVAL from the ice crystals to the junction points and the formation of more crosslinked crystallites in the polymer-rich regions. It is worth mentioning that the rigidity of the PVAL gel is directly related to the concentration of PVAL as well as the number of freezing thawing cycles (Stauffer & Peppas, 1992). The more concentrated PVAL has higher amount of polymer to add to the polymer-rich region (PVAL network). In addition to freeze-thaw cycles, the aging process of PVAL gels produces extra crystallites to their three-dimensional polymeric network (Hassan & Peppas, 2000). These additional crystallites, known as secondary crystallites, strengthen the mechanical properties of the PVAL network. Figure 7.3 shows the polymer-poor and polymer-rich regions. It also shows the formation of crystallites in the gel due to freeze-thaw cycles and/or the aging process (Willcox, et al., 1999).

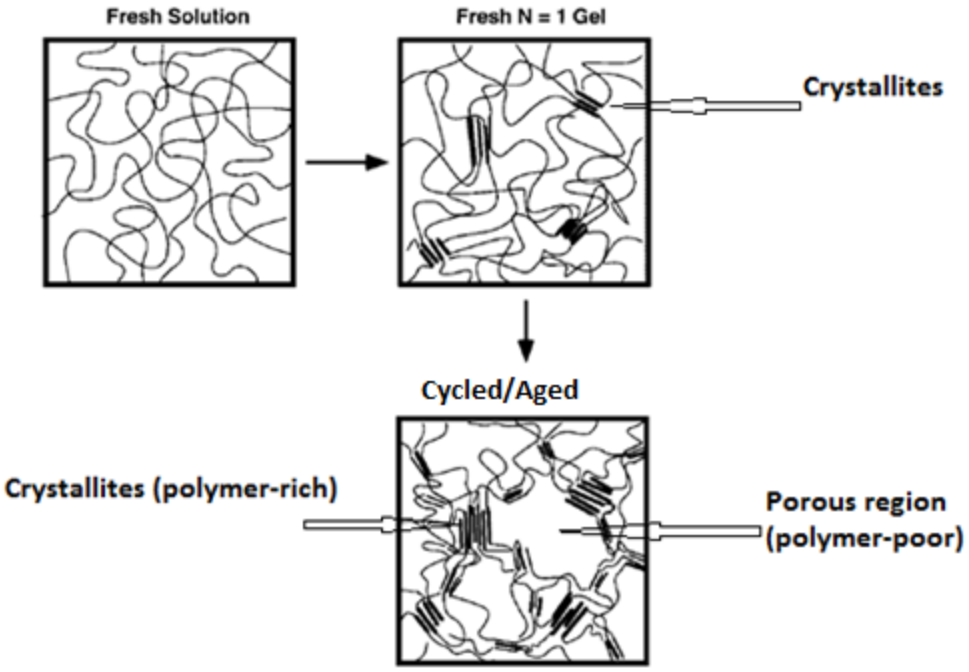

Figure 7.3 Polymer-rich and polymer-poor regions after freezing thawing cycles

7.2 STIFFNESS OF PVAL GELS

Mechanical properties of PVAL gel have made this material distinguished to construct tissue mimicking phantoms. A strict control over the fabrication of the gel is required in order to build the PVAL gel with the right mechanical properties. The PVAL phantoms which are produced in uncontrolled or low controlled environments do not have the expected mechanical properties. Hence, they will not be appropriate to be employed in phantoms studies.

As was mentioned earlier, the stiffness of the PVAL gel is directly related to the number of freezing thawing cycles. Thawing rate is another parameter which controls the stiffness of the gel. A slower thawing rate provides a longer time for the water to expel from the gel and longer time for the PVAL polymer chains to reorganize. The rejection of water and the reorganization of PVAL polymer chains resulted in stiffer PVAL gel and consequently higher Young's modulus (see 10.1.6 on page 126) (Wan, Campbell, Zhang, Hui, & Boughner, 2002). Variations in the freezing thawing temperature have remarkable impact on the Young's modulus (YM) of the PVAL gel. For example, two studies from the same researchers showed a great difference between the YM of the 10% PVAL gels fabricated based on various freezing thawing temperature and rates. According to Fromageau and his collaborators, PVAL is a suitable tissue-mimicking material (TMM) which can simulate the Young's moduli across a range of pressures from 20 kPa (similar to breast and liver) to 600 kPa (Fromageau, Gennisson, Schmitt, Maurice, Mongrain, & Cloutier, 2007). In one of the first studies by Fromageau and his researchers (Fromageau, Brusseau, Vray, Gimenez, & Delachartre, 2003) based on the unregulated control over freezing thawing temperature, the YM of a 10% PVAL gel with 5 freezing thawing cycles was measured as 90±6 kPa while under regulated temperature the YM was measured as 300±35 kPa. In the unregulated temperature experiment the freezing

temperature was -40 °C while in the regulated temperature the freezing temperature was -20 °C (Fromageau, Gennisson, Schmitt, Maurice, Mongrain, & Cloutier, 2007). This great difference in YM shows the effect of the freezing thawing temperature in the crosslinking process of PVAL gel. It is important to mention that unlike the freezing temperature and thawing rate which have direct impacts on the stiffness of the PVAL gel, the moderate freezing rate does not have drastic effects on the properties of the hydrogel (Lozinsky & Plieva, 1998). Providing a moderate freezing rate would be another challenging factor during the production of PVAL gel. In order to have moderate freezing temperature, first the degree and rate of freezing have to be defined clearly. Also the appropriate freezing equipment is needed in order to reach the right temperature with an appropriate rate.

The YM of 5%-6% PVAL mixed with glycerol and Al_2O_3 (acoustic scatterers) was measured and had values ranging between 1.6-16.1 kPa using a 'gold standard' mechanical testing technique and transient elastography (Cournane, Cannon, Browne, & Fagan, 2010). As was described in this section, the environmental parameters can directly affect the mechanical properties of the PVAL gel. Diversity in the methods to produce PVAL gel and also diversity in the ways to measure the mechanical properties could cause variations in the measurement of the mechanical properties of the PVAL gel.

7.3 METHODS TO PRODUCE PVAL GELS IN THE LAB

PVAL gels are created through a combination of heating/stirring and freezing-thawing processes. Various articles have suggested similar methods to fabricate PVAL gel. The freezing time can vary from 1 to 24 hours with stable PVAL gels forming after only 1 hour of freezing. The stability and stiffness of the PVAL gels increase in relation to their freezing time (Stauffer & Peppas, 1992).

Several articles have suggested varying methods for the preparation of PVAL gels including: heating at 90 °C for 3 hours and freezing at -20 °C for an hour (Millon, Mohammadi, & Wan, 2006); making transparent PVAL gels applying 80 °C for dissolving the PVAL crystal and 0 °C - 37 °C for freezing-thawing cycle (Gupta, Webster, & Sinha, 2011); heating at 90 °C for six hours followed by freezing at -20 °C for 18 hours then thawing at 25 °C for 6 hours (Peppas & Scott, 1992); heating at 100 °C for an hour then freezing at -20 °C and thawing for 14 hour at room temperature (King, Moran, McNamara, Fagan, & Browne, 2011); heating at 90 °C in a water bath followed by freezing at -30 °C for 12 hours and thawing for 12 hours at 15 °C (Cournane, Cannon, Browne, & Fagan, 2010).

Variations in the construction of PVAL phantoms might make the process of PVAL production difficult for researchers to follow. However, variations in the time and temperature of boiling, freezing, and thawing might be the results of utilising various lab equipment (for example, magnetic stirrer versus mechanical stirrers), concentration of PVAL crystal, molecular weight of PVAL crystals, and size of the PVAL phantoms.

Chapter 8 CT scan

In order to measure the relationship between the lesion visibility and the breast thickness in mammography, an anthropomorphic breast phantom/lesion was essential. As no such phantom was readily available, this research developed a phantom (see 10.1 on page 117). For the phantom developed to be suitable as a human substitute, it must exhibit similar X-ray imaging properties to human tissues. A CT scanner was employed to measure the X-ray properties of the phantoms independent of compression and to validate their similarity to human tissue. Once the phantoms developed were validated, then the phantoms could be taken to a mammography unit to measure the effect of compression.

Computed tomography (CT) is a medical imaging modality which utilises X-rays. A CT scanner comprises of an X-ray tube which rotates around a patient lying on a CT bed. The patient continuously moves through the rotating tube. In order to image the tissue of interest, the X-ray beams have to strike the detectors on the opposite side of the body.

8.1 PHYSICS AND MECHANISM OF CT SCAN

In order to ensure the proper utilisation of the CT machine and understand the results of the imaging performed, it was necessary to know the corresponding physics and mechanism of the system. In this research, the X-ray properties of the breast phantom/lesions were measured using a measure called Hounsfield unit (HU), therefore knowing about this concept and the features affecting HU was crucial.

In CT scan, window setup, protocols, image acquisition, and image reconstruction can have influence on the image quality. Therefore acquiring some knowledge regarding these concepts was recommended.

Unlike two-dimensional imaging modalities such as mammography, CT is a three-dimensional medical imaging modality. The images acquired from CT imaging are a sequence of slices, hence knowing about the mechanism of acquiring these slices and the factors which can affect the quality of these slices could be beneficial in order to acquire high quality CT images.

This chapter intends to discuss briefly the following concepts: Hounsfield unit (HU), windowing, kVp, CT protocols, pixel and voxel, axial/sequential versus helical/spiral acquisition, and CT image reconstruction.

8.1.1 Hounsfield unit (HU)

In CT scan, a measurement called Hounsfield unit (HU) or CT number is used in order to measure the radiodensity of the tissues. In other words, HU determines the radiation attenuation in various tissues. This represents the linear transformation of the linear attenuation coefficient of the object. As the linear attenuation coefficient of water does not change based on the energy of the X-ray, it is commonly used as a reference point for measuring the HU or CT number (Kalender, 2011).

Based on the definition of the CT value, if the linear attenuation coefficient of the X-rayed tissue (μ_t) is equal to water, then the HU is 0 for that tissue. If μ_t is less than μ_{water}, the HU will be negative and if μ_t is greater than μ_{water}, the HU will be positive. Dense tissues such as bone have high positive HU while tissues with low μ such as fat have negative HU (Kalender, 2011).

$$CT\ Number = 1000 * \frac{(\mu_t - \mu_{water})}{\mu_{water}}\ \text{HU}$$

As the above formula displays, The CT number is a function of the linear attenuation coefficient. Linear attenuation coefficient, μ is the product of density (ρ) and

the mass attenuation coefficient (μ/ρ). The amount of mass attenuation coefficient is related to the energy of the X-ray and the atomic number (Z) of the X-rayed tissue (Kalender, 2011).

$$\mu = \left[\left(\frac{\mu}{\rho}\right)(E, Z)\right] * \rho$$

The following image (Figure 8.1) depicts the HU of various tissues. These numbers indicate the linear attenuation coefficient of the tissues relative to the linear attenuation coefficient of water (Kalender, 2011).

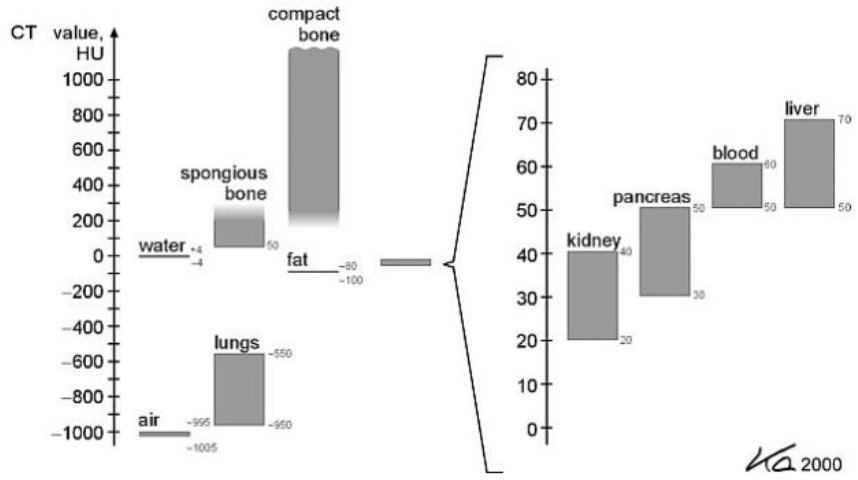

Figure 8.1 The Hounsfield scale (Kalender, 2011)

8.1.2 Windowing

It is impossible to view 4096 grey scales in a single view. Therefore, a process called windowing is utilised to view the CT images. Windowing narrows down the range of shades of grey by altering the contrast scale and brightness levels. In a selected window, values above the chosen window are displayed as white and the values below the window are shown as black. In order to choose a window of interest, the centre and

the width of the window have to be determined on the CT console. The centre is selected based upon the mean CT value (brightness) of the anatomy of interest and the window width shows the contrast in the image. The following image (Figure 8.2) illustrates the windowing procedure in order to view various anatomical structures such as bone, mediastinal, and lung (Kalender, 2011).

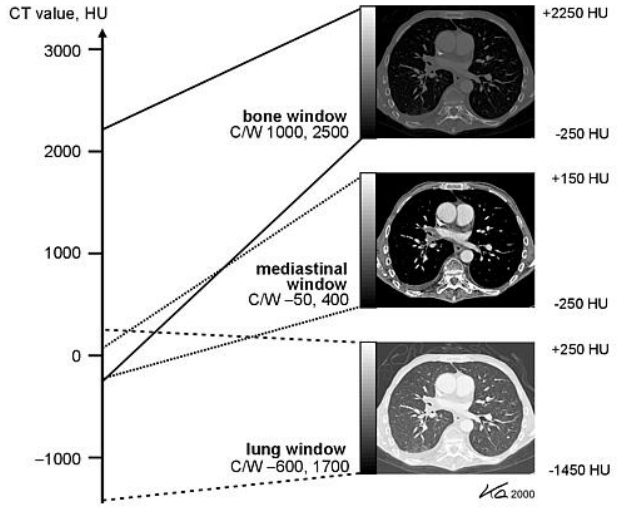

Figure 8.2 Windowing in CT (Kalender, 2011)

8.1.3 The role of kVp in CT

When the X-ray beams pass through an object the beams become attenuated and their intensity decreases. The energy of the incoming beam (kVp) has direct effect on the linear attenuation coefficient values. This indicates that a higher kVp generates a lower linear attenuation coefficient. Since the measurement of attenuation in CT is based on Hounsfield Units (HU) and the HUs are function of linear attenuation coefficient, then the kVp has direct effect on the HU in CT imaging (Philips, 1999).

In CT imaging the proper selection of kVp has an important effect on image quality and patient radiation dose. Although the lower kVp produces more photoelectric

effect and causes the object to be more attenuating, it also has impact on the overall signal and the amount of noise in the image. Therefore, it generates a lower signal to noise ratio. In order to compensate the decrease in signal to noise ratio, the mAs has to increase and the increase of mAs in turn increases the radiation dose to the patient. Hence, selecting the right value for kVp is important in CT imaging (Philips, 1999).

Depending on the vendors, different kVp spectra values scans can be utilised clinically. Commonly the following values are employed: 80, 100, 120 and 140 kVp (Upstate medical university, 2011). It is important to mention that one of the main differences between the CT scan and mammography is the range of kVp used in these two imaging modalities. This will be discussed in the mammography chapter (6.2.1 on page 56).

The Compton scatter interaction has the highest probability in these ranges of kVp. The likelihood of Compton scattering for the 120 to 140 kVp spectra in soft tissues is 10 times more than photoelectric effect (Bushberg, Seibert, Leidholdt, & Boone, 2012).

8.1.4 CT protocols

A CT scanner typically utilises pre-set protocols prior to its performance. A CT protocol is a set of defined parameters to instruct the CT scanner. These protocols include a wide range of acquisition parameters such as mAs, kV, rotation time, window width/window level, pitch, and slice thickness. These parameters are set based upon the nature of the anatomy of interest. For example, for a large patient, a higher mAs has to be set in the protocol in order to generate enough photons to produce good quality images. A typical CT scanner might have between 100 and 300 preloaded protocols for various purposes (Bushberg, Seibert, Leidholdt, & Boone, 2012).

8.1.5 Pixel and Voxel

In the CT scan, the raw image data is converted to a series of continuous axial images. Although each individual image from the series is 2 dimensional in itself, the images together display a 3 dimensional representation of the body/organ. Therefore the term of volume element or voxel is commonly used in CT imaging in order to refer to a specific location in the patient. The picture element or pixel is referred to the specific location in each individual image from the series. The following image illustrates the pixel and voxel in CT images (Figure 8.3 Pixel and voxel in CT images (Bushberg, Seibert, Leidholdt, & Boone, 2012).

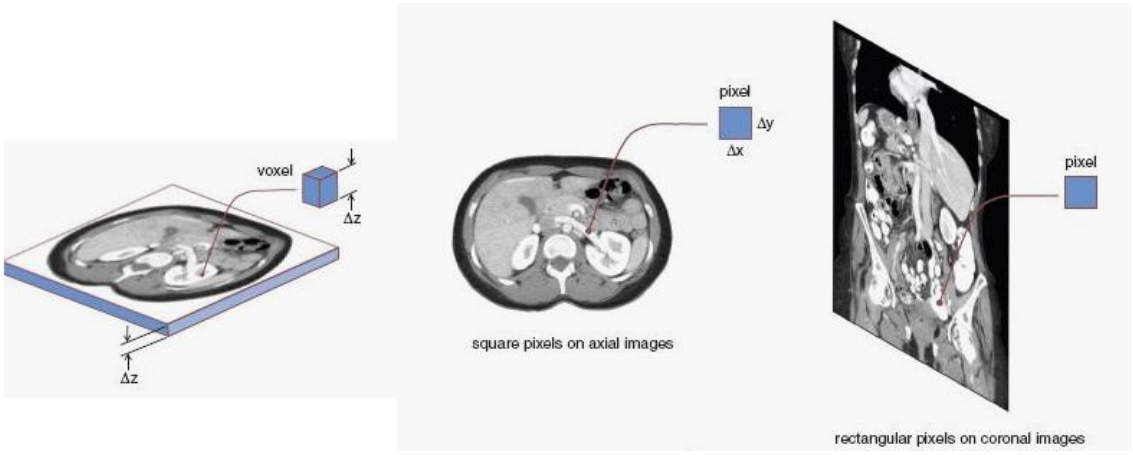

Figure 8.3 Pixel and voxel in CT images (Bushberg, Seibert, Leidholdt, & Boone, 2012)

8.1.6 The CT process

In order to produce a CT image, two major steps have to be carried out. These steps are data acquisition and image reconstruction. Data acquisition is defined by scanning the patient in order to collect the X-ray attenuation data (Jones, Hogg, & Seeram, 2013). There are multiple data acquisitions methods in CT such as axial/sequential, helical/spiral, and cone beam methods (Bushberg, Seibert, Leidholdt, &

Boone, 2012). This section is aimed to discuss only axial/sequential and helical/spiral methods.

In the image reconstruction process, the attenuation readings from the image acquisition step with the assistance of mathematical algorithms are employed in order to generate the CT images (Jones, Hogg, & Seeram, 2013). The reconstruction algorithms discussed in this chapter are backprojection and filtered backprojection.

8.1.7 Axial/ Sequential Acquisition

Axial or sequential acquisition is based on step-and-shoot mode. This means that when the table moves, the X-ray tube is off and when the table is stationary, the X-ray is activated and data acquisition starts. During data acquisition, the X-ray tube rotates 360° around the area of interest. This process is repeated until the entire anatomical area is covered.

This process is time consuming because of the continuous start-stop sequence of the table and the X-ray tube. Basically, the distance that the table moves is equal to the detector array's width. Practically the X-ray beam's width is slightly wider than the table distance before each exposure; this difference causes overlapping X-ray on the body between the acquisitions (Figure 8.4) and the X-ray overlapping increases the patient radiation dose.

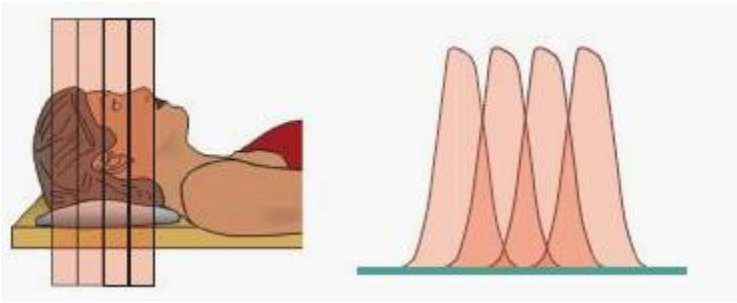

Figure 8.4 Axial/ Sequential Acquisition (Bushberg, Seibert, Leidholdt, & Boone, 2012)

8.1.8 Helical/Spiral Acquisition

In helical or spiral acquisition, the table moves constantly while the X-ray tube rotates around the patient. Unlike the sequential acquisition which forms a full circle around the patient, this method of acquisition forms a helix (Figure 8.5). Due to the elimination of the start-stop processes, this method is faster than the sequential one (Bushberg, Seibert, Leidholdt, & Boone, 2012).

In helical acquisition, the ratio of the table distance per 360° tube rotation to the thickness of the X-ray beam is referred to as pitch. When the pitch is equal to 1, this acquisition is similar to sequential acquisition. The pitch lower or greater than 1 results in overscanning or underscanning the anatomical area. The overscanning increases the patient radiation dose, while the underscanning results in lower patient radiation dose (Bushberg, Seibert, Leidholdt, & Boone, 2012).

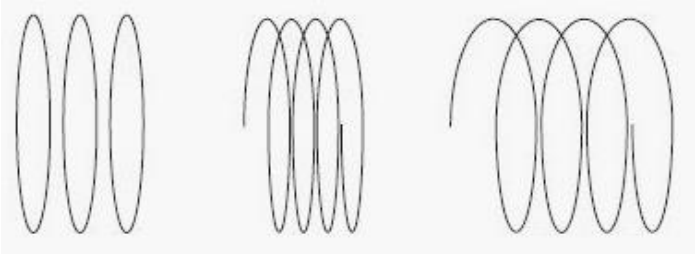

Figure 8.5 Formation of circle and helix in sequential (left) and helical (middle and right) CT acquisitions (Bushberg, Seibert, Leidholdt, & Boone, 2012)

8.1.9 CT image reconstruction

In CT imaging, in order to form the image from the raw data, a specific algorithm or method has to be employed. One of these reconstruction methods is called backprojection. In backprojection reconstruction, first the profiles of the object from multiple angles are provided. In order to form the final image of the object, all of the collecting views are then summed up along the path they were originally collected. The

following image (Figure 8.6) illustrates a reconstructed image employing the backprojection method (Goldman, Principles of CT and CT Technology, 2007).

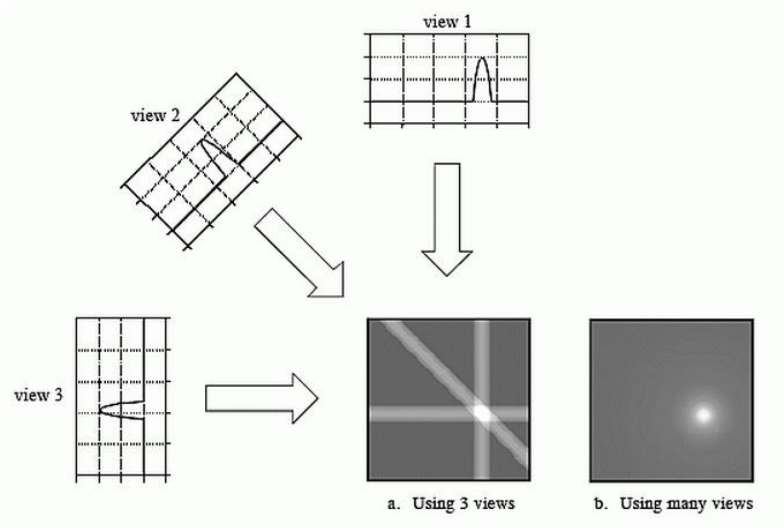

Figure 8.6 Backprojection image reconstruction (Smith, 1997)

In order to combat the poor spatial resolution and image blurring with the back projection image reconstruction method, a filter can be used. This filter is a mathematical function which is convoluted with individual views before the backprojection procedure (Goldberger & Ng, 2010). This method of image reconstruction is called filtered backprojection (FBP). Interestingly, despite all the significant progress in the hardware of detectors, X-ray sources, gantry, and system performance, the FBP as a method of image reconstruction remains unchanged over a period of 25 years (Pan, Sidky, & Vannier, 2009). Perhaps employment of new algorithms for image reconstruction requires an entire re-design for the CT scanner. The following image displays the filtered back projected image (Figure 8.7).

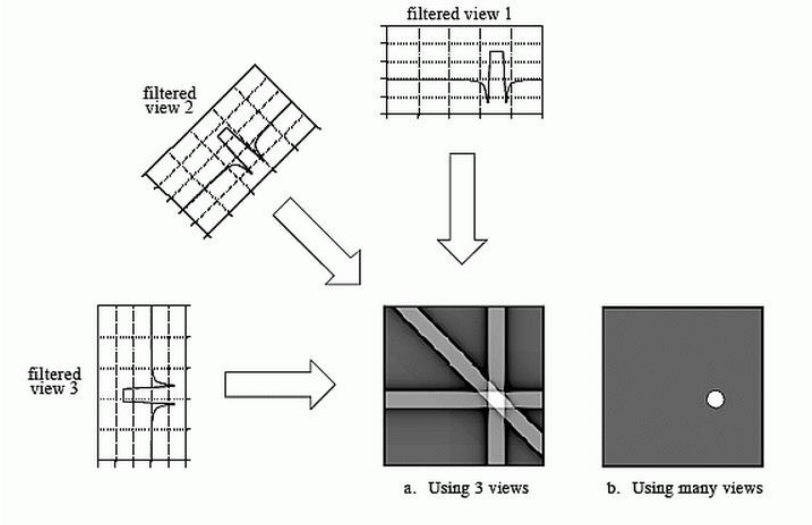

Figure 8.7 Filtered backprojection image reconstruction (Smith, 1997)

Chapter 9 Medical Image Perception

In clinical practice, missing a lesion can be life threating and falsely detecting abnormalities can cause the patient to undergo unnecessary procedures such as biopsy. Although computer technology such as computer-aided diagnosis (CAD) and artificial intelligence can assist in detecting lesions/abnormalities, they can never replace human expertise (Sabih, Sabih, Sabih, & Khan, 2011). Therefore visual perception remains an essential part of medical imaging and must be included as part of this research.

In a visual perception experiment, an image or a set of images is viewed by an observer and a set of predetermined questions are answered about the images in order to create an interpretation of the image data. In order to avoid confusion and ambiguity for the observer, the questions have to be clear, specific, and related to the objective of the research. For instance, the observer might be asked about the presence of a lesion within the image. It is essential for the observer to know what he/she is looking for in the images.

9.1 FACTORS IN PERCEPTION STUDIES

This section is aimed to discuss the factors which are necessary to conduct visual perception studies. These factors include the number of samples/observers, the methodologies employed, the sources of errors, speed/accuracy, and the effect of the observation environment.

9.1.1 Numbers

In a perception experiment the number of samples, observers, and repeated readings per observer have to be determined prior to the experiment. Typical numbers of samples for pilot studies are tens of cases. While clinical studies will often have hundreds to thousands of cases. Depending on the goals of the studies, the appropriate number of

observers can vary between studies (Obuchowski, 2004). For example in a visual perception study with mammograms and power-law noise (Burgess, Jacobson, & Judy, 2001), three observers participated while in another perceptual study over one hundred observers performed the visual perception tasks (Beam, Layde, & Sullivan, 1996). In most of the perception studies, a minimum of three observers are employed and in large-scale clinical trials tens or even hundreds of observers can be used (Samei & Li, 2010)

Variations in the number of observers/sample size can be justified by the nature of the study. In the studies with significant differences in results between observers, increasing the number of observers/samples might lead the study to acquire more accurate and robust results. In contrary, in the studies which can be performed adequately with a smaller number of observers and sample size, increasing the number of observers/sample size could increase the cost of the study.

In order to measure the reliability of the acquired data by the observers there are a variety of methods to measure inter-rater (between readers or observers) reliability. These methods can help to see if the number of samples/observers was sufficient. Kappa and intraclass correlation coefficient are examples of methods for measuring the reliability of the acquired data by independent observers (Gisev, Bell, & Chen, 2013). This research has used intraclass correlation coefficient to measure the reliability of the data.

9.1.2 Methodology

In the medical imaging field two common methodologies are employed used to perceive the images visually; alternative forced choice (AFC) and receiver operating characteristic (ROC). This section is intended to discuss the main principles of AFC and ROC.

9.1.2.1 Alternative Forced Choice (AFC)

The AFC method has been used in various studies (Tugwell, et al., 2014) (Allen, Hogg, Ma, & Szczepura, 2013).

In the Alternative Forced Choice (AFC) method, multiple sets of images are compared against each other in order to assess the presence of an abnormality within one of the images. The number of images being compared at a time is typically represented by a prefix to the AFC acronym. Two-alternative forced choice (2AFC) denotes that two images are compared with each other while four alternative forced choice (4AFC) would compare four images.

In 2AFC one of the images would act as a reference image while the other might contain an abnormality such as a lesion. The observer is asked to identify the image with the abnormality. A Likert scale is sometimes employed to score the random image compared to the reference one (Tugwell, et al., 2014) (Allen, Hogg, Ma, & Szczepura, 2013). After collecting and analysing all the data, the results are used to assess the percentage of the correct decisions (Samei & Li, 2010). This is carried out by dividing the number of correctly detected images by the total number of trials (Svahn & Tingberg, 2014).

9.1.2.2 Receiver operating characteristics (ROC)

Receiver operating characteristics (ROC) graphs are widely used in medical decision making (Tourassi, 2010). In ROC study the observer classifies the presence (positive) or absence (negative) of the disease to the diagnostic cases. For example, the presence of a lesion in a mammogram is a positive state while the absence of the lesion is the negative state assigned to the diagnostic case. The observer's classification is compared to the gold standard reference (Fawcett, 2006) .

In the interpretation of radiographs there is a trade-off between sensitivity and specificity. Sensitivity, also known as the true positive rate measures the proportion of actual positives identified, while specificity (true negative rate) measures the amount of the cases where the abnormality is correctly identified as not being present. Basically a ROC curve (Figure 9.1) shows a simple variation of the sensitivity versus specificity. This trade-off depends on the observer's threshold for considering a case positive. Low-threshold exams have high sensitivity and lower specificity while high-threshold exams have low sensitivity and higher specificity. In high sensitivity systems, fewer positive cases will be missed whereas with high specificity fewer negative cases will be mistakenly called positive.

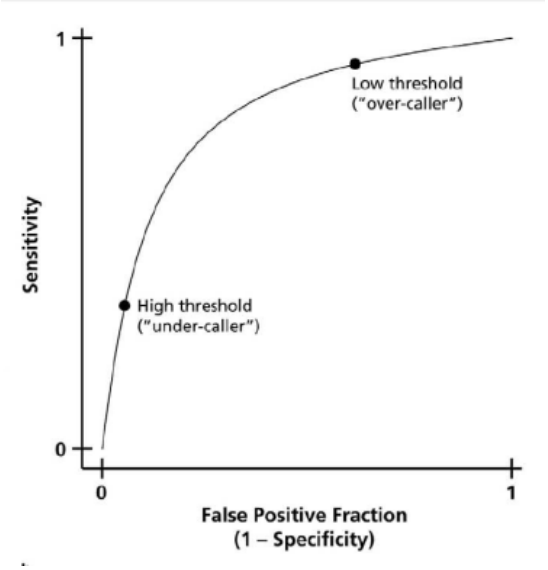

Figure 9.1 ROC curve (Eng, 2005)

The area under the ROC curve (AUC) can be used to show the diagnostic performance or average accuracy of the diagnostic test. This area can be interpreted as the average sensitivity over the entire range of possible specificities or the average specificity over the range of possible sensitivities. AUC values range from 0 to 1. AUC

is 1 for 100% sensitivity and specificity and 0.5 for blind guessing. The graph below (Figure 9.2) shows the plots for the 100% sensitivity/specificity and the random guessing.

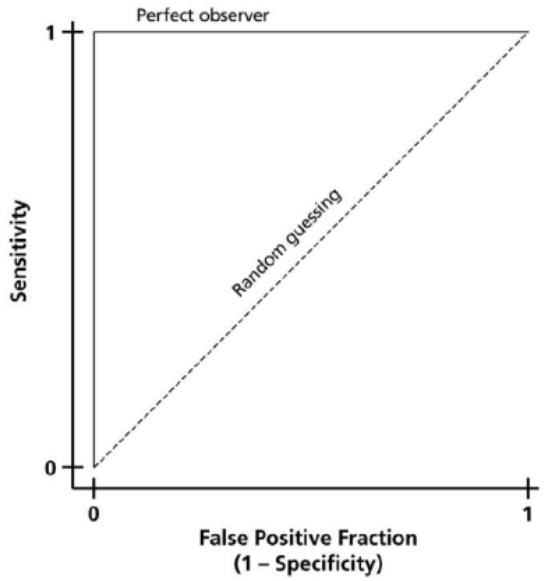

Figure 9.2 100% sensitivity/specificity and the random guessing (Tourassi, 2010)

The advantage of using AUC over the traditional methods such as classification accuracy based on true positive, true negative, false positive and false negative is the independency of the test from the threshold that the observer selects (Tourassi, 2010).

Although ROC analysis is commonly used in clinical research to express the diagnostic accuracy of imaging examinations, it is not always a well-equipped method for all types of clinical studies. For example, conventional ROC cannot be useful when the location of the lesion in addition to its presence is required to be known (Eng, 2005). Conventional ROC is not also suitable for the cases when more than one occurrence of the abnormality such as a lesion happens in an image (Eng, 2005). Depending on its application, ROC has some derivatives. These derivatives include localization ROC (LROC), free-response ROC (Eng, 2005), and jack-knife free-response ROC (JAFROC) (Chakraborty, 2005).

9.1.2.3 Comparison of AFC and ROC

Generally speaking, ROC provides improved statistical power and clinical relevance in comparison to AFC. One of the examples of clinical irrelevance of AFC is that, unlike ROC curve, AFC does not present a trade-off between sensitivity and specificity (Samei & Li, 2010). Since the evaluation of the images is direct in AFC, this method results in a lower level of variation. Reading times in AFC are also faster than in the ROC method (Svahn & Tingberg, 2014). The AFC method can be used to compare the subtle differences between the performances of various imaging modalities effectively. Although, the scenario of comparing two or more random images with each other is not performed clinically (Svahn & Tingberg, 2014), it is used as a method to evaluate the image quality in phantom studies (Tugwell, et al., 2014) (Allen, Hogg, Ma, & Szczepura, 2013).

9.1.3 Sources of errors in medical image perception

Errors associated with visual perception experiments can be categorized as visual or cognitive errors. Visual errors (55% of the errors) are usually due to an incomplete search. Alternately, cognitive errors (45% of the errors) occur when the observer makes the wrong decision while evaluating an image (Samei & Krupinski, 2010). Not detecting a lesion in an image can be an example of visual errors and recognizing the lesion, but calling the cancer lesion non-cancerous (false negative) due to a wrong decision can be an example of a cognitive error.

According to Manning et al, the majority of errors were failures of decision making rather than detection (Manning, Ethell, & Donovan, 2004). Visual errors might happen because of not looking at the area of abnormality or not fixating on the pathological territory for sufficient amount of time (Samei & Krupinski, 2010).

Most information collected from the eye is during a fixation. The highest spatial resolution or ability to see the detail happens when the visual input falls on the fovea centralis (fovea) area of the retina. In perception research it is necessary to search or scan with the fovea, especially the small and low-contrast features of the image (Krupinski, 2010) .

9.1.3.1 Sources of errors in mammographic perceptions

Interpreting mammograms is a tedious task because of the uniqueness of each mammogram. Unlike the brain, uterus, liver and other organs, the mammograms are like a unique map for every individual. Moreover, the mammogram of a patient changes over time based upon the age, hormonal changes, and menopausal status (Zuley, 2010). Since breast cancer is the most commonly diagnosed cancer among women (Zuley, 2010), addressing the source of errors in the visual perception in mammograms is extremely important.

Zuley has classified the mistakes in perceiving mammogram into three categories: search errors, recognition errors, and decision making errors. In search errors, the area of lesion is never identified by the reader. Recognition errors occur when the lesion is fixed on by the eye but quickly dismissed. The eye does not re-fix on the lesion again. Satisfaction of search (SOS) is a well-known occurrence in radiology, in which the lesions remain undetected after identifying the initial lesions (Mello-Thoms, Trieu, & Brennan, 2014). SOS can play an important role in missing abnormalities within an image. In this case, an experienced observer might ignore some possible abnormalities after finding the first one.

Decision making errors occur when the lesion is found but the assessment of its nature is incorrectly made. This results in the lesion either being falsely identified as

cancerous (false-positive) or being dismissed as benign when it is actually cancerous (false-negative). Normal tissue structure in medical radiographs or anatomical noise can mask the abnormal tissue. Anatomical noise is one of the main contributors in decision errors. Decision making errors will cause either false positive or false negative decisions while search and recognition errors cause only false negatives (Zuley, 2010). The following diagram (Figure 9.3) depicts these three types of perceptual mistakes in reading mammograms.

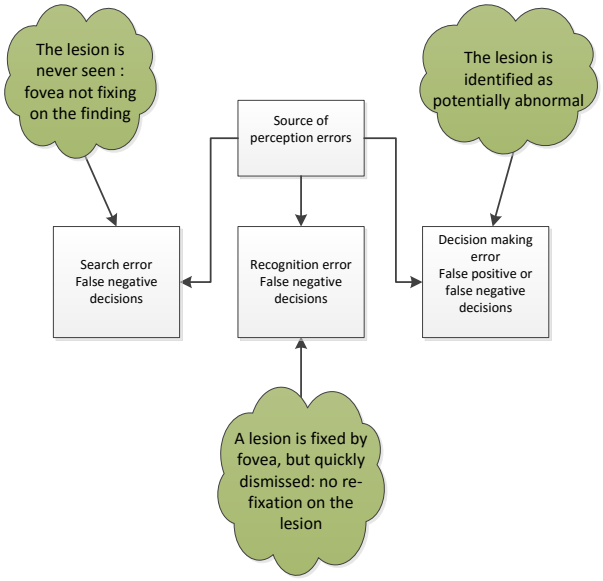

Figure 9.3 Zuley's classification of perceptual errors (Zuley, 2010)

9.1.4 Speed/Accuracy

In visual perception studies, the speed of the search/detection and the accuracy of the assessment made, corresponding to the level of expertise is important. Research has shown that the speed and the accuracy of the decisions are improved with experience (Krupinski & Borah). For example a radiologist who has read thousands of mammograms with normal variations of breast tissue, benign nodules and cancer lesions has built up a mental catalogue or data base of normal and abnormal breast features in his/her mind.

This database helps him/her to be rapid and accurate perceptually. Several research studies have shown that wrong decisions take longer than correct ones. For example, in clinical studies, true positive decisions are faster that false positives and similarly true negatives are faster than false negatives (Zuley, 2010).

9.1.5 The effect of the observation environment

Observational environmental factors including monitor technology, calibration of the monitors, positioning and ambient lighting have crucial roles in visual perception tasks such as the assessment of mammograms.

One of the key environmental factors for visual perception tasks is the display technology employed. Cathode ray tube (CRT) and liquid crystal display (LCD) monitors are two display technologies commonly used. CRT displays have a high refresh rate with the screen being redrawn approximately 30000 times per minute. The LCD display technology does not require the entire screen to be redrawn and therefore can result in less eye fatigue for the observers. In order to be clinically acceptable, a display screen must have at least a five megapixel resolution (Zuley, 2010).

Proper calibration of mammography monitors is essential to allow the observers to visualize different shades of grey in the mammogram from the brightest to the darkest regions. All medical displays must comply with particular specifications. One of these specifications is the fixed relationship of the maximum and the minimum luminance output of any monitor pair. Detection of more shades of grey can be achieved by having the higher maximum luminance. Since there is a fixed relationship between the maximum and minimum luminance, the minimum luminance has to increase too. The maximum and minimum luminance control how white and black the bright and dark areas will appear respectively (Zuley, 2010).

Due to the limitation of maximum luminance in CRT monitors, there should be no light in the room at perception time. Conversely, for LCD monitors a low level of background ambient light is recommended.

For better visual perception, it is also recommended by the manufacturers to turn the monitors slightly toward each other. This allows the observer to see the entire image without the need for leaning his/her body or head. This results in a lower level of strain on the neck/eyes and decreases the fatigue (Zuley, 2010).

9.2 PERCEPTUAL ISSUES IN MAMMOGRAPHY

The viewing conditions in mammography have influence on the results of the image perception. The screening mammograms are read in batches, possibly several hundred cases in some busy hospitals. Viewing numerous normal cases (approximately 3 cancer cases in 1000 screening mammograms) requires more awareness in order to avoid false negatives (Zuley, 2010). It is worth mentioning that 11% of the suspicious cases have to come back for further tests. Due to overlapping breast tissue and/or benign fibrocystic problems, a large proportion of the recalled cases are incorrectly assessed and become false positives. Interpretation of high volume of mammograms, short viewing time and rare cases of cancer might cause physical/mental fatigue leading to misperceptions. Therefore, it is essential to optimize the screening reading environment in order to reduce the rate of misperceptions (Zuley, 2010).

Chapter 10 Methods

10.1 METHODS FOR THE DEVELOPMENT OF PVAL PHANTOM AND LESIONS

The aim of this chapter was to demonstrate how to design and fabricate the PVAL phantoms with embedded lesions. In order to simulate phantoms/lesions similar to human tissue, the X-ray and mechanical properties of the phantoms/lesions have to be similar to the breast tissue and cancer lesions. Therefore several experiments have been performed to assess this resemblance.

This chapter has been classified into the following categories: Producing the PVAL phantoms by heating the solution followed by freezing-thawing; measuring the mechanical and X-ray properties of the phantoms/lesions; determining the adequate amount of contrast agent doped with the lesions; and evaluating the shelf life of the PVAL lesions based on the effect of the environment.

10.1.1 Equipment used for the formation and analysis of the PVAL gel

In this research, the equipment listed in the following table (Table 10.1) was employed in order to fabricate PVAL breast phantoms/lesions. Some of the materials such as staple gun and ratchet strap were utilised in order to attach the phantom to the wooden torso for the mammography procedure.

Material	Use
1 litre three socket boiling flask	To prepare the aqueous solution of PVAL
Glass Thermometer	To measure the temperature of the PVAL solution
Digital Thermometer (VWR, EU620-0916, -50 °C to +200 °C)	To measure the temperature of the water bath
500 mm Air Condenser	To condense the PVAL/water steam during preparing PVAL solution
Magnetic bar	To stir the PVAL solution
Water Bath	To control the temperature of the PVAL solution
Ceramic hotplate/stirrer VWR Model 444-0599	To boil the PVAL solution by heating and stirring the solution
Digital scale	To measure PVAL crystal
Measuring cylinder	To measure deionised water
Clamp Stand	To hold the boiling flask inside the water bath
Fume cupboard	To protect against the hot bath boiling water and possible evaporated mixture of water and PVAL
Flat bottomed plastic cylindrical moulds (140 cc)	To make cylindrical phantoms measurable with the Instron machine
Domestic chest freezer (Nova Scotia CF 380)	To freeze the PVAL solution in order to make gel
Axminster Digital Electronic Calipers (0 - 150 mm)	To measure the height and diameter of the phantoms for Instron machine
Nylon Thread	To suspend the PVAL lesions in the PVAL solution
Bead cutter	To make 9 mm round lesions
Ratchet strap	To attach the wooden board to the mammography unit
Wooden board with the base	To attach the breast phantom/skin to the board during the mammographic imaging
Plastic breast mould	To fabricate breast-shaped phantom
Staple gun	To attach the latex skin to the wooden board

Table 10.1 Equipment for development of PVAL breast phantoms/lesions

The following image (Figure 10.1) shows the equipment used inside the fume cupboard.

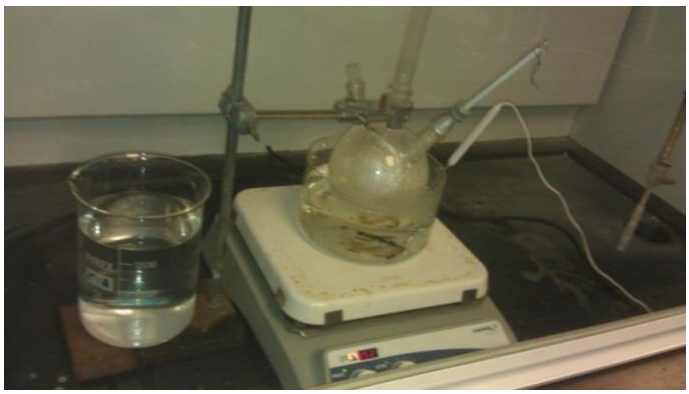

Figure 10.1 Equipment used inside a fume cupboard: A magnetic hotplate/stirrer, water bath, glass thermometer, digital thermometer, air condenser, and clamp stand.

10.1.2 Materials used in the formation of the phantoms and lesions

The following materials listed in the following table (Table 10.2) were utilised in order to fabricate PVAL breast phantoms/lesions.

Material	Use
PVAL from Sigma-Aldrich - having an average molecular weight from 85,000-124,000 and 99+% degree of hydrolysis	To produce PVAL phantom/lesion
Deionised water	To make PVAL phantom
Optiray 320 - Non-ionic X-ray contrast agent	To increase the attenuation coefficient of PVAL lesions
Ultrasound gel	To lubricate the latex skin of the breast phantom during breast compression
Latex paint	To make latex skin for the breast phantom

Table 10.2 Materials used in this research

The following image (Figure 10.2) shows the PVAL crystal and the Optiray contrast agent used in this research.

Figure 10.2 Left to right: PVAL from Sigma-Aldrich and Optiray 320 contrast agent.

10.1.3 Producing a PVAL solution

As is illustrated in Figure 10.3, a water bath was filled half way with tap water and placed on a magnetic hotplate and brought to a boil at 100 °C. The hotplate was set to 400 °C in order to bring the water bath to a boil at 100 °C (Appendix A). The PVAL solutions were prepared by dissolving weighed amounts (wt%) of PVAL crystal in deionised water. Deionised water is usually used in lab experiments due to low ionic contents and dissolved solids (Puretec Industrial Water, 2012) .

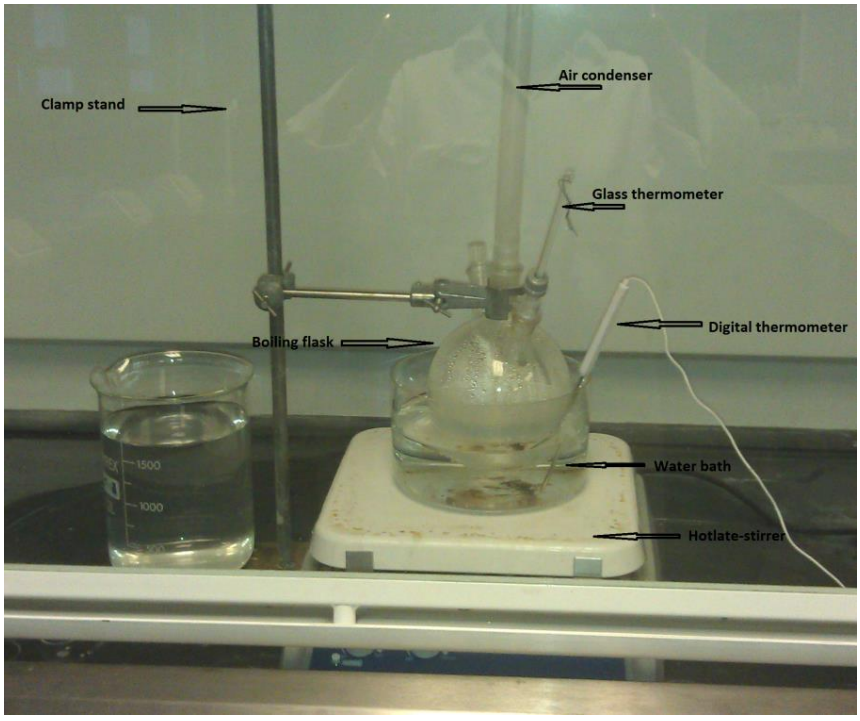

Figure 10.3 Apparatus used for the dissolving PVAL crystals into solution

The initial experiment created a solution of PVAL in deionised water by adding 40 g of PVAL crystals to 360 ml of deionised water. The phantoms which were made with this amount of PVAL crystals are called 10 wt% (weight percent in solution) or 10% PVAL phantoms throughout this thesis (Mehrabian & Samani, 2009). This means that the PVAL comprised 10% of the weight of the entire mixture. If the amount of deionised water and PVAL crystals doubled, the phantoms are still called 10% PVAL phantoms.

The mixture was placed in a 3 socket round bottomed boiling flask with a magnet bar (Figure 10.3). A glass thermometer was connected to the first socket of the boiling flask. A 500 mm glass air condenser was connected to the second socket of the boiling flask in order to minimise the loss of solution by bringing the drops of the evaporated solution back into the boiling flask. The final socket was capped as it was not needed for this experiment.

The boiling flask was then suspended, using a clamp stand, in the water bath until the level of the water in the bath was level with the solution in the flask. The magnetic hotplate was set to stir at 400 rpm. Once the water bath had returned to a boil, the internal temperature of the solution was measured to have reached 95 °C. This was then continuously heated for an hour until the solution was transparent with no visible un-dissolved PVAL crystals. The undissolved crystals do not take part in the polymeric network of the PVAL phantom results in the unstable and non-rigid phantoms.

The aqueous PVAL solution then was allowed to rest at room temperature for 3 hours to remove any air bubbles resulting from the process of stirring while heating (Figure 10.4). The removal of air bubbles from the aqueous solution of PVAL helps not to add undesirable extra features such as air bubbles to the CT images and mammograms.

This experiment was then repeated with the following PVAL concentrations: 2.5%, 5%, 7.5%, and 15%. Since the human breast and cancer lesions can have various levels of stiffness, different percentages of PVAL were tested in this research in order to simulate the appropriate rigidity for the breast phantoms/lesions. 5% and 10% PVAL phantoms were already used by researchers (Mehrabian & Samani, 2009), hence in addition to 5% and 10% PVAL, concentration lower than 5%, between 5% and 10% and above 10% were taken into consideration in this study.

Figure 10.4 transparent PVAL solution before freeze-thaw cycles

10.1.4 Creation of a PVAL gel from a PVAL solution using freezing/thawing

Freezing the PVAL solution is the next phase in PVAL gel formation. As the PVAL solution cooled to room temperature, a skin formed on the surface. Before pouring the solution into the moulds, this skin was removed and discarded in order to ensure that the PVAL solution was homogenous. The gel was then poured into flat bottomed cylindrical plastic moulds and placed into a domestic freezer (Nova Scotia) at -26 °C for 12 hours (7.3 on page 95). The frozen gel was then thawed at room temperature until it was fully thawed. The phantom was considered thawed when no solid lumps could be detected by gently squeezing the phantom. Once the phantoms were fully thawed, they were immersed in deionised water in order to keep them from becoming dehydrated and stored in a refrigerator at 5 °C (King, Moran, McNamara, Fagan, & Browne, 2011).

As a result of these experiments, a set of deformable, mechanically stable, non-transparent PVAL phantoms ranging from PVAL concentrations of 2.5% to 15% were produced (Figure 10.5). Examining the phantoms by hand indicated the highest rigidity and stiffness for 15% PVAL phantom and in contrast the lowest rigidity and stiffness for the 2.5% phantom. It is important to mention that this experiment was not a convincing

prelude to estimation of breast phantom compressibility. Hence, later on an Instron machine was utilised to measure the Young's modulus of the breast phantoms.

Figure 10.5 PVAL gel created using a single freezing-thawing cycle (FTC)

10.1.5 Measuring the HU for the prepared phantoms

Due to the availability of a CT scanner within the University of Salford (16-slice Toshiba - Aquilion TSX-101A), the HU of the PVAL phantoms (2.5%, 5%, 7.5%, 10% and 15%) were measured by this machine. A suitable CT protocol was derived for CT imaging the PVAL phantoms. In this protocol, mAs=100, kVp=120, Window Length (WL)=0 and Window Width (WW)=300. This protocol was used throughout this research. The kVp of 120 was used in this research in order to increase the likelihood of the Compton scattering (see 8.1.3 on page 100). This kVp is also commonly used in clinical practice (Huda, Scalzetti, & Levin, 2000) (Johnson & Robins, 2012).

The CT scanner reached specification on rigorous quality assurance tests and it was operated in accordance with the manufacturer's specifications. Although the latest CT machines, up 320-slice, can provide a higher sensitivity, shorter examination time, and reduced likelihood of motion artefacts, the 16-slice CT scanners are still considered as good general purpose scanners (Centre for Evidence-based Purchasing, 2009).

In order to measure the optimal Hounsfield unit, a proper location and size with low standard deviation for the region of interest is required. Avoiding the edges of the

samples, water and air pockets, and other types of possible artefacts are other factors affecting the reading of the HU. A rectangular area in the centre of the phantom image midway from the surface and the bottom of the phantom was selected as the region of interest (ROI) for the measurements. The following image (Figure 10.6) illustrates how the ROI was selected in a CT image of a 5% PVAL phantom.

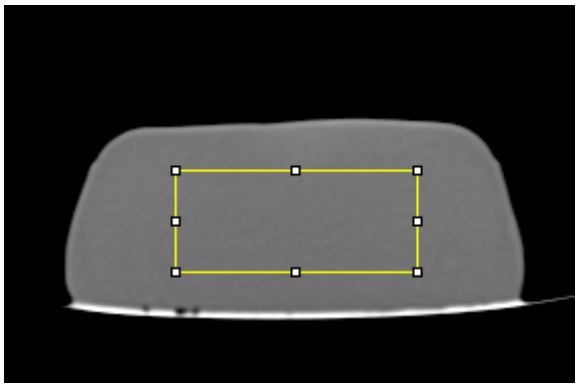

Figure 10.6 CT image of a 5% PVAL phantom with the ROI (WL=0, WW=300)

10.1.5.1 Results and analysis

The following table (Table 10.3) and graph (Figure 10.7) demonstrate the initial exploratory HU in relation to PVAL concentration. 1 FTC indicates that the number of freezing-thawing cycle was 1.

PVAL% 1 FTC	HU ± sd
2.5%	25.50±5.7
5%	25.60±4.2
7.5%	43.60±4.3
10%	39.10±2.7
15%	45.60±3.3

Table 10.3 Initial exploratory HU in relation to PVAL concentration

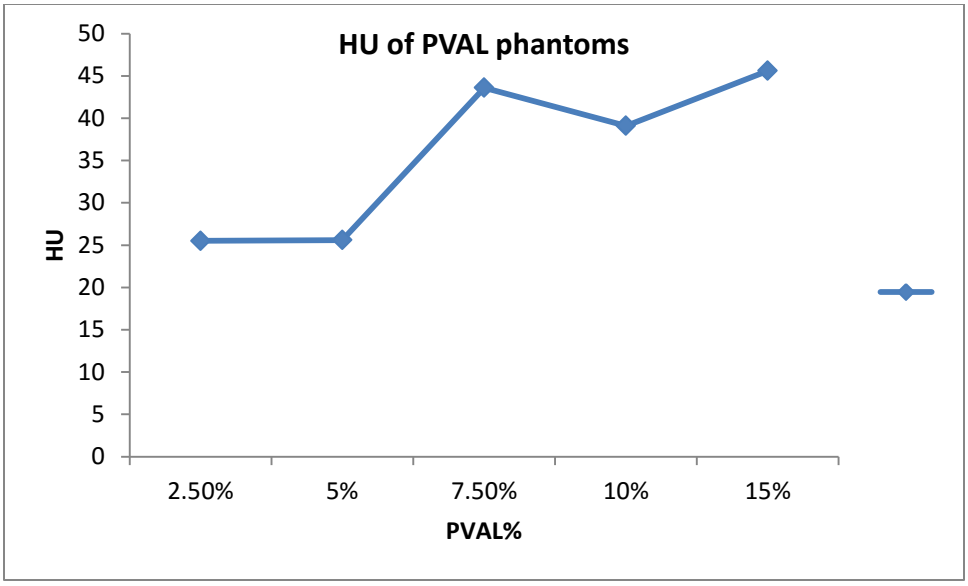

Figure 10.7 Initial exploratory HU in relation to PVAL concentration

The HU measurements of the specimens acquired show the highest HU values belonged to the specimens with a 15% PVAL concentration and the lowest values belonged to those with a 2.5% PVAL concentration. The data demonstrates the rise of the HU in relation to the PVAL concentration.

By increasing the concentration of PVAL, the density of PVAL (ρ) increases. This results in an increase of the attenuation coefficient (μ) of the X-rayed PVAL. Therefore, an increase of the attenuation coefficient results in an increase of the HU (see 8.1.1 on page 98) (Kalender, Computed Tomography, 2011).

10.1.6 Measuring of the compressibility of the prepared phantoms

In order to prepare an anthropomorphic breast phantom, it is essential to simulate mechanical compressibility properties similar to the breast tissue. Young's modulus is a measure of the stiffness of materials and this has been used as the measure of the mechanical compressibility properties.

An Instron machine (model 4469 Series IX) was used to measure the Young's modulus of the PVAL gel. This machine was available within the mechanical engineering department of the University of Salford and is commonly used for testing a wide range of materials in tension or compression.

The Instron machine with the assistance of Instron software measures the Young's modulus of various materials (Figure 10.8). Literature shows that Instron machine has been utilised to measure the mechanical properties of PVAL in order to calculate Young's modulus (Fromageau, Brusseau, Vray, Gimenez, & Delachartre, 2003). To measure the Young's modulus of the phantoms, first the height and diameter of the cylindrical specimen have to be measured by a digital calliper. The sample is then pressed by the crosshead of the machine. Displacement of the crosshead and the load based on Newton are main parameters to measure the Young's modulus by the software. The formulation below shows how the Young's modus is calculated.

Young's modulus is the ratio of axial stress to axial strain or $E=\frac{\sigma}{\varepsilon}$ where $\sigma=\frac{F}{A}$ (Force/cross sectional Area) and $\varepsilon=\frac{\Delta L}{L}$ (Changes in the length/original length). The cross sectional of cylindrical objects is $A=\pi R^2$ where R is the radius of the cylinder (Erkamp, Wiggins, Skovoroda, Emelianov, & O'Donnell, 1998).

The Instron machine was operated in accordance with manufacturer guidance and quality control checks indicated it to be working within manufacturer specification.

Measuring the YM of the above set of phantoms using an Instron machine was the next exploratory experiment. The above 5 phantoms were compressed individually by the Instron machine. Due to the lack of rigidity of 2.5% PVAL, it was not practical to measure the YM for that phantom. The following image shows (Figure 10.8) how the phantom was placed in the designated area below the compressor of the Instron machine. The initial load (1 N) or pre-compression force was determined manually using the left

panel of the machine and the type and compression parameters were controlled utilizing the Instron software.

The Instron software required the height and diameter of the samples in order to measure the YM. Therefore the height and diameter of the samples had to be measured with a digital calliper prior to utilizing the machine. The measuring of the height and diameter of 5% and 7.5% phantoms with 1-FTC with a digital calliper was quite challenging due to the softness and flexibility of these phantoms. To determine the correct height and diameter for the Instron machine's software, the measurement was performed three times and the average of the height and diameter were entered in the software. The following table (Table 10.4) shows an example of three readings of the height and diameter of a 5% phantom. The small standard deviation demonstrates a high consistency in the measurement.

5%PVAL phantom	First reading	Second reading	Third reading	Average	SD
Height	35.94	35.63	35.82	35.79	0.15
Diameter	41.63	41.47	42.02	41.70	0.28

Table 10.4 Height and diameter of a 5% cylindrical phantom

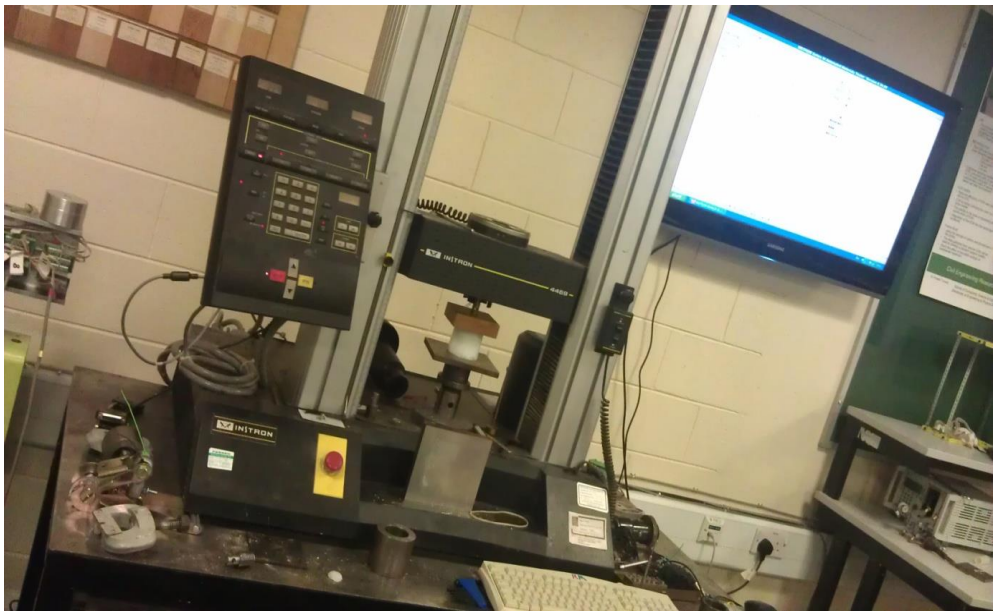

Figure 10.8 An Instron machine compressing a PVAL phantom

10.1.6.2 Results and analysis

The YM of the phantoms are demonstrated in Table 10.5 and Figure 10.9.

PVAL% 1 FTC	Young's modulus (kPa)
2.5%	NA
5%	27.50
7.5%	13.50
10%	10.60
15%	41.70

Table 10.5 YM in relation to PVAL concentration in initial exploratory

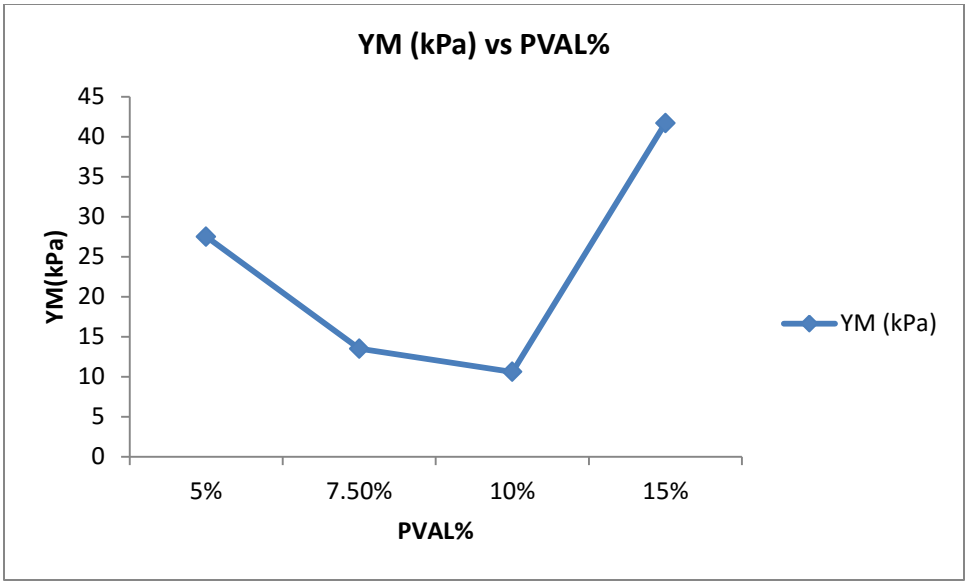

Figure 10.9 YM of PVAL with various concentrations

The results show 3.9 times increase of YM of the 15% PVAL phantom compared to 10%. Generally, the YM of the PVAL gels is expected to increase in relation to the increase in the PVAL concentration. The decrease in the YM of the 5% to 10% can be explained by the uneven surface of the phantoms. When the phantom gelled in the freeze-thaw cycle, the surface bulged in the centre. The Instron machine requires that the shape of the measured sample have a flat surface perpendicular to the axis of the compression.

In the experiments that follow, the bulged surfaces were flattened by a cutter and the YM increased in a more predictable manner. This eliminated the error when measuring YM due uneven surfaces.

10.1.7 Measuring the HU and YM of PVAL phantoms with multi freeze-thaw cycles

In order to assess the number of freeze thaw cycles required to adequately represent the Young's modulus and imaging properties of breast tissue, the following experiment was conducted. Fifteen 120 ml cylindrical samples were made: five each of

the 5%, 7.5% and 10% solutions (Figure 10.10). The 2.5% and 15% solutions were excluded due to the issues with the rigidity as demonstrated in previous experiments.

Figure 10.10 PVAL phantoms with 1-5 FTC

The following process was utilised for each wt% set of solutions to create one sample of each of the following FTC: 1 FTC, 2 FTC, 3 FTC, 4 FTC, and 5 FTC.

Into each of five identical plastic cylindrical containers, 120 ml of the desired concentration PVAL solution was measured. In order to allow for expansion during the freezing thawing process containers with a capacity of 140 ml were chosen. Prior to beginning the first FTC the poured samples were allowed to rest at room temperature for 3 hours in order allow any bubbles in the solution to come to the surface.

The samples then underwent a series of freeze-thaw cycles, freezing for 12 hours at -26 °C and then thawing at room temperature. After each successive FTC one phantom was removed from the set, placed in deionised water, and stored in a refrigerator at 5 °C.

This process was repeated until one sample of each of the desired numbers of FTC had been created. Each sample was flattened using a cutter.

Once all samples had been created, Young's modulus and Hounsfield units were measured and recorded for the samples.

10.1.7.1 Results and analysis

The effect on YM and HU is summarised in Table 10.6, Figure 10.11 and Figure 10.12. The standard deviation (±sd) in Table 10.6 was within the ROI as displayed by the CT unit. In this pilot study, in order to narrow down the range of the PVAL concentration, one sample per FTC for each concentration (5%, 7.5%, and 10%) was built. The total number of samples was 15. The HU and YM of multiple samples of the right concentration of PVAL were measured later in this research.

FTC	5% PVAL		7.5% PVAL		10% PVAL	
	HU ± sd	YM (kPa)	HU ± sd	YM (kPa)	HU ± sd	YM (kPa)
1 FTC	23.9±4.3	8.5	32.5±4.1	8.8	43.2±3.7	13.9
2 FTC	27.5±3.2	16.9	33.0±3.5	33.6	43.3±2.9	42.9
3 FTC	28.1±3.0	20.6	33.3±3.3	45.3	43.2±3.2	66.2
4 FTC	28.6±3.1	25.0	34.7±3.5	67.7	43.8±3.2	79.9
5 FTC	29.3±3.4	26.5	35.3±3.6	88.9	44.5±3.1	94.0

Table 10.6 HU and YM for phantoms by PVAL concentration and number of FTC

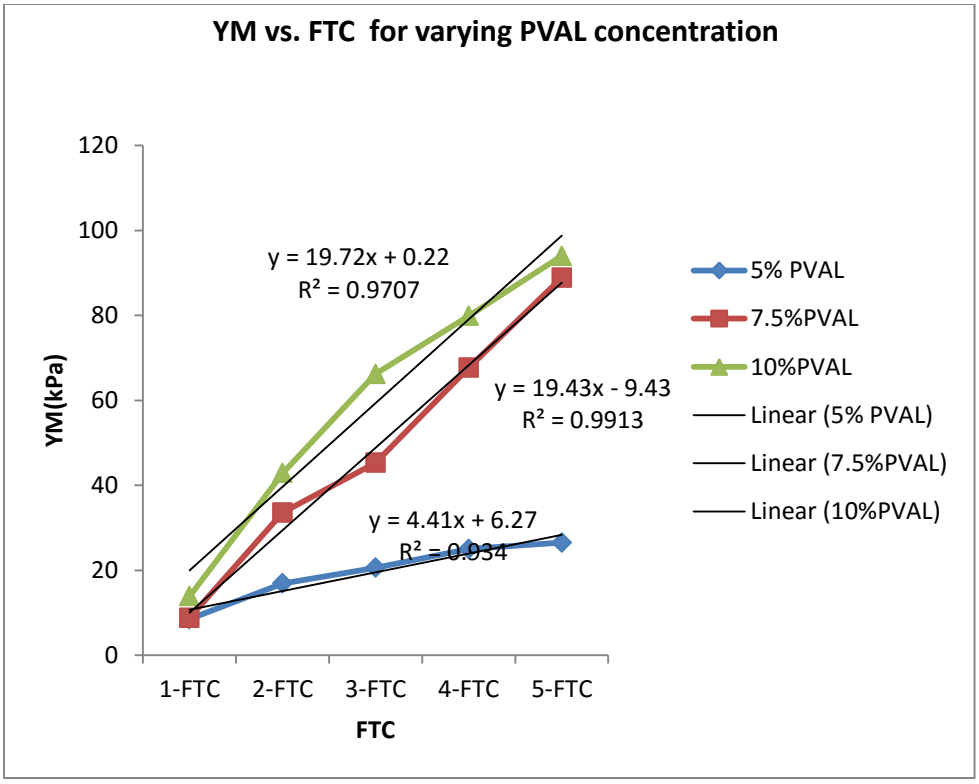

Figure 10.11 YM of 5%, 7.5% and 10% PVAL phantoms with 1-5 FTC

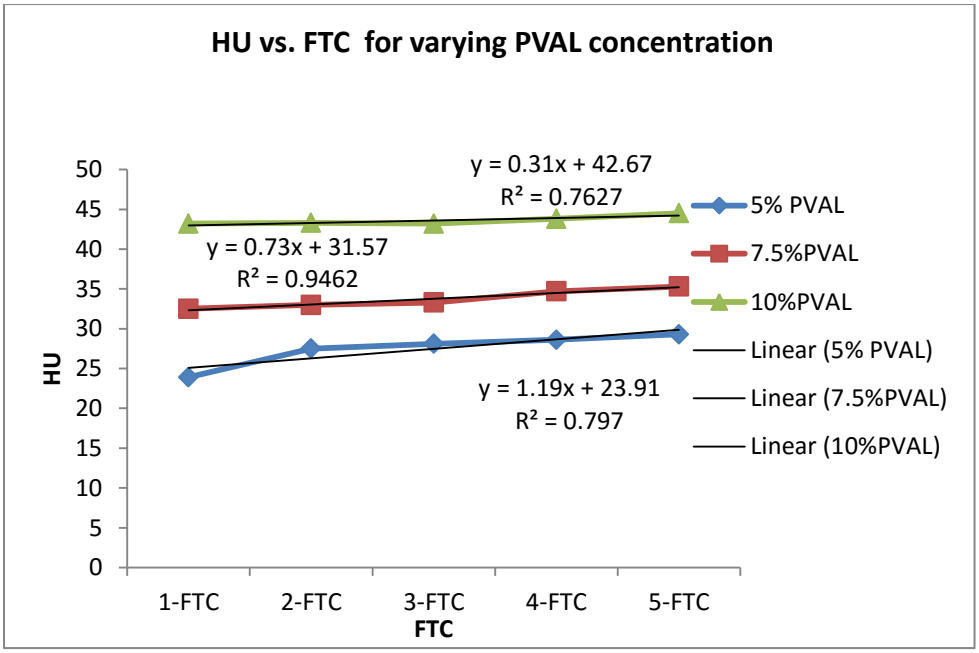

Figure 10.12 HU of 5%, 7.5% and 10% PVAL phantoms with 1-5 FTC

Based on Figure 10.11 and Figure 10.12 the graphs demonstrate the increase in HU and YM in relation to the increase of PVAL concentration. The increase of PVAL concentration generates more molecular bonds in the polymeric network resulting in a higher PVAL stiffness in the gel.

The increase in FTCs demonstrated an increase in YM across each PVAL concentration. The increase of YM for 5%, 7.5%, and 10% PVAL with 5FTCs is 3.1, 10.10, and 6.7 times more than 1FTC. However, the effect of increasing FTCs on HU, for each concentration, was less notable (see the corresponding equation on the HU graph). This means that the increase in the number of freeze-thaw cycles does not have a remarkable effect on the HU.

The YM graph (Figure 10.11) demonstrates a steeper curve for the 10% FTCs compared to 5%. As the graph shows, the slope for 10% and 5% PVAL are 19.72 and 4.41 respectively. This means that the number of freeze-thaw cycles has greater impact on YM with increasing PVAL concentrations.

As the YM graph (Figure 10.11) shows there is no notable difference between the YM of the PVAL phantoms with 1-FTC, especially between the YM of the 5% and 7.5% PVAL gels which are 8.5 and 8.8 respectively. The phantoms with 1-FTC have PVAL molecules which are not tied to the polymeric network. This incompletion of the polymeric network of PVAL causes the lack of rigidity for the phantoms with 1-FTC (Ru-yin & Dang-sheng, 2008). As the graph (Figure 10.11) shows, the effect of FTC in increasing the stiffness of the gel due to the increase in the crosslinked PVAL molecules (see 7.1 on page 91) is more observable with higher number of freezing-thawing cycles.

10.1.7.2 Discussion

A typical Young's modulus for soft tissues such as breast and liver is 20 kPa (Fromageau, Gennisson, Schmitt, Maurice, Mongrain, & Cloutier, 2007). As the graph above (Figure 10.11) shows, the YM of a 5% gel with 2 FTCs exhibits 16.9 kPa and the YM of the 5% gel with 3 FTCs shows 20.6 kPa. The proximity of the results to 20 kPa makes the 5% gel with 2 FTCs, and 3 FTCs good candidates for fatty and glandular tissues. Since the focus of this research is fabricating breast phantoms similar to breast fat, and the YM of fat is less than 20 kPa (Samani, Zubovits, & Plewes, 2007) a 5% PVAL with 2 FTCs with lower YM compared to 3 FTC was chosen as candidate for the breast fat (Table 10.6).

Based on a research by Samani and his research collaborators, the fibroadenomas has nearly twice the stiffness of normal breast fat. According to other findings by these researchers, the YM of fibrocystic breast condition and malignant lesions show 3-6 times higher than normal breast fat while the YM of invasive ductal carcinoma is up to 13 times higher (Samani, Zubovits, & Plewes, 2007). Based on the YM results from Table 10.6, a 10% phantom with 5 FTCs can be a good candidate for the malignant lesions. The YM of this phantom is 94 kPa which is 5.5 times higher than the YM of the breast fat candidate (5% PVAL, 2 FTCs) which is 16.9 kPa. This is in agreement with the range that has been introduced by Samani's research for the malignant lesions.

According to Boone et al. (Boone, Nelson, Lindfors, & Seibert, 2001), the HU of the breast fat, glandular, and cancer lesions are -180, 40, 80 respectively (Figure 10.13). Whereas based on the acquired results from this research, the HU was ranged from 23.9 (5%, 1 FTC) to 44.5 (10%, 5 FTCs) at 120 kVp. Since the HU difference between the breast fatty tissue and the cancer lesions is 260 (80-(-180)), this HU difference can be simulated by increasing the HU of the lesion. As was discussed in 6.2.2.1 on page 61, a

contrast agent can be employed in order to increase the attenuation coefficient of the region of interest. The lesions mixed with contrast agent exhibit higher contrast compared to the surrounding phantom area. This high contrast simulates the contrast between the cancer lesions and the fatty tissues.

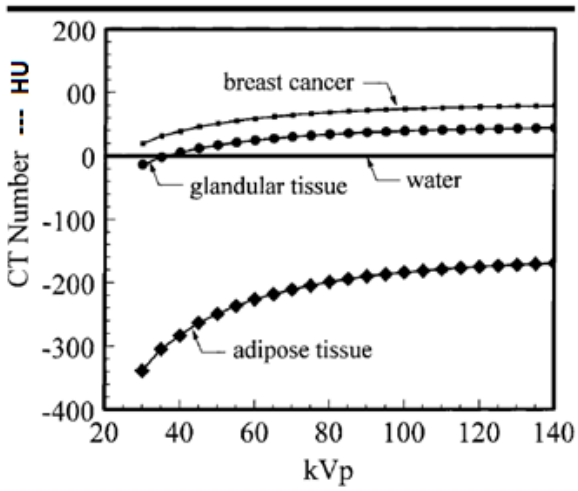

Figure 10.13 HU for breast cancer, glandular tissue, adipose tissue, and water (Boone, Nelson, Lindfors, & Seibert, 2001).

10.1.8 Measuring the HU of the final candidate for the breast phantom

In order to verify the reliability and reproducibility of HU of 5% PVAL phantom as a candidate for breast mimicking tissue, 6 phantoms with 5% PVAL and 2 FTCs were produced. The HU of each phantom was measured and the average and standard deviation were calculated.

10.1.8.1 Results and analysis

The following table (Table 10.7) shows the average HU (≃17) for six 5% phantoms (Phan1 to Phan6) with 2FTCs.

HU-Phan1	HU-Phan2	HU-Phan3	HU-Phan4	HU-Phan5	HU-Phan6	Average HU	sd
17.81	23.89	15.44	14.92	16.82	14.64	17.25	3.46

Table 10.7 HU of 5% PVAL phantom with 2FTCs

10.1.8.2 Discussion

The average HU of a 5% PVAL with 2 FTCs is 17.25 with the standard deviation of 3.46. As was discussed earlier, the difference between HU of the breast fatty tissue and the cancer lesions is 260 (80-(-180)) which means the HU of the lesion needs to be 277 in order to make the 260 HU difference between the breast phantom and the PVAL lesion (Table 10.8).

Tissue Type (at 120 kVp)	HU_{Real}	HU_{Target}
Adipose	**-180**	**17**
Cancerous	**80**	**277**

Table 10.8 Adjusted target values by tissue type

10.1.9 Measuring the YM of the final candidate for the breast phantom/lesion

In order to check the reliability of the phantom production, the Young's modulus was measured independently for three batches of the 5% and 10% PVAL concentrations for 2, 3, 4 and 5 FTCs, additionally a 6 FTC was measured for the 10% PVAL concentration (Table 10.9). Since the YM of lesions such as invasive ductal carcinoma can be 13 times more than the YM of the breast (20 kPa) and the maximum YM measured with 5 FTCs was 94 kPa, an additional FTC was added to the number of FTCs to cover broader range of simulated cancer lesions.

PVAL concentration	FTCs	Number of batches	Batch1 - number of phantoms per FTC	Batch2 - number of phantoms per FTC	Batch3 - number of phantoms per FTC	Total number of phantoms per FTC	Total number phantoms for all FTCs
5%	2-5	3	1	5	5	11	44
10%	2-6	3	1	4	4	9	45

Table 10.9 Number of phantoms and FTCs for measuring the YM of 5% and 10% PVAL phantoms

PVC piping was used to ensure consistent diameters of the samples, the samples were cut to ensure all surfaces were flat, and then the Young's modulus was measured for all samples as in the previous experiments (Figure 10.14).

Figure 10.14 PVC moulds

The YM of the phantoms were measured using an Instron machine (Figure 10.15). The bulged surfaces of the phantoms were flattened by a sharp cutter in prior to the measurement (Figure10.16). Uneven surfaces can deteriorate the accuracy of data acquired by Instron machine, as indicated earlier.

Figure 10.15 PVAL lesions, 2 to 6 FTCs, 4 phantoms per FTC

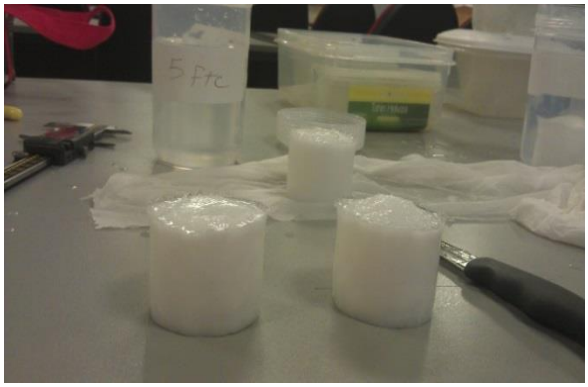

Figure10.16 Phantom on the left with flat surface

Due to the aging process, PVAL phantoms produce secondary crystallites which results in changes in the stiffness of the phantoms (Hassan & Peppas, 2000) (Willcox, et al., 1999). However, in these studies, the rate of increase of YM over time is not clear. Hence, in this research, the X-ray properties of the phantoms/lesions will be measured over time. If fresh phantoms/lesions are required in order to complete the research due to time related changes in the X-ray properties, then the measurement of YM of PVAL phantoms over time will not be necessary.

10.1.9.2 Results and analysis

The following graphs (Figure 10.17 and Figure 10.18) show the YM for 5% and 10% phantoms with 2-5 and 2-6 FTCs respectively.

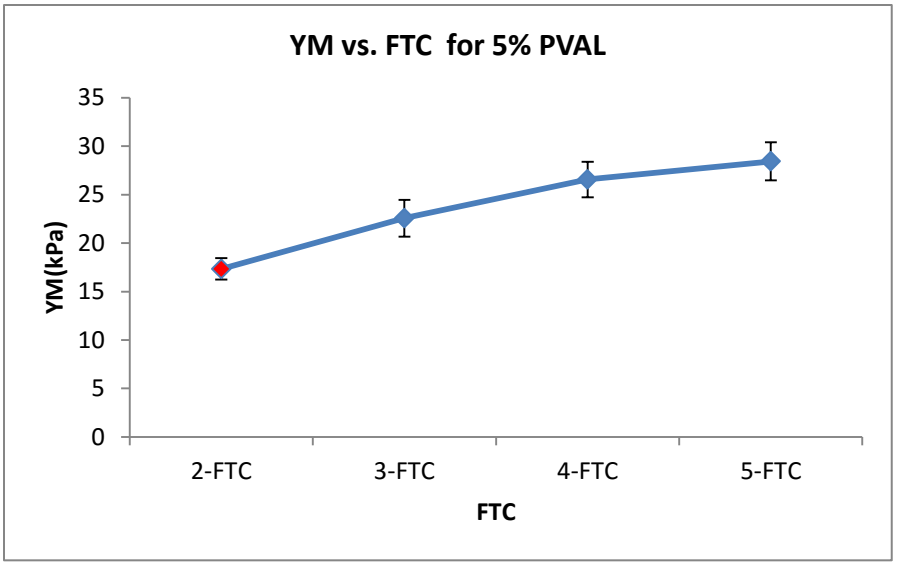

Figure 10.17 YM of 5% phantom from 2-5 FTCs

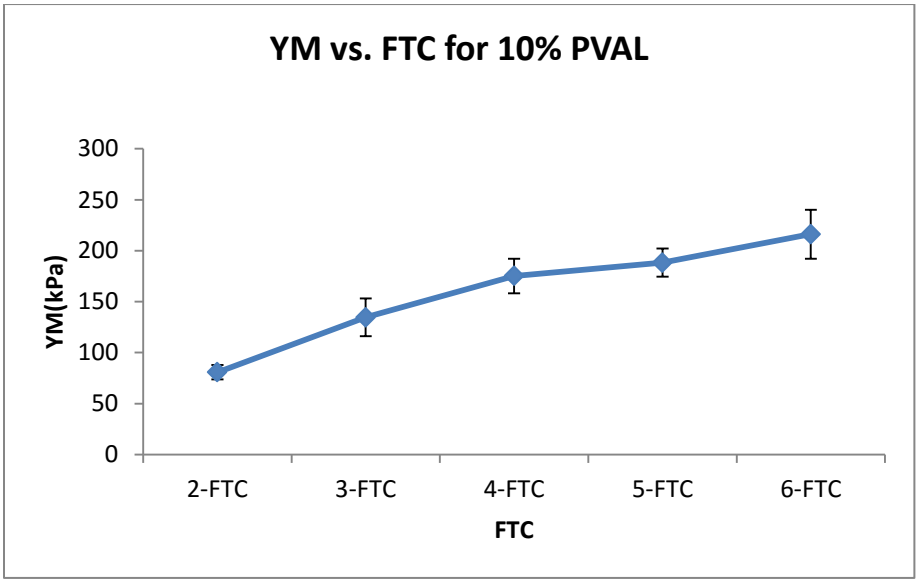

Figure 10.18 YM of 10% phantom from 2-6 FTCs

Both graphs display the increase of YM corresponding to the increase of FTC. The graphs are the average of the results of the YM for three separate batches of 5% and 10% PVAL phantoms. Since the average YM of breast tissue is about 20 kPa which

includes the glandular, fat and other breast structures, therefore, the YM of a 5% PVAL phantom with 2 FTCs (17.34 kPa) is acceptable as the successful candidate for the breast phantom. Although the YM of the 5% phantom with 3FTCs (22.56 kPa) is also near 20 kPa, the 5% with 2 FTCs is a better candidate to simulate the fat-based breast since the YM of the fat is under 20 kPa (Samani, Zubovits, & Plewes, 2007).

In order to compare the acquired YM for the breast phantoms/lesions with Samani's research (Samani, Zubovits, & Plewes, 2007), the ratio of the YM of 10% PVAL lesions with 2-6 FTCs to the YM of the breast phantom (17.34 kPa) was measured. The following table and graph (Table 10.10 and Figure 10.19) display the ratio of the YM of the phantom lesions to the YM of breast phantom. The ratios of the YM of the PVAL cancer lesions to the PVAL breast phantoms are in agreement with Samani et.al (Samani, Zubovits, & Plewes, 2007). According to Samani's research, the Fibrocystic and malignant lesions show 3-6 times increased stiffness and high grade invasive carcinoma exhibits up to 13 times increase in stiffness compared to fibroglandular tissue. The following table and graph show this ratio for PVAL lesions from three batches of 10% PVAL solution.

FTC	Y1/17.34	Y2/17.34	y3/17.34	Average
2-FTC	5.00	4.20	4.75	4.65
3-FTC	8.75	6.63	7.89	7.76
4-FTC	9.89	9.25	11.16	10.10
5-FTC	10.13	10.71	11.72	10.85
6-FTC	11.34	12.03	14.02	12.46

Table 10.10 The ratio of the YM of the PVAL lesion to breast phantom

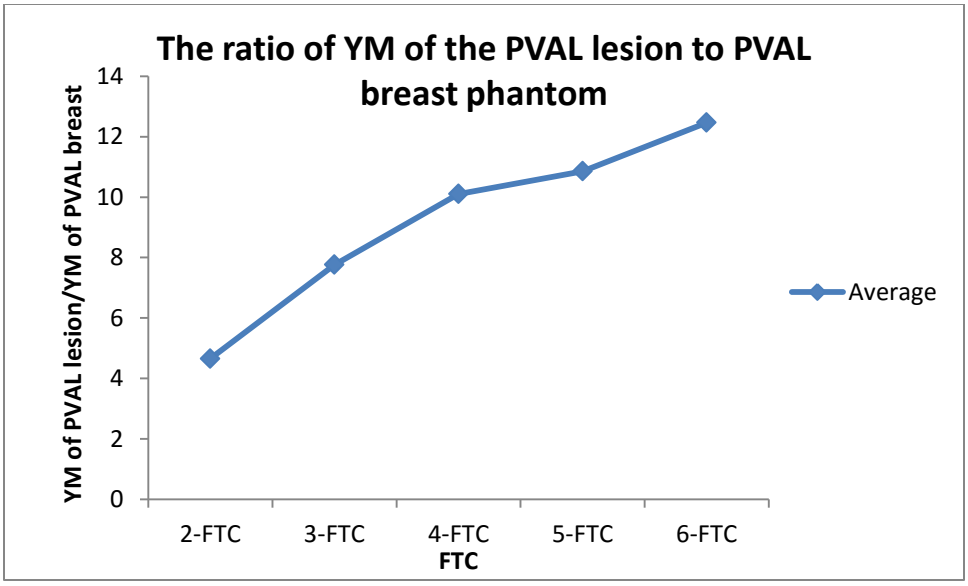

Figure 10.19 the ratio of YM of the PVAL lesion to PVAL breast phantom

10.1.9.3 Discussion

The YM values acquired in this research for 10% PVAL lesions are in agreement with Samani et al. (Samani, Zubovits, & Plewes, 2007). 10% PVAL phantoms with 2 FTCs can cover the Fibrocystic and malignant tumours and 10% PVAL phantoms with 3, 4, 5 and 6 FTCs can cover the high grade invasive ductal carcinoma.

10.1.9.4 Conclusion

Based on these YM measurements, a 5% PVAL, 2 FTCs phantom has similar mechanical properties to breast fatty tissue with a measured YM of 17.34 kPa

10% PVAL lesions with 2-6 FTCs have similar mechanical properties to benign and cancer lesions. The number of FTCs can be chosen based on the type of the cancer lesion. 2 FTCs can mimic fibrocystic and malignant tumours, whereas higher FTCs mimic the varying high grade invasive ductal carcinoma.

10.2 METHODS FOR DETERMINATION OF THE RIGHT AMOUNT OF CONTRAST AGENT

The focus of this section is to determine the correct amount of contrast agent to dope with the PVAL lesions. This measured amount of contrast agent increases the linear attenuation coefficient of the PVAL lesions in the mammograms. Excess amount of contrast agent makes the lesion too bright in the radiograph resulting in dissimilarity to cancer lesions. While an inadequate amount of it does not allow the lesions to be visualized in the radiographs. Therefore the right amount of contrast agent was required to be measured and doped correctly with the PVAL solution.

In order to find the adequate amount of contrast agent for the PVAL caner lesions multiple lesions with various concentration of contrast agent from 0.1 ml to 5 ml in 20 ml of PVAL were conducted through several separate experiments.

Due to a leeching problem with contrast agent (Goergen, 2009) (Maddox, 2002) doped with the PVAL lesions inside the phantoms, the shelf life of the embedded lesions in the PVAL phantoms was specified. The leeching PVAL lesion causes the edge of the lesion to be blurred when imaged. Since the blurred edge of the lesion hinders the experiments regarding the determination of lesion visibility in relation to the changes in breast phantom thickness, it was necessary to find ways to reduce the leeching and find the optimum time of the usage of the phantom with the embedded lesions.

10.2.1 HU in relation to the concentration of contrast agent mixed with PVAL phantoms

In order to determine an appropriate amount of contrast agent, first the relationship between the various concentration of contrast agent and the HU of the mixed solution of contrast agent and PVAL was determined. This experiment determined a baseline relationship for HU of the CA in PVAL.

This experiment starts with the preparation of 10% PVAL aqueous solution. 120 ml of PVAL solution was poured into 5 cylindrical plastic moulds with a 60 ml syringe respectively. 1-5 ml radiopaque contrast agent (Optiray 320) was added to each PVAL solution respectively. To ensure that the contrast agent dissolved uniformly in the PVAL solution, a separate simple test was achieved by mixing 3 ml of contrast agent in one drop of food colouring. Then the food/contrast combination was mixed with 120 ml of PVAL solution. This demonstrated visually that after stirring, the coloured contrast was mixed evenly with the PVAL solution. For comparative purposes, another mould was filled with 120 ml of 10% PVAL with no contrast agent. 5 PVAL gels were prepared. After thawing the phantoms, the phantoms were placed in a container, covered with deionised water, and placed in a refrigerator at 5 °C. The samples were then imaged by a CT scanner and the results were demonstrated in Table 10.11.

10.2.1.1 Results and analysis

Figure 10.20 shows the relationship between the HU of PVAL phantoms mixed with CA.

CA (ml)	HU± sd
0	47.60±4.2
1	88.00±3.6
2	143.20±5.9
3	221.80±6.4
4	305.70±16.4
5	330.40±14.6

Table 10.11 HU of 10% PVAL, 1 FTC with 1-5 ml of contrast agent

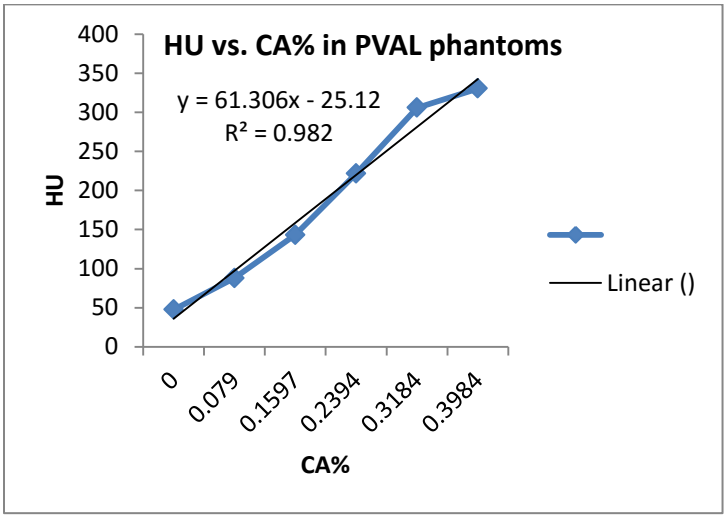

Figure 10.20 HU of 10% PVAL, 1 FTC in relation to 1-5 ml of contrast agent

The above graph (Figure 10.20) displays a linear increase of HU in relation to the increase in the concentration of CA.

10.2.2 Matrix of PVAL lesions - visualization of the PVAL lesions in mammography

The following experiments (10.2.2.1 and 10.2.2.2) were conducted in order to evaluate and compare the visibility of the PVAL lesions enriched with various concentrations of contrast agent in CT images and mammograms. Since CT scanners and mammography units employ difference image acquisition mechanisms (Chapter 6, Chapter 8), comparison between the acquired images from CT and mammograms was necessary in order to utilise the right amount of contrast agent mixed with the lesions to make them visible in mammograms.

Since the right amount of contrast agent was not determined at this stage of the research, these experiments were carried out in order to narrow down the range of concentration of contrast agent.

10.2.2.1 Determine a contrast agent to HU curve covering the needed HU values for the cancer-mimicking lesions

A matrix of 10% aqueous solution of PVAL was prepared (Figure 10.21). For the matrix, 20 ml of 10% PVAL solution was poured into each cup of a 12-cup silicon baking tray respectively. The PVAL solution in each cup was then enriched with contrast agent starting from 0.1 ml in the first cup, increased by 0.1 per cup until 1 ml was added to the 10th cup. The last two cups were used as control with no contrast agent. The phantoms underwent 2 FTCs.

Figure 10.21 A Lesion matrix with 10% PVAL enriched with 0.1 - 1 ml contrast agent

10.2.2.2 Evaluation of the visibility of the PVAL lesions doped with contrast agent in mammogram

20 ml of 10% PVAL was poured into each compartment of an eighteen compartment bead organizer (Figure 10.22). 0.1 ml to 1.8 ml of CA was added to each compartment and stirred with toothpicks. The bead organizer then underwent 3 FTCs. The cancer mimicking lesions were removed from the compartments and were sewed together with nylon thread into two sets of nine blocks (Figure 10.22 right). 5% PVAL

solution was then added to the lesions and both sets underwent 2 FTCs. Both phantoms, one with 9 block PVAL lesions from 0.1 to 0.9 ml of CA and the second one with 9 block PVAL lesions from 1 ml to 1.8 ml of CA underwent the mammography procedure right after fabrication.

Figure 10.22 Left: PVAL cancer lesions doped with 0.1 ml to 1.8 ml of CA in a bead sorter. Right: blocks of lesions sewed to each other and placed in 5% PVAL phantom

10.2.2.3 Results and analysis

The graph below (Figure 10.23) shows a linear increase of HU in relation to the concentration of contrast agent. All the lesions were visible in the CT images.

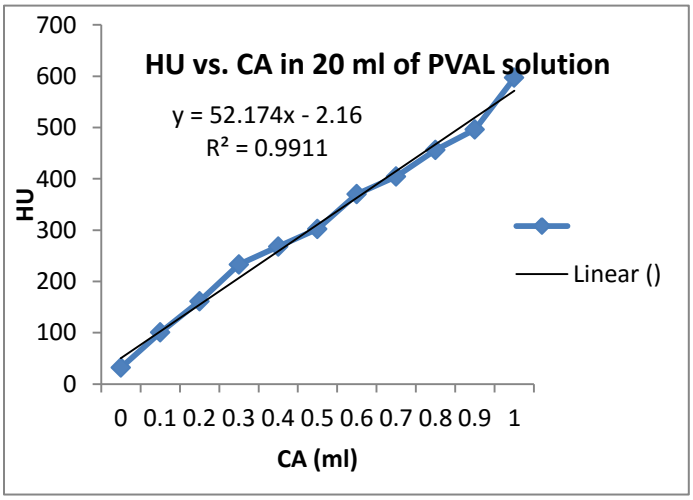

Figure 10.23 HU vs. CA (ml) for a matrix of PVAL phantoms doped with 0.1-1 ml of contrast agent

The following mammograms show the blocks of PVAL lesions enriched with various concentration of contrast agent. The PVAL lesions with lower concentrations of

CA (0.1 ml to 0.8 ml) were observed vaguely in mammogram (Figure 10.24) and PVAL cancer lesions with higher concentrations of CA (1.3 ml to 1.8 ml) were partially visible in mammogram (Figure 10.25). It is also noted that the more visible lesions do not demonstrate homogenous brightness in the entire PVAL lesion block.

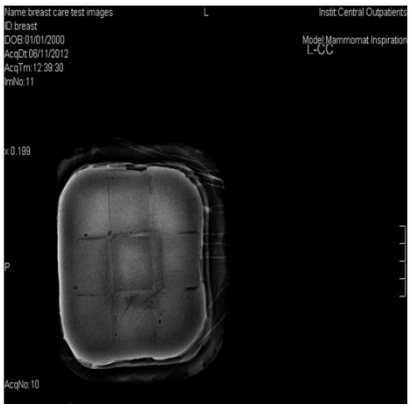

Figure 10.24 Mammogram of a phantom with embedded PVAL cancer lesions doped with 0.1 ml to 0.9 ml of CA

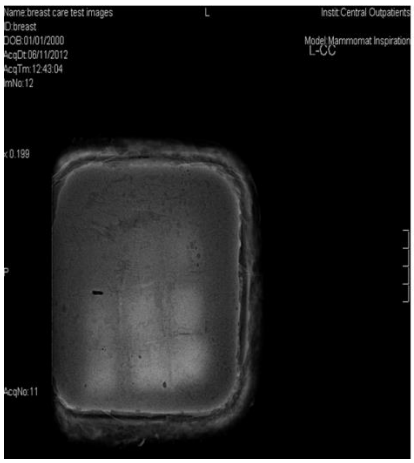

Figure 10.25 Mammogram of a phantom with embedded PVAL cancer lesions doped with 1.0 ml to 1.8 ml of CA

10.2.2.4 Discussion

As was discussed earlier, the required HU for the PVAL cancer mimicking lesions is about 277. Based on the graph (Figure 10.23) the phantoms doped with 0.4 ml of contrast agent provide the HU of 267.7. This HU number is close to 277 (10.1.8)

which is the desirable HU for the cancer mimicking PVAL lesions. The mammography has shown that lower concentration of contrast agent up to 1.3 ml generates vague lesions which cannot be used in the visibility study. This means that the 0.4 ml of contrast agent is inadequate to provide the sufficient visibility in mammograms. In order to address this issue, three factors had to be taken into consideration: first increase of the amount of contrast agent, second, the improvement of the process of doping the contrast agent and aqueous PVAL solution, and third controlling the leeching of the contrast agent from the PVAL lesions.

As the mammograms (Figure 10.24 and Figure 10.25) demonstrated, the lesions were shown blurred with unsharp edges. Even the more visible lesion blocks displayed the uneven brightness through the entire block of lesion. The inhomogeneity of the brightness was possibly due to the insufficient mixing process. While the invisibility of the lesions, was due to insufficient amount of contrast agent and the possible leeching of the contrast agent to the adjacent regions. Leeching of the contrast agent from the PVAL lesion to the surrounding PVAL region reduces the concentration of the contrast agent resulting in a decrease in the attenuation coefficient of the PVAL lesion. The reduction of the attenuation coefficient decreases the visibility of the PVAL lesion. Hence, further experiments were carried out in order to address these three issues.

10.2.2.5 Conclusion

Due to the insufficient visibility of the PVAL lesions enriched with 0.1-1.8 ml of contrast agent, the following factors have to be taken into consideration: first increase of the amount of contrast agent, second, the improvement of the process of doping the contrast agent and aqueous PVAL solution, and third controlling the leeching of the contrast agent from the PVAL lesions.

10.2.3 Making homogenous mixture of PVAL and contrast agent

In Figure 10.24 and Figure 10.25, the uneven brightness of the PVAL lesion blocks was assumed due to the inadequate stirring of the mixture of contrast agent and the aqueous solution of PVAL. This experiment was aimed to prove first the assumption of inadequate stirring was correct, then to find a solution to produce a homogeneous mixture of PVAL solution enriched with contrast agent. The corresponding experiments have been classified into part1 and part2.

10.2.3.1 Making homogenous mixture of PVAL and contrast agent - part1

20 ml of 10% PVAL was poured into three 40 ml glass jars respectively (20 ml per jar). 1 ml of CA was added to each jar and the solution was stirred gently with a toothpick for 60 seconds. The solution was then put through 2 FTCs to produce a phantom. The phantom was then CT imaged and the resultant images were analysed.

10.2.3.2 Making homogenous mixture of PVAL and contrast agent - part2

Four samples of 20 ml of 10% PVAL solution were doped with 0.5 ml CA respectively and placed into 40 ml glass jars. Each sample was first stirred manually with a toothpick tor 60 seconds. The jar was then sealed and gently inverted and rolled by hand for 4 minutes until it was no longer possible to distinguish the CA in the solution with the naked eye.

This method was then repeated 5 more times with each successive set increasing the CA quantity by 0.5 ml of CA until the final set contained 20 ml PVAL solution and 3 ml CA. In total 24 samples were prepared in 6 different CA concentrations. The percentage of CA by volume produced is shown in Table 10.12.

CA (ml) in 20 ml PVAL	% CA by Volume
0.5	2.44%
1.0	4.76%
1.5	6.98%
2.0	9.09%
2.5	11.11%
3.0	13.04%

Table 10.12 Percentage of CA by volume when added to 20 ml of PVAL solution

The 24 samples were then placed through 1 FTC. The samples (Figure 10.26) were CT scanned three times over a five day period, after each scan an additional FTC was performed on the samples. The samples were never kept in deionised water through the entire experiment.

Figure 10.26 Left- 10% PVAL mixed with CA in sealed jars. Right- 24 samples ready for CT scan.

10.2.3.3 Results and analysis

Table 10.13 and Figure 10.27 show the average HU of 0.5-3 ml CA mixed with 10% PVAL on day0, day3, and day4. The low standard deviations indicate the high consistency and low errors in the HU of the samples with the same concentration of CA.

Days	Ave 0.5	sd	Ave 1.0	sd	Ave 1.5	sd	Ave 2.0	sd	Ave 2.5	sd	Ave 3.0	sd
0	260.02	5.84	468.00	5.92	653.05	23.81	804.42	5.67	936.77	23.12	1085.92	4.12
3	283.27	5.42	483.67	7.47	686.02	11.25	849.67	4.25	1003.67	22.87	1148.17	8.31
4	293.32	4.08	491.67	7.99	687.20	3.69	854.52	8.03	1003.87	13.941	1156.20	6.20

Table 10.13 Average (Ave) HU 0f 10% PVAL lesions doped with 0.5-3 ml CA on day0, day3, and day4

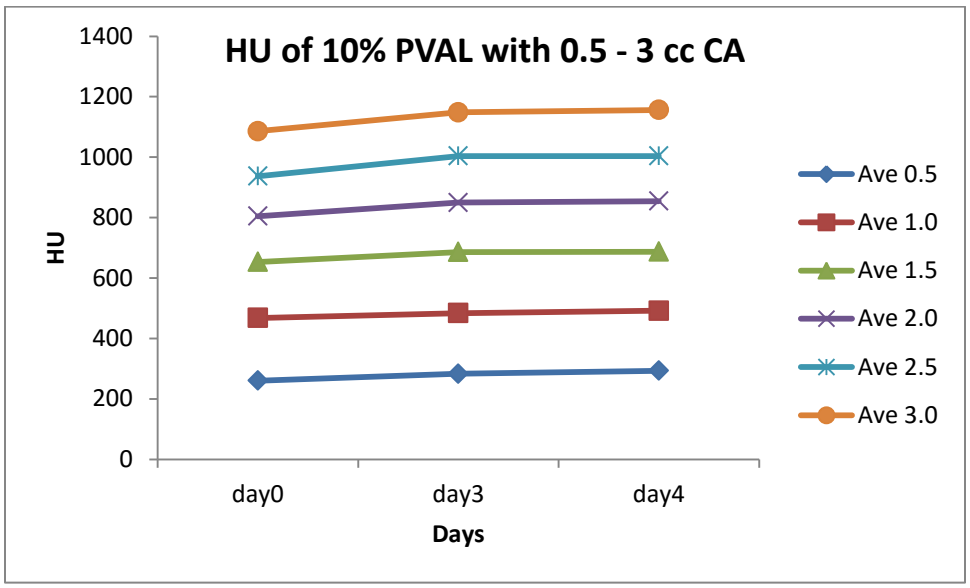

Figure 10.27 HU 0f 10% PVAL mixed with 0.5-3 ml CA on day0, day3 and day4

There is an increase in the HU of the samples from day0 to day4. The increase from left to right (Table 10.13) is due the concentration of CA and the increase in each column from top to bottom is due to the increase in FTC. The increase of HU from day0 to day3 for 0.5 ml, 1 ml, 1.5 ml, 2 ml, 2.5 ml and 3 ml lesions doped with CA are 33.30, 23.67, 34.15, 50.10, 67.10 and 70.27.

The CT images in Figure 10.28 show the separation between the PVAL and CA indicating the ineffectiveness of the mixing technique (10.2.3.1). Figure 10.29 demonstrates CT images of the lesions from day0 to day4 (10.2.3.2). The phantoms look homogenous in the images and the gap from day0 to day4 did not cause the separation of the contrast agent from the PVAL phantoms.

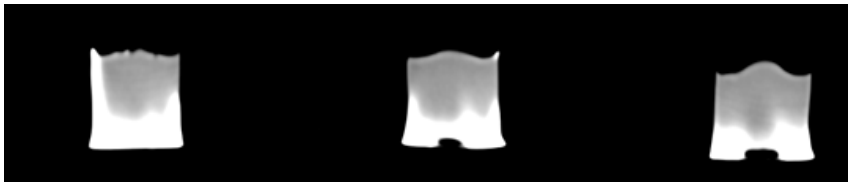

Figure 10.28 Separation of PVAL and CA in PVAL phantoms (WL=0, WW=300)

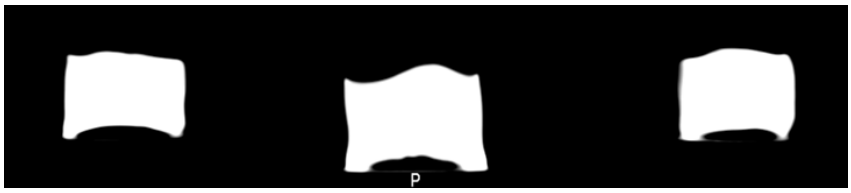

Figure 10.29 a sample PVAL lesion enriched with contrast agent. The left phantom was CT scanned on day0, middle on day3 and right one on day4 (WL=0, WW=300)

10.2.3.4 Discussion

The rectified mixing technique of contrast agent and PVAL solution has shown a remarkable improvement in the results. The acquired images of 24 samples with various concentration of contrast agent show that the contrast agent did not separate from the PVAL lesions between freezing thawing cycles and after the completion of all the cycles.

10.2.3.5 Conclusion

Enriching the aqueous solution of PVAL with CA by stirring, inverting and rolling the sealed containers for 5 minutes resulted in a homogenous mixture of PVAL and CA.

10.2.4 The effect of environment of the PVAL lesions

In the previous sets of experiments regarding finding the appropriate mixing technique, the lesions were not kept in deionised water. Therefore, the effect of the water on the HU of the lesions was not determined. Generally, during production of PVAL in order to keep the samples fresh, the phantoms are kept in deionised water. The surface of PVAL phantoms exposed to the air gets dry over time. The dryness of the phantoms/lesion makes the phantoms stiff resulting in changes in the value of

compressibility (YM). Hence, the PVAL phantoms are stored in deionised water after fabrication.

In a phantom with an embedded lesion mixed with contrast agent, the PVAL phantom bulges in the water which means the water penetrates inside the phantom. The presence of water inside the phantom can wash the contrast agent resulting in a decrease in the HU of the lesion. The decrease in the final phantom used for the visibility study, deteriorates the visibility of the lesions in the mammograms. Therefore, in these series of experiments the effect of water on the HU of the PVAL lesions with various concentrations was determined. Conversely, the effect of dryness (dehydration) on the HU of the lesions was conducted in order to see if the dryness can prevent the leeching effect.

The aim of series of experiments was to minimize the changes in the value of the accepted HU of the lesions from the time that the lesions are produced until the end of mammography procedure.

10.2.4.1 HU of samples kept in deionised water (hydrated) measured over 5 consecutive days

The rectified mixing method was used to prepare four samples of 10% PVAL solution doped with 0.5 ml of CA.

This method was then repeated 5 more times with each successive set increasing the CA quantity by 0.5 ml of CA until the final set contained 20 ml PVAL and 3 ml of CA. In total 24 samples were prepared in 6 different CA concentrations. Cancer mimicking lesions were then created by putting the PVAL solutions through 5 FTCs.

The samples stored in deionised water were then CT scanned over a 5 day period with each successive day's scan being taken roughly 24 hours after the previous scan. The DICOM (see glossary on page 305) images were collected for each scan and the HU of the samples were measured using the ROI manager tool of ImageJ software.

ImageJ is a Java-based open source image processing program which includes standard image processing functions. This program can display, analyse, and process various image formats such as DICOM (Ferreira, 2012).

10.2.4.2 Results and analysis

Each HU in the following table (Table 10.14) is the average of the HU of the four PVAL samples in each concentration group (0.5 ml to 3.0 ml of CA). The low standard deviations indicate the high consistency and low errors in the HU of the samples with the same concentration of CA.

The following graph (Figure 10.30) show the HU of PVAL lesions mixed with 0.5-3 ml of contrast agent from day0 to day4.

Days	Ave 0.5	Sd	Ave 1.0	sd	Ave 1.5	sd	Ave 2.0	sd	Ave 2.5	sd	Ave 3.0	sd
0	274.42	2.59	474.39	3.16	649.67	15.41	798.50	3.34	945.47	4.60	1083.66	2.51
1	254.23	3.48	443.15	6.67	603.23	9.89	748.93	5.28	894.81	5.59	1009.12	2.45
2	236.75	3.85	415.55	5.86	556.97	5.96	696.16	7.32	841.67	9.47	922.64	13.42
3	230.95	3.14	403.34	8.52	534.73	4.49	674.72	10.32	814.34	4.61	847.11	32.77
4	235.36	6.48	421.92	11.43	551.43	9.32	701.98	14.35	841.07	13.74	851.88	43.39

Table 10.14 Average (Ave) HU of 10% PVAL lesions doped with 0.5 to 3 ml CA, kept hydrated and measured from day0 to day4.

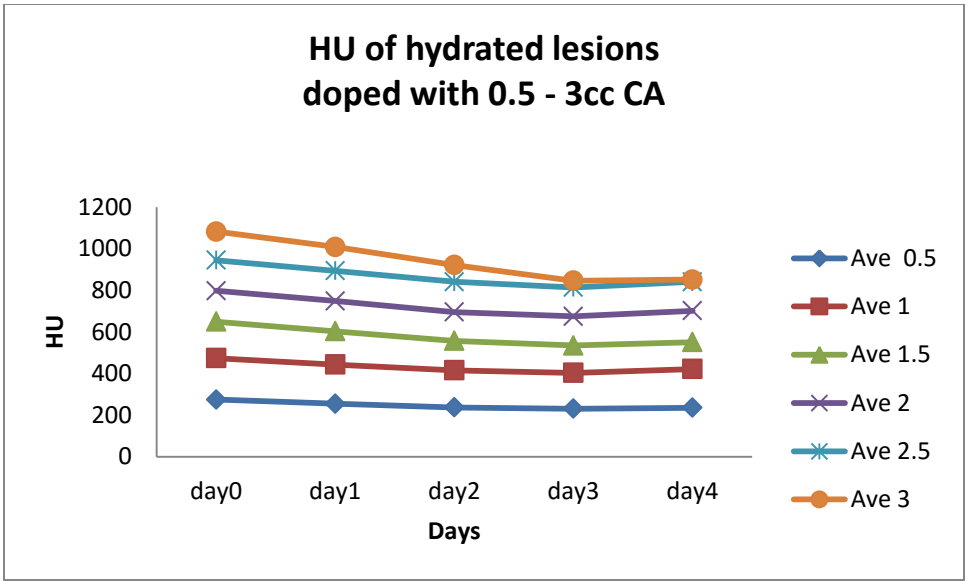

Figure 10.30 HU of hydrated lesions doped with 0.5 to 3 ml CA from day0 to day4

The following tables (Table 10.15 and Table 10.16) display the changes in the HU from day0 to day4.

Days	0.5 ml CA	1.0 ml CA	1.5 ml CA	2.0 ml CA	2.5 ml CA	3.0 ml CA
0	N/A	N/A	N/A	N/A	N/A	N/A
1	-20.19	-31.23	-46.44	-49.56	-50.65	-74.53
2	-17.47	-27.59	-46.26	-52.76	-53.14	-86.47
3	-5.80	-12.21	-22.24	-21.44	-27.32	-75.53
4	+4.41	+18.58	+16.70	+27.26	+26.72	+4.76

Table 10.15 Average day on day change in HU by amount of CA

0.5 ml CA	1.0 ml CA	1.5 ml CA	2.0 ml CA	2.5 ml CA	3.0 ml CA
39.06	52.47	98.24	96.54	104.40	231.78

Table 10.16 Drop of the HU from day0 to day4

Each of the series in Figure 10.30 follows the similar pattern which is a drop in HU from day0 to day3 (3 full days) and increase in HU from day3 to day4.

Table 10.15 shows an increase in day-to-day HU drop for the PVAL cancer lesions from day1 to day3 from left to right based on the concentration of CA. For

example, the drop of HU from day0 to day1 for a lesion doped with 0.5 ml of CA was 20.19 whereas the drop for the lesion doped with 3.0 ml of CA was 74.53.

Table 10.16 displays the drop of the HU from day0 to day4 for 0.5 ml - 3 ml of CA mixed with the PVAL phantoms. A larger drop of HU is observed for the higher concentration of the contrast agent. For example the drop of the HU on day4 for a PVAL phantom doped with 3 ml of contrast agent is about 21% of the initial HU.

Figure 10.31 shows the CT images of a PVAL cancer lesions doped with 2 ml of CA from day0 to day4 (left to right). The sample looks homogenous and there is no separation between the PVAL gel and the contrast agent.

Figure 10.31 Left to right: CT images of 10% PVAL mixed with 2 ml of CA day0 to day4 (WL=0, WW=300)

10.2.4.3 Dryness (dehydration) of 10% PVAL doped with contrast agent over a several hour period

The rectified mixing method was used to prepare four samples of 10% PVAL solution doped with 0.5 ml CA.

This method was then repeated 5 more times with each successive set increasing the CA quantity by 0.5 ml of CA until the final set contained 20 ml PVAL and 3 ml CA. In total 24 samples were prepared in 6 different CA concentrations.

Cancer mimicking lesions were then created by putting the PVAL solutions through 5 FTCs. The PVAL lesions were then CT scanned 3 times after the last FTC over a 5 hour period. The first scan was directly after the last FTC followed by subsequent scans at 1 hour and 5 hours respectively.

The samples were exposed to the air during the imaging period. The DICOM images were collected for each scan and the HU of the samples were measured using ImageJ software.

10.2.4.4 Results and analysis

Table 10.17 and Figure 10.32 show the HU of the PVAL samples mixed with 0.5-3 ml of CA over a period of 5 hours.

CA (ml)	First (t+0hrs)	Second (t+1hrs)	HU change in 1 hour	Third (t+5hrs)	HU change in 5 hours	Drop %
0.5	279.40	277.77	-1.63	274.16	-5.23	1.87
1.0	486.01	485.60	-0.40	475.31	-10.70	2.20
1.5	658.84	657.51	-1.32	646.95	-11.89	1.80
2.0	825.10	825.51	+0.40	811.63	-13.47	1.63
2.5	966.21	964.33	-1.88	952.81	-13.39	1.38
3.0	1103.86	1106.95	+3.08	1091.24	-12.62	1.14

Table 10.17 HU of PVAL mixed with 0.5 ml - 3 ml CA exposed to the air over a period of several hours

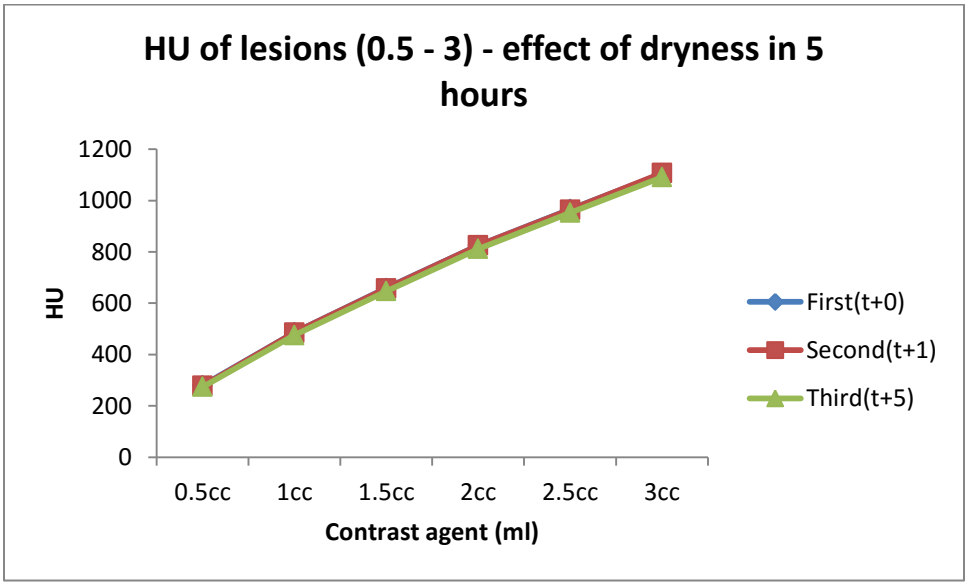

Figure 10.32 HU of PVAL lesions doped with 0.5 ml - 3 ml of CA exposed to the air over a period of 5 hours. t+0 , t+1 and t+5 were starting time, an hour later and 5 hours later respectively.

The “HU change in 5 hours” column (Table 10.17) shows a higher drop for the higher concentrated PVAL lesions than the lower ones (For example, -5.23 for 0.5 compared to -13.39 for the 2.5 ml of CA). The drop in HU can be justified due the leeching of CA from the PVAL samples.

The linear series in Figure 10.32 are nearly overlapped. In other words, the 5 hour period of dryness did not make a big difference in the HU of the PVAL lesions. The correlation coefficient between the samples in the first and fifth hours is > 0.99.

10.2.4.5 Effect of dryness (dehydration) on HU over a 5 day period

Four PVAL doped with 2.5 ml of CA and four PVAL lesions doped with 3 ml of CA were selected from the previous experiment as candidates for this experiment. The reason that the high concentrated PVAL lesions were selected for this experiment was due to their better visibility in the CT images and higher HU drop from day-to-day.

The samples then were kept sealed (dehydrated) in their 40 ml sealed jars over a 5 day period. It is worth mentioning that the samples were exposed to the air on the first day for 5 hours to perform the previous experiment.

All the 8 samples were CT scanned over a 5 day period and the DICOM images were collected for each scan. The HU of the samples were measured using ImageJ software.

10.2.4.6 Results and analysis

The following tables (Table 10.18 and Table 10.19) and their corresponding graphs (Figure 10.33 and Figure 10.34) show the average HU and standard deviation of the phantoms from day0 to day4 for PVAL lesions with 2.5 ml and 3 ml of CA.

Days	Sample1	Sample2	Sample3	Sample4	Average HU	sd
0	958.53	961.55	963.41	981.35	966.21	10.29
1	913.08	903.18	916.16	935.16	916.90	13.37
2	879.79	872.96	866.17	898.91	879.46	14.11
3	879.63	858.27	848.62	893.10	869.90	20.17
4	903.26	858.70	912.57	883.47	889.50	23.84

Table 10.18 Effect of dryness on the HU of PVAL lesions doped with 2.5 ml of CA from day0 to day4

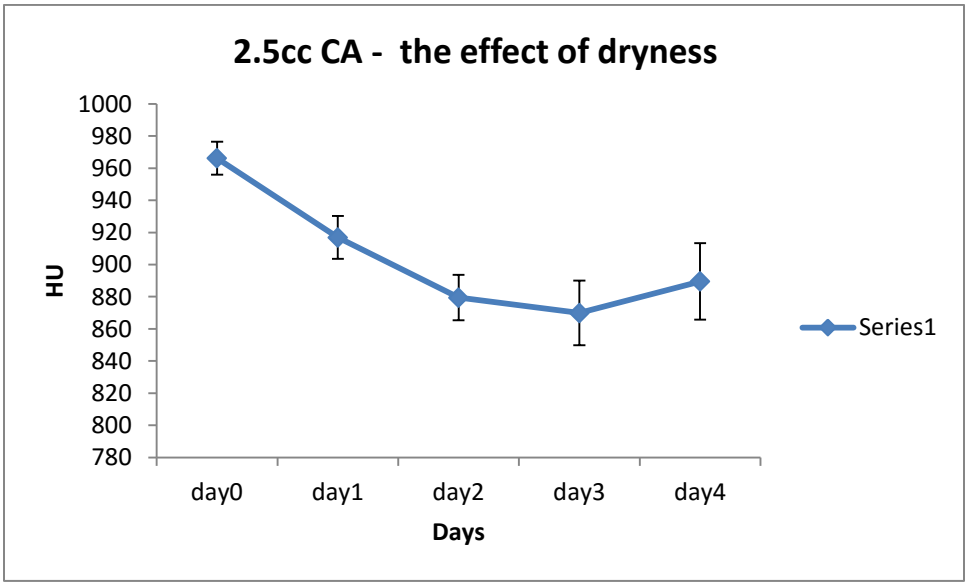

Figure 10.33 Effect of dryness on the HU of PVAL lesions with 2.5 ml of CA from day0 to day4

Days	Sample1	Sample2	Sample3	Sample4	Average HU	sd
0	1102.13	1105.44	1106.62	1101.27	1103.86	2.56
1	1054.21	1057.21	1046.61	1038.01	1049.01	8.58
2	1015.29	1014.72	997.47	994.90	1005.59	10.91
3	998.39	1003.05	989.20	976.90	991.88	11.52
4	997.08	1004.38	978.75	984.45	991.17	11.67

Table 10.19 Effect of dryness on the HU of a lesion with 3 ml CA from day0 to day4

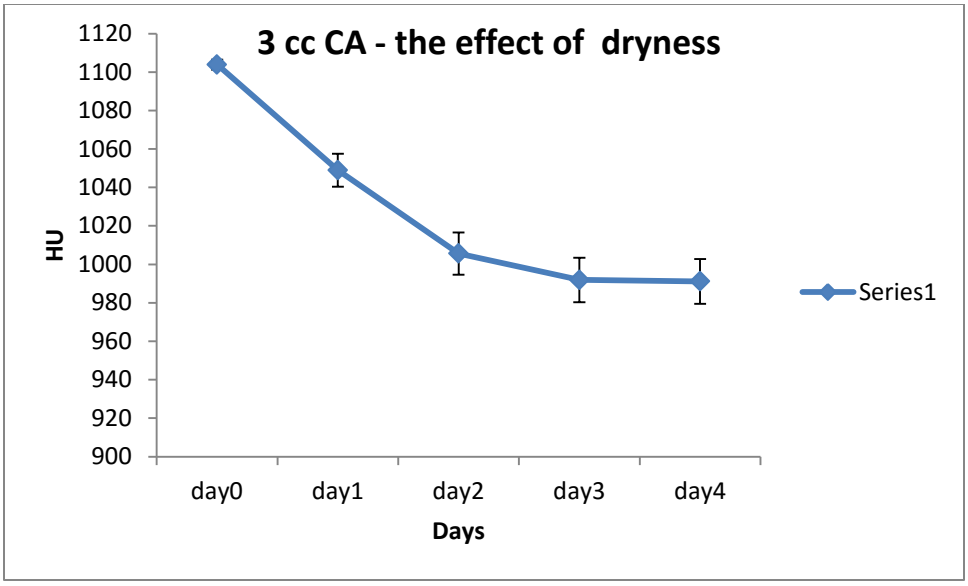

Figure 10.34 Effect of dryness on the HU of a lesion with 3 ml CA from day0 to day4

The HU drop for 2.5 ml and 3 ml PVAL samples from day0 to day4 were 76.71 (7.9% drop) and 112.70 (10.2% drop) respectively.

Table 10.20 shows the change of HU from day0 to day4 for PVAL lesions doped with 2.5 ml and 3 ml of CA.

Days	2.5 ml CA	3.0 ml CA
0	N/A	N/A
1	-49.31	-54.85
2	-37.43	-43.41
3	-9.55	-13.70
4	+19.59	-0.71

Table 10.20 Average day on day change in HU for PVAL lesions doped with 2.5 ml and 3.0 ml of CA

10.2.4.7 Comparison between the HU of a hydrated and sealed lesions

Two phantoms (5% PVAL, 2 FTCs) including two embedded lesions in each were prepared for this experiment. The lesions were prepared and embedded in each phantom based on the following steps: four lesions were prepared with 20 ml of 10% PVAL solution doped with 2.5 ml of CA. After three FTCs, the lesions were divided into

two groups. Two of the lesions were kept sealed in 40 ml glass jars with no deionised water (sealed lesions) for three days and the other two lesions were stored in deionised water (hydrated lesions) for three days. The reason that a three day period was picked for this part of the experiment is due to the predictable drop of HU in a three day period (10.2.4.6). Two PVAL lesions (one hydrated and one sealed) were each suspended inside a plastic mould using nylon thread attached to plastic straws (Figure 10.35).

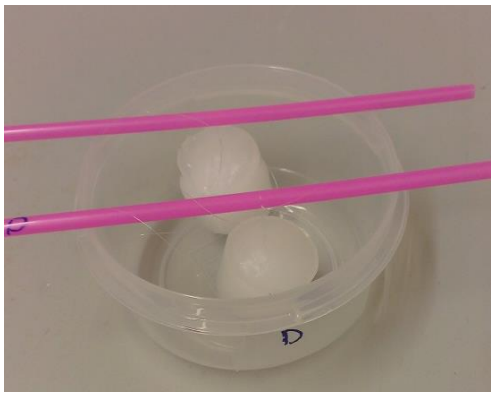

Figure 10.35 Sealed and hydrated lesions ready to be embedded in 5% PVAL solution.

The lesions were neither in contact with each other nor the plastic mould and were placed midway between the surface and bottom of the container. In order to distinguish between the lesions in the CT and mammography images, a metal marker was placed near the sealed lesion. After placing the sealed and hydrated lesions into the container and adding 5% PVAL solution, the solution/lesions underwent 2 FTCs before the CT scan procedure. Similarly, the second phantom with two lesions was fabricated.

The total FTCs for all the lesions were 5 days, three days before the three day storage period and two days after the storage period. Two phantoms, each with two lesions were the result of this part of the experiment. Both phantoms were CT scanned over a two week period right after fabrication and the DICOM images were collected for each scan. The HU of the samples were measured using ImageJ software. Note: both

phantoms were stored in deionised water in order to avoid dehydration of the phantoms over the two week period of scanning.

The phantoms prepared in this experiment underwent mammography procedure two days after preparation. The mammography unit used in this experiment was Hologic Lorad Selenia utilizing kVp= 29 and mAs=129. No compression force was applied in this experiment to the phantoms.

10.2.4.8 Results and analysis

Figure 10.36 displays the mammogram of the sealed and hydrated lesions. Both sealed and hydrated lesions doped with 2.5 ml of CA embedded in 5% PVAL phantoms were shown in mammogram without applying compression force during mammography. The hydrated lesion was more visible than the other one. The edges of both lesions were unsharp and difficult to observe.

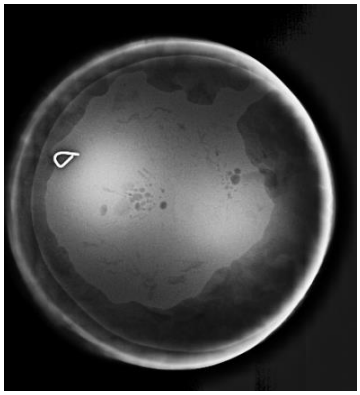

Figure 10.36 Mammogram of a sealed (left) and hydrated (right) PVAL lesions

Figure 10.37 shows the CT images of the sealed lesion from day0 to day9 of the following week acquired from ImageJ. The sealed lesion becomes less visible from left to right due to the leeching of contrast agent over time. The lesion looks quite clear and visible in the first week from day0 to day3 with clear well defined edge.

Figure 10.37 CT images of sealed lesion in phantom1 (day0, day1, day2, day3, day6, and day9) (WL=0, WW=300)

Figure 10.38 shows the edges of the sealed lesion over a two week period using Find Edge function based on Sobel edge detector in ImageJ. The edge of the lesion (far right) is completely unclear and ill-defined.

Figure 10.38 Delineated edges applying ImageJ edge detector for CT images of sealed lesion in phantom1

The line profiles (Figure 10.39, Figure 10.40, Figure 10.41 and Figure 10.42) of both lesions in phantom1 and phantom2 show the drop of grey value over time. The following graphs demonstrate that the fresh lesions which had been sealed display higher grey value. It is important to mention that the grey values in CT images correspond to X-ray attenuation (University of Texas, 2014). In other words, the grey values demonstrate the HU of the imported DICOM files to ImageJ.

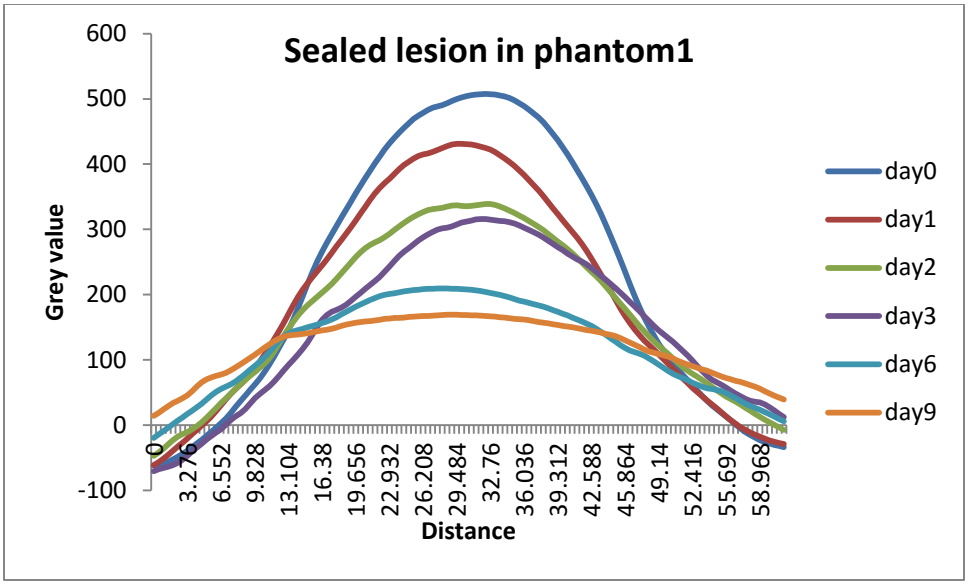

Figure 10.39 Profile of the sealed lesion in phantom1

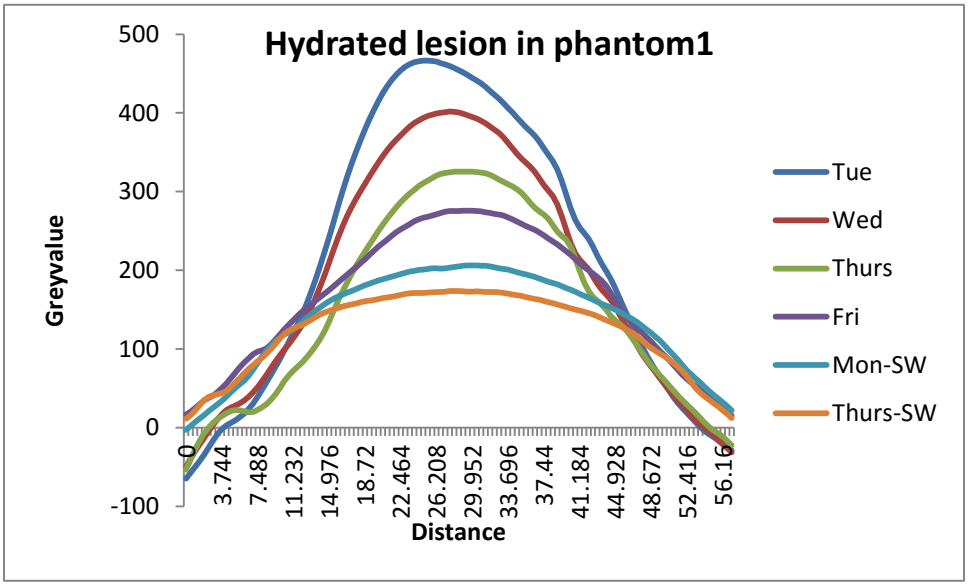

Figure 10.40 Profile of the hydrated lesion in phantom1

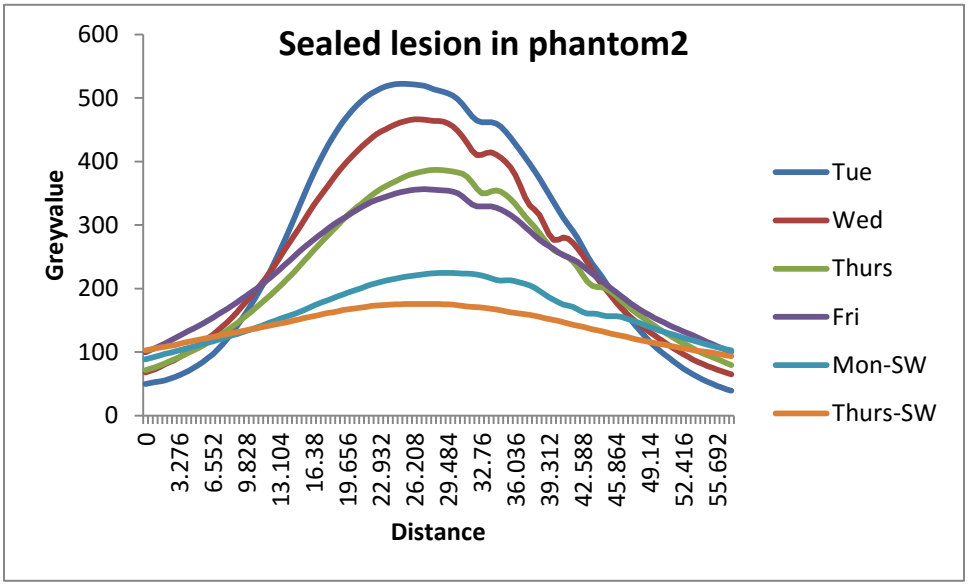

Figure 10.41 Profile of the sealed lesion in phantom2

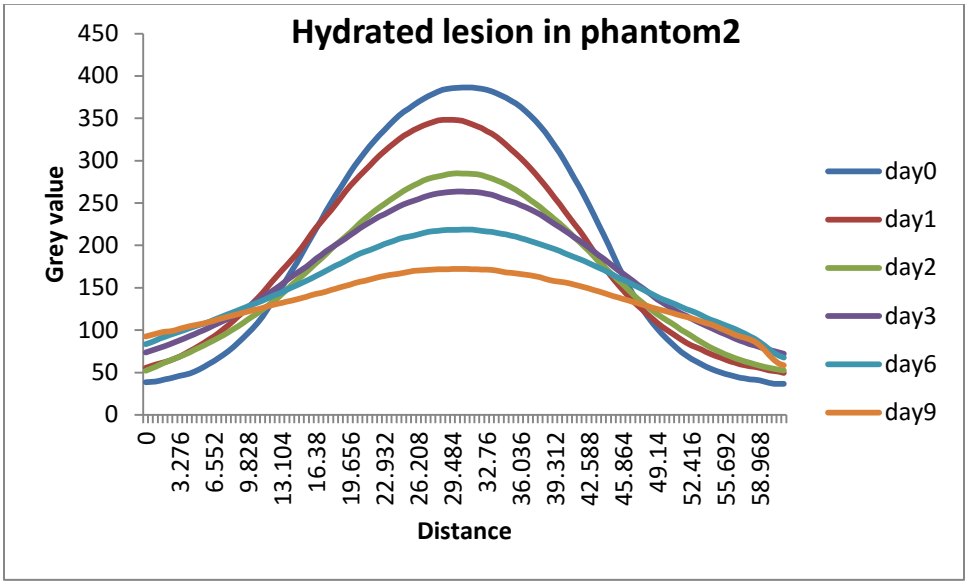

Figure 10.42 Profile of the hydrated lesion in phantom2

As Figure 10.45 (combination of Figure 10.43 and Figure 10.44) shows, The HU of the sealed lesions in phantom1 and 2 is higher than the hydrated ones. In phantom1, the HU difference dropped from 111.60 on day0 to 8.40 on day9 (Table 10.21). Similarly, the HU difference between the sealed and hydrated lesions dropped from

178.20 to 25.30 (Table 10.22). The HU drops over 9 days for the sealed and hydrated lesions in phantom1 were 601.40 (75.5% drop), 498.20 (72.7% drop) and 582.80 (74.6%), 429.90 (71.3% drop) for the phantom2 respectively. Although the grey value of the fresh sealed phantoms show higher values, the percentage of the drop displays higher for the sealed phantoms.

Days	HU-sealed-Ph1	sd-sealed-Ph1	HU-hydrated-Ph1	sd-hydrated-Ph1	HU diff between sealed & hydrated
0	796.60	61.60	685.00	70.50	111.60
1	632.50	56.80	550.20	55.70	82.30
2	477.70	49.40	426.40	39.60	51.30
3	428.70	31.60	335.40	25.30	93.30
6	263.10	13.20	241.40	14.80	21.70
9	195.20	14.80	186.80	7.50	8.40

Table 10.21 HU of sealed and hydrated lesions in phantom1

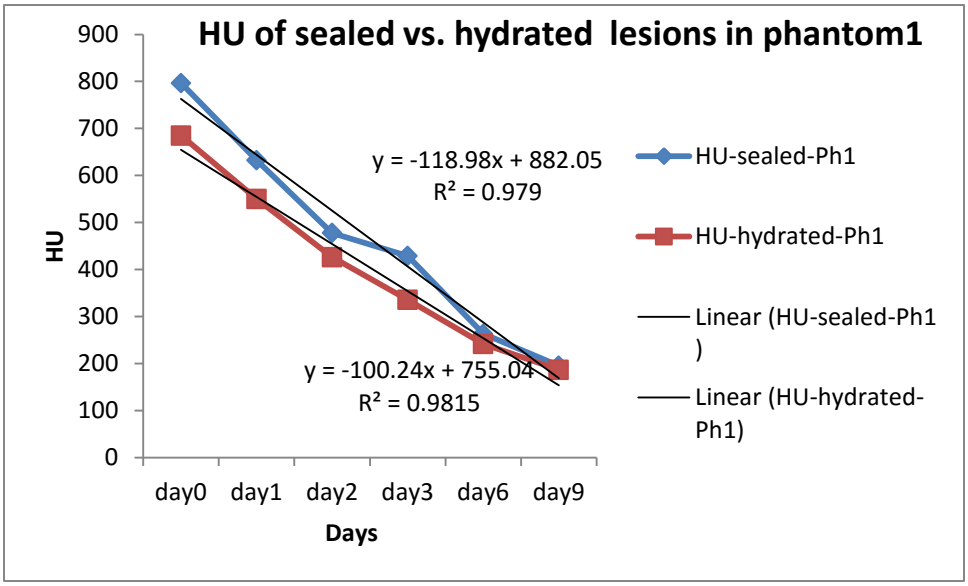

Figure 10.43 HU of sealed and hydrated lesions in phantom1 from day0 to day9

Weekdays	HU-sealed-Ph2	sd-sealed-Ph2	HU-hydrated-Ph2	sd-hydrated-Ph2	HU-diff
0	781.30	72.10	603.10	58.20	178.20
1	642.10	62.10	484.60	47.00	157.50
2	494.90	49.30	373.70	31.30	121.20
3	409.70	31.20	331.20	26.00	78.50
6	264.10	12.80	210.50	9.50	53.60
9	198.50	6.60	173.20	6.10	25.30

Table 10.22 HU of sealed and hydrated lesions in phantom2

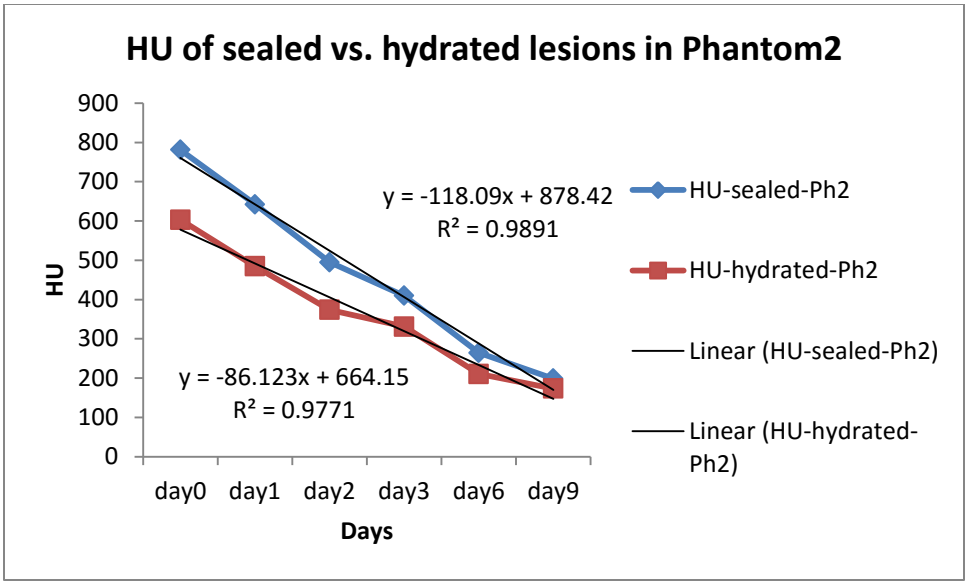

Figure 10.44 HU of sealed and hydrated lesions in phantom2 from day0 to day9

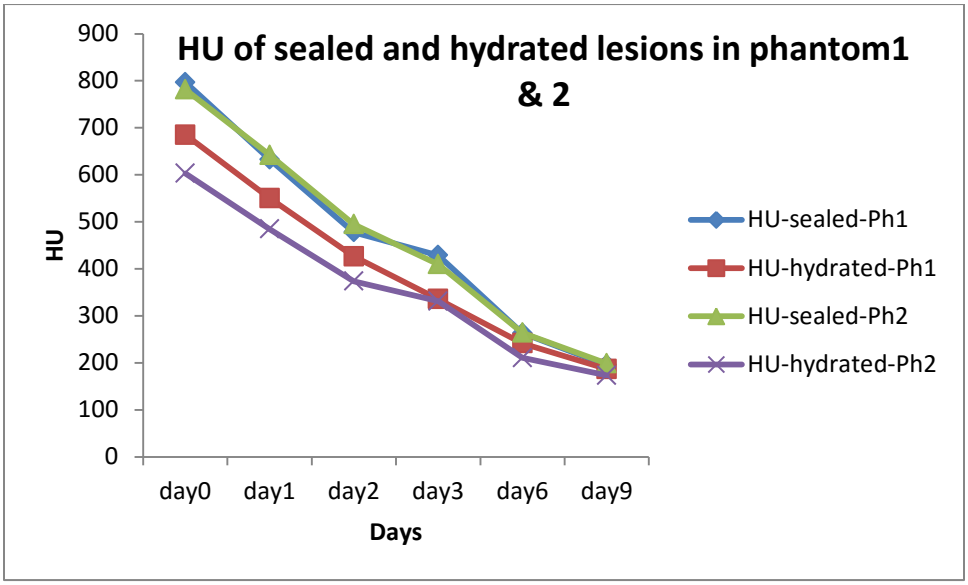

Figure 10.45 HU of sealed and hydrated lesions in phantom1 and 2 from day0 to day9

10.2.4.9 Observing the effect of the removal of deionised water during the storage period for a phantom wrapped in cling film

For this experiment a 2.5 ml CA in 20 ml 10% PVAL phantom was created and subjected to 3 FTCs. This PVAL cancer lesion was then embedded in a 5% PVAL phantom was created and subjected to 2 further FTCs.

The phantom was then wrapped in cling film in order to reduce the effect of the dryness (Figure 10.46) and stored in a sealed plastic container. The phantom was CT scanned on day0 and day3.

Figure 10.46 Phantom wrapped in cling film

10.2.4.10 Results and analysis

The drop of HU (210.2) from day0 to day3 was less than the drop in the sealed and hydrated PVAL cancer lesions from day0 to day3. The drops were 367.90 and 349.60 in sealed and hydrated PVAL cancer lesions for phantom1 and 371.60 and 271.90 in sealed and hydrated lesions for phantom2 (see 10.2.4.7 on page 161).

10.2.4.11 Discussion

Based on the acquired HU values from both hydrated and dehydrated lesions after fabrication, there is a demonstrated drop in HU for both experiments over time. The drop of HU for the hydrated lesions was due to the presence of water in the lesions. This facilitated the dilution of the contrast agent within the lesion. In the lesions which were not stored in deionised water, rather than dilution of the contrast agent, the agent instead leeched out of the sample.

Given that the PVAL solution forms a skin while cooling, it was postulated that the resulting phantom may also form a skin when exposed to the air. Two tests were

performed to evaluate this possibility: storing the lesion in a sealed container, and storing the lesion in an open container. In each case the lesions were held for several days. In both cases the leeching effect could not be eliminated by either storage method.

The rates of the leeching of contrast agent into the surrounding tissues for both the hydrated and dehydrated samples were observed to be linear in the first three days before reaching stability. Some samples showed a slight increase in HU on the fourth day. It is suggested that this may be due to the formation of additional crystallites in PVAL lesions (Peppas, 1976). While this change is interesting, further investigation of this is outside the bounds of this research.

Exposing the lesions to the air for a few hours did not change the HU remarkably (1.4% for 3 ml of CA). This experiment indicates that the HU of the lesion will not suddenly drop after fabrication of the lesion.

In order to determine the best storage method for the lesions during the fabrication process, a comparison between the sealed lesion and the hydrated lesions was performed. The result of this experiment shows that the HU of the lesions with identical amount of contrast agent which were not stored in deionised water was higher than the ones which have been hydrated after fabrication. This suggests that the lesions stored in water are more affected by the leeching process than those stored in a sealed container.

As was demonstrated in the last experiment of these sets, keeping the breast phantom wrapped in a cover such as cling film caused the HU of the embedded lesions to reduce less compared to the lesions which had been kept sealed or hydrated. Therefore the utilisation of a skin for the breast phantom is recommended in order to decrease the HU reduction of the lesions and to protect the breast phantom during the mammography procedure.

10.2.4.12 Conclusion

Based upon the results from the experiments related to the effect of the environment on the PVAL lesions mixed with contrast agents, it is probable that the lesions could not be stored for an extended period of time. Therefore it is concluded that any experimentation should be performed with freshly created lesions embedded within PVAL phantoms. This also explains why further testing of the YM over time was not needed.

Based on the results, it is not advised to keep the phantoms in deionised water during storage. The mammography procedure should be performed soon after the fabrication of the phantom/lesions.

Due to the unsharpness of the edge and inadequate visibility of the lesions made up of 2.5 ml of contrast agent in mammogram, it is important to utilise higher amount of contrast agent. This is discussed in the next chapter.

Chapter 11 Methods

The aim of this chapter is to obtain the relationship between the lesion visibility and the breast phantom thickness. In order to find this relationship the embedded lesion had to be visible in mammograms. Based on the results from Chapter 10, a fresh 5% PVAL phantom with 2 FTCs containing a 10% lesion with 6 FTCs was appropriate for mammography. In the previous chapter contrast agent with higher concentration than 2.5 ml in 20 ml of PVAL solution was suggested. Therefore the experiments in this chapter started with the evaluation of the visibility of the lesions with higher concentration of contrast agent (>2.5 ml) in mammograms.

Compression of the PVAL phantom/lesion, data collection, and evaluation of the visibility of the lesions are also covered in this chapter. Evaluation of the lesion visibility was based on visual and mathematical methods. For the visual assessment, a 2AFC method was utilised and for the mathematical evaluation, CNR, SNR, FOM, and profile analysis were employed.

Once a suitable phantom/lesion was found, the method was repeated multiple times. This provided the means to acquire robust datasets for data analysis. The acquired mammograms were evaluated visually and mathematically based on the phantom thickness.

11.1 MAMMOGRAPHY OF BREAST PHANTOM INCLUDING A LARGE EMBEDDED LESION

A flexible plastic breast mould (Figure 11.1) was utilised to fabricate the breast phantom. In order to produce skin for the breast phantom, the mould was painted with latex paint. The number of coats for the paint was dependent upon the consistency of the latex paint. It can vary from 5 to 14 coats in order to make a sufficient thickness of 0.8 mm similar to human breast skin (Pope, Read, Medsker, Buschi, & Brenbridge, 1984).

Figure 11.1 Breast mould

A domestic hair dryer was used to accelerate the latex paint drying time from 4 hours to 10 minutes. A 4 FTC disk-shaped PVAL lesion (20 ml of 10%PVAL solution + 3 ml CA) was placed in the bottom of the mould, then 5% PVAL solution was added to the mould. The breast mould including the latex skin, PVAL lesion and PVAL solution underwent 2 FTCs (Figure 11.2).

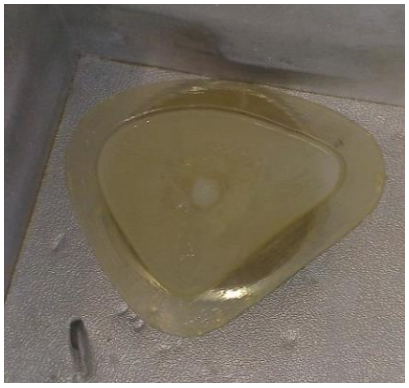

Figure 11.2 Breast phantom with an embedded lesion inside a breast mould painted with layers of latex paint.

In order to fabricate the top surface of the phantom, a thick flat latex skin with 100 gr of latex paint was made in a tray separately. The latex paint was first poured into the tray and the tray was tilted until it was covered with the paint evenly (Figure 11.3).

Figure 11.3 Top surface (chest part) of the breast phantom made up of latex paint.

In this experiment the breast phantom was not kept in deionised water instead the phantom was covered with the latex skin. The latex skin kept the phantom hydrated.

First the wooden torso (45.72 cm X 95.25 cm X 1.9 cm of plyboard) was painted with latex paint. After drying the surface, the top surface was peeled gently from the tray and laid on the dried coat of latex paint on the plyboard. The skin of the thawed phantom was gently peeled from the mould with the phantom in. The skin including the breast phantom then was laid on the surface skin and with the assistance of a staple gun the breast skin was stapled to the wooden torso. In order to avoid the interference of the metal staples in the mammography procedure, they needed to be hammered to have a flat surface. About 5 coats of latex paint were required to cover the staples and to attach the breast skin to the top surface (Figure 11.4).

Figure 11.4 Attachment of the breast phantom/skin to the wooden torso

The CT scan was performed over a 6 day period (Figure 11.5). In order to measure the drop of HU per minute, the first CT scan was performed immediately after fabrication of phantom. This took 10 minutes continuously every one minute.

The DICOM images were collected and the grey scale was measured utilizing ImageJ software.

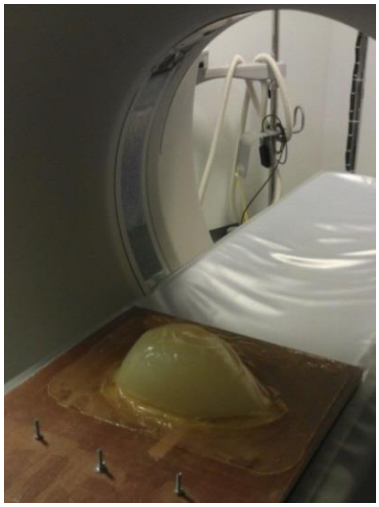

Figure 11.5 A breast phantom wrapped in latex skin in CT scanner

The CT scan performed on the first day right after fabrication of phantom, on the third, fourth, fifth, and sixth days. The mammography procedure was performed 5 hours after the second CT scan. The breast phantom was compressed applying 51 N to 132 N. The compression paddle used in this experiment was 24x30 cm. The resultant

mammograms were collected and visualized. The 2AFC (Two-alternative forced choice) method was utilised in this experiment. Molybdenum (Mo) was the target anode and experiment was based on the increase of the compression force. The following table (Table 11.1) demonstrates the mAs, kVp, compression force and the breast phantom thickness.

Compression (N)	51	65	92	106	117	132
Thickness (cm)	9.4	8.5	8.0	7.6	7.3	6.8
mAs	238.2	282.7	229.5	271.1	247.7	219.8
kVp	34	33	33	32	32	32

Table 11.1 Settings for the mammography of a breast phantom.

11.1.2 Results and analysis

11.1.2.1 CT results

The following table (Table 11.2) and graph (Figure 11.6) display the drop of HU over 10 minutes. The initial and final HU values were recorded as 633.17 and 632.21 respectively over 10 minutes.

Time (min)	Area	HU	
1		298.14	633.17
2		298.14	633.13
3		298.14	633.07
4		298.14	633.10
5		298.14	632.85
6		298.14	632.70
7		298.14	632.67
8		298.14	632.41
9		298.14	632.35
10		298.14	632.21

Table 11.2 HU of an embedded lesion in a breast phantom with skin over 10 minutes

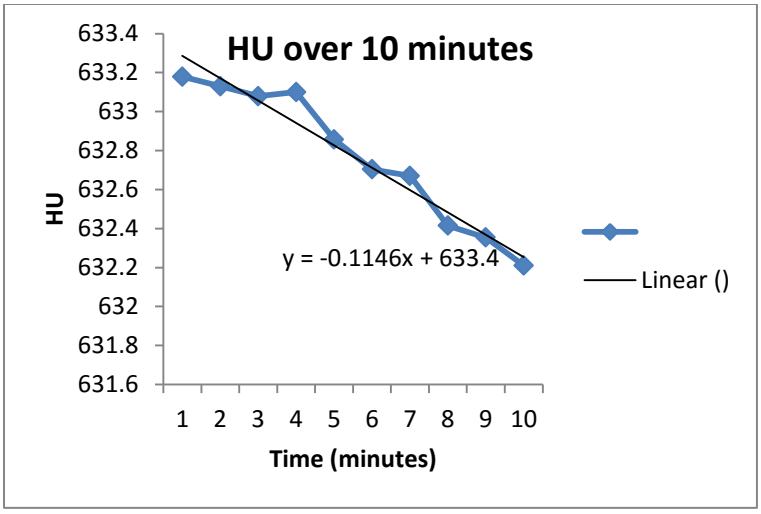

Figure 11.6 HU of an embedded lesion in a breast phantom with skin over 10 minutes

The measured drop of HU per minute was 0.0969/min (0.15% drop over 10 minutes).

As Figure 11.7 shows, the border of the lesion becomes less delineated and defined over time. The CT image on day0, right after fabrication of the breast phantom/lesion shows a sharp border of the lesion with a good contrast with the background.

Figure 11.7 Left to right: CT image of an embedded lesion in a phantom with latex skin on day0, day3, day4, day5, and day6 (WL=0, WW=300)

The drops of HU were 152.80, 37.50, 55.70, and 26.90 respectively from day0 to day6. The results (Table 11.3) shows the smaller HU drop (609-336.1=272.90) over a week period for a sealed phantom in latex skin compared to the sealed and hydrated PVAL lesions from Chapter 10. The HU drops in phantom1 (Table 10.21) for the sealed and hydrated lesions over a week period were (796.60-263.10= 533.50) and (685.00-

241.40= 443.60). The drops for the sealed and hydrated PVAL lesions in phantom2 were (781.30-264.10=517.20) and (603.10-210.50=392.60).

Days	HU
0	609.00
3	456.20
4	418.70
5	363.00
6	336.10

Table 11.3 HU of an embedded lesion in a phantom with latex skin on day0, day3, day4, day5, and day6

The following graph (Figure 11.8) shows the drop of the HU for the embedded lesion from day0 to day6 of the following week. The trend line shows a linear relation between the HU and the time.

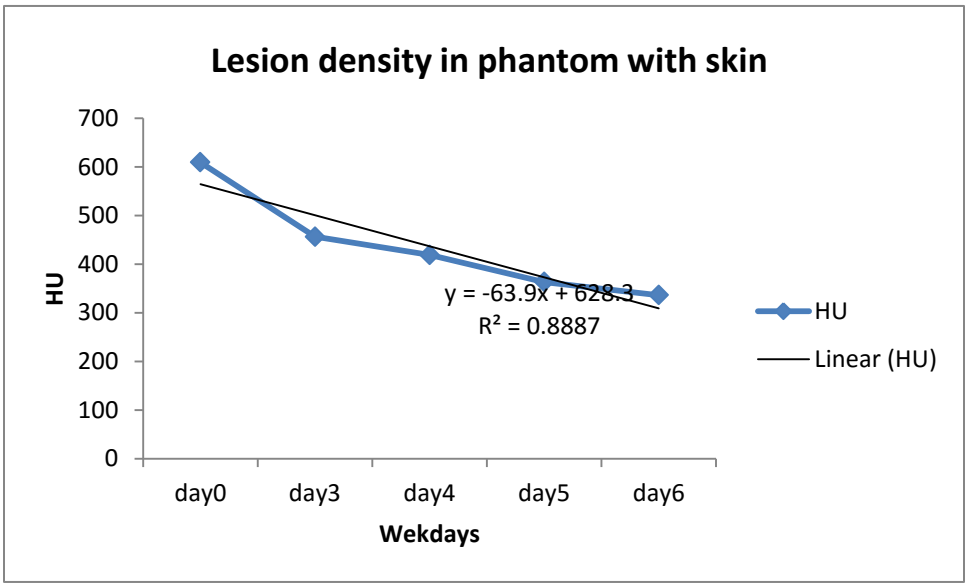

Figure 11.8 HU of an embedded lesion in a phantom with latex skin on day0, day3, day4, day5, and day6

11.1.2.2 Mammography results

The embedded lesion was visualized successfully in the mammograms (Figure 11.9) applying 51 N to 132 N compression force. Comparing the far left image and the far right images visually shows the slight improvement in the lesion visibility based on the increase of compression force. The phantoms looks expanded with slightly reduced noise. Even though the mammograms show slight improvement visually between the far left image and the far right image, it is still difficult to evaluate the image quality of the middle images perceptually. Therefore further experiments with a larger sample size are required to confirm the results. Mathematical evaluations are also required for additional and complementary evaluation of the image quality.

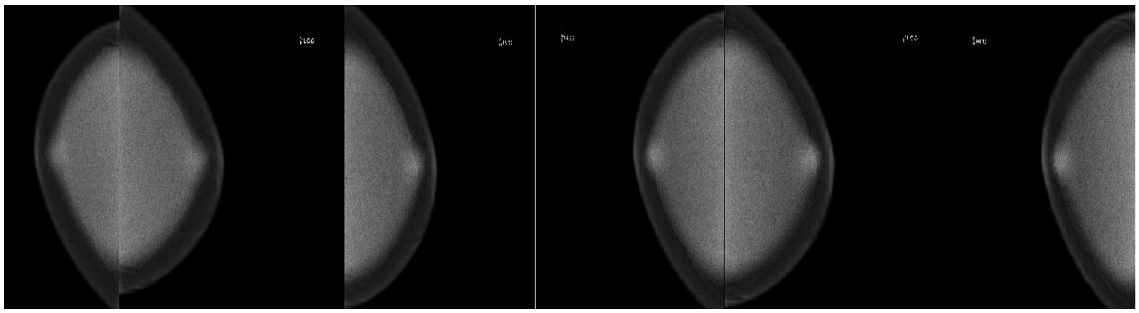

Figure 11.9 From left to right: 51, 65, 92, 106, 117 and 132 N were applied to the breast phantom. The lesion shows in the nipple area

The following graph (Figure 11.10) shows the linear relation between the compression force and the breast phantom thickness. The higher pressure results in reduction in the thickness.

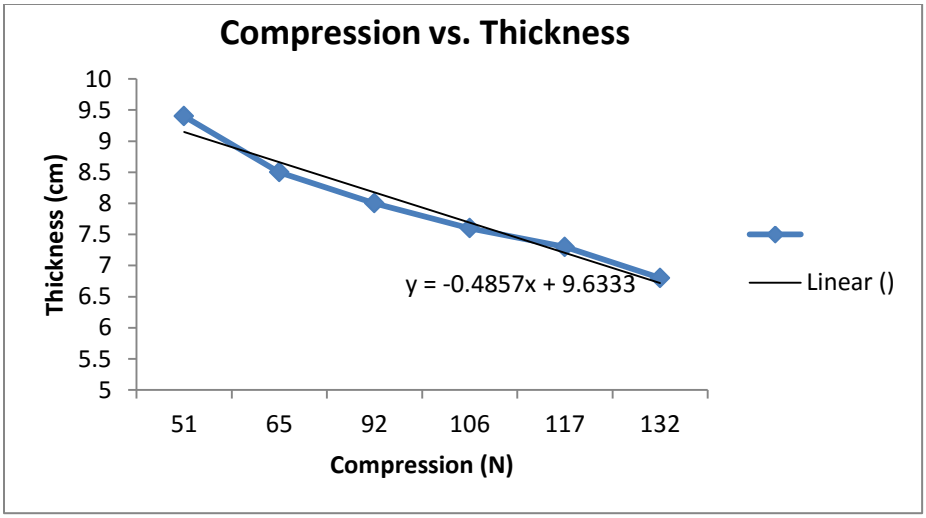

Figure 11.10 Compression vs. thickness for the breast phantom

11.2 MAMMOGRAPHY OF BREAST PHANTOMS WITH 9 MM EMBEDDED LESIONS

Three 5% phantoms were prepared separately. Due to the large size of the breast moulds (2L) used in this experiment, the aqueous solution of PVAL was prepared in a 5L round bottom boiling flask. The boiling flask was put in a large water bath during heating (Figure 11.11). Magnetic stirrer was set between 60 RPM - 200 RPM.

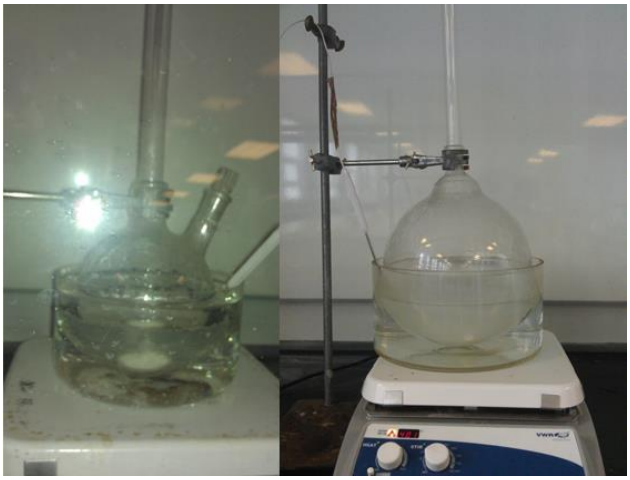

Figure 11.11 Right: The setup used in the current experiment. Left: The setup used in the previous experiments

The lesions utilised in this experiment were 9 mm sphere-shaped of 200 ml of 10% PVAL doped with 30 ml of CA. Since the size of the human breast tumours can be smaller than 1 cm and larger than 5 cm (Elkin, Hudis, Begg, & Schrag, 2005), therefore 9 mm for diameter of the lesions was in the range of breast tumours. One of the reasons that the round-shaped lesions were chosen in this research was because the real breast masses can be round (Bassett, 2000). The other reason for constructing the round-shaped lesions was consistency in size and shape throughout this research compared to the shape of spiculated masses.

A 9 mm plastic bead cutter (Figure 11.12) was employed as a mould to form the round cancer mimicking lesions. The bead cutter was closed and sealed immediately after immersing into the container of the PVAL doped with contrast. The beat cutter can be sealed with a bulldog clip or clothespin. After sealing the homogeneous and transparent lesion solution in the bead cutter, the mixture was placed into the freezer and underwent 4 FTCs.

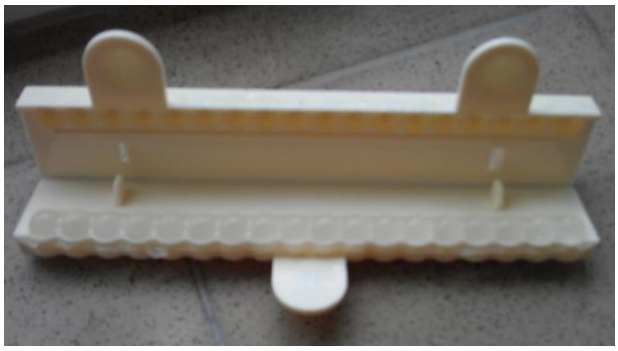

Figure 11.12 A plastic bead cutter to make round cancer mimicking lesions.

After drying the latex paint in the breast mould, one lesion per breast phantom was suspended in the middle of the breast moulds with the assistance of 10 cm nylon thread (Figure 11.13).

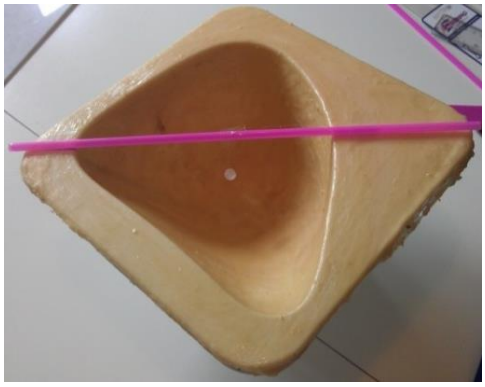

Figure 11.13 A 0.9 cm cancer mimicking lesion suspended in a painted breast mould

All three phantoms were put into a domestic freezer for 2 FTCs (Figure 11.14). Consequently, the 5% breast phantoms underwent 2 FTCs and the 10% embedded lesions underwent 6 FTCs (4 FTCs in prior to their embedment).

Figure 11.14 Three large beast phantoms in the freezer.

After 2 FTCs, the skin of the thawed breast phantoms was attached to the wooden torso (Figure 11.15). Then the phantoms attached to the wooden torso underwent the CT scan procedure (Figure 11.16). The DICOM images were collected and the grey scale was measured utilizing ImageJ software.

Figure 11.15 Large breast phantoms with 0.9 cm cancer mimicking lesions per phantom attached to the wooden torsos

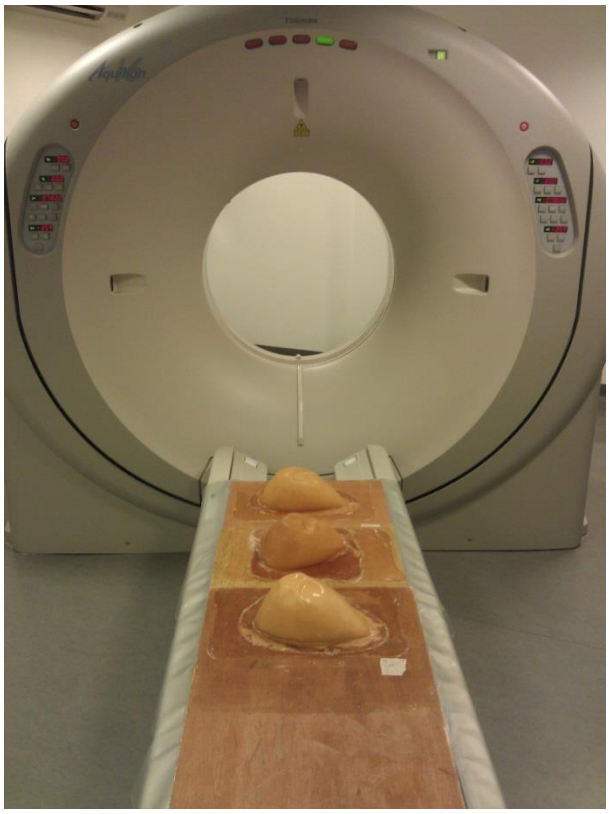

Figure 11.16 Three large breast phantoms in a CT scanner.

The phantoms underwent mammography procedure an hour after CT imaging. The compressions forces applied for the phantoms were 197 N, 193 N and 163 N respectively utilizing an 18x24 cm compression paddle. The maximum compression was applied for each phantom in order to see if the lesions were visible with the highest compression.

Table 11.4 shows the force, the phantom thickness, kVp, mAs, filter and paddle used in this experiment.

Phantoms	#1	#2	#3
Force (N)	197	193	163
Thickness (cm)	6.2	6.6	7.2
kVp	31	32	32
mAs	268.1	224.8	264.5
Filter	Rh	Rh	Rh
Paddle	24cmx29 cm	24cmx29 cm	24cm x29cm

Table 11.4 Mammography parameters

As the following image illustrates (Figure 11.17), the breast phantom, attached to the wooden torso, approximates the human female anatomy. The image shows the breast phantom at maximum compression between the compression paddle (top) and the support table (bottom).

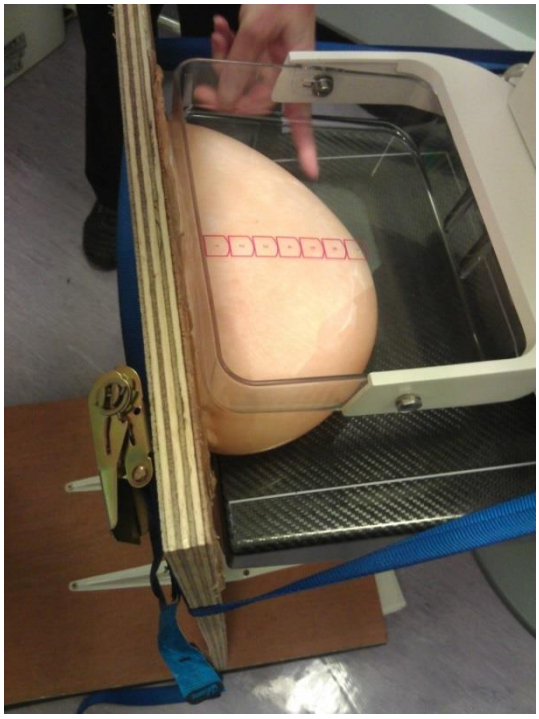

Figure 11.17 A compressed breast phantom during mammography

11.2.2 Results and analysis

The embedded lesions were barely visible in the CT images (Figure 11.18). The lesions were not visible in the mammograms (Figure 11.19).

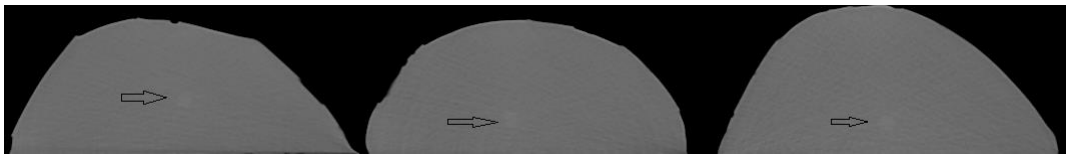

Figure 11.18 CT images of three large breast phantoms with one 0.9 cm embedded lesion in each (WL=0, WW=300)

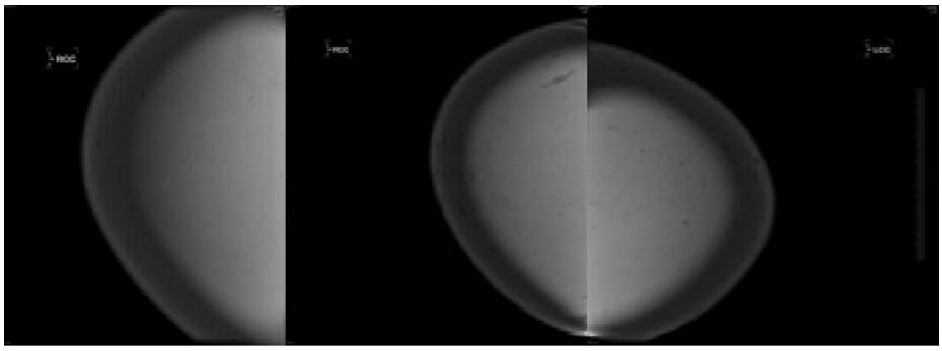

Figure 11.19 Mammograms of three large breast phantoms with one 0.9 cm embedded lesion (WL=0, WW=300)

11.2.3 Discussion

In this research, a suitable PVAL breast phantom with embedded lesions must have X-ray imaging properties similar to human female breast tissue. These imaging properties can be evaluated using CT imaging and are affected by electron density and atomic number (Z) (Thomas, 1999). The electron density of each tissue influences its linear attenuation coefficient (absorption or weakening of the X-ray). In CT, the Hounsfield unit (HU) is a function of the linear attenuation coefficient. This means that the HU is indirectly a function of electron density. The HU is also affected by the kVp and since the kVp range in CT and mammography are completely different, the attenuation of the objects is different from CT to mammography. For example, a phantom may simulate the human tissue at certain energy, but could display inaccurate properties

in other energy ranges. CT scan and mammography are good examples of these energy differences (Dewerd & Kissick, 2014). The energy difference between mammography and CT could make the visibility of the lesion different between those imaging modalities.

In order to find an adequate attenuation for the breast phantom/lesion, the acquired images have to be compared between these two imaging modalities. After acquiring the sufficient attenuation in mammography for the lesion, the recorded HU from the CT procedure is accepted as an appropriate HU for the breast phantom/lesion.

Generally, in order to make a phantom similar to human tissue, the appropriate properties for the phantom are critical. The most common property to represent the tissue equivalence is attenuation coefficient.

This experiment is the extension of a previous experiment (11.1 on page 173). One of the differences between this experiment and the previous one was the size of the lesion. Although the amount of contrast agent in this experiment was 0.5 ml more than the previous experiment, the size and location of the lesion made it harder to view in CT images and impossible to view in mammograms. According to the literature, there is a linear relationship between the signal difference to noise ratio (SDNR) and the lesion size in mammography. This means that the SDNR which is the product of radiation contrast and signal to noise ratio (Yaffe, 2010) improves with the increase of the lesion size (Kempston, Mainprize, & Yaffe, 2006).

In the previous experiment the lesion was placed in the nipple area (bottom of the mould) which was close to the detector while in this experiment the lesion was instead located in the middle of the phantom which was further away from the detector. This could decrease the visibility of the lesion due to the increased distance between the lesion and the detector.

One solution to overcome the visibility differences between CT images and mammograms is the increase of the contrast agent in the lesion. Since the visibility of the lesion is related to its size, location within the phantom, and the thickness of the breast phantom, the right amount of contrast agent has to be calculated, measured and utilised in the next experiment. It is noted that the excess amount of contrast agent, will make the lesions easily detectable. It will also help keep the lesion from being anthropomorphic.

One of the encountered problems in this experiment was the presence of water in the phantom which possibly has caused the dilution of the contrast agent in the lesion. This issue might be addressed by imaging the fresh phantoms immediately after fabrication.

Making three phantoms at the same time also increased the temperature of the freezer consequently increasing the freezing time. In the experiment, the freezing started 5 hours after the insertion of the phantoms into the freezer (7.2 on page 94).

Another factor which might have affected the presence of water in the phantom might have been the usage of a 5L boiling flask during heating. Although the temperature of the water bath in this setup reached to 100 °C, the size and the thickness of the boiling flask may have affected the temperature of the PVAL solution, consequently leaving some un-dissolved PVAL in deionised water behind.

In order to view the lesions, another experiment was carried out. During this experiment, only one phantom was placed into the freezer at a time and a 1L boiling flask which was used in early experiments was utilised. The freshly prepared phantom was imaged immediately after fabrication.

11.3 IMPROVEMENT OF FABRICATION OF BREAST PHANTOMS/LESIONS - PART1

This experiment was conducted in order to overcome the inability to visualize the PVAL lesion in a large breast phantom.

In order to fill a 2L breast mould, three batches of 5% aqueous PVAL solution were prepared with 40 gr of PVAL and 760 ml of deionised water per batch. 10% PVAL solution with 80 gr of PVAL and 720 ml of deionised water was prepared to make lesions. Both 10% and 5% PVAL solutions were boiled in a 1L round-bottom boiling flask. For the lesion part, 200 ml of 10% PVAL was doped with 50 ml of CA.

The intensity formula, $I=I_0e^{-\mu x}$ (The Collaboration for NDT Education, 2012) was used to measure the amount of contrast agent. Because of the mammographic visibility of the lesion used in the above experiment (see 11.1 on page 173), the lesion with the height of 1.5 cm and 3 ml of CA in 20 ml of PVAL solution was considered as a reference. Based upon the intensity formula, the equivalent intensity was expected, therefore the ratio of the μ of the lesion used in this experiment (0.9 cm) to the lesion used in of the above (1.5 cm) became 1.66 (1.5/0.9). In order to provide the desired intensity, the amount of the contrast agent had to be trebled (1.66x3 = 4.98 ml≈5 ml). In this experiment 50 ml of contrast agent in 200 ml of PVAL solution was utilised.

One 10% PVAL/CA lesion with 4 FTCs fabricated in a bead cutter was suspended in the middle of the breast mould. 2 L of 5% PVAL solution was then poured over the lesion into the latex painted mould. The breast mould including the PVAL solution and one lesion was placed into a domestic freezer for 2 FTCs. CT and mammography procedures were carried out after thawing the phantom. The CT procedure was repeated 4 days after fabrication of the phantom.

The mammography procedure was carried out an hour after the CT scan. The high compression was applied first in order to make sure that the lesion was viewable under high pressure. The paddle size was 24x29cm.

11.3.1 Results and analysis

11.3.1.1 CT results

The lesion was seen in the CT image (Figure 11.20) of freshly thawed phantom. The HU of the lesion was 90 and the surrounding tissue was 12.

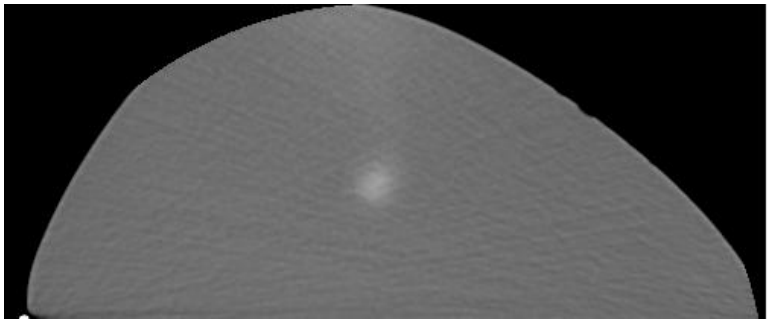

Figure 11.20 CT image of a fresh phantom right after thawing (WL=0, WW=300)

The lesion was barely visualized in the CT image (Figure 11.21) of the same phantom 4 days later.

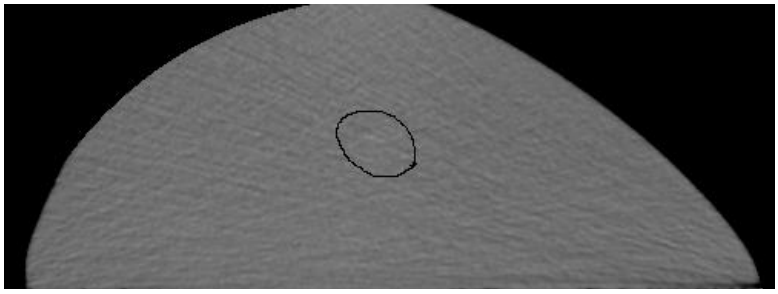

Figure 11.21 CT scan of the breast phantom 4 days after fabrication (WL=0, WW=300)

11.3.1.2 Mammography results

The table (Table 11.5) shows the data acquired from the mammography procedure. Due to the thickness of the phantom, the mammography unit cut out on

exposure 60 N. The last column of the table is the repetition of the first column with 197 N to ensure that the lesion has similar visibility and the pressure changes did not deteriorate the lesion.

Force (N)	Compression (cm)	KvP	mAs	Filter	Organ (mGy)	Entrance (mGy)
197	5.9	30	275.5	Rh	7.04	29.00
190	6.1	31	227.5	Rh	6.41	26.70
173	6.4	31	259.2	Rh	7.14	30.70
177	6.4	31	258.1	Rh	7.11	30.60
164	6.5	32	214.1	Rh	6.50	28.60
152	6.9	32	253.3	Rh	6.87	31.20
139	7.0	32	242.2	Rh	7.00	32.20
130	7.2	32	245.2	Rh	7.00	32.80
119	7.7	32	295.1	Rh	8.11	40.20
110	7.8	32	307.1	Rh	8.39	42.00
100	8.3	33	264.9	Rh	7.69	40.30
90	8.6	33	276.6	Rh	7.86	42.60
80	8.9	33	295.4	Rh	8.20	45.90
70	9.3	34	256.7	Rh	7.62	44.10
60 cut out on exposure	9.6	34	154.5	Rh	4.49	26.80
197	6.1	31	242.5	Rh	6.84	28.40

Table 11.5 Mammography parameters

The lesion was viewed in the mammograms (Figure 11.22) with low visibility. All the mammogram images are in Appendix C.

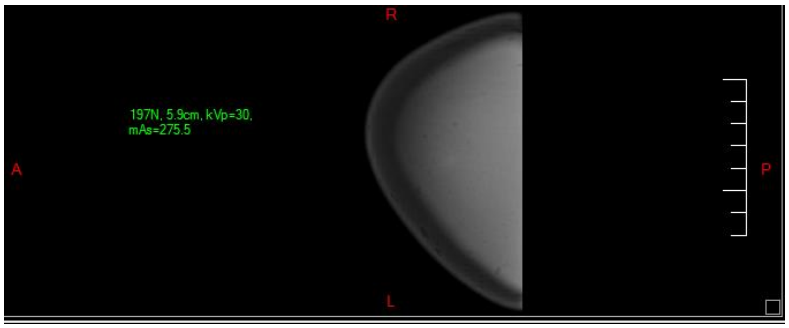

Figure 11.22 Mammograms of the breast phantom with various compressions

11.4 IMPROVEMENT OF FABRICATION OF BREAST PHANTOMS/LESIONS - PART2

This experiment was conducted in order to improve the visibility of the lesion in mammograms. Low mammographic visibility such as the one in the previous experiment (see 11.3 on page 190) would make the visual perception and mathematical evaluation methods either difficult or impossible to employ. For example, the insufficient visibility of the lesion will hinder the observers' ability to evaluate the details of the lesions. Examples of the details which could be hindered include the sharpness of the edge and the contrast of the lesion and its surrounding area. Therefore, mammographic improvement of the lesion visibility is required in order to assess the image quality for the phantom/lesion. The following experiment is aimed at improving visibility of the lesions in mammograms.

Two medium sized (1L, 5% PVAL and 2 FTCs) breast phantoms were fabricated in this experiment. Based on the mastectomy specimen volume results by Kayar et al, a one litre breast phantom is appropriate as breast volume. In Kayar's research, the breast volumes ranged from 150–1490 mL (Kayar, Civelek, Cobanoglu, Gungor, Catal, &

Emiroglu, 2011). The one litre mould used in this research was originally a mastectomy prosthesis cradle (mould) to hold the prosthesis undamaged.

Each phantom included two 10% lesions with 6 FTCs. The lesions were made up of 5 ml and 3 ml of CA mixed with 20 ml of PVAL solution. One of the each lesion was embedded in each phantom. In order to save contrast agent, the lesions were made in the bead cutter slightly different than in the previous experiment. A smaller batch of 10% PVAL doped with contrast agent was made and poured into each side of the bead cutter. The two hemispheres were then pressed together after the first freezing/thawing cycle. Surgical tweezers were used in order to reduce the contact between the lesions and the fingers.

CT scan and mammography were performed immediately after fabrication of phantoms. In the mammography procedure using AEC, the compression force ranged from 50 N to 150N with an interval of 10 N (Table 11.6 and Table 11.7) and paddle size 18x24 cm. After applying 150 N, 50 N was re-applied in order to see the changes in the visibility of the lesions from the first application of 50 N (last row of Table 11.6 and Table 11.7). The filter used in mammography was molybdenum (Mo) throughout the procedure. This means that due to the inadequate thickness of phantom for the rhodium filter, this filter was not required during the mammography procedure.

Breast phantom 5% PVAL, 1FTC with 2 lesions						
Force (N)	Compression (cm)	kVp	mAs	Filter	Organ (mGy)	Entrance (mGy)
47	3.2	25	89.1	Mo	2.10	7.86
59	3.1	25	87.4	Mo	2.09	7.68
70	2.9	24	105	Mo	2.13	7.66
80	2.6	24	87.3	Mo	2.08	6.59
85	2.7	24	92.2	Mo	2.08	6.98
99	2.5	24	81.6	Mo	1.95	6.14
109	2.4	24	80.9	Mo	1.98	6.06
117	2.2	24	71.3	Mo	1.84	5.31
129	2.2	24	70.5	Mo	1.82	5.25
138	2.0	24	65.0	Mo	1.75	4.81
141	2.0	24	66.0	Mo	1.78	4.88
50	3.0	25	76.1	Mo	1.85	6.67

Table 11.6 Mammography parameters for the medium size breast shaped phantom (5%PVAL, 1FTC) with two lesions.

Cylindrical phantom 5%, 2FTCs with 2 lesions						
Force (N)	Compression (cm)	KvP	mAs	Filter	Organ (mGy)	Entrance (mGy)
50	3.5	26	88.2	Mo	2.32	8.91
61	3.3	25	107.6	Mo	2.50	9.52
69	3.0	25	90.2	Mo	2.19	7.90
79	2.7	24	103.3	Mo	2.33	7.89
92	2.6	24	89.9	Mo	2.09	6.78
100	2.5	24	88.1	Mo	2.10	6.63
107	2.3	24	85.7	Mo	2.15	6.40
114	2.3	24	81.1	Mo	2.04	6.06
130	2.2	24	76.1	Mo	1.96	5.67
137	2.1	24	75.3	Mo	1.99	5.59
149	2.2	24	80.9	Mo	2.08	6.03
52	3.0	25	85.3	Mo	2.07	7.48

Table 11.7 Mammography parameters for a cylindrical phantom (5%PVAL, 2FTCs) with two lesions

In this experiment, Two-alternative forced choice (2AFC) as a visual perception method was applied to evaluate the image quality of the lesions based on 5-point Likert scale (1= much worse, 2=worse, 3=equal, 4= better, 5=much better). The Likert scale, commonly used in research, is a scale which is used in questionnaires to obtain the

observers' degree of agreement with the set of statements (criteria) (Mathers, Fox, & Amanda, 2009). In this research a 5-point Likert scale was chosen over a 3-point scale in order to collect more detailed perceived image quality opinions from the observers. The clarity of the lesion edges was the selected criteria in this experiment.

In order to select the reference image, enter the scores from the visual evaluation and collect the results of scoring the images a bespoke software (Blindell & Hogg, 2012) was utilised to perform the 2AFC method. The following image (Figure 11.23) depicts the main user interface of this 2AFC software. The images employed in 2AFC experiments, the reference image, the criteria and other 2AFC options are specified in this user interface.

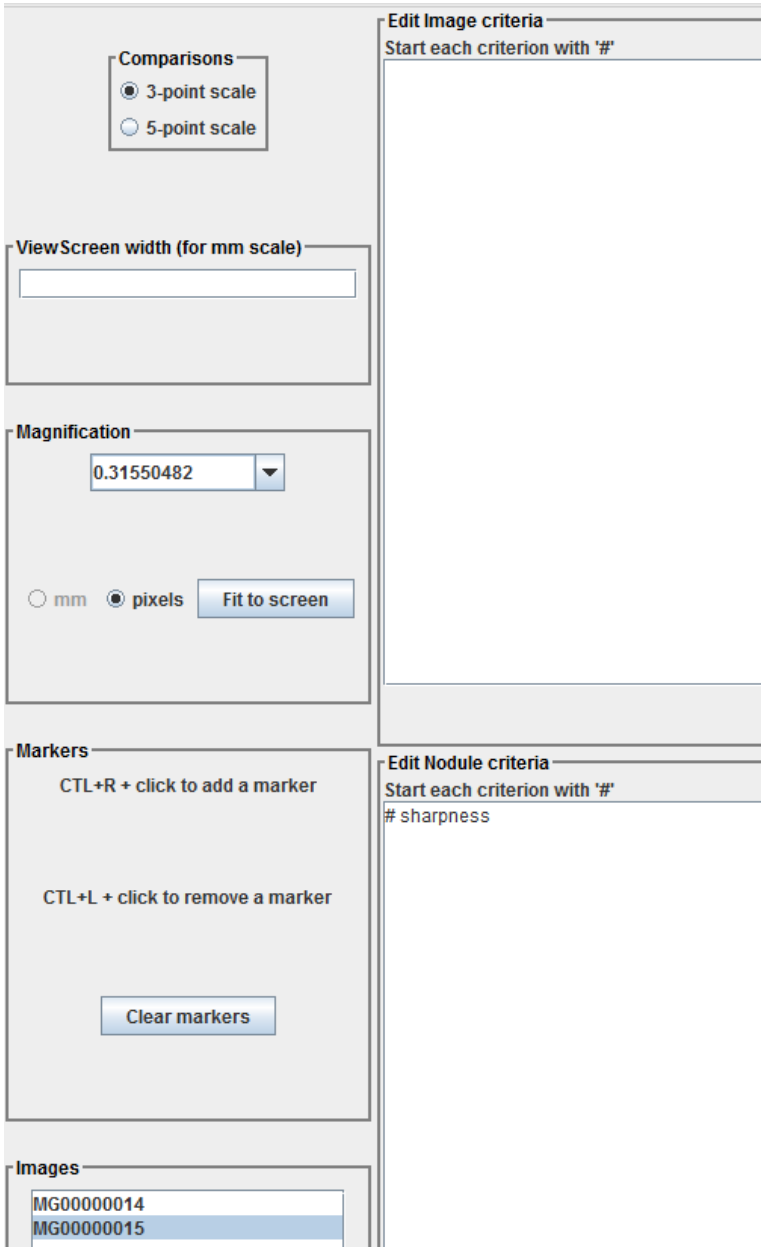

Figure 11.23 The main user interface of the 2AFC software

11.4.2 Results and analysis

11.4.2.1 CT results

Figure 11.24 shows the line profiles of two embedded lesions in one of the breast phantoms.

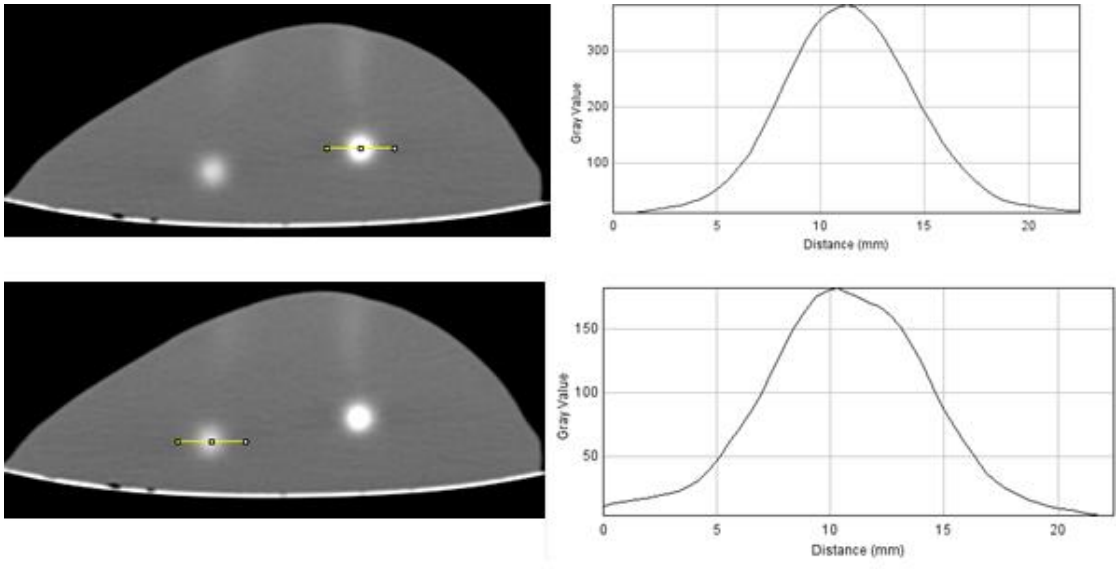

Figure 11.24 Left: CT scan of a breast shaped phantom with two lesions. Right: line profile of the lesions acquired from ImageJ

The brighter lesion (right) was made up of 5 ml of CA in 20 ml of 10% PVAL and the blurry lesion (left) was made up of 3 ml of CA in 20 ml of 10% PVAL. The bright and blurry lesions are called High Density (HD) and Low Density (LD) in this experiment. Similarly, the lesion with 5 ml of CA was displayed brighter in the second phantom.

The HU of the HD and LD lesions were 382 and 182 respectively. The HU of the surrounding breast mimicking tissue was 14.

11.4.2.2 Mammography results

The following mammogram (Figure 11.25) shows the lesions embedded in the breast phantom. The brighter lesion (top) in the image was made up of 5 ml of contrast agent while the other lesion was made up of 3 ml of contrast agent. All the mammograms are in Appendix D.

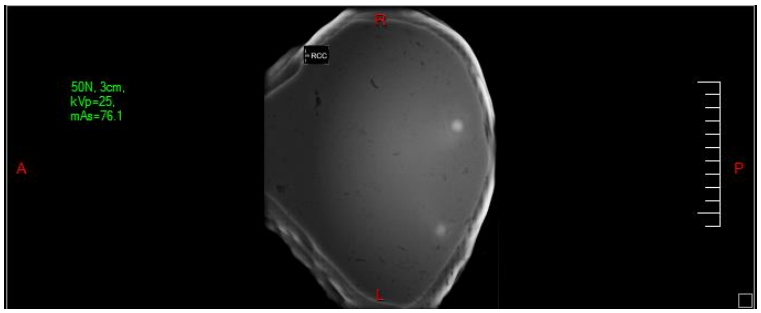

Figure 11.25 Mammograms of the breast phantom with two lesions

11.4.2.3 2AFC results

The following graph (Figure 11.26) was acquired based on the edge clarity criteria.

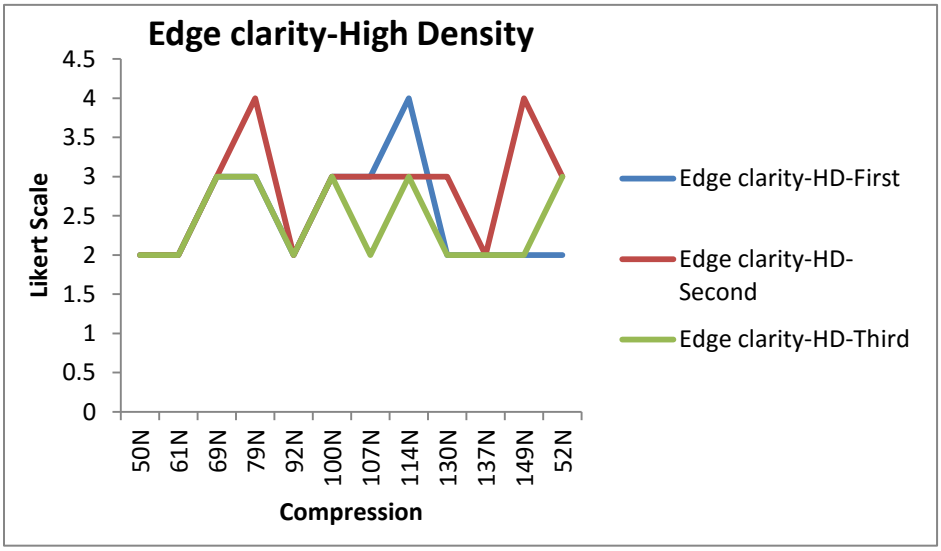

Figure 11.26 2AFC, 3 repetitions for the High Density lesion in a cylindrical phantom

The graph shows three readings for the same lesion. The jagged results show improvement from 61 N to 69 N. The drop was observed at 92 N and 137 N. The rest of the edge clarity graphs are in Appendix E.

11.4.3 Discussion

In order to improve the visibility of the 9 mm lesions in breast phantoms, two sets of experiments were performed (11.3 and 11.4). In both sets of experiments, lesions were fabricated using the same amount of contrast agent (5 ml of contrast agent in 20 ml of 10% PVAL). The main difference between these two sets of experiments was the size of the breast mould. In the first set, a 2L breast mould was employed while a 1L breast mould was utilised in the second set of experiments. The lesion which was embedded in a 1L breast mould was more conspicuous than the lesion which was produced in a 2L breast mould. Clinically the size of the breast can affect the mammogram. Women with large breasts might require more images taken than women with small breasts (Espat, 2012). Therefore in this study, using a 1L medium breast mould was suggested instead of a 2L large breast mould.

11.4.4 Conclusion

This experiment, having successfully produced a phantom in which lesions could be viewed in a mammography procedure, provides a basis for the evaluation of the lesion in relation to the breast phantom. This shows that a 5% PVAL phantom with 2FTCs fabricated in a 1L breast mould is appropriate for the breast phantom as required for this research. It also shows that a 10% PVAL lesion enriched with 5 ml of contrast agent is appropriate for the embedded lesions in the lesion visibility studies.

11.5 EVALUATION OF THE VISIBILITY OF THE LESION BASED ON THE BREAST PHANTOM THICKNESS

After completion of the design and fabrication of a breast phantom with embedded lesions, the following sets of experiment were conducted in order to determine the lesion visibility in relation to the phantom thickness.

A 5% breast phantom with one embedded lesion was created and underwent 2 freeze-thaw cycles. An embedded lesion was prepared with 10% PVAL solution doped with 5 ml of CA. The lesion underwent 4 freeze-thaw cycles prior to being placed in the 5% PVAL solution. A 1L plastic breast mould was utilised to shape the breast phantom during fabrication. As Figure 11.27 shows, the lesion was suspended from plastic supports 4.5 cm below the top of the mould utilising nylon thread.

Figure 11.27 Suspended lesion inside the breast mould.

In order to keep the surface of the mould level, the mould was placed into a plastic container (Figure 11.28). Then, a 5% PVAL solution was poured slowly into the mould until the mould was filled completely. The 5% PVAL solution underwent 2 FTCs. Each freezing cycle was 12 hours at -26 °C. After the completion of each freeze cycle, the phantom was left out at room temperature to thaw. The phantom was considered thawed when no solid lumps could be detected by manual manipulation. The first thawing took 13 hours and the second thawing took 18 hours at room temperature. The total freezing/thawing time for both cycles took 55 hours.

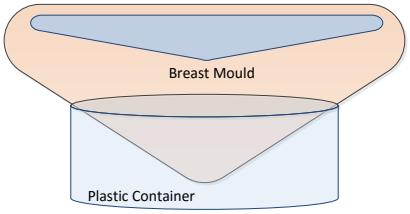

Figure 11.28 Levelling the breast mould

After thawing the phantom, the phantom was imaged by a CT scanner followed by the mammography imaging (Figure 11.29). As the image shows, the phantom was attached to a wooden frame and secured to the mammography unit with the assistance of a ratchet strap. The base of the wooden frame was tilted by placing an object under one side of the frame in order to position the top of the frame 1.5 cm away from the compression paddle. This gap allows the paddle to move easily without being blocked by the wooden frame during compression. It also prevents damaging the mammography unit by the wooden torso.

Figure 11.29 Mammography of a breast phantom attached to a wooden torso

The following image depicts (Figure 11.30) the gap between the mammographic paddle and the wooden torso.

Figure 11.30 Gap between the wooden board and the mammographic paddle

Prior to the imaging procedure, the phantom was lubricated with ultrasound gel in order to reduce friction during the compression which could result in tearing the latex skin and damaging the phantom. This transparent ultrasound gel did not interfere with acquired mammograms.

In order to simulate the mammography experiment similar to the mammography of the real breast tissue, AEC and Auto-Filter were both utilised during the mammography procedure. They both were set "on" prior to the mammography on the mammographic acquisition workstation. The Hologic Lorad Selenia mammography unit

employed in this research supports three Automatic Exposure Control (AEC) modes: Auto-time, Auto-kV, and Auto-filter.

In the Auto-Filter mode, the machine automatically switches between Rhodium (Rh) and Molybdenum (Mo) filters. The machine decides which filter to utilise based upon the compression thickness of the tissue being imaged and a lookup table. The Auto-kV mode fixes the filter based upon the anode being utilised. If the anode utilised is Mo then a Mo filter will be employed. If a tungsten (W) anode is utilised then a Rh filter will be used. The machine computes the appropriate kV based upon thickness and a lookup table. With the Auto-Time mode, the filter and kV are user-selected. In all three modes the mAs is calculated based upon the results of a pre-exposure scout pulse (Hologic Inc.).

Common clinical practice when performing mammography is to use AEC with the Auto-Filter mode and allow the mammography unit to control a wide range of exposure factors (Astley, 2006). Therefore, this study relied on the Auto-Filter mode to control the imaging factors and determine the optimal filter together with the optimal X-ray tube voltage based on the breast phantom thickness.

The compression was started with the thickness of 9 cm and was gradually increased manually by 2 mm intervals using an 18x24 cm flexible paddle. The last image was acquired when no more compression could be applied. The imaging was continued by reducing the compression thickness by 4 mm from the last thickness to reach the starting thickness. 28 mammograms were acquired from increasing of the compression force and 14 mammograms were acquired from decreasing of the compression force. The reduction of compression resulted in collecting more datasets and helped verify if the phantom/lesion had been damaged because of the compression.

The following image (Figure 11.31) shows the phantom with initial compression on the left and maximum compression on the right (5.4 cm thickness reduction). As the

image shows the compressed phantom (right) looks more spread out than the phantom with initial compression. The lesion has higher visibility with sharper edge and higher contrast on the phantom with maximum compression. The image on the left with initial compression looks noisier than the image with maximum compression.

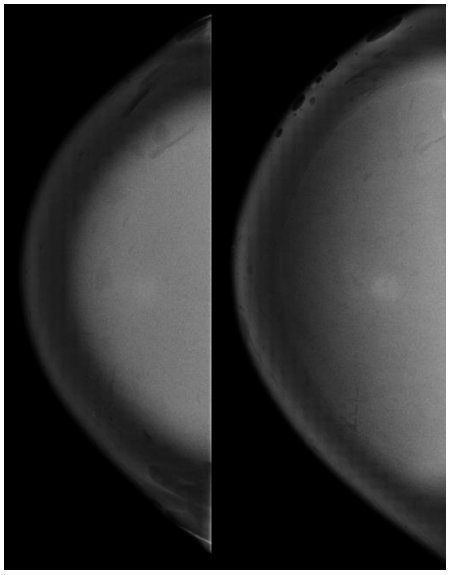

Figure 11.31 Phantom1 with 1 embedded lesion - left: Initial compression. Right: Final compression

The same experiment was repeated with two lesions inserted into two separate quadrants of the phantom. The lesions were placed in the phantoms diagonally in order to avoid being overlapped during mammography. The reason that two lesions were chosen was to visualise the effect of location on the visibility of the lesion. This also helped collect more datasets. As the following image (Figure 11.32) shows, the location (left) of the two lesions was determined prior to suspending them inside the painted breast mould utilizing a plastic support.

Figure 11.33 shows the breast phantom including two lesions with the initial compression (left image) and the final compression (right image). The image with initial compression displays some artefacts. These artefacts are mostly on the surface or skin of

the breast phantom and they are less visible with the reduction of the thickness (left image).

Figure 11.32 Measuring (left) and suspending (right) two PVAL lesions in a breast mould

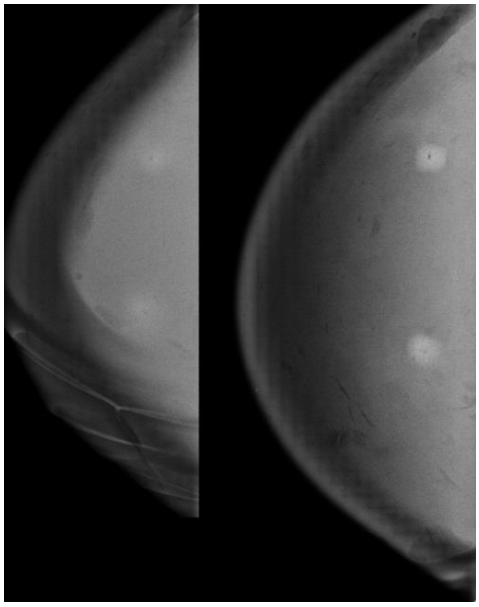

Figure 11.33 Phantom6 with 2 embedded lesions - left: Initial compression. Right: Final compression

In order to provide robust and reliable results, this experiment was repeated 6 times using 3 phantoms with one embedded lesion and 3 phantoms with two embedded lesions. In total 228 mammograms were acquired (38 images per phantom).

The images were evaluated perceptually and mathematically. In the perceptual experiment, a 2AFC method was utilised using a bespoke software (Blindell & Hogg, 2012). A 5-point Likert scale (1=much worse, 2=worse, 3=equal, 4=better, 5=much better) was used to score the images. The criteria for visual perception included lesion visibility, sharpness, contrast, noise and size of the lesion.

Since image quality in mammography is affected by sharpness, contrast and noise ((Rajendran, Krishnapillai, Tamanang, & Chelliah, 2012), these criteria were added to the visual perception of this research. Generally unsharpness or blurring in the image limits the visibility of the details. Not being able to visualise the details in the breast image such as spicules of spiculated cancer lesions or microcalcifications might cause false negative or misdiagnosis. Since visualizing the shapes and margins of the lesions helps to differentiate a benign lesion from a malignant one, taking this criterion into account is valid. Similar to sharpness, a noisy image can hide the subtle lesions or fine microcalcifications; hence it is important to include noise to the criteria.

One of the challenges in mammography is to distinguish cancer lesions from glandular tissue. This differentiation becomes harder in denser breast with larger glandular tissue. Having a good contrast between breast structures facilitates the detection of cancer lesions. Therefore contrast can be considered as an appropriate criterion in mammographic visual perception studies (Smith, 2014).

One of the main purposes of this research is to assess the relationship between the lesion visibility and the breast phantom thickness, thus, it is necessary to include visibility as a criterion in visual perception studies. It is important to mention that visibility of a lesion is affected by multiple factors such as brightness, contrast, sharpness, noise and the presence of artefacts.

The size as a criterion was considered in the visual perception part of this research. This was to see if the lesion size was perceived wider due to the spreading out of the compressible PVAL lesion with the increase of the compression force.

Three observers (see 9.1.1 on page 107) with medical imaging background evaluated the lesions in 6 phantoms separately. The observers did not have to be qualified with medical imaging background since this part of the research was perceptual not cognitive. These observers wore corrective lenses as required for 2AFC. 3 datasets were collected for data analysis.

In a dimmed room (a low level of background ambient light) at Salford University, two calibrated 5 Mega-Pixel diagnostic monitors, slightly angled towards each other were utilised to evaluate the images. In order to reduce the effect of eye strain on the evaluation, the readers only evaluated one set of mammograms in maximum 30 minutes at a time for images related to a single phantom. The reader would then take a break whilst another reader would evaluate the same set of mammograms.

During the visual experiment (2AFC), each participant had to evaluate/score a set of images in a randomized order with no identifying information per phantom against a reference image. There was no information presented to observers regarding breast thickness and observers scored the images blind.

The reference images with average quality were selected prior to the commencement of the visual experiment by one experienced medical physicist and one experienced radiographer. These observers were different than the three observers who evaluated the image quality of the images. The selection was carried out by going through the images sequentially from the first acquired image to the last. The two observers were blinded to the acquisition conditions. For each phantom, one average quality image was selected from the decreased thickness set of images and one average

quality image was selected from the increased thickness set. The reason that an average quality image was selected as a reference image was to cover scores above and below the reference image, not necessarily only above or below.

The collected scores from a .tsv file were copied to an Excel file and the related graphs were plotted per criteria as a function of the change in thickness (thickness reduction). Since the raw data acquired from the 2AFC experiment were in a random order, the results needed to be sorted prior to the plotting.

In the non-perceptual analysis, four different measures were calculated and plotted. These measures were contrast-to-noise ratio (CNR), signal-to-noise ratio (SNR), Figure of Merit (FOM), and line profile (noise profile).

CNR and SNR measures are directly related to the visibility of lesions in the mammograms. This is diagnostically important for clinicians. The decrease of the CNR and SNR results in the increase of the possibility of missing features such as lesions (Smith & Webb, 2010). In order to measure CNR and SNR, homogeneous regions were first selected as region of interest (ROI) for the lesions and the backgrounds. The region of interest was measured by following a method from Bushberg et al. (Bushberg, Seibert, Leidholdt, & Boone, 2011). Then the mean grey value of the lesions/background and the standard deviation of the background (noise) were collected using ImageJ. The mean grey values of the lesions/backgrounds were used in the following equations to measure CNR and SNR (Cush, 2007):

$$CNR = \frac{meangreyvalue(lesion) - meangreyvalue(background)}{stdev(background)}$$

$$SNR = \frac{meangreyvalue(lesion)}{stdev(background)}$$

In general, Figure of Merit (FOM) as a numerical quantity is used to characterize the performance of the devices. In digital mammography, FOM is a tool which evaluates

the performance of the mammography system in terms of image quality and patient radiation dose (Acton, 2013). In order to measure the FOM, various formats and definitions have been used in mammography. One of these definitions is signal-difference-to-noise ratio (SDNR) squared per unit exposure or radiation dose (Samei, Dobbins III, Lo, & Tornai, 2005). Since the CNR is another definition for SDNR, therefore CNR squared can be used as numerator of the formula to measure FOM. Mean glandular dose (MGD), as a denominator in FOM formula is commonly used to calculate FOM.

The breast glandular tissues are more radiosensitive and at a higher risk from X-ray exposure compared to fatty tissues (International Atomic Energy Agency, 2013). Therefore, the estimation of the MGD dose (the average dose to the breast glandular tissue) as a specific mammographic radiation dose is essential (Donga, et al., 2002). MGD cannot be measured directly from the mammography procedure, but research has shown the similarity between the organ dose which is displayed on the console of the mammography unit and the measured MGD dose. MGD can also be read from the DICOM header (McCullagh, Baldelli, & Phelan, 2010).

In order to measure the MGD, the entrance surface exposure, or air kerma to the breast has to be calculated. Kinetic energy released per unit mass (kerma) is the amount of radiation energy placed in or absorbed in a unit of mass of air. In other words, air kerma is the absorbed dose in air. The unit of air kerma is J/Kg which is the radiation unit (Gy) (Sprawls, 1995).

The air kerma can be directly measured by placing small dosimeters on the breast. MGD is the product of the air kerma and the dose factors. The amount of dose factors are related to the size and composition of the breast (percentage of fat/glandular), and the characteristics of the X-ray radiation. The characteristics of the X-ray beam are defined

by the target/filter materials and the energy of the beam (Sprawls, 1995) (Dance, Skinner, Young, Beckett, & Kotre, 2000). The following formula calculates the MGD (Dance, Skinner, Young, Beckett, & Kotre, 2000).

$$MGD = K \cdot g \cdot c \cdot s$$

Where K is the entrance surface air kerma and g, c and s are conversion factors for X-ray radiation and breast characteristics.

FOM can be measured using SNR squared divided by MGD (Borg, Badr, & Royle, 2011). Regardless of the applied FOM formula, the higher values of FOM represent better imaging performance in terms of image quality at lower radiation dose.

In this research, the following equations were used to measure FOM. Radiation dose in the FOM formula was replaced with organ dose and entrance dose acquired from the mammography procedure.

$$FOM_{SNR} = \frac{SNR^2}{radiation\ dose}$$
$$FOM_{CNR} = \frac{CNR^2}{radiation\ dose}$$

Generally, line profiles demonstrate a two-dimensional graph of the pixels values (grey values) along a line within the image. Line profile graphs are able to show how sharp the edges of the objects are within the image. They also can display how noisy the images are. In this method, the line profile graphs utilizing the ImageJ software were employed in order to compare the magnitude of the noise and the sharpness of the edge of the lesions in multiple mammograms of the same phantom with various thickness reductions.

In the visual perception study, in order to evaluate the reliability of the measurements (inter-rater reliability) a specific test was carried out utilising a piece of statistical software called MedCalc. This test is referred to as intraclass correlation

coefficient (ICC). The ICC model 2 with “consistency” and “absolute agreement” types were employed to measure the reliability of the scores collected by the three observers (MedCalc , 2015).

11.5.1 Results and analysis

11.5.1.1 CT results

The following CT images with the corresponding profile graphs plotted in ImageJ (Figure 11.34, Figure 11.35, Figure 11.36, and Figure 11.37) demonstrate a lesion in a breast phantom containing two lesions and a lesion in a phantom holding one lesion respectively. Both graphs show the maximum grey value over 300.

The lesions in the CT images look sharp and visible with high contrast. As was mentioned in 10.2.4.8 on page 163, the grey values demonstrate the HU of the lesions in the DICOM files imported to ImageJ.

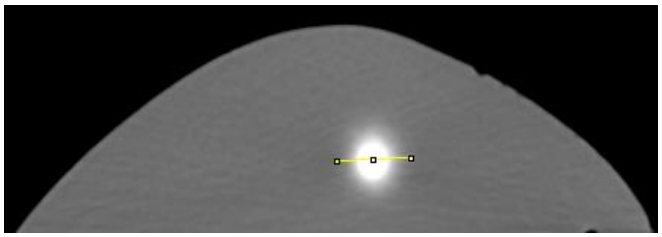

Figure 11.34 CT scan of a lesion in a two-lesion phantom (WL=0, WW=300)

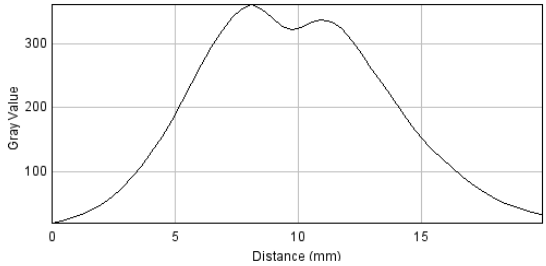

Figure 11.35 Profile plot of a lesion in a two-lesion phantom

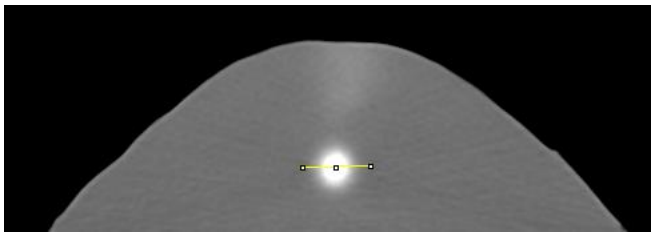

Figure 11.36 CT scan of a lesion in a one-lesion phantom (WL=0, WW=300)

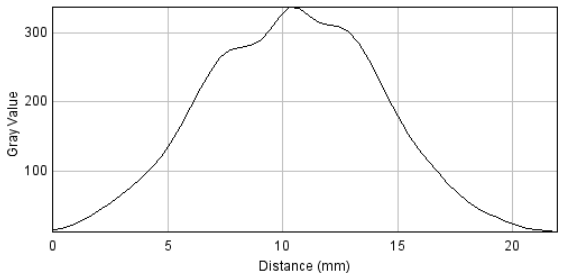

Figure 11.37 Plot profile of a lesion in a one-lesion phantom

11.5.1.2 Mammography results

The following mammograms (Figure 11.38) demonstrate the fabricated lesions compared to a real breast mass. As the images show, the visible phantom lesions (left) and the breast lesion (right) all resemble each other. While The PVAL phantom has a homogenous texture compared to the real breast.

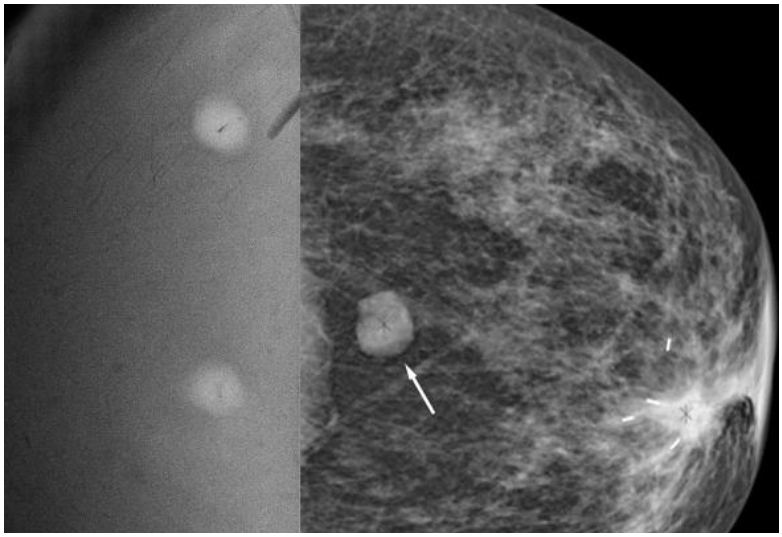

Figure 11.38 Left: Embedded lesions in PVAL phantom. Right: Craniocaudal mammogram of the left breast (Harish, Konda, MacMahon, & Newstead, 2007)

The data acquired from the mammography of 6 phantoms are demonstrated in Appendix F. The following table (Table 11.8) as a sample mammographic data demonstrates thickness of the breast, force, kVp, mAs, Target/Filter, organ dose and entrance dose.

Breast phantom: 5% PVAL, 2 FTCs Lesion(s): One lesion, 10% PVAL, 5 ml CA, 6FTCs Paddle size: 18x24						
Thickness (cm)	Force (N)	KvP	mAs	Filter	Organ dose (mGy)	Entrance dose (mGy)
9.0	--------	34	205.9	Rh	6.24	35.00
8.8	--------	33	258.4	Rh	7.23	40.00
8.6	--------	33	254.3	Rh	7.23	39.10
8.4	--------	33	238.4	Rh	6.88	36.40
8.2	45	33	219.1	Rh	6.41	33.20
8.0	50	33	211.0	Rh	6.25	31.80
7.8	54	32	260.8	Rh	7.11	35.70
7.6	53	32	235.0	Rh	6.51	31.90
7.4	60	32	223.6	Rh	6.29	30.10
7.2	64	32	211.4	Rh	6.03	28.30
7.0	71	32	202.3	Rh	5.85	26.90
6.8	75	32	198.7	Rh	5.86	26.20
6.6	81	32	185.1	Rh	5.57	24.30
6.4	87	31	226.8	Rh	6.25	26.90
6.2	92	31	206.6	Rh	5.78	24.30
6.0	100	31	198.9	Rh	5.65	23.20
5.8	104	30	228.4	Rh	5.90	23.90
5.6	113	30	213.2	Rh	5.62	22.20
5.4	120	29	244.7	Mo	7.59	36.60
5.2	127	29	225.7	Mo	7.11	33.50
5.0	138	29	212.3	Mo	6.79	31.30
4.8	145	28	268.1	Mo	7.73	35.40
4.6	157	28	247.1	Mo	7.27	32.40
4.4	171	27	327.0	Mo	8.60	38.20
4.2	182	27	269.1	Mo	8.00	34.40
4.0	196	27	280.0	Mo	7.75	32.30
3.8	207	26	352.5	Mo	8.80	36.00
3.6	217	26	318.5	Mo	8.24	32.30

Table 11.8 Acquired data from the mammography procedure of the compressed phantom

Since the purpose of this research is to find the relationship between the breast thickness and the visibility of the lesion, recording the breast thickness was crucial. Organ/entrance dose were gathered in order to measure the figure of merit (FOM). Mo was the target through the entire mammography procedure, but the filter altered between

Rh to Mo, depending on kVp, therefore recording the automatically selected filter was important to see the effect on radiation dose and image quality, thereby representing clinical reality.

The force below 45 N was not recorded by the mammography unit. Therefore all the graphs were plotted based on the thickness of phantom not the force. The initial compressed phantom was 9 cm and before each exposure, the phantom was manually compressed by 2 mm. The last image was taken with a phantom thickness of 3.6 cm. This equates to a 5.4 cm reduction of thickness from the starting point.

The following data (Table 11.9) shows the effect of compression on the mammograms as the compression on the breast was reduced from maximum compression (minimum breast thickness) down to minimum compression (maximum breast thickness). In this set, the first image is taken with a breast phantom thickness of 4 cm. Successive images were taken each time reducing compression and increasing thickness of the phantom by 4 mm per exposure. It is worth mentioning that, in the following graphs, ‘inc’ and ‘dec’ in the “chart title” refer to the increase of compression (decrease of the thickness) and decrease of the compression (increase of the thickness) respectively.

Breast phantom: 5% PVAL, 2 FTCs Lesion(s): One lesion, 10% PVAL, 5 ml CA, 6FTCs Paddle size: 18x24						
Thickness (cm)	Force (N)	KvP	mAs	Target/Filter	Organ dose (mGy)	Entrance dose (mGy)
3.6	**217**	**26**	**318.5**	**Mo**	**8.24**	**32.30**
4.0	**153**	**27**	**241.5**	**Mo**	**6.68**	**27.90**
4.4	**117**	**27**	**271.0**	**Mo**	**7.13**	**31.70**
4.8	**96**	**28**	**228.4**	**Mo**	**6.59**	**30.20**
5.2	**78**	**29**	**184.1**	**Mo**	**5.80**	**27.30**
5.6	**64**	**30**	**171.0**	**Rh**	**4.51**	**17.80**
6.0	**48**	**31**	**154.8**	**Rh**	**4.40**	**18.10**
6.4	--------	**31**	**176.6**	**Rh**	**4.88**	**20.90**
6.8	--------	**32**	**151.7**	**Rh**	**4.48**	**20.00**
7.2	--------	**32**	**171.7**	**Rh**	**4.90**	**23.00**
7.6	--------	**32**	**190.4**	**Rh**	**5.28**	**25.90**
8.0	--------	**33**	**167.5**	**Rh**	**4.97**	**25.20**
8.4	--------	**33**	**181.0**	**Rh**	**5.26**	**27.50**
8.8	--------	**33**	**193.3**	**Rh**	**5.45**	**29.80**
9.2	--------	**34**	**160.7**	**Rh**	**4.81**	**27.50**

Table 11.9 Acquired data from the mammography procedure of the compressed phantom during the reduction of the compression

As the following graphs (Figure 11.39 and Figure 11.40) show, the breast phantom thickness changes corresponding to the applied compression force.

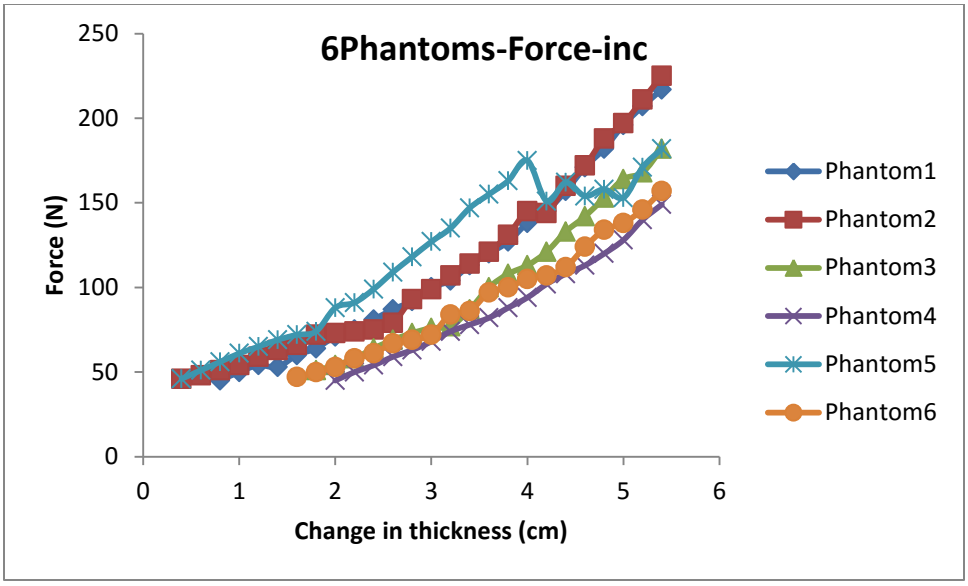

Figure 11.39 Force vs. change in thickness - decreasing thickness

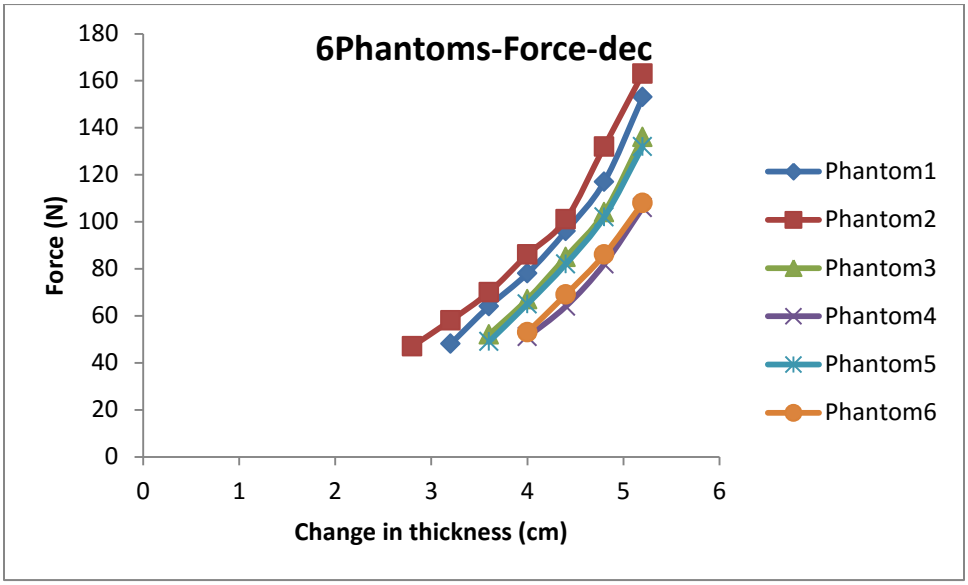

Figure 11.40 Force vs. change in thickness - increasing thickness

In Figure 11.39 the mammography unit was unable to record compression forces less than certain compressions (for example 45 N for phantom1). Therefore, there is a lack of data in phantom thicknesses for compression forces less than this value. This is more noticeable in the second graph (Figure 11.40).

The following entrance and organ dose graphs (Figure 11.41 to Figure 11.44) were directly recorded from the mammographic data (Table 11.8 and Table 11.9).

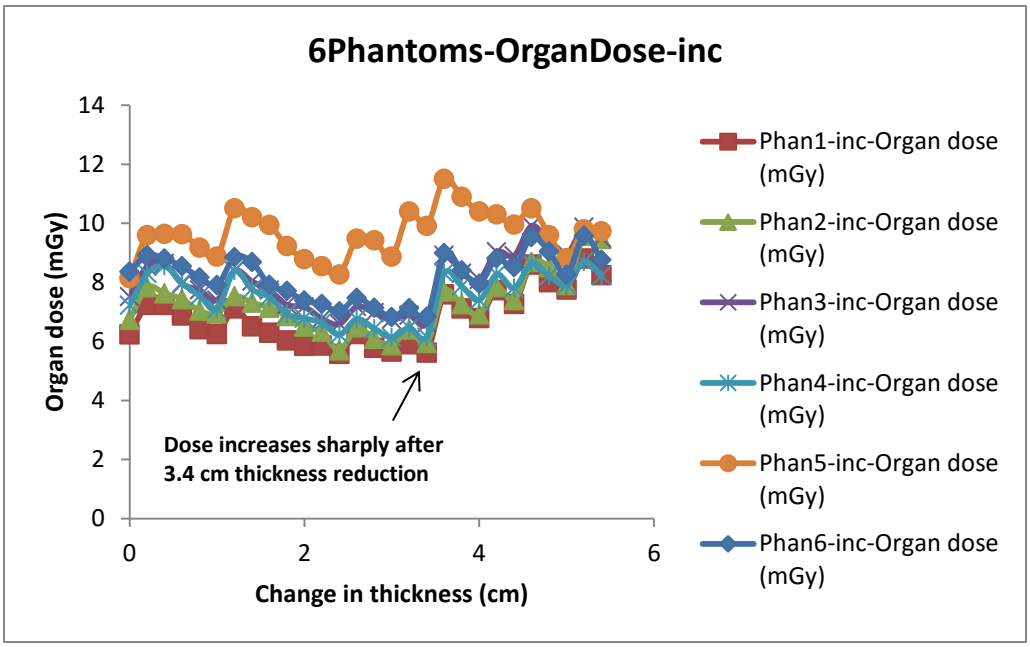

Figure 11.41 Organ dose vs. change in thickness - decreasing thickness

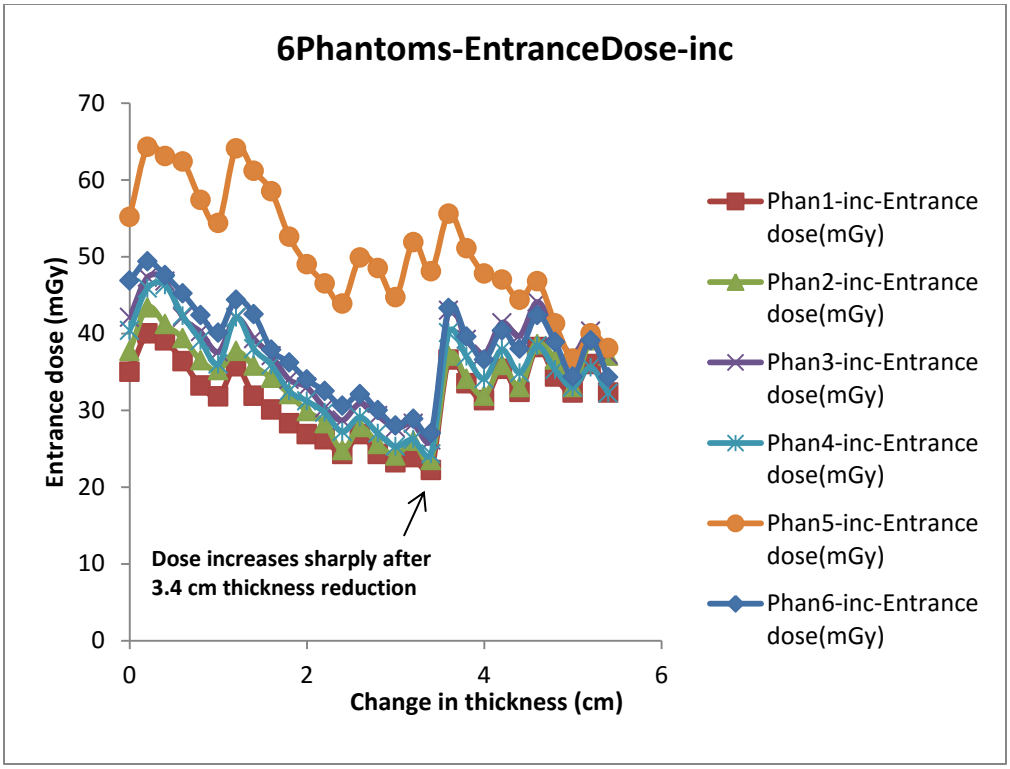

Figure 11.42 Entrance dose vs. change in thickness - decreasing thickness

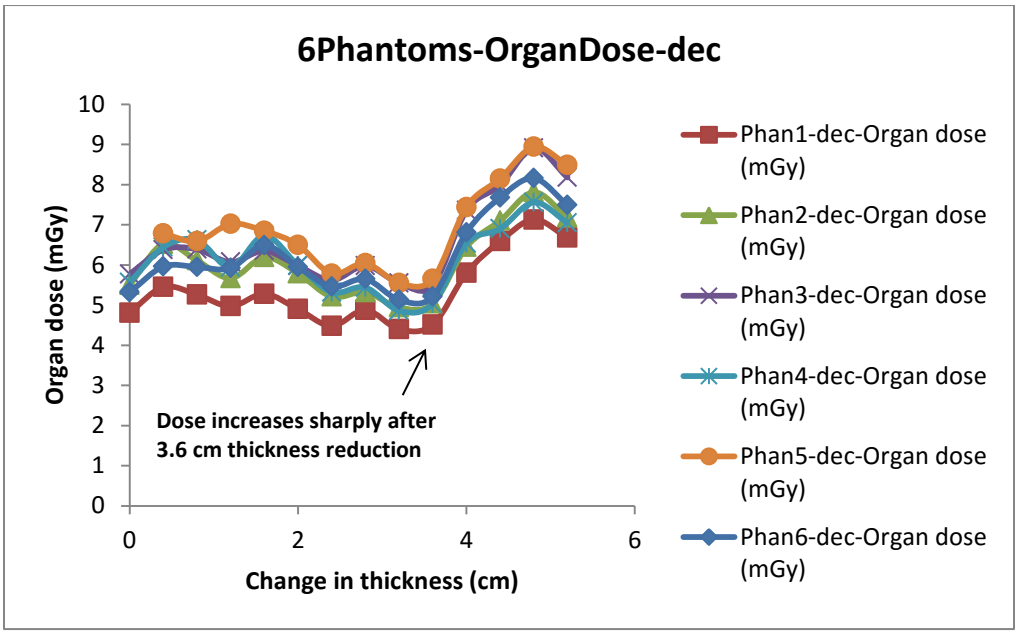

Figure 11.43 Organ dose vs. change in thickness - increasing thickness

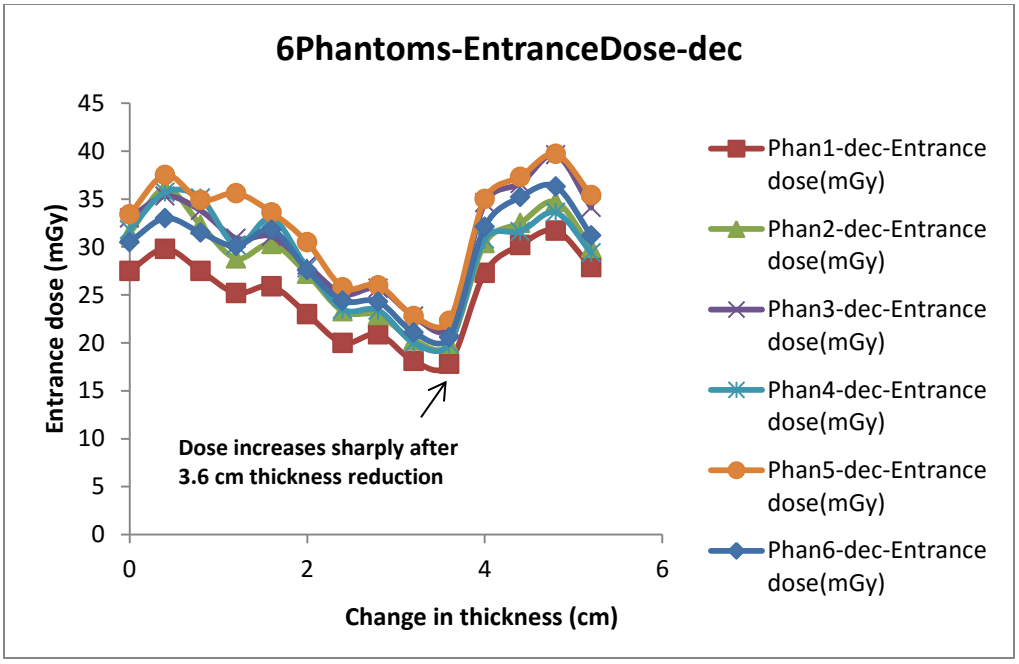

Figure 11.44 Entrance dose vs. change in thickness - increasing thickness

The size and density of the breast tissue have direct impact on the radiation dose (International Atomic Energy Agency, 2013). This means that higher radiation dose or more photons are required for the bigger size and denser breasts to penetrate through and reach the detector. The phantom graphs have shown this relationship up to the point that the filter is changed (Table 11.8 and Table 11.9). The graphs above show the radiation dose decrease until 3.4 cm of thickness reduction in both organ dose and entrance dose.

As was expected, the decrease in the thickness requires fewer photons to pass through the breast phantom. Hence, the organ dose and the entrance dose decrease until the 3.4 cm reduction of thickness. At this point the filter was changed from Rh to Mo. The kVp dropped to 29 from 30 and mAs increased up to 48.3 in order to compensate the decrease of photon energy. The big increase of mAs caused the increase in radiation dose after 3.4 cm of thickness reduction.

Phantoms 5 in the above graphs (Figure 11.41 and Figure 11.42) shows higher radiation dose. This is due to the lack of utilisation of the Rh filter through the mammography during the increased compression. This problem was automatically resolved during mammography with the decreased compression (Figure 11.43 and Figure 11.44).

The following graphs (Figure 11.45 and Figure 11.46) show the average organ/entrance dose for 6 phantoms for both increased and decreased compression.

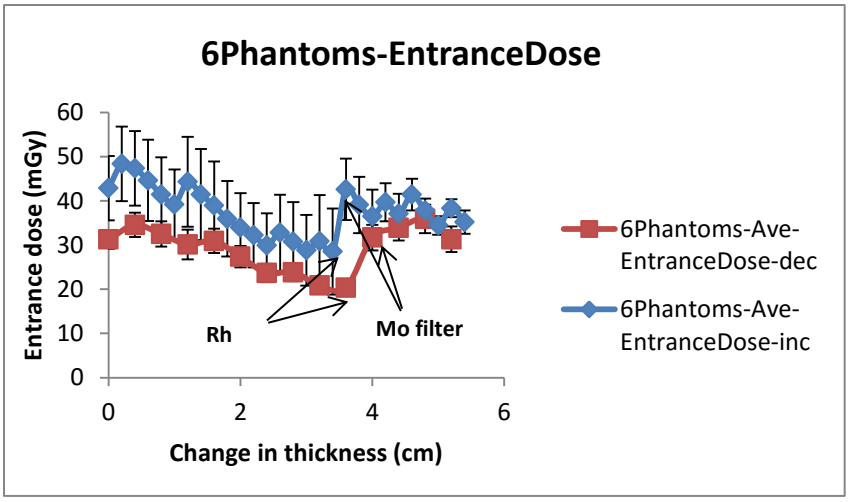

Figure 11.45 Entrance dose for 6 phantoms

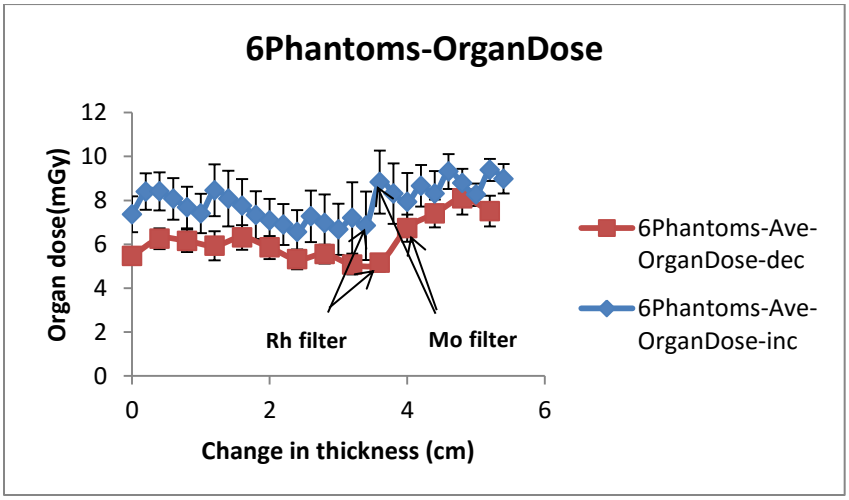

Figure 11.46 Organ dose for 6 phantoms

The ‘inc’ series show the radiation dose increase after 3.4 cm of thickness reduction and the ‘dec’ series demonstrates the radiation dose increase after 3.6 cm of thickness reduction. The increase of the entrance dose is 14.08 mGy from 3.4 to 3.6 cm thickness reduction (inc) and 11.34 mGy from 3.6 to 4 cm thickness reduction (dec). The increase of organ dose shows as 1.99 mGy from 3.4 to 3.6 cm thickness reduction (inc) and 1.58 mGy from 3.6 to 4 cm thickness reduction (dec). The organ dose ranged from 6.56-9.38 mGy in decreased thickness (inc) and 5.07-8.08 mGy in increased thickness (dec) for 3.6-9 cm phantom thickness. Based on European Guidelines, mean glandular dose (MGD) ranged from 1.5-6.5 mGy for 3-7cm PMMA thickness (Perry, Broeders, De Wolf, Törnberg, Holland, & Von Karsa, 2013).

As the thickness of the breast phantom decreases, the amount of photon energy required to penetrate through the breast phantom decreases. Therefore the filter changes automatically from Rh to Mo. At the point where the filter changes from Rh to Mo, the mAs increases. This is the point which kVp drops from 30 to 29.

The following graphs (Figure 11.47 to Figure 11.49) show the relationship between the kVp and mAs in relation to the thickness reduction.

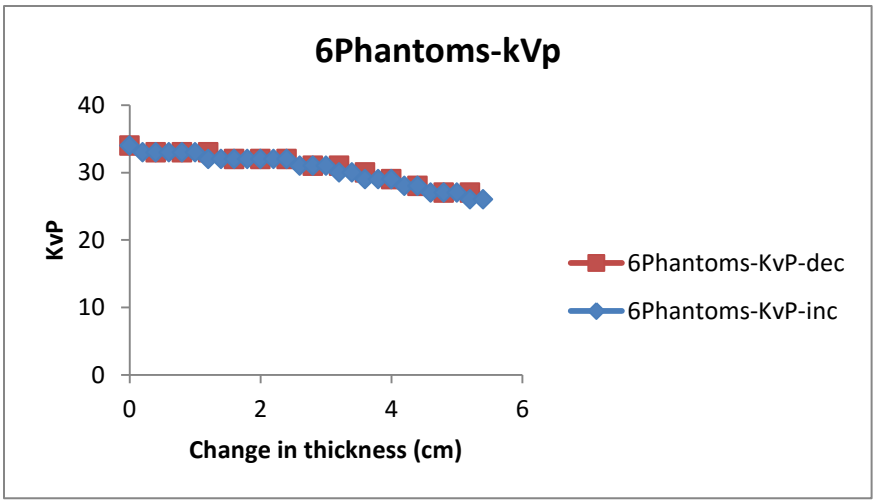

Figure 11.47 Mammographic kVp vs. change in thickness for 6 phantoms

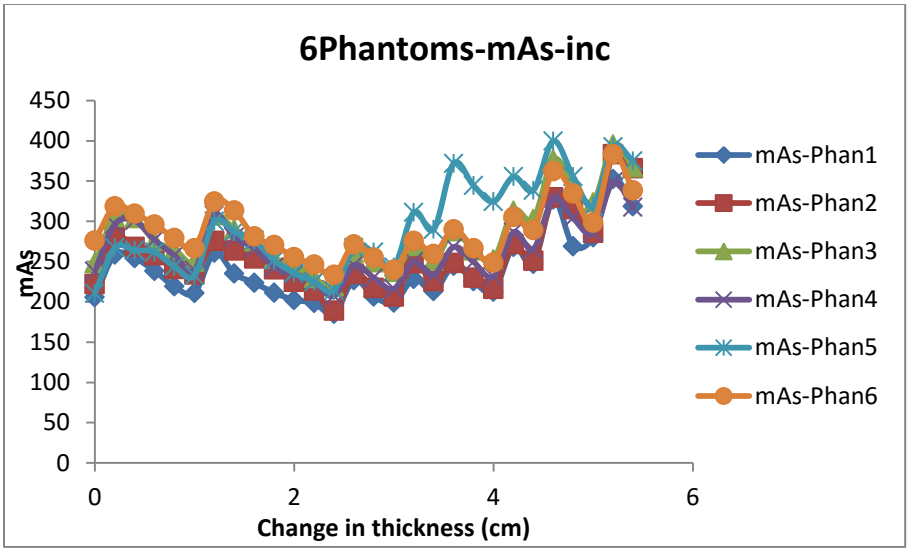

Figure 11.48 Mammographic mAs vs. change in thickness for 6 phantoms - decreasing thickness

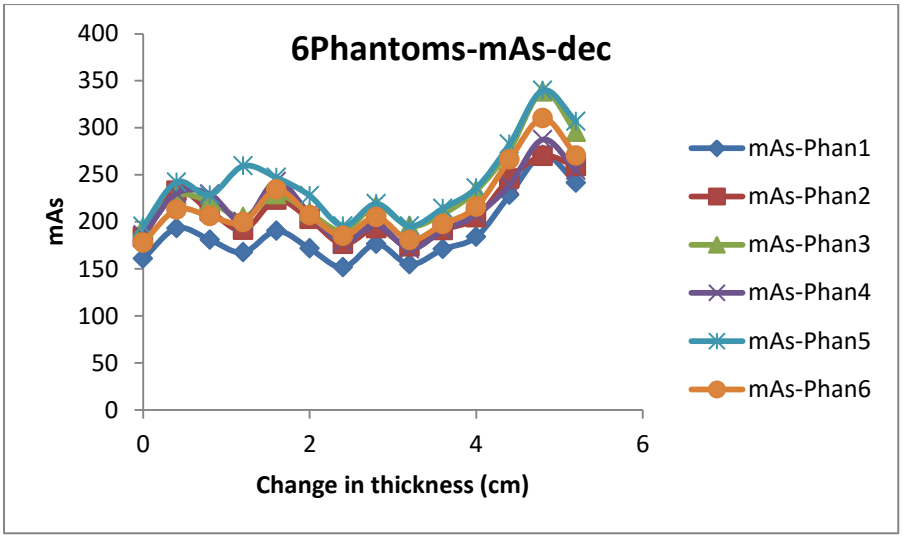

Figure 11.49 Mammographic mAs vs. change in thickness for 6 phantoms - increasing thickness

The above graphs display the increase of mAs with the decrease of kVp. It also shows that when the kVp stayed constant, the mAs was reduced due to the thickness reduction.

Generally, the range of kVp in mammography varies from 22 to 32. However, this can be varied among different system manufacturers. Higher ranged kVp has been used

in more modern mammographic systems (Sechopoulos, 2014). Typically mammographic tube currents are between 80 to 200 mA. The exposure time varies between 1 to 4 seconds depending on the type of the breast (Huda & Slone, 2007). For example for a 3-second exposure time with the mA of 80, the calculated mAs would be 240. In this experiment, the employed kVp (26-34) and mAs (151.7-399.8) are clinically appropriate.

As was discussed above, the maximum radiation dose reduction occurred at 3.4 cm and 3.6 cm of thickness reduction in increase and decrease experiments respectively. In the increased compression experiment, the average mAs at 3.4 cm thickness reduction was 245.38 and in the decreased compression experiment, the average mAs at 3.6 cm thickness reduction was 195.61. The data for the following graphs (Figure 11.51 to Figure 11.53) were acquired from the mammograms of the 6 phantoms in ImageJ in order to measure CNR and SNR. CNR and SNR are measures used in medical imaging to quantify the quality of the images. These numbers show the ratio of contrast to noise and signal to noise. CNR and SNR were used to calculate the figure of merit based on organ dose and entrance dose.

Mean grey value of the lesion, background and the standard deviation of the background were used to measure the SNR and CNR. The ROI for the lesion was a circle inside a homogenous area of the lesion and the ROI for the background was the nearby homogenous area around the lesion (Figure 11.50). The mean grey value of the lesion and background were plotted against the thickness. The standard deviation of the background (noise) was plotted against the thickness. These plots show the variations of the background noise and grey values against the thickness of phantoms.

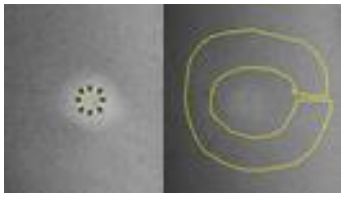

Figure 11.50 Left: ROI for the lesion. Right: ROI for the background

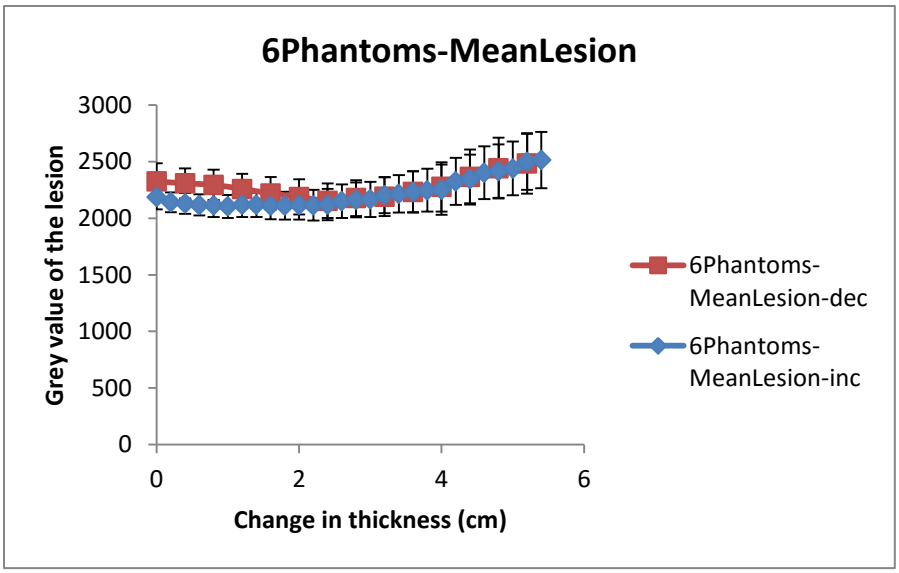

Figure 11.51 Grey value of the lesion vs. change in thickness for 6 phantoms

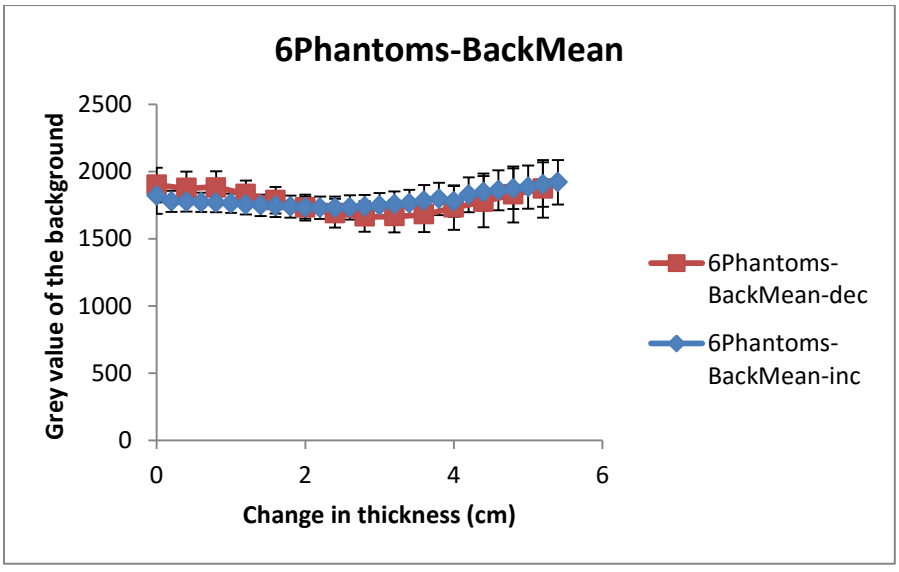

Figure 11.52 Mean grey value of the background vs. change in thickness for 6 phantoms

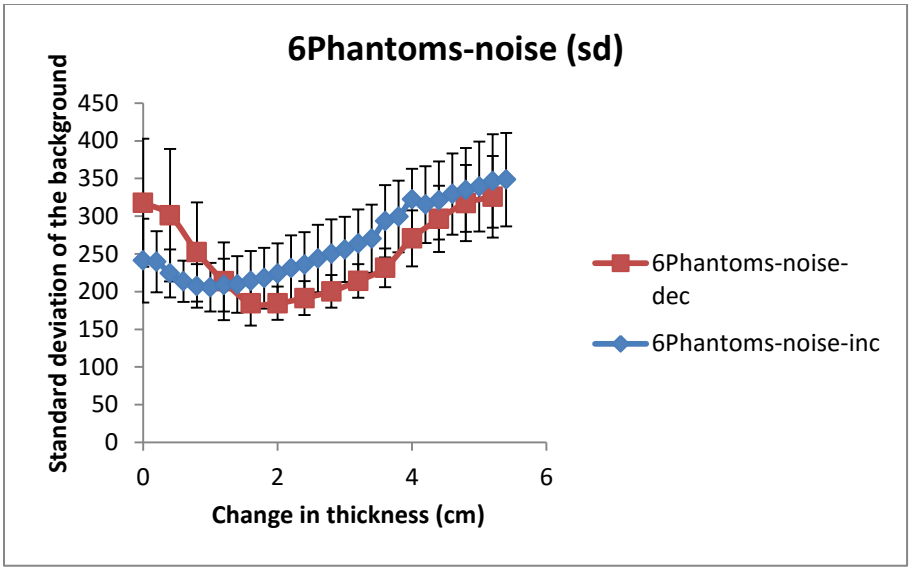

Figure 11.53 Standard deviation of the background or noise vs. change in thickness for 6phantoms

The mean grey value of the lesion and the background show the decrease followed by the increase in the grey value. A similar pattern is observed for the noise or standard deviation of the background. The minimum and maximum noise for the increased compression phantoms were at 1 cm and 5.4 cm of thickness reduction. The minimum and maximum noise for the decreased compression phantoms were at 1.6 cm and 5.2 cm of thickness reduction.

11.5.1.3 2AFC results

The data below (Table 11.10) was collected in order to accomplish the visual perception experiment using 2AFC. The following table shows the sum of image quality criteria per participant. The criteria used in this examination were Image noise, visibility of the lesion, sharpness of the edge, contrast between the lesion and the adjacent background and the lesion size. In order to provide an adequate dataset for analysis, 3 sets of scores per phantom with three participants were collected and averaged.

thickness (mm)	Image noise	Visibility	Sharpness	Contrast	Size	SUM-IQ
9.0	2	2	2	2	3	8
8.8	3	2	2	2	2	9
8.6	3	2	2	2	2	9
8.4	3	1	2	2	3	8
8.2	3	2	2	2	2	9
8.0	3	2	2	3	3	10
7.8	3	3	3	3	3	12
7.6	4	4	3	3	4	14
7.4	3	3	3	3	3	12
7.2	2	3	3	3	3	11
7.0	4	4	4	4	3	16
6.8	3	3	3	3	3	12
6.6	4	4	4	4	3	16
6.4	3	4	3	4	3	14
6.2	3	4	4	4	4	15
6.0	3	4	4	4	4	15
5.8	2	4	5	4	5	15
5.6	3	4	4	4	3	15
5.4	3	4	4	3	3	14
5.2	3	3	3	4	3	13
5.0	3	3	4	3	3	13
4.8	3	4	4	4	3	15
4.6	4	4	4	4	3	16
4.4	4	4	4	4	4	16
4.2	4	4	4	4	3	16
4.0	3	5	4	5	4	17
3.8	5	5	5	5	5	20
3.6	4	5	4	5	4	18

Table 11.10 An example of measuring the image quality per participant.

The average score of the participants per criteria for each phantom (Table 11.11) and the average of the averages for multiple phantoms (Table 11.12) were calculated and plotted versus the change in thickness. The standard deviation of the participants for each phantom and average score of multiple phantoms were calculated and added to the graphs. The low standard deviations indicate that the scores from the readers were close to each other.

The average scores for the 6phantoms, 3phantoms with one lesion and three phantoms with two lesions were calculated and plotted separately (Appendix G). The

graphs for the phantoms with 2 lesions were classified into top and bottom lesions. In the collected mammograms the lesions which were closer to the detector show on top and the lesions farther from the detector show below the top lesions. Because of this in the graphs, the lesions were labelled as top and bottom. The 6phantom graphs are based on the average scores of three phantoms with one lesion, three phantoms with the top lesion and three phantoms with the bottom lesion.

Change in Thickness (mm)	contrast-R1	contrast-R2	contrast-R3	Phan1-contrast-inc	stdev
0.0	2	2	1	1.66	0.57
0.2	2	2	2	2.00	0.00
0.4	2	2	1	1.66	0.57
0.6	2	2	2	2.00	0.00
0.8	2	2	3	2.33	0.57
1.0	2	3	2	2.33	0.57
1.2	3	3	3	3.00	0.00
1.4	4	3	3	3.33	0.57
1.6	4	3	3	3.33	0.57
1.8	4	3	3	3.33	0.57
2.0	4	4	5	4.33	0.57
2.2	4	3	3	3.33	0.57
2.4	4	4	3	3.66	0.57
2.6	4	4	3	3.66	0.57
2.8	4	4	3	3.66	0.57
3.0	4	4	4	4.00	0.00
3.2	4	4	4	4.00	0.00
3.4	4	4	4	4.00	0.00
3.6	4	3	3	3.33	0.57
3.8	4	4	3	3.66	0.57
4.0	4	3	3	3.33	0.57
4.2	4	4	4	4.00	0.00
4.4	4	4	4	4.00	0.00
4.6	4	4	4	4.00	0.00
4.8	4	4	4	4.00	0.00
5.0	4	5	4	4.33	0.57
5.2	4	5	4	4.33	0.57
5.4	4	5	4	4.33	0.57

Table 11.11 Example of calculation of average of contrast scored by 3 separate readings (R1, R2 and R3 were visual perception participants/readers)

Change in Thickness (mm)	Phan1-contrast-inc	Phan2-contrast-inc	Phan3-contrast-inc	Phantoms 123-Ave-inc-Contrast	Std
0.0	1.66	1.66	1.00	1.44	0.38
0.2	2.00	1.66	1.33	1.66	0.33
0.4	1.66	2.33	1.33	1.77	0.50
0.6	2.00	2.00	2.00	2.00	0.00
0.8	2.33	2.33	1.66	2.11	0.38
1.0	2.33	2.00	1.66	2.00	0.33
1.2	3.00	2.33	2.00	2.44	0.50
1.4	3.33	2.33	2.00	2.55	0.69
1.6	3.33	2.33	2.00	2.55	0.69
1.8	3.33	2.33	2.66	2.77	0.50
2.0	4.33	2.66	2.33	3.11	1.07
2.2	3.33	2.33	2.33	2.66	0.57
2.4	3.66	2.33	2.33	2.77	0.76
2.6	3.66	3.00	3.00	3.22	0.38
2.8	3.66	3.00	2.33	3.00	0.66
3.0	4.00	2.66	2.66	3.11	0.76
3.2	4.00	2.66	2.66	3.11	0.76
3.4	4.00	3.33	3.00	3.44	0.50
3.6	3.33	2.33	3.00	2.88	0.50
3.8	3.66	3.66	2.66	3.33	0.57
4.0	3.33	3.33	2.66	3.11	0.38
4.2	4.00	3.33	3.00	3.44	0.50
4.4	4.00	3.66	4.00	3.88	0.19
4.6	4.00	4.00	4.00	4.00	0.00
4.8	4.00	4.00	4.00	4.00	0.00
5.0	4.33	4.00	4.00	4.11	0.19
5.2	4.33	4.33	4.00	4.22	0.19
5.4	4.33	4.66	4.66	4.55	0.19

Table 11.12 Example of average contrast of three phantoms (Ave=Average)

The following graphs (Figure 11.54 to Figure 11.59) display all the image quality graphs in relation to the reduction of the breast phantom thickness. These graphs are the results of the visual perception method.

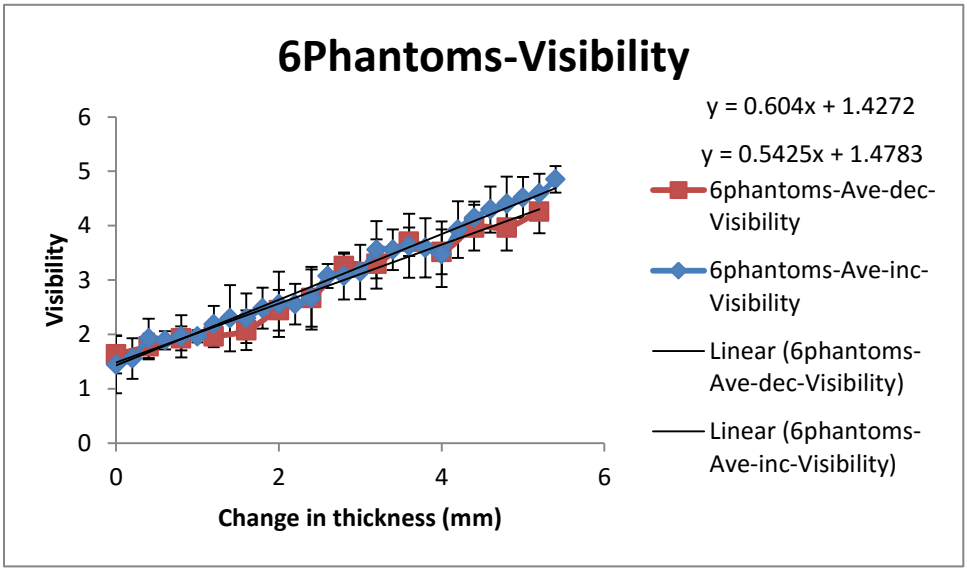

Figure 11.54 Average visibility of the lesions for 6 phantoms

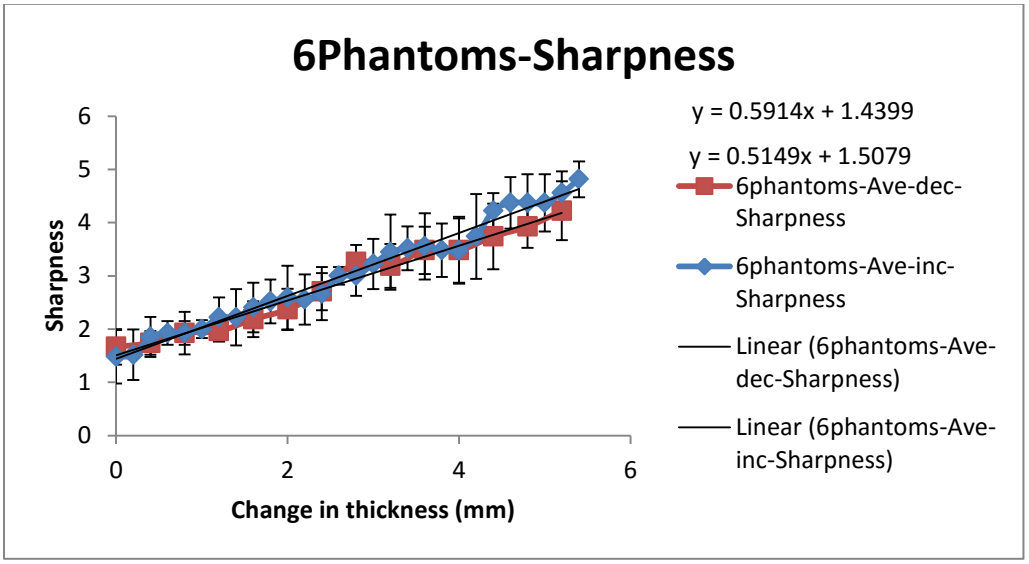

Figure 11.55 Average sharpness of the lesions for 6 phantoms

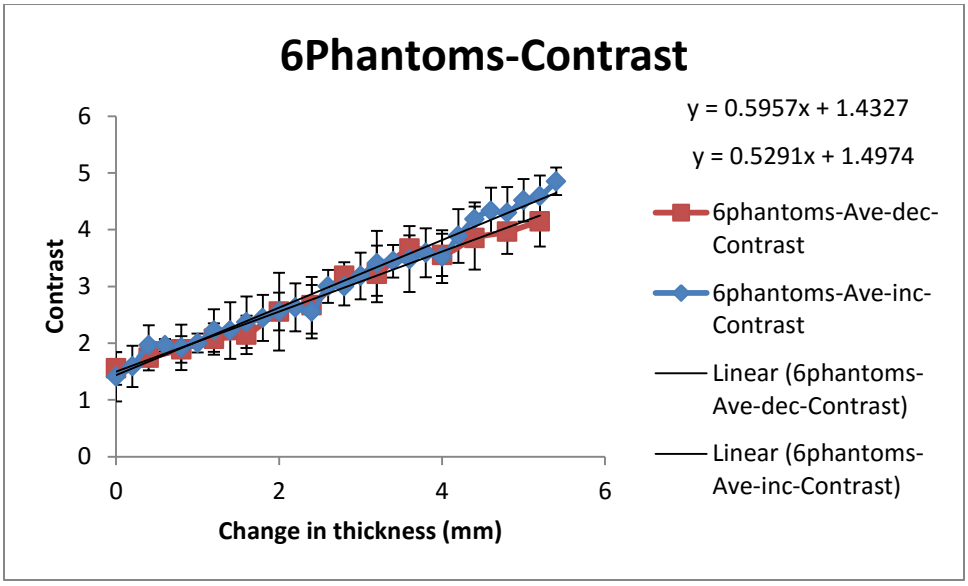

Figure 11.56 Average contrast of the lesions for 6 phantoms

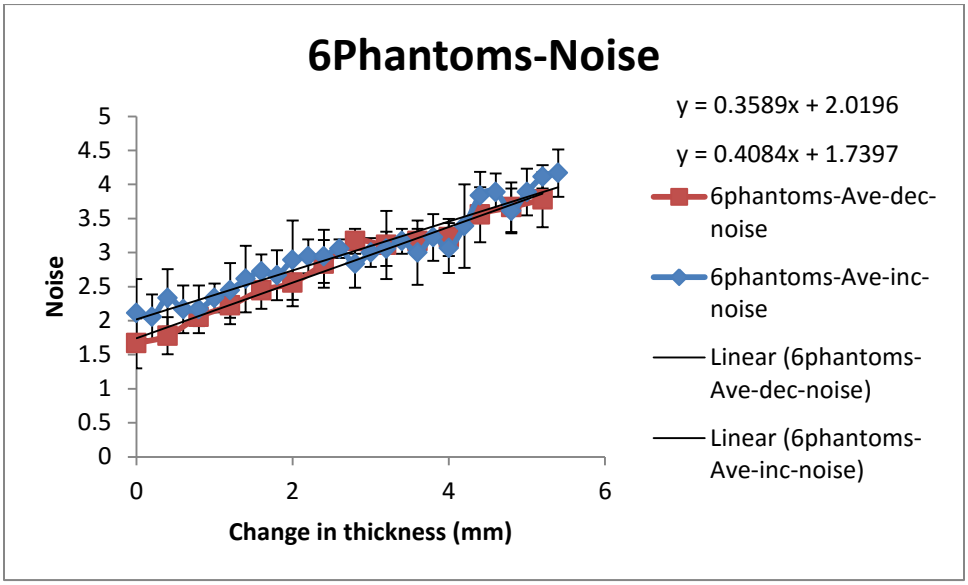

Figure 11.57 Average noise for 6 phantoms

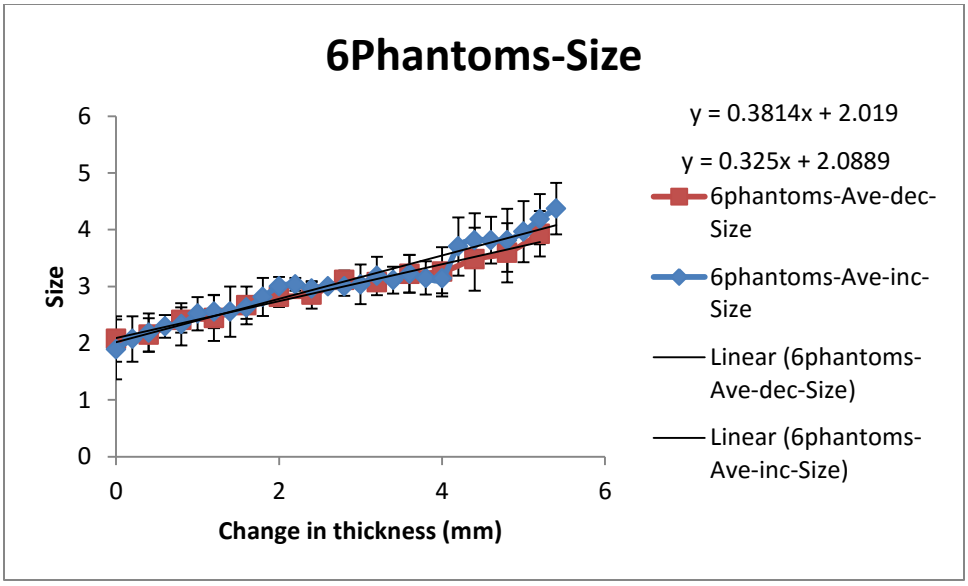

Figure 11.58 Average size of the lesions for 6 phantoms

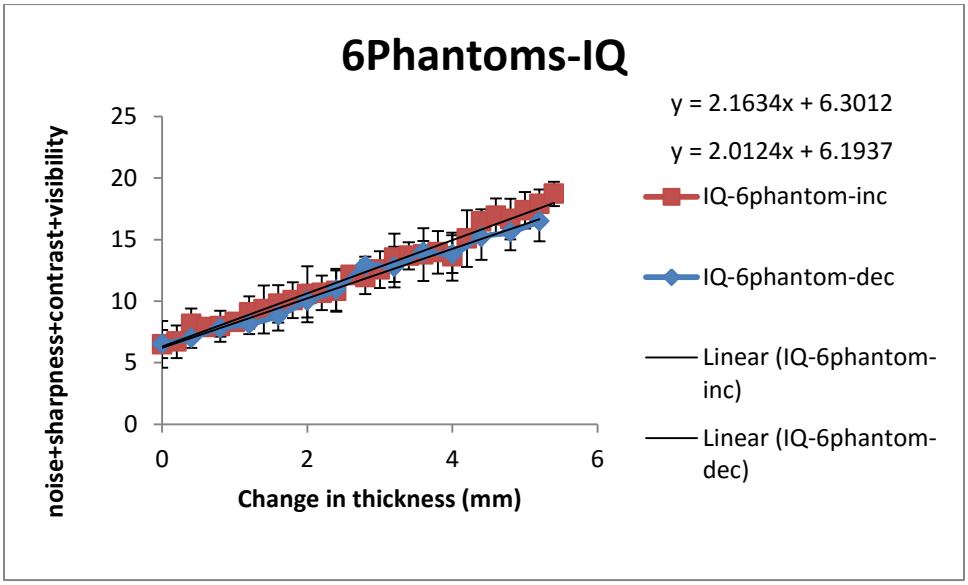

Figure 11.59 Average Image Quality (IQ) for 6 phantoms

Each of the criteria in the 2AFC measures, visibility, sharpness, contrast, noise, and size, improved with a decrease in thickness linearly. The minimum visibility was with the initial thickness and the maximum visibility was with 5.4 cm thickness reduction. The perceived size of the lesion increased with a decrease in thickness

(Figure 11.58). This means that the largest size for the lesion was observed when the phantom thickness was at a minimum.

Figure 11.59 shows the overall image quality score which was the average of summation of visibility, sharpness, contrast, and noise for all 6 phantoms. This means that first the summation of visibility, sharpness, contrast, and noise per phantom for each thickness (IQ_i) was calculated and then the average ($\frac{\sum_1^6 IQ_i}{6}$) for 6 phantoms was calculated and displayed in the graph (Figure 11.59). Since size was affected by the image quality parameters, it was excluded from the calculation of the image quality (IQ).

Note: Appendix G displays all the related image quality score graphs.

Phantoms	Min image quality score-inc	Max image quality score-inc	Min image quality score - dec	Max image quality score - dec
6Phantoms	**6.48**	**18.70**	**6.51**	**16.48**
Phantoms123	**6.77**	**17.66**	**6.33**	**14.66**
Phantoms456-TopLesion	**6.44**	**19.22**	**6.88**	**17.33**
Phantom6456-BottomLesion	**6.22**	**19.22**	**6.22**	**17.44**

Table 11.13 Min/Max image quality (IQ) scores

As Figure 11.59 shows, the increase in image quality (IQ) increases linearly with the decrease in phantom thickness. Comparison of the minimum and maximum IQ values in Table 11.13 shows the maximum image quality is roughly 3 times higher than the minimum.

11.5.1.4 Plot profile results

The following graphs (Figure 11.60) were acquired from ImageJ in order to see the profile of the phantom and lesion per compression force. The profile helps see the magnitude of the background noise of the lesion. It also shows the sharpness of the lesion related to the phantom thickness.

A horizontal straight line was drawn through the entire phantom including the lesion. The latex skin was excluded from the measurement since the main purpose of using latex skin was to hold the phantom attached to the wooden torso and to keep the phantom hydrated.

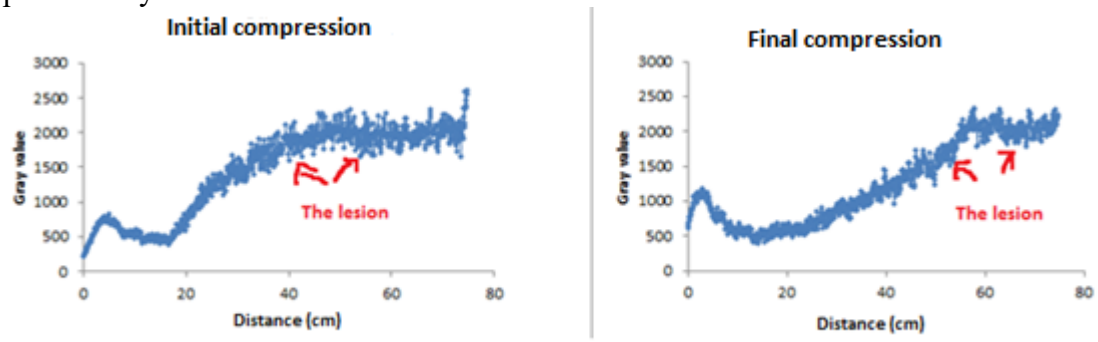

Figure 11.60 Lesion - background profile. Left: Initial compression. Right: Final compression of breast phantom

The magnitude of the noise drops from the initial thickness reduction to the final thickness reduction. The edge of the lesion also looks sharper for the reduced thickness phantom. This analysis has been repeated three times for both increase and decrease of the compression force in three phantoms with one embedded lesion. All the results unanimously have proved the improvement of the edge sharpness with the increase of compression force. It is also noticeable that the noise magnitude is higher around the chest wall which is the thicker part of the phantom compared to the nipple area which is thinner. The thicker part of the phantom causes more scattering of the X-ray beam than the thinner part, so the higher amount of noise shows in that area.

11.5.1.5 CNR, SNR, and FOM results

The following graphs (Figure 11.61 to Figure 11.64) Show the relationship between CNR and the thickness reduction. The CNR graphs demonstrate improvement of

image quality up to 3.4 cm and 3.6 cm of thickness reduction for the increased and decreased compression phantoms respectively.

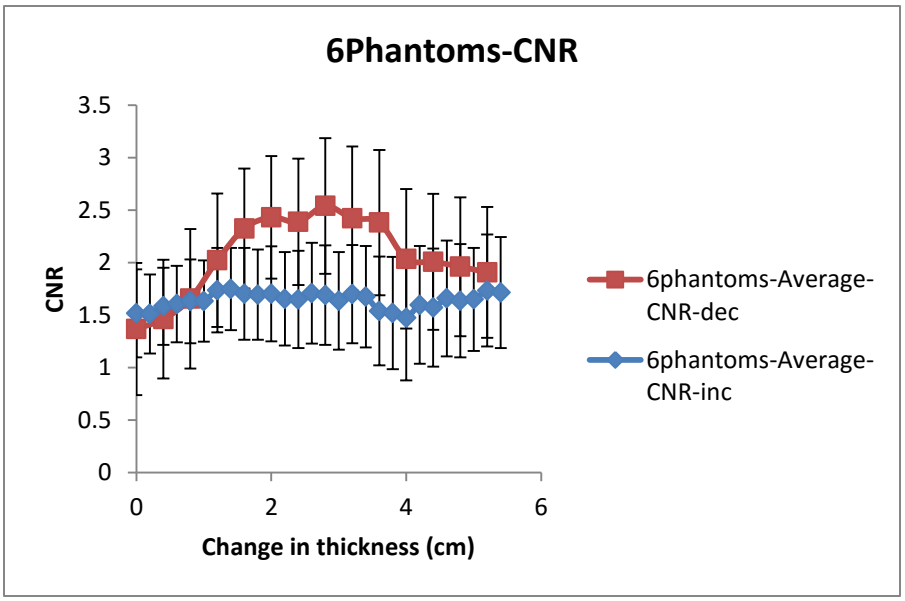

Figure 11.61 Average CNR for 6 phantoms

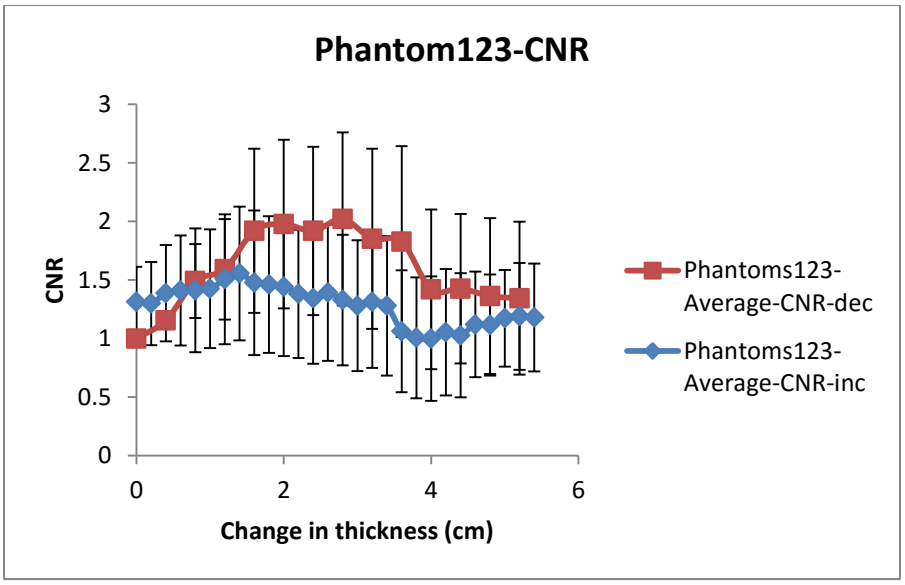

Figure 11.62 Average CNR for phantoms 1, 2 and 3

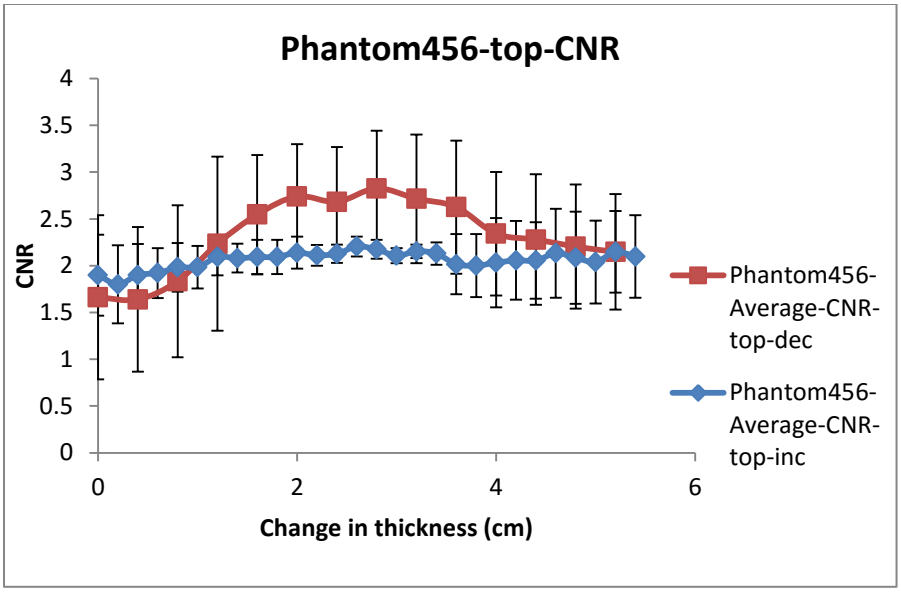

Figure 11.63 Average CNR for the top lesions of phantoms 4, 5 and 6

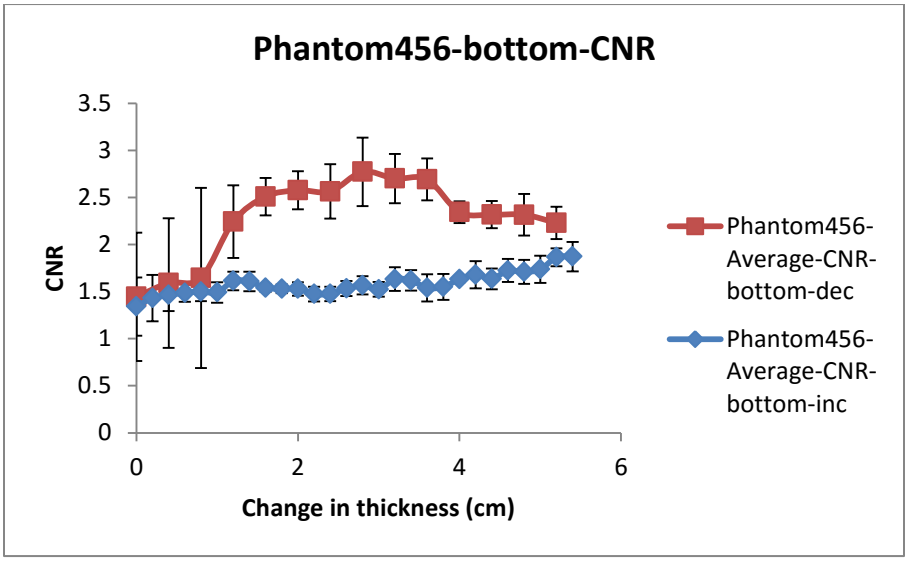

Figure 11.64 Average CNR for the bottom lesions of phantoms 4, 5 and 6

The following graphs (Figure 11.65 to Figure 11.68) show the relationship between SNR and the thickness reduction.

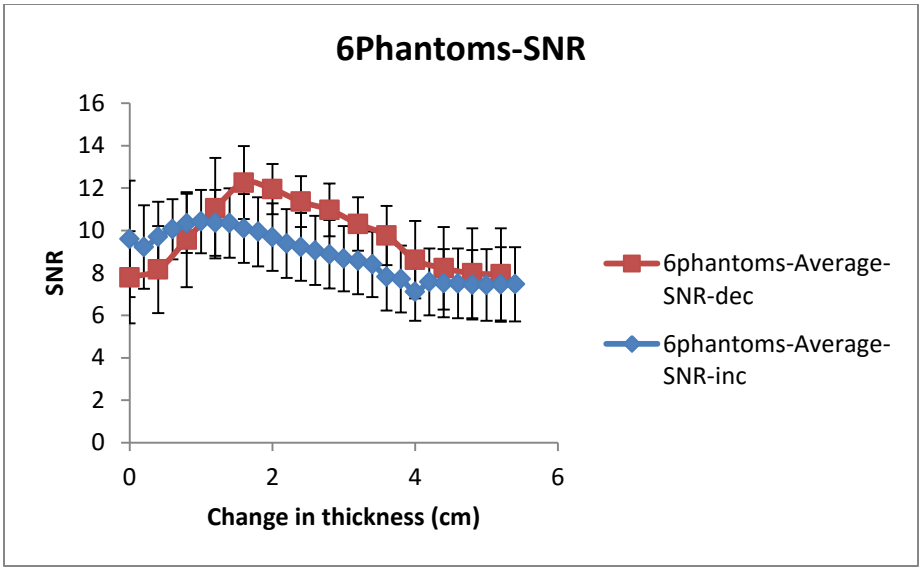

Figure 11.65 Average SNR for 6 phantoms

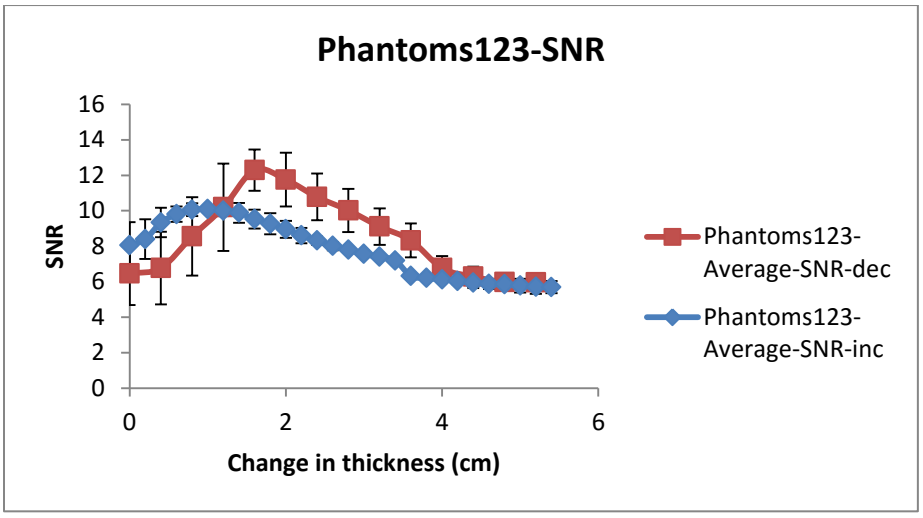

Figure 11.66 Average SNR for phantoms 1, 2 and 3

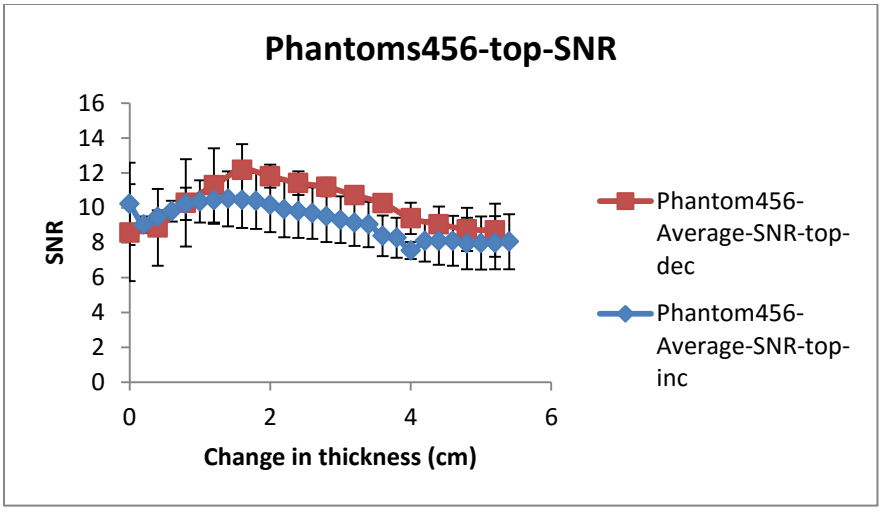

Figure 11.67 Average SNR for the top lesions of phantoms 4, 5 and 6

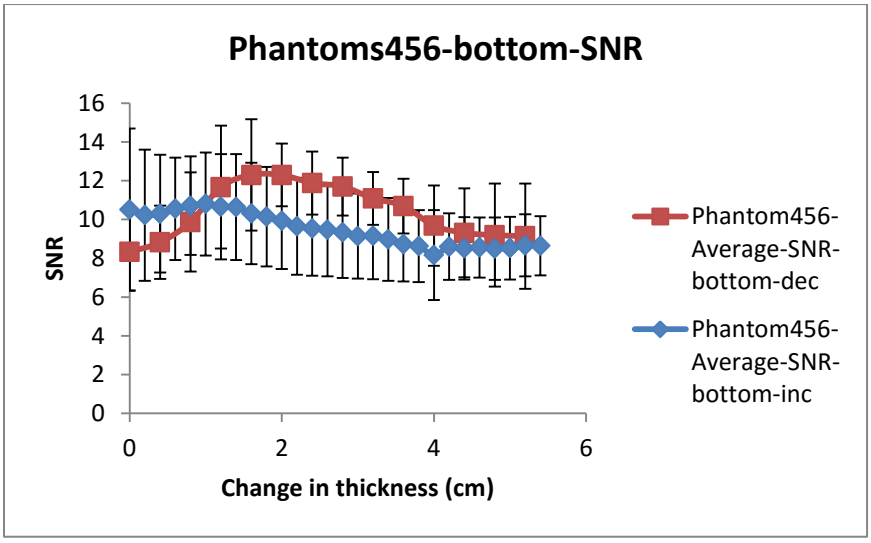

Figure 11.68 Average SNR for the bottom lesions of phantoms 4, 5 and 6

The following graphs (Figure 11.69 to Figure 11.72) demonstrate Figure of Merit (FOM) for 6 phantoms.

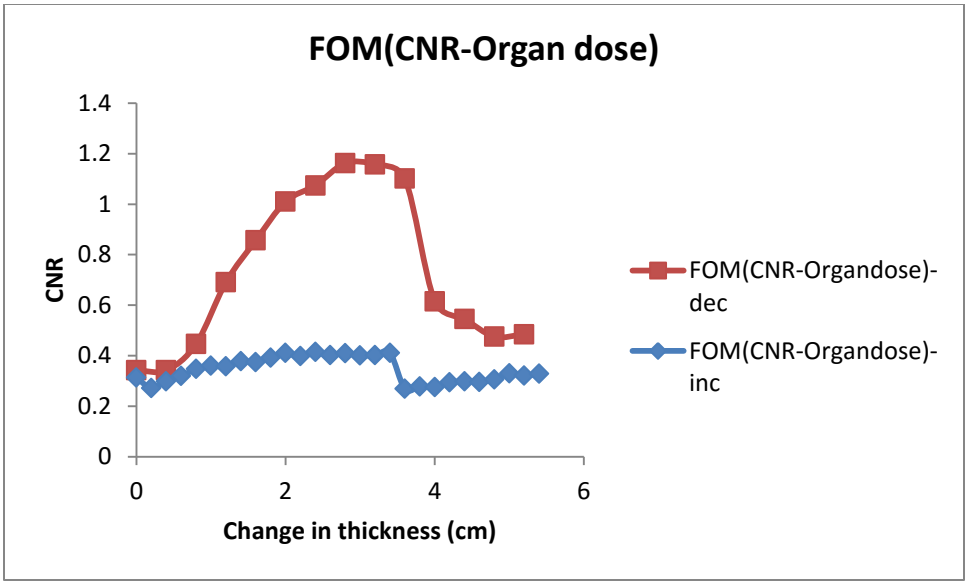

Figure 11.69 FOM (CNR - Organ dose)

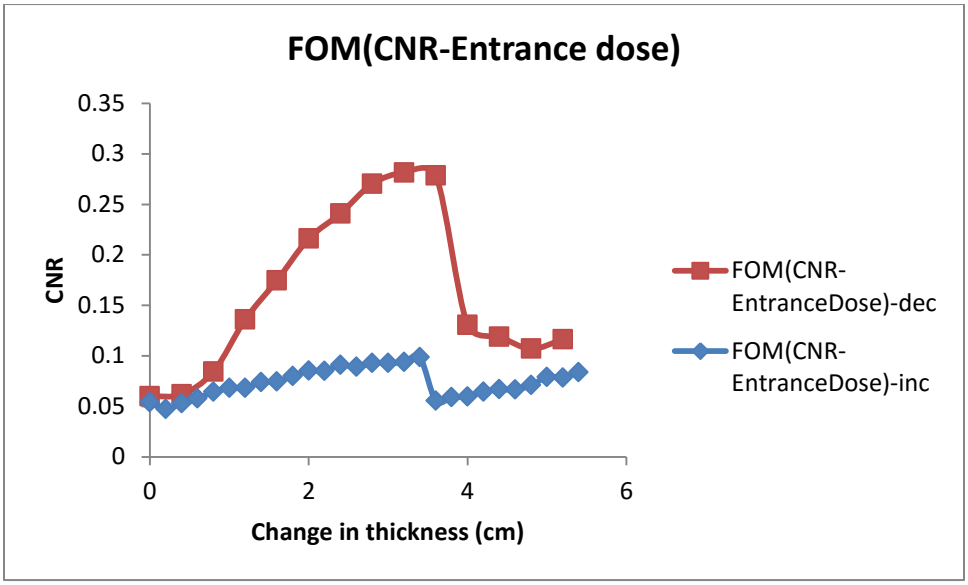

Figure 11.70 FOM (CNR-Entrance dose)

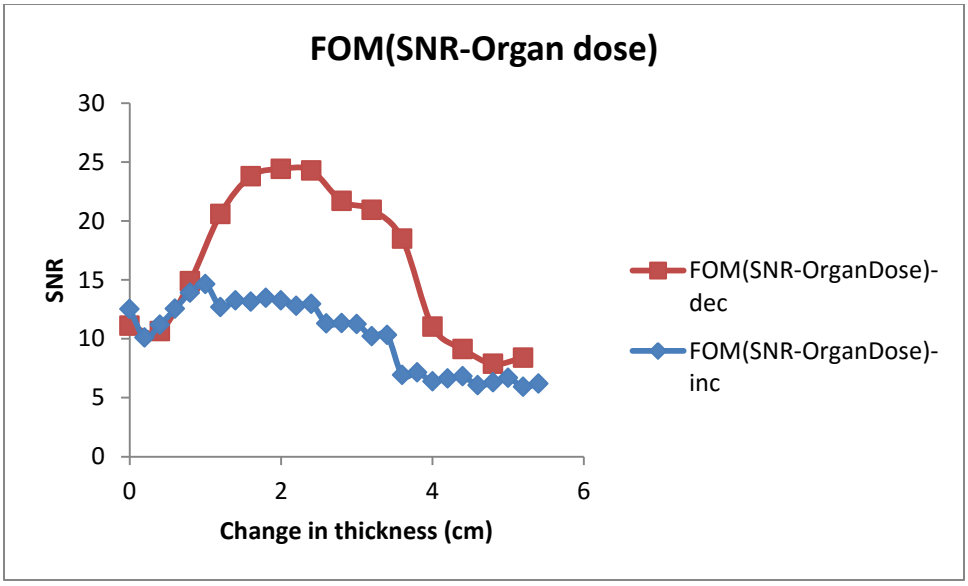

Figure 11.71 FOM (SNR-Organ dose)

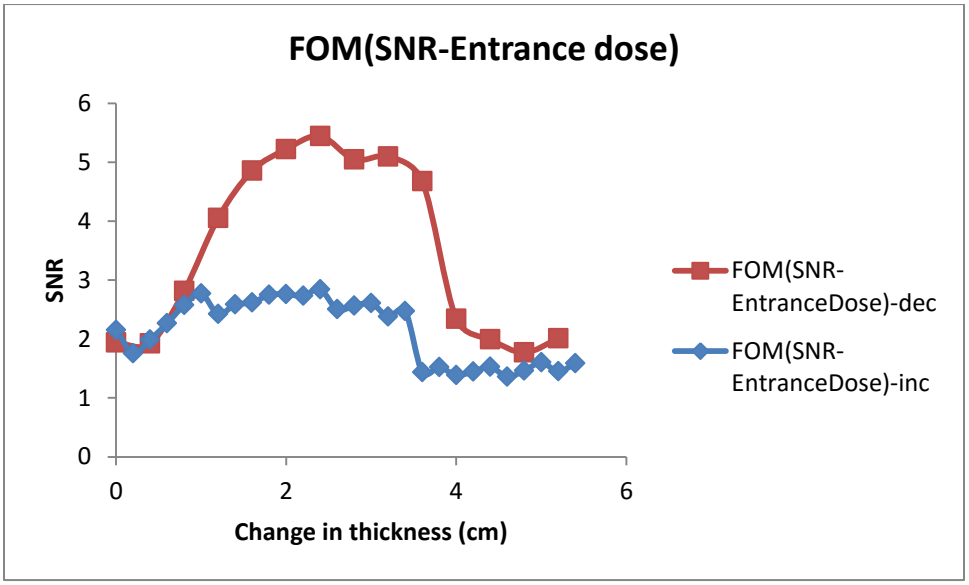

Figure 11.72 FOM (SNR - Entrance dose)

The entrance dose and organ dose were directly recorded from the mammography unit. As can be seen in the above graphs (Figure 11.69 to Figure 11.72), the FOM drops after 3.4 cm of thickness reduction in decreased thickness (increased compression). The FOM also drops after 3.6 cm of thickness reduction in increased thickness (decreased

compression). Since FOM is inversely related to radiation dose and radiation dose increases after 3.4 cm (inc) and 3.6 cm (dec), then FOM decreases after these points.

11.5.1.6 Intraclass correlation coefficient

Appendix H shows the results of the intraclass correlation coefficient (ICC). The results display a high consistency and agreement among the three observes. Generally, an ICC is measured on a scale of 0 to 1; where 1 represents perfect reliability and 0 indicates no reliability. The majority of the acquired ICC results for image quality (visibility, sharpness, and contrast) display a high reliability over 0.9 (+0.9). The majority of the acquired ICC results for noise was over 0.8 (+0.8).

Among all the criteria of visibility, sharpness, contrast, noise and size, ICC displays the lowest reliability for the size criterion. This is mostly noticeable for the phantoms with only one lesion. For the size criterion of phantoms with two lesions, the percentage of "consistency" over 0.8 (+0.8) among the readers is 83.33% while the percentage of "absolute agreement" is 58.33%. Size was excluded from the measurement and graphs of image quality.

The high rate of consistency and agreement among the observers variability describes how strongly the measurements by various readers resemble each other. Due to the high percentage of the similarity between the readers, this test also shows the number of the observers for this specific research was adequate.

11.5.2 Discussion

In this research, it was found that applied compression force and the resultant change in thickness are inversely related, as expected. This means that increase of compression force resulted in a decrease in the breast phantom thickness and vice versa. Therefore the initial mammographic experiments were based on compression force with

the recording thicknesses. However, the advantage of using thickness over force in the graphs/tables is that there is always a reading for each thickness, but not for each force. For the lower compression forces, below 45, the mammography unit is unable to record the compression force (N). The main sets of experiments of this research (11.5 on page 200) were completely based on the breast phantom thickness.

In reality, due to the variations of breast density, a specific amount of compression force might not reduce the breast thickness sufficiently to view the cancer lesions. Hence, relying on the breast thickness reduction provides more consistent and reproducible data for the lesion visibility studies.

Research shows differences between the readout and measured thickness by the mammography units. The discrepancies between the readout and measured breast thickness might be due to the tilted paddle, mechanical/electrical design of the readout unit, or the compressible structure of the breast which tries to push back to the original shape. Some studies have suggested corrective methods to measure the actual breast thickness during the mammography procedure (Hauge, Hogg, Connolly, McGill, & Claire, 2012) (Mawdsley, Tyson, Peressotti, Jong, & Yaffe, 2009). Generally, in clinical practice during the screening and diagnostic mammography, the machine readout is used. Therefore, in this research, the machine readout was utilised to simulate the clinical mammography procedure.

During the decrease/increase thickness experiment (11.5.1.5 on page 236), in addition to radiation dose, the measurements of CNR and FOM as mathematical image quality parameters demonstrated decreased values once the breast phantom had been reduced in thickness beyond 3.4 cm (37.7%) thickness reduction. This result was also reflected in the increase thickness/decrease compression experiment (11.5.1.5 on page

236) after 3.6 cm (40%) thickness reduction. This means that the CNR and FOM drop when the breast phantom thickness is approximately 5.5 cm.

SNR is one of the most meaningful metrics to demonstrate the visibility of an object. It has been selected as one of the mathematical metrics for image quality. According to the Rose Criterion, an object will be recognizable and detectable if the value of SNR ≥ 5 (Bushberg, Seibert, Leidholdt, & Boone, 2011). Unlike all other image quality parameters, only SNR graphs demonstrated the signal to noise ratio improvement up to 1 cm of the thickness reduction. However, the value of SNR was greater than 5 for all the data points (11.5.1.5 on page 236). This indicates that regardless of the breast phantom thickness, all the lesions were detectable in the phantoms.

The visual perception results have shown a reduction in the amount of noise for the reduced thickness. Similarly, the profile plots of the lesions have demonstrated the noise reduction for the reduced phantom thickness. However, the standard deviation graphs of the background (around the lesion) have displayed a decrease followed by an increase of the noise around the lesion. The increase of the noise is contradictory with the results of the visual perception and the profile plot. Generally speaking, the standard deviation is a metric which is employed in order to quantify the noise in the image. This metric does not measure the noise texture (Bushberg, Seibert, Leidholdt, & Boone, 2012). Therefore, this might be the cause of the discrepancy between the noise scored visually and the noise measured by standard deviation. This was discussed in 6.4.5 on page 81.

The perceived size of the lesion increased with the decrease of the phantom thickness. The increase in size was possibly due to the improvement of image quality parameters such as sharpness of the lesion, contrast between the lesion and the adjacent region, and noise. This means that due to the improvement of the image quality, it was easier to see exactly where the actual edge of the lesion was. Another possible reason for

the improvement of the lesion size could be the spreading out of the lesion with the increase of the compression force. Similar to a malleable ball, the lesion can look wider from the top when it is compressed. The results of ICC for this experiment have shown low consistency and agreement for the phantoms with one lesion among the observers; however for the phantoms with two lesions the agreement and consistency among the observers have shown the improvement of the lesion size with the increase of the compression force.

11.5.3 Conclusion

In this research, based on the results from 2AFC, a consistent linear improvement relative to the decrease of the breast phantom thickness was observed for all of the following image quality criteria: lesion visibility, sharpness, contrast, noise and size of the lesion. Similar to 2AFC, the profile plot, as a mathematical method, demonstrated the improvement in the sharpness of the edge of the lesion. It also showed the reduction of noise corresponding to the reduction of the breast phantom thickness. Unlike the 2AFC and the profile plot, the values of CNR, SNR, and FOM graphs demonstrated increase up to certain points. This means that the results of CNR, SNR, and FOM as mathematical methods and 2AFC as perceptual method do not match after certain thicknesses. It is important to mention that visual perception does not take into account radiation dose, where FOM does. This means although image quality may improve in visual perception, the images are not necessarily optimised.

As was mentioned in Chapter 1 on page 2, the reduction in tissue thickness has the effect of reducing the required radiation dose of radiation necessary to acquire the mammographic image. This was verified by this research up to the point that the filter was changed from Rh to Mo. After this point, the radiation dose increased regardless of

phantom thickness. It is important to mention that at this thickness, the FOM which represents the performance of the mammography system in terms of image quality and patient radiation dose dropped. The CNR, as a mathematical image quality parameter also dropped at this thickness. This indicates that the usage of Automatic Exposure Control (AEC) might not be the appropriate option for phantom studies for specific breast phantom thickness. This research shows that, for a breast phantom thickness of approximately 5.5 cm, alternative methods for the selection of exposure factors and filter may be required including manual selection. This is in agreement with the research by Bor et al. regarding variations in breast radiation doses for an automatic mammography unit (Bor, Tükel, Olgar, & Aydın, 2008).

The results from this thesis are likely to have implications for clinical practice, as they support the need for compression/thickness reduction to enhance lesion visibility. It is suggested to compare the radiation dose, and image quality parameters such as FOM using AEC and manual selection when the breast thickness reaches to approximately 5.5 cm during compression.

11.5.4 Limitation/future work

Microcacifications are tiny calcium deposits smaller than 1/50 of an inch in size which can appear as a cluster. The cluster of microcalcifications is a common mammographic indicator of ductal carcinoma in situ (DCIS) (Imaginis Corporation, 2010). Since this type of breast cancer is associated with microcalcifications and detecting microcalcifications can help early detection of breast cancer, it is important to design and fabricate embedded clusters of microcalcifications.

Masses with spiculated margins (stellate) as primary breast cancer indicators have a high chance of being malignant. Unlike well-defined margin masses, this type has thin

elongated pieces (spicules) of tissue coming out of the perimeter. Since this spiculated margin masses are the most common manifestation of invasive carcinoma (Fornage, 2006) , design and fabrication of this shape of lesions in the future is recommended.

In this study, the homogenous breast phantoms similar to fatty tissue were designed and fabricated. The real breast tissue is composed of fat and fibroglandular tissues; therefore fabrication of breast phantoms including both fatty and fibroglandular tissue creates higher resemblance to real human tissue. Since the percentage of glandular tissues change corresponding to the age and menopausal status, the breast phantoms can be designed with various percentages of fat and glandular tissues. For example 50% of fat and 50% glandular, 25% of fat and 75% of glandular or 75% of fat and 25% of glandular.

Although the mammography unit used in this research supports multiple AEC modes, only the Auto-Filter mode was utilised. In the Auto-Filter mode, the machine automatically switches between Rh and Mo filters. The machine decides which filter to utilise based on the thickness of the tissue being imaged.

As the radiation dose results from this research shows (Figure 11.41 on page 219 to Figure 11.46 on page 222), a radiation dose increase occurred during the automatic filter change from Rh to Mo as the compression was increased. Future research could seek to minimise the radiation dose increase by utilising other AEC modes including manual mode. The following sections explain the clinical opportunities for the use of PVAL phantoms/lesions.

11.5.4.1 Breast examination and biopsy purposes

PVAL phantoms/lesions can be used to teach medical students how to perform clinical breast examinations. In order to make the PVAL lesions palpable, bigger-sized lesions can be produced and embedded in various locations of the different-sized beast

phantoms. In these phantoms, X-ray imaging is not performed, therefore the presence of contrast agent is not required.

PVAL phantoms/lesions can also be used in multiple biopsy techniques. Usually, ultrasound-guided biopsy or stereotactic mammography is used in order to guide the needle to the location of the abnormalities. In these procedures, depending on the patient's situation, different biopsy techniques can be performed to access the abnormalities. The removed sample of abnormal lesion is then sent to the pathology lab. These techniques include: Fine needle aspiration biopsy, core needle biopsy, and vacuum-assisted breast biopsy (Donahue, 2013).

The PVAL phantoms designed in this research can be used for training purposes in various types of biopsy techniques. They also can be employed to perform quality control for different biopsy needles. In order to extract sample lesions, various shapes, sizes and locations have to be taken into account. Since mammographic stereotactic can be used to extract microcalcifications, it is important to design microcalcifications and embed them into various places of the PVAL phantoms.

During mammographic stereotactic biopsy the breast tissue is compressed. Hence, in these types of studies, a compressible breast phantom is required. In order to make the lesions attenuating in stereotactic biopsy, the use of contrast agent is required.

11.5.4.2 Comparing different mammography systems

Several studies have been carried out by researchers regarding dosimetry and measuring the image quality for different mammographic units using either CDMAM or PMMA phantoms (Emanuelli, Rizzi, Amerio, Fasano, & Cesarani, 2011) (Oberhofer, Fracchetti, Nassivera, Valentini, & Moroder, 2010) (Oberhofer & Bolzano, 2011). These phantoms do not have the mechanical properties of the human breast. The compressible

PVAL phantom could be used in these types of studies in order to compare the same system with various setups such as anode/filter or mammography units from various manufacturers. These phantoms can also be utilised to compare various detector technologies.

11.6 SUMMARY OF THE RESEARCH

As part of this research custom Polyvinyl alcohol (PVAL) breast phantoms with embedded lesions were fabricated and utilised. These breast phantoms exhibited mechanical and X-ray properties which were similar to female breast/breast cancer tissues.

After acquiring the mammograms of phantoms under varying compression forces, the image quality of the embedded lesions were evaluated both perceptually and mathematically. The two-alternative forced choice (2AFC) perceptual method was used to evaluate the image quality of the lesions. For mathematical evaluation the following methods were utilised: line profile analysis, contrast- to-noise ratio (CNR), signal-to noise ratio (SNR) and figure of merit (FOM).

Using the 2AFC method observers evaluated and scored the captured mammograms on a number of image quality measures including lesion visibility, sharpness of the edge of the lesion, contrast between the lesion and the surrounding area, noise and size of the lesion. The results were then plotted and analysis was performed on the resulting graphs. All of the graphs consistently demonstrated linear improvement in image quality related to the increase of compression force and decrease of the breast phantom thickness.

Radiation dose graphs (organ and entrance) demonstrated a general reduction of radiation dose in relation to the thickness reduction. This reduction of radiation dose had

a thickness reduction threshold after which further reduction of thickness resulted in an increase in radiation dose rather than a decrease.

Mathematical evaluation results also showed a correlation of improvement in the image quality with the reduction in breast thickness. The results showed that for the measures CNR, SNR, and FOM, the increase in image quality has a threshold after which the image quality ceases to improve and instead begins to degrade.

The profile plot analysis of the phantoms/lesions displayed the improvement in noise and the lesion sharpness relative to the thickness reduction. This is in agreement with the visual perception results.

11.6.1 Alternative approaches

This section discusses the alternative approaches to this research. These approaches consist of the use of mastectomy breast specimen, production of lesion and gel, use of other types of materials to make the phantoms, utilisation of different mammography units, use of hybrid mammograms, and discussion of visual perception methods.

11.6.1.1 Mastectomy breast specimen

One of the alternative approaches to this research is using real breast with cancer lesions from the surgical mastectomy. Ethical approval and possibly patient consent are required for these types of research. The advantage of this method is that the use of synthetic phantom/lesions is not necessary. Diversity in the breast tissue and lesion shapes, sizes and locations can hinder the reproducibility of research. In other words, only one sample would be available to test for each case. The mastectomy specimen might have different mechanical and X-ray properties compared to the live breast tissue, hence, the mechanical and X-ray properties of the mastectomy specimen have to be

tested. Furthermore, the methods for storing and transferring the samples to the research sites have to be taken into consideration.

11.6.1.2 Production of lesions

One of the problems with the employment of PVAL lesions doped with contrast agent is the leeching problem with the contrast agent to the surrounding area. Encapsulation of the lesions (making membrane) might stop leaching of contrast agent from the lesion to the surrounding area; therefore the phantom/lesions can be used for a longer period of time. Due to the possible changes in X-ray and mechanical properties of the encapsulated lesions, these properties have to be measured prior to use.

11.6.1.3 Production of gel

When a magnetic stirrer is used, especially with a higher concentration of PVAL crystals, the magnet in the magnetic stirrer can become stuck in the condensed solution. Due to the continuous stirring mechanism of a mechanical overhead stirrer, it could be more suitable than a magnetic stirrer in this case.

11.6.1.4 Other types of materials

The HU of PVAL phantoms cannot be negative, therefore in this research the presence of contrast agent was required in order to produce the HU difference between the simulated breast fatty tissue and the cancer mimicking lesions. On the other hand, the controlled mechanical properties of PVAL make this material desirable for biomedical engineering studies. X-ray properties of this material encourage the researchers to utilise other materials to acquire the required HU.

Research shows that plastics can have a large range of HU from -125 to +364 (Henrikson, Mafee, Flanders, Kriz, & Peyman, 1987) (Zhang, Roa, Sehga, He, & Al-Ghazi, 2011). Materials such as polyethylene and polystyrene can have negative HU

which are suitable to simulate fatty tissue. Since the mechanical properties of these materials do not match the breast tissue's mechanical properties, these materials could be blended with the appropriate percentage of PVAL in a controlled way.

11.6.1.5 Mammography units

The mammography unit used in this study was a Hologic Selenia with selenium flat panel detector, Mo anode and Mo/Rh filters. In order to compare the results among different mammography units, other systems could be tested. For example General Electric (GE) mammography unit with flat panel phosphor, dual-track (Mo/Rh) anode and Mo/Rh filters or a Sectra mammography unit with photon counting detector and a W/Al anode/filter combination (McCullagh, Baldelli, & Phelan, 2011).

11.6.1.6 Hybrid mammograms

In reality, human breasts contain multiple internal structures. The glandular, fatty, and connective tissues make the breast heterogeneous and textured. In this study, the developed PVAL phantoms were homogeneous, In order to generate the real anatomical background, similar techniques such as hybrid images could be utilized (Li & Samei, 2010). The hybrid images consist of the real anatomical background acquired from the patients' mammograms and PVAL phantom/lesions images.

11.6.1.7 Visual perceptual methods

In this study, the visual perception goal is just to assess the quality of the target not the presence or absence of it. In other words, just noticeable differences between the images are important. Hence, two-alternative forced choice (2AFC) is an appropriate perceptual method in order to assess the image quality.

Receiver operating characteristic (ROC) is not a suitable visual perception method for this study. Typical conventional ROC deals with two states which are either presence

or absence of the target in the images (Krupinski, 2010). In this research the target (lesion) is always present and visible in the image with different degree of visibility.

11.6.2 Key findings

- A 5% PVAL phantom with 2 FTCs, HU≈17, YM≈17.34 kPa is suitable for breast phantom.
- A 10% PVAL phantom with 6 FTCs, HU≈43, YM≈216 kPa is suitable for breast cancer lesions. In order to make the PVAL lesions attenuation as invasive ductal carcinoma cancer lesions, 20 wt% of contrast agent is required to be mixed with 10% PVAL solution prior to FTCs.
- Fresh PVAL phantoms/lesions are required in mammographic lesion visibility studies. It is important to mention that the fresh phantoms/lesions do not need to be stored in deionized water.
- Linear improvement in the perceived image quality was observed in relation to the reduction of PVAL breast phantom thickness.
- The intracass correlation coefficient (ICC) has shown a great consistency and agreement among the observers/readers for visibility, sharpness, contrast and noise. The ICC results are not as conclusive for the size criterion.
- The profile plot displayed improvement in the sharpness of the lesion edge and also the noise in accordance with the thickness reduction.
- Contrast to noise ratio (CNR) and figure of merit (FOM) improved in relation to the breast phantom reduction up to the point that the filter was changed from Rh to Mo.

- Signal to noise ratio (SNR) increased after about 1 cm of the thickness reduction followed by a decrease after this point. The reduction started before the changes in the filter from Rh to Mo.
- Radiation dose versus breast phantom thickness dropped up to the point that the filter was changed from Rh to Mo, after this point the radiation dose increased.
- The increase of radiation dose and the reduction of FOM and CNR started when the thickness of the breast phantom was about 5.5 cm (the initial thickness was 9cm)

Appendices

APPENDIX A: FREEZER AND HOTPLATE CURVES

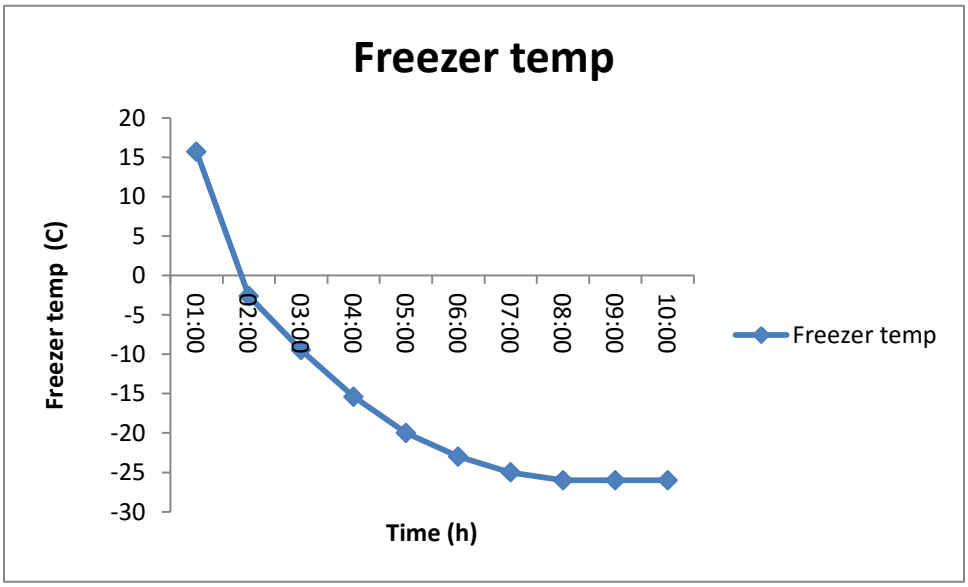

Figure A.1 Freezer temperature curve of Nova Scotia chest freezer

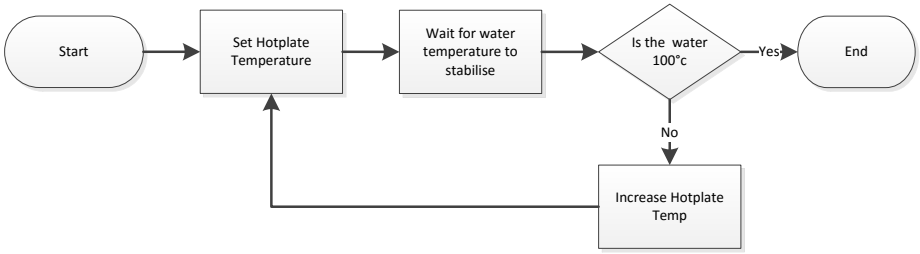

Figure A.2 Hotplate calibration flow chart

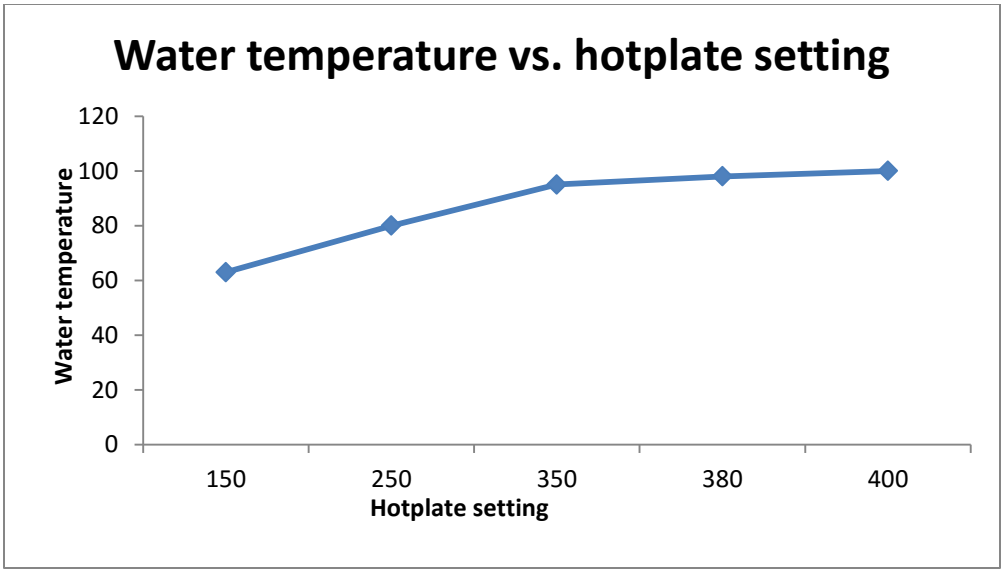

Figure A.3 Water temperature vs. Hotplate Setting

APPENDIX B: HU OF PVAL LESION OVER 10 - MINUTE PERIOD

Time (min)	Area	HU
1	298.14	633.17
2	298.14	633.13
3	298.14	633.07
4	298.14	633.10
5	298.14	632.85
6	298.14	632.70
7	298.14	632.67
8	298.14	632.41
9	298.14	632.35
10	298.14	632.21

Table B.1 HU of an embedded lesion in a breast phantom with skin over 10 minutes

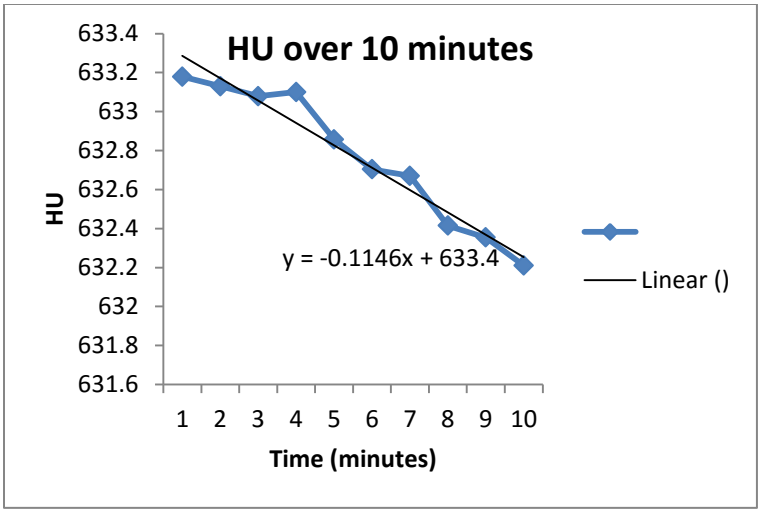

Figure B.1 HU of an embedded lesion in a breast phantom with skin over 10 minutes

APPENDIX C: MAMMOGRAMS OF BREAST PHANTOM/LESION

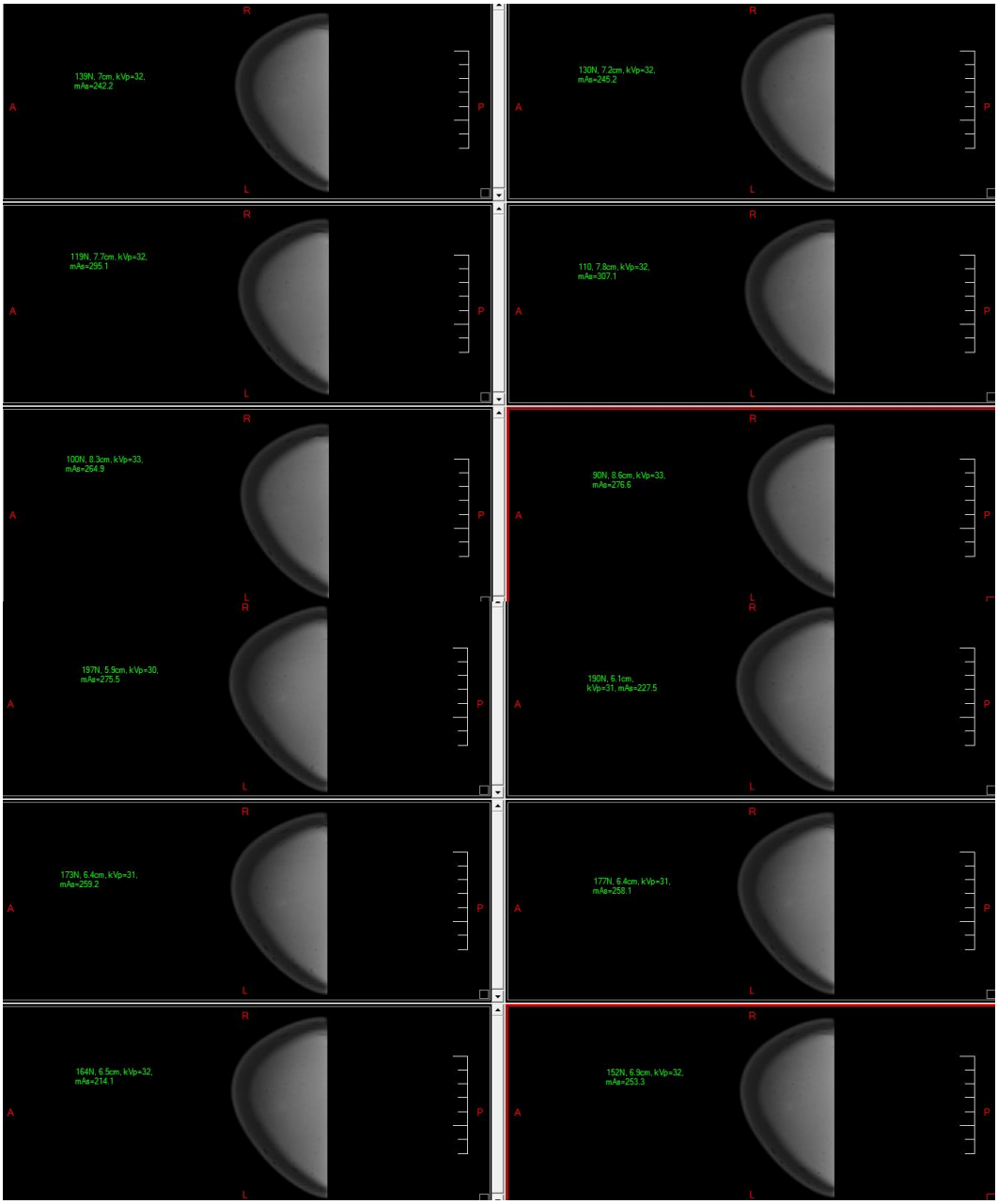

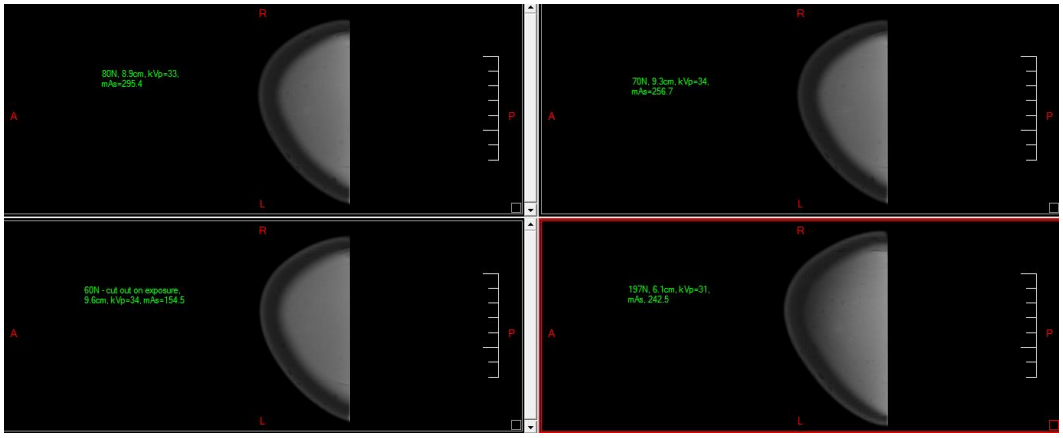

Figure C.1 Mammograms of the breast phantom with various compressions

APPENDIX D: MAMMOGRAMS OF BREAST PHANTOM/LESIONS

The following mammograms (Figure D.1) show the lesions embedded in the breast phantom compressed from 50 N to 150 N. The last image shows the compressed phantom with 50 N after applying 150 N.

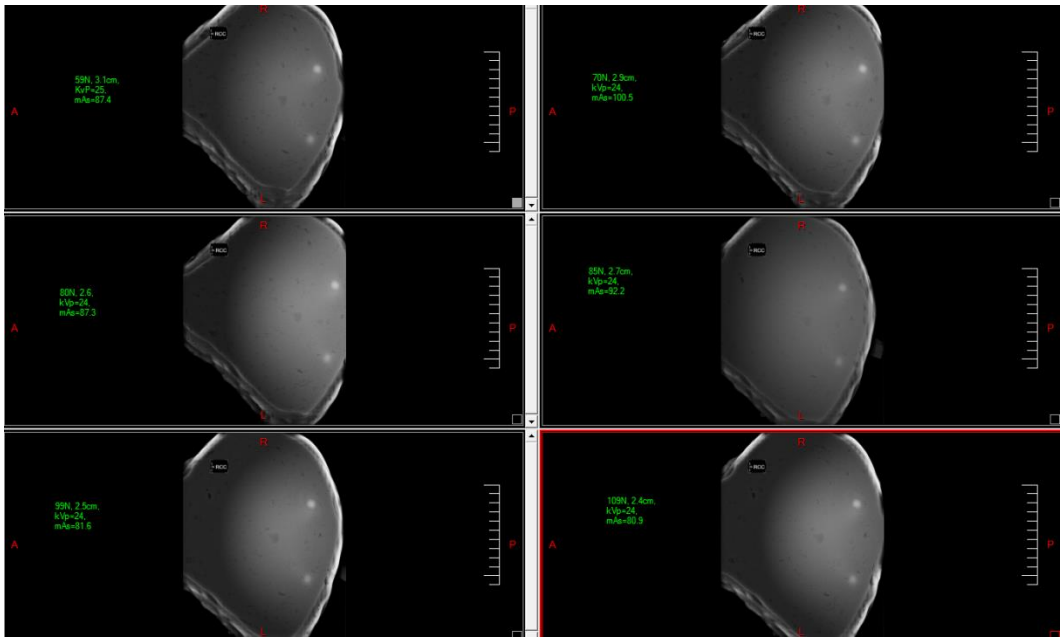

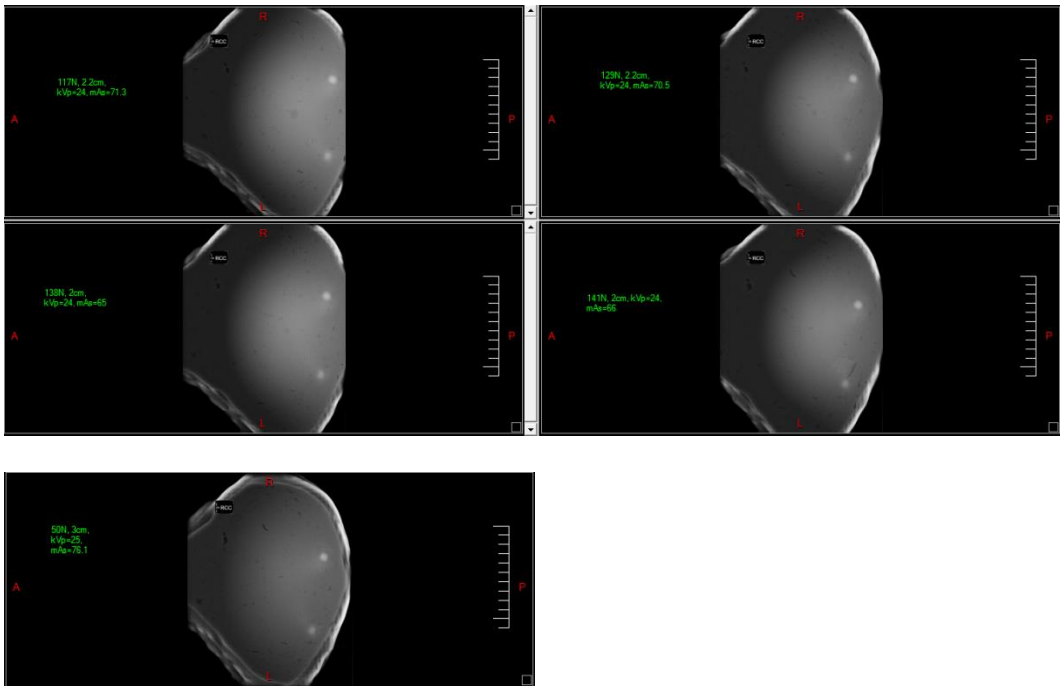

Figure D.1 Mammograms of the breast phantom with two lesions

The following mammograms (Figure D.2) show the lesions embedded in a cylindrical phantom compressed from 50N to 150 N. The last image shows the compressed phantom with 50N after applying 150N. The recorded images were from 14 to 25.

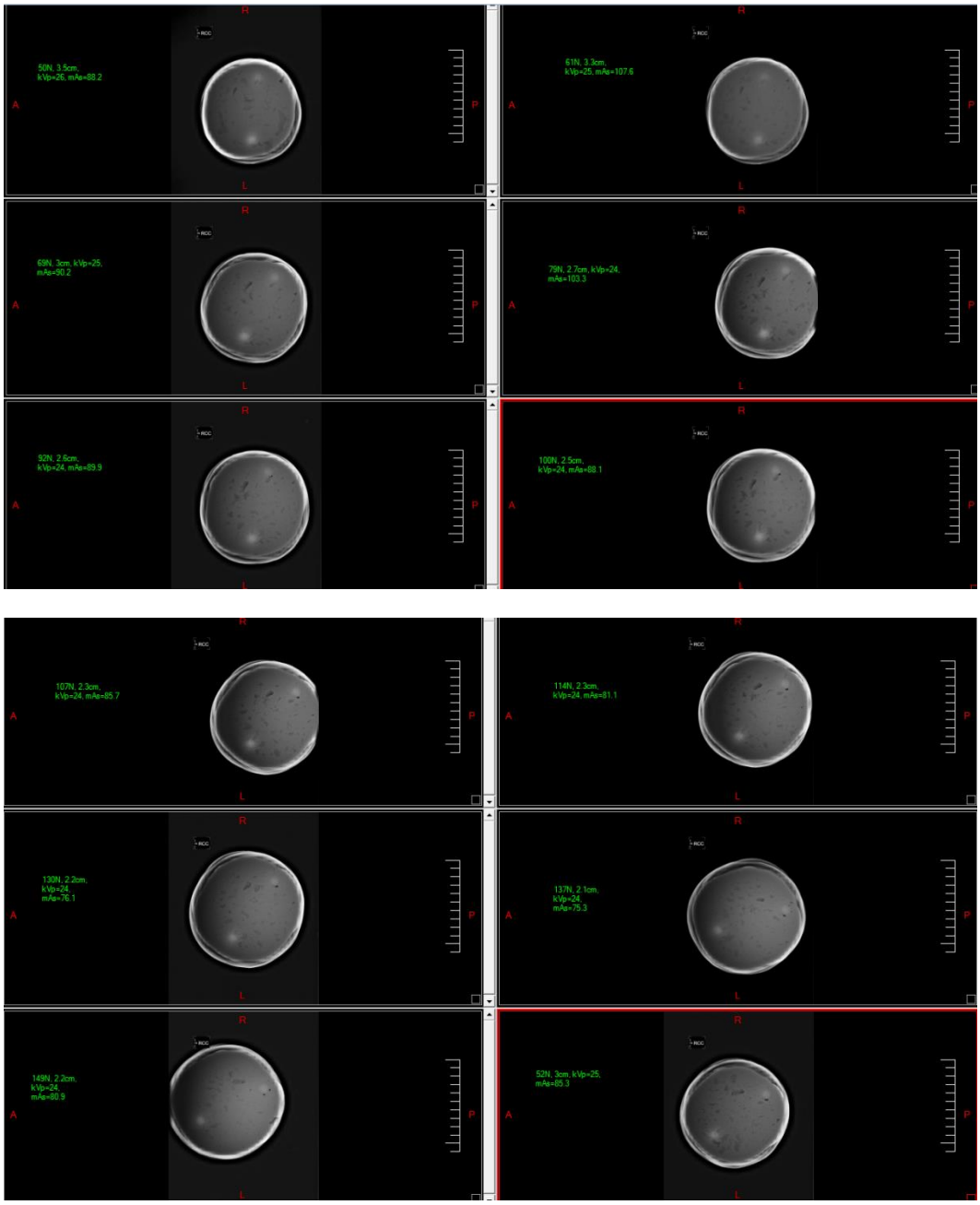

Figure D.2 Mammograms of a cylindrical phantom with two lesions

APPENDIX E: 2AFC GRAPHS FOR 2 PHANTOMS WITH 2 LESIONS

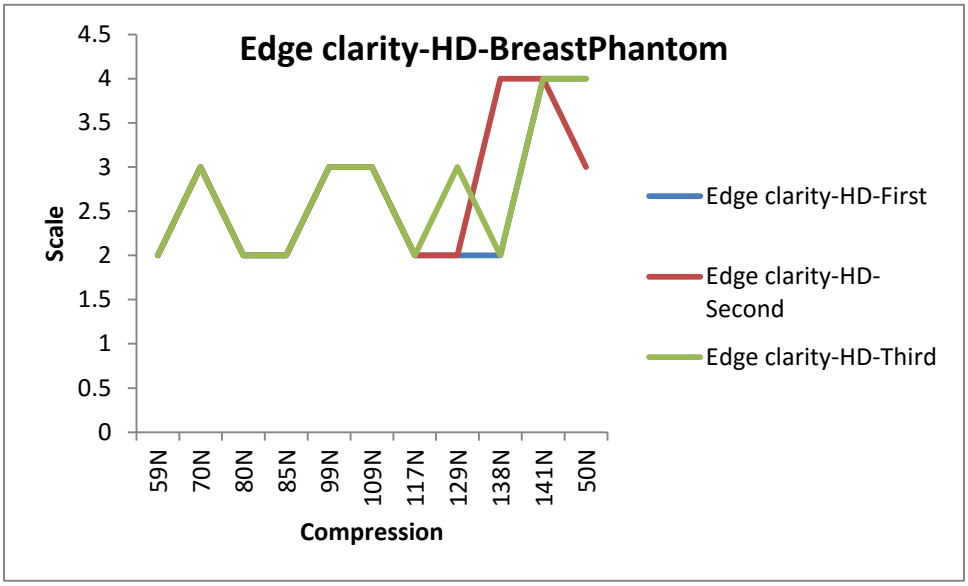

Figure E.1 2AFC, 3 repetitions for the High Density lesion in breast phantom

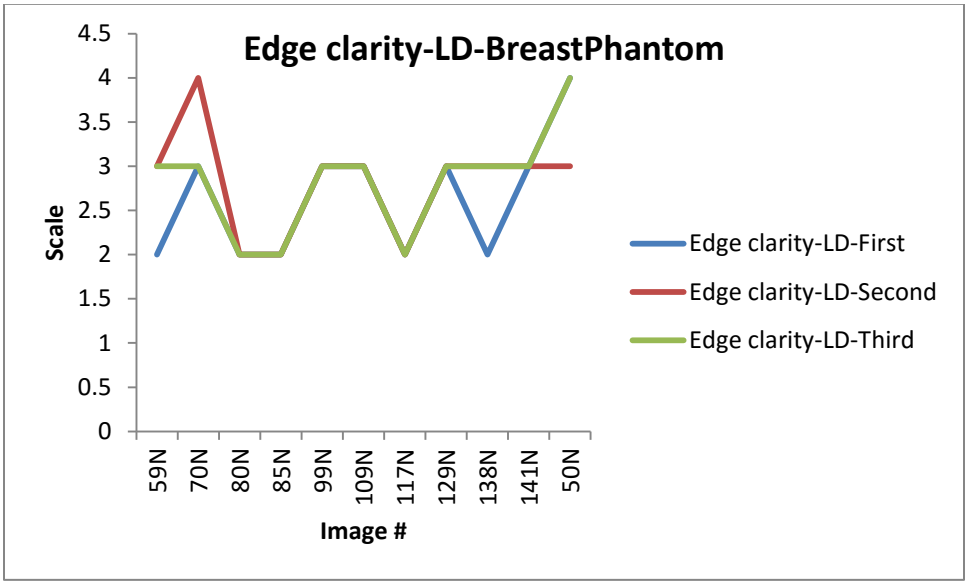

Figure E.2 2AFC, 3 repetitions for the Low Density lesion in breast phantom

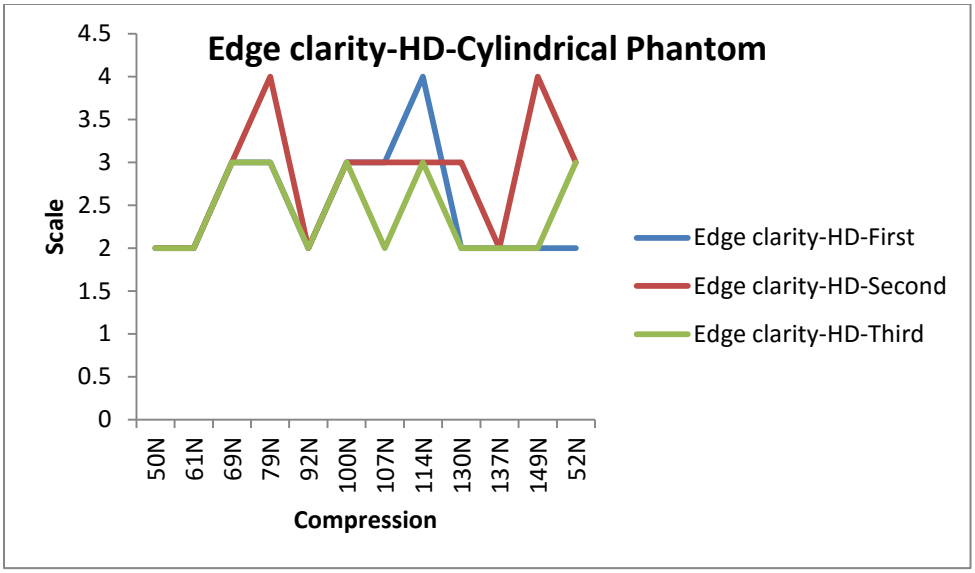

Figure E.3 2AFC, 3 repetitions for the High Density lesion in a cylindrical phantom

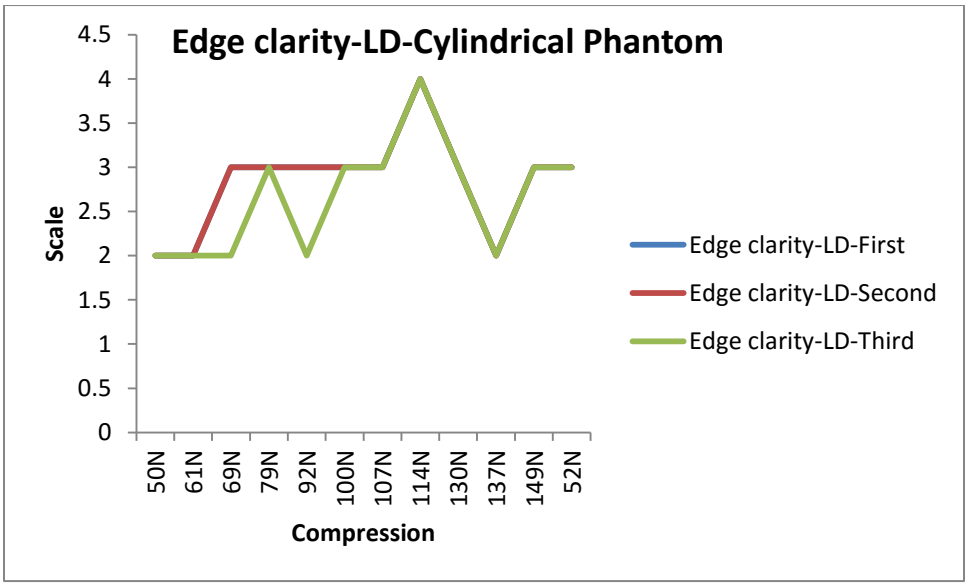

Figure E.4 2AFC, 3 repetitions for the Low Density lesion in a cylindrical phantom

APPENDIX F: DATA ACQUIRED FROM THE MAMMOGRAPHY PROCEDURE

Breast phantom: 5% PVAL, 2-FTCs
Lesion(s): One lesion, 10% PVAL, 5cc CA, 6-FTCs
Paddle size: 18x24

Thickness (cm)	Force (N)	kVp	mAs	Target/Filter	Organ dose (mGy)	Entrance dose(mGy)
9	----------	34	221.9	Rh	6.72	37.70
8.8	----------	33	279.9	Rh	7.83	43.40
8.6	46	33	268.0	Rh	7.62	41.20
8.4	48	33	257.7	Rh	7.43	39.40
8.2	51	33	240.6	Rh	7.04	36.50
8.00	54	33	234.0	Rh	6.94	35.20
7.8	59	32	275.7	Rh	7.52	37.70
7.6	63	32	263.7	Rh	7.31	35.80
7.4	66	32	253.8	Rh	7.14	34.20
7.2	72	32	240.1	Rh	6.85	32.10
7.0	73	32	224.9	Rh	6.50	29.90
6.8	74	32	214.0	Rh	6.32	28.30
6.6	75	32	189.2	Rh	5.69	24.80
6.4	79	31	234.9	Rh	6.47	27.80
6.2	93	31	217.3	Rh	6.08	25.60
6.0	99	31	206.6	Rh	5.87	24.10

5.8	107	30	247.7	Rh	6.40	26.00
5.6	114	30	225.5	Rh	5.94	23.50
5.4	121	29	248.1	Mo	7.69	37.10
5.2	131	29	230	Mo	7.25	34.10
5.0	145	29	216.1	Mo	6.91	31.90
4.8	144	28	271.8	Mo	7.84	35.90
4.6	160	28	251.0	Mo	7.39	33.00
4.4	172	27	329.8	Mo	8.68	38.60
4.2	188	27	314.9	Mo	8.51	36.60
4.0	197	27	285.5	Mo	7.90	33.00
3.8	211	26	383.4	Mo	9.57	39.10
3.6	225	26	365.9	Mo	9.47	37.10

Table F.1 Mammography data

Breast phantom: 5% PVAL, 2-FTCs

Lesion(s): One lesion, 10% PVAL, 5cc CA, 6-FTCs

Paddle size: 18x24

Thickness (cm)	**Force (N)**	**KvP**	**mAs**	**Target/Filter**	**Organ dose (mGy)**	**Entrance dose(mGy)**
4	163	27	259.3	Mo	7.18	29.90
4.4	132	27	269.9	Mo	7.81	34.70
4.8	101	28	246.0	Mo	7.10	32.50

5.2	86	29	204.6	Mo	6.45	30.40
5.6	70	30	191.2	Rh	5.04	19.90
6.0	58	31	173.9	Rh	4.94	20.30
6.4	47	31	193.1	Rh	5.32	22.90
6.8	----------	32	176.4	Rh	5.21	23.30
7.2	----------	32	202.9	Rh	5.79	27.20
7.6	----------	32	223.4	Rh	6.19	30.30
8.0	----------	33	191.3	Rh	5.67	28.80
8.4	----------	33	211.7	Rh	6.11	32.30
8.8	----------	33	232.8	Rh	6.52	36.10
9.2	----------	34	183.8	Rh	5.50	31.40

Table F.2 Mammography data

Breast phantom: 5% PVAL, 2-FTCs

Lesion(s): One lesion, 10% PVAL, 5cc CA, 6-FTCs

Paddle size: 18x24

Thickness (cm)	**Force (N)**	**KvP**	**mAs**	**Target/Filter**	**Organ dose (mGy)**	**Entrance dose(mGy)**
9	----------	34	247.7	Rh	7.51	42.10
8.8	----------	33	305.1	Rh	8.54	47.30
8.6	----------	33	303.9	Rh	8.64	46.80
8.4	----------	33	275.5	Rh	7.95	42.10

8.2	----------	33	265.0	Rh	7.74	40.20
8.00	----------	33	249.8	Rh	7.40	37.60
7.8	----------	32	307.4	Rh	8.39	42.00
7.6	----------	32	289.8	Rh	8.03	39.30
7.4	----------	32	274.9	Rh	7.73	37.10
7.2	51	32	253.7	Rh	7.24	34.00
7.0	54	32	248.1	Rh	7.17	33.00
6.8	58	32	229.4	Rh	6.77	30.30
6.6	64	32	219.2	Rh	6.59	28.70
6.4	69	31	260.7	Rh	7.18	30.90
6.2	73	31	249.1	Rh	6.97	29.30
6.0	76	31	237.2	Rh	6.74	27.70
5.8	77	30	269.3	Rh	6.89	28.30
5.6	87	30	250.9	Rh	6.61	26.10
5.4	100	29	287.5	Mo	8.91	43.00
5.2	108	29	263.8	Mo	8.31	39.20
5.0	113	29	252.7	Mo	8.09	37.30
4.8	121	28	313.1	Mo	9.03	41.40
4.6	133	28	302.5	Mo	8.90	39.70
4.4	142	27	376.8	Mo	9.91	44.10

4.2	153	27	346.4	Mo	9.36	40.20
4.0	164	27	323.5	Mo	8.95	37.30
3.8	168	26	395.4	Mo	9.87	40.30
3.6	182	26	367.2	Mo	9.50	37.20

Table F.3 Mammography data

Breast phantom: 5% PVAL, 2-FTCs **Lesion(s): One lesion, 10% PVAL, 5cc CA, 6-FTCs** **Paddle size: 18x24**						
Thickness (cm)	**Force (N)**	**KvP**	**mAs**	**Target/Filter**	**Organ dose (mGy)**	**Entrance dose(mGy)**
4.0	136	27	295.6	Mo	8.18	34.10
4.4	104	27	338.5	Mo	8.91	39.60
4.8	85	28	276.8	Mo	7.99	36.60
5.2	67	29	233.4	Mo	7.36	34.60
5.6	52	30	208.5	Rh	5.49	21.70
6.0	----------	31	195.5	Rh	5.55	22.80
6.4	----------	31	217.0	Rh	5.98	25.70
6.8	----------	32	190.4	Rh	5.62	25.10
7.2	----------	32	209.6	Rh	5.98	28.10
7.6	----------	32	229.2	Rh	6.35	31.10
8.0	----------	33	204.9	Rh	6.07	30.90
8.4	----------	33	221.5	Rh	6.39	33.80

8.8	----------	33	227.8	Rh	6.38	35.30
9.2	----------	34	193.1	Rh	5.77	33.00

Table F.4 mammography data

Breast phantom: 5% PVAL, 2-FTCs **Lesion(s): Two lesions, 10% PVAL, 5cc CA, 6-FTCs** **Paddle size: 18x24**						
Thickness (cm)	**Force (N)**	**kVp**	**mAs**	**Target/Filter**	**Organ dose (mGy)**	**Entrance dose(mGy)**
9	----------	34	238.1	Rh	7.22	40.40
8.8	----------	33	296.3	Rh	8.29	45.90
8.6	----------	33	300.8	Rh	8.55	46.30
8.4	----------	33	276.8	Rh	7.98	42.30
8.2	----------	33	257.7	Rh	7.54	39.10
8.00	----------	33	239.2	Rh	7.09	36.00
7.8	----------	32	307.6	Rh	8.39	42.10
7.6	----------	32	280.1	Rh	7.76	38.00
7.4	----------	32	266.6	Rh	7.50	35.90
7.2	----------	32	243.0	Rh	6.93	32.50
7.0	45	32	234.5	Rh	6.78	31.20
6.8	50	32	224.7	Rh	6.63	29.70
6.6	54	32	207.2	Rh	6.23	27.20

6.4	59	31	245.5	Rh	6.76	29.10
6.2	63	31	229.9	Rh	6.43	27.00
6.0	68	31	216.3	Rh	6.14	25.30
5.8	74	30	250.0	Rh	6.46	26.20
5.6	78	30	233.4	Rh	6.15	24.30
5.4	82	29	268.2	Mo	8.31	40.10
5.2	88	29	249.6	Mo	7.87	37.00
5.0	94	29	231.4	Mo	7.40	34.10
4.8	102	28	286.6	Mo	8.27	37.90
4.6	108	28	265.5	Mo	7.81	34.90
4.4	113	27	328.4	Mo	8.64	38.40
4.2	120	27	303.7	Mo	8.21	35.30
4.0	128	27	285.6	Mo	7.90	33.00
3.8	140	26	348.8	Mo	8.70	35.60
3.6	149	26	317.5	Mo	8.22	32.20

Table F.5 Mammography data

Breast phantom: 5% PVAL, 2-FTCs **Lesion(s): One lesion, 10% PVAL, 5cc CA, 6-FTCs** **Paddle size: 18x24**						
Thickness (cm)	**Force (N)**	**kVp**	**mAs**	**Target/Filter**	**Organ dose (mGy)**	**Entrance dose(mGy)**
4.0	106	27	254.9	Mo	7.05	29.40

4.4	82	27	287.5	Mo	7.56	33.60
4.8	64	28	239.2	Rh	6.90	31.60
5.2	51	29	207.4	Rh	6.54	30.80
5.6	----------	30	191.1	Rh	5.03	19.90
6.0	----------	31	171.2	Rh	4.86	20.00
6.4	----------	31	197.5	Rh	5.44	23.40
6.8	----------	32	178.6	Rh	5.32	23.50
7.2	----------	32	208.5	Rh	5.99	27.80
7.6	----------	32	242.9	Rh	6.73	33.00
8.0	----------	33	200.3	Rh	5.94	30.20
8.4	----------	33	229.5	Rh	6.62	35.10
8.8	----------	33	230.2	Rh	6.44	35.70
9.2	----------	34	185.9	Rh	5.56	31.80

Table F.6 Mammography data

Breast phantom: **5% PVAL, 2-FTCs**

Lesion(s): **Two lesions, 10% PVAL, 5cc CA, 6-FTCs**

Paddle size: **18x24**

Note: **The system stopped a few times due to the heat problem. The filter never changed to Rh. The First image on the disk has to be removed from the set. Radiation dose and mAs are high in this dataset. 4.2cm has been repeated twice.**

Thickness (cm)	Force (N)	KvP	mAs	Target/Filter	Organ dose (mGy)	Entrance dose(mGy)

9	----------	34	210.5	Mo	8.14	55.20
8.8	----------	33	267.2	Mo	9.60	64.30
8.6	46	33	264.0	Mo	9.64	63.10
8.4	51	33	261.9	Mo	9.63	62.40
8.2	56	33	243.9	Mo	9.17	57.40
8.00	61	33	232.7	Mo	8.87	54.40
7.8	65	32	299.8	Mo	10.50	64.10
7.6	69	32	287.3	Mo	10.20	61.20
7.4	72	32	276.6	Mo	9.94	58.50
7.2	74	32	251.4	Mo	9.23	52.60
7.0	88	32	235.9	Mo	8.78	49.00
6.8	91	32	225.1	Mo	8.54	46.50
6.6	99	32	214.1	Mo	8.26	43.90
6.4	109	31	267.4	Mo	9.48	49.90
6.2	118	31	261.6	Mo	9.42	48.50
6.0	127	31	242.9	Mo	8.87	44.70
5.8	135	30	311.2	Mo	10.40	51.90
5.6	147	30	290.0	Mo	9.91	48.10
5.4	155	29	371.9	Mo	11.50	55.60
5.2	163	29	344.5	Mo	10.90	51.10

5.0	175	29	324.5	Mo	10.40	47.80
4.8	151	28	355.4	Mo	10.30	47.00
4.6	162	28	338.5	Mo	9.95	44.40
4.4	154	27	399.8	Mo	10.50	46.80
4.2	158	27	355.4	Mo	9.60	41.30
4.2	153	27	345.1	Mo	9.32	40.10
4.0	153	27	318.4	Mo	8.81	36.70
3.8	171	26	392.5	Mo	9.79	40.00
3.6	182	26	375.0	Mo	9.72	38.10

Table F.7 Mammography data

Breast phantom: 5% PVAL, 2-FTCs **Lesion(s): One lesion, 10% PVAL, 5cc CA, 6-FTCs** **Paddle size: 18x24**						
Thickness (cm)	**Force (N)**	**kVp**	**mAs**	**Target/Filter**	**Organ dose (mGy)**	**Entrance dose(mGy)**
4.0	132	27	306.7	Mo	8.49	35.40
4.4	102	27	339.8	Mo	8.94	39.70
4.8	82	28	282.5	Mo	8.15	37.30
5.2	65	29	236.0	Mo	7.44	35.00
5.6	49	30	214.3	Rh	5.65	22.30
6.0	----------	31	195.5	Rh	5.55	22.80
6.4	----------	31	219.3	Rh	6.04	26.00

6.8	----------	32	195.7	Rh	5.78	25.80
7.2	----------	32	227.9	Rh	6.50	30.50
7.6	----------	32	247.2	Rh	6.85	33.60
8.0	----------	32	259.4	Rh	7.02	35.60
8.4	----------	33	228.6	Rh	6.59	34.90
8.8	----------	33	242.2	Rh	6.78	37.50
9.2	----------	34	195.2	Rh	5.84	33.40

Table F.8 Mammography data

Breast phantom: 5% PVAL, 2-FTCs

Lesion(s): Two lesions, 10% PVAL, 5cc CA, 6-FTCs

Paddle size: 18x24

Thickness (cm)	**Force (N)**	**kVp**	**mAs**	**Target/Filter**	**Organ dose (mGy)**	**Entrance dose(mGy)**
9.0	----------	34	276.0	Rh	8.36	46.90
8.8	----------	33	318.7	Rh	8.92	49.40
8.6	----------	33	309.6	Rh	8.80	47.60
8.4	----------	33	296.0	Rh	8.54	45.20
8.2	----------	33	279.3	Rh	8.17	42.40
8.00	----------	33	266.5	Rh	7.90	40.10
7.8	----------	32	324.6	Rh	8.85	44.40
7.6	----------	32	313.3	Rh	8.68	42.50

7.4	47	32	281.1	Rh	7.91	37.90
7.2	50	32	270.4	Rh	7.71	36.20
7.0	53	32	255.4	Rh	7.38	34.00
6.8	58	32	246.3	Rh	7.27	32.50
6.6	61	32	233.4	Rh	7.02	30.60
6.4	67	31	271.1	Rh	7.47	32.10
6.2	69	31	254.8	Rh	7.13	30.00
6.0	72	31	240.0	Rh	6.82	28.00
5.8	84	30	275.6	Rh	7.12	28.90
5.6	86	30	259.3	Rh	6.83	27.00
5.4	97	29	289.9	Mo	8.99	43.30
5.2	100	29	266.5	Mo	8.40	39.60
5.0	105	29	248.6	Mo	7.95	36.60
4.8	107	28	305.5	Mo	8.81	40.40
4.6	112	28	289.2	Mo	8.51	38.00
4.4	124	27	362.2	Mo	9.53	42.40
4.2	134	27	334.4	Mo	9.04	38.90
4.0	138	27	298.3	Mo	8.26	34.40
3.8	146	26	383.4	Mo	9.57	39.10
3.6	157	26	338.5	Mo	8.76	34.30

Table F.9 Mammography data

Breast phantom: 5% PVAL, 2-FTCs **Lesion(s): One lesion, 10% PVAL, 5cc CA, 6-FTCs** **Paddle size: 18x24**						
Thickness (cm)	**Force (N)**	**kVp**	**mAs**	**Target/Filter**	**Organ dose (mGy)**	**Entrance dose(mGy)**
4.0	108	27	270.5	Mo	7.49	31.20
4.4	86	27	310.1	Mo	8.16	36.30
4.8	69	28	266.2	Mo	7.68	35.20
5.2	53	29	216.1	Mo	6.81	32.10
5.6	----------	30	197.6	Rh	5.21	20.60
6.0	----------	31	180.6	Rh	5.13	21.10
6.4	----------	31	205.1	Rh	5.65	24.30
6.8	----------	32	185.1	Rh	5.46	24.40
7.2	----------	32	207.2	Rh	5.95	27.60
7.6	----------	32	234.2	Rh	6.49	31.80
8.0	----------	33	199.6	Rh	5.92	30.10
8.4	----------	33	206.2	Rh	5.95	31.50
8.8	----------	33	213.0	Rh	5.96	33.00
9.2	----------	34	178.0	Rh	5.32	30.50

Table F.10 Mammography data

APPENDIX G: IMAGE QUALITY GRAPHS

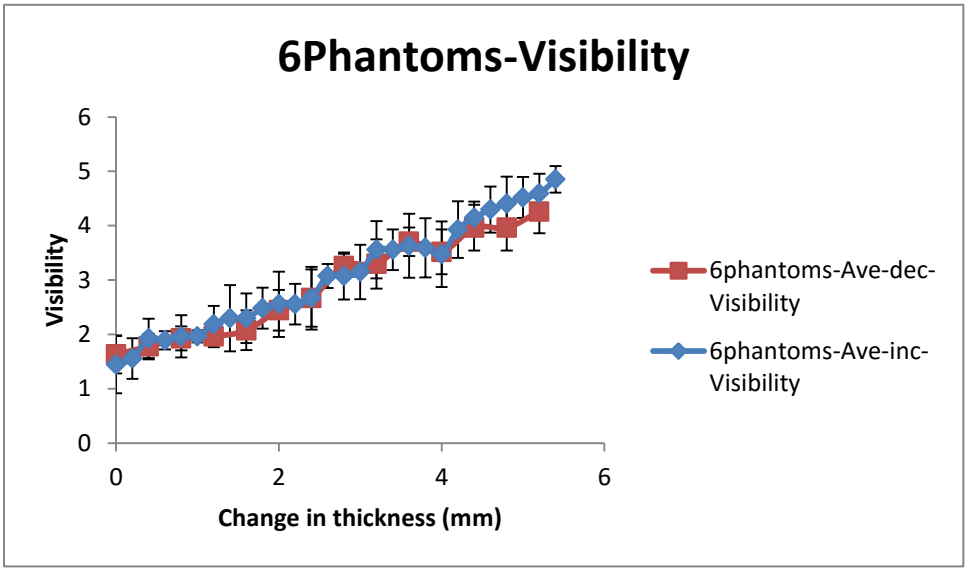

Figure G.1 Average visibility of the lesions for 6 phantoms

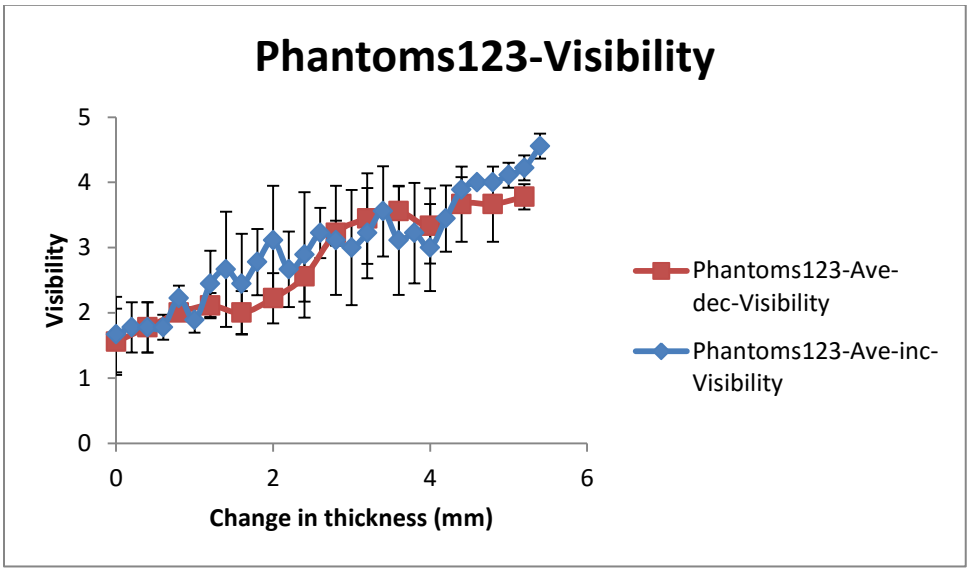

Figure G.2 Average visibility of the top lesions for phantoms 1, 2 and 3

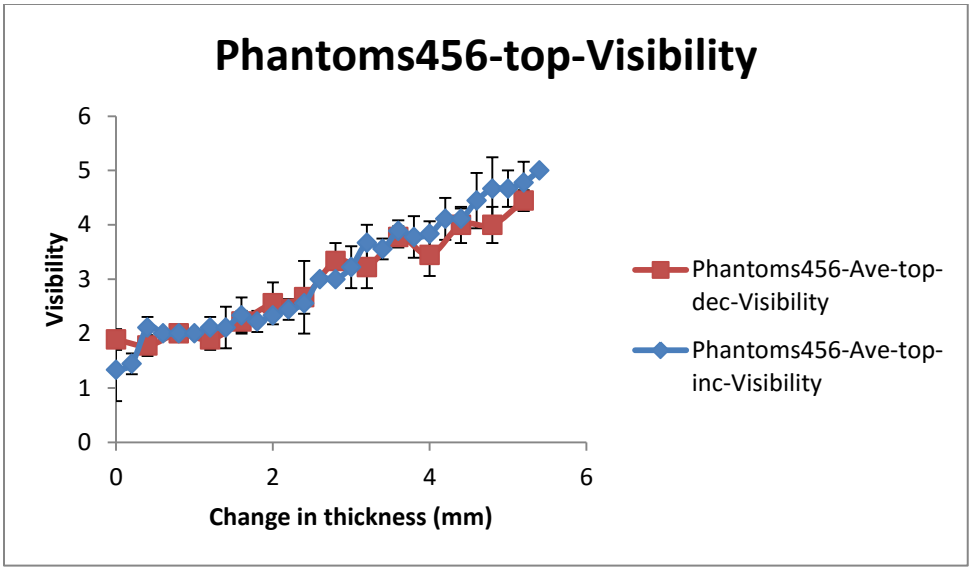

Figure G.3 Average visibility of the top lesions for phantoms 4, 5 and 6

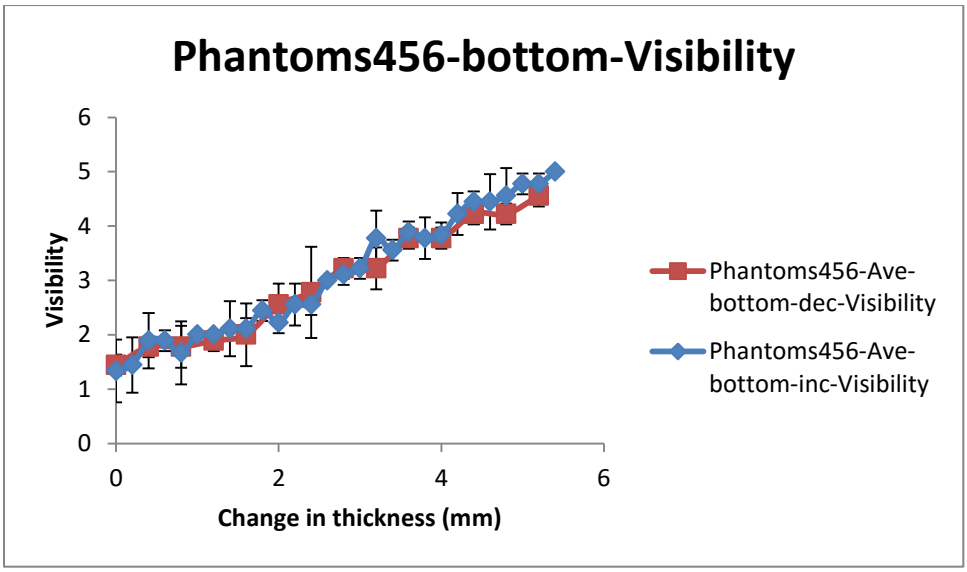

Figure G.4 Average visibility of the bottom lesions for phantoms 4, 5 and 6

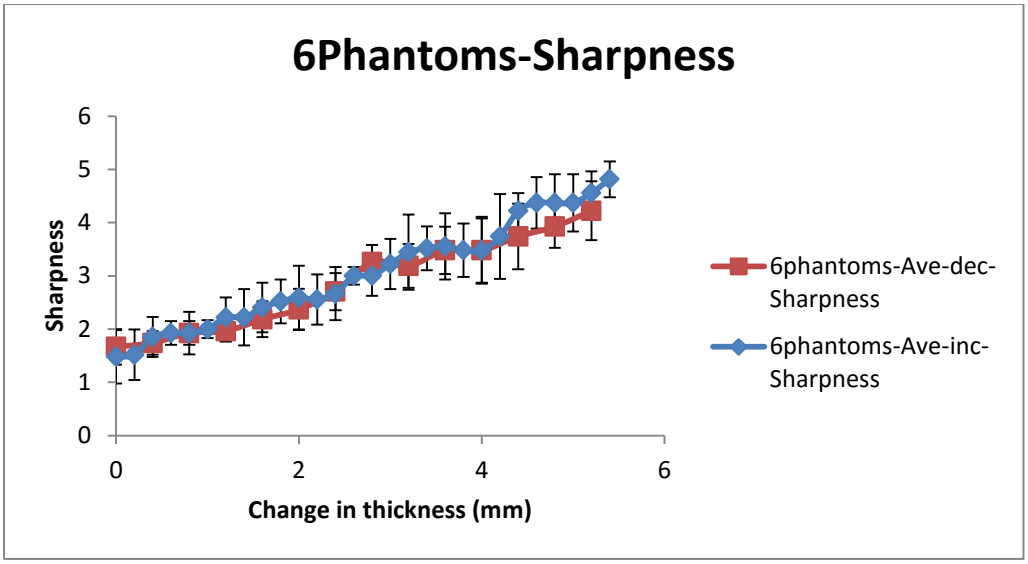

Figure G.5 Average sharpness of the lesions for 6 phantoms

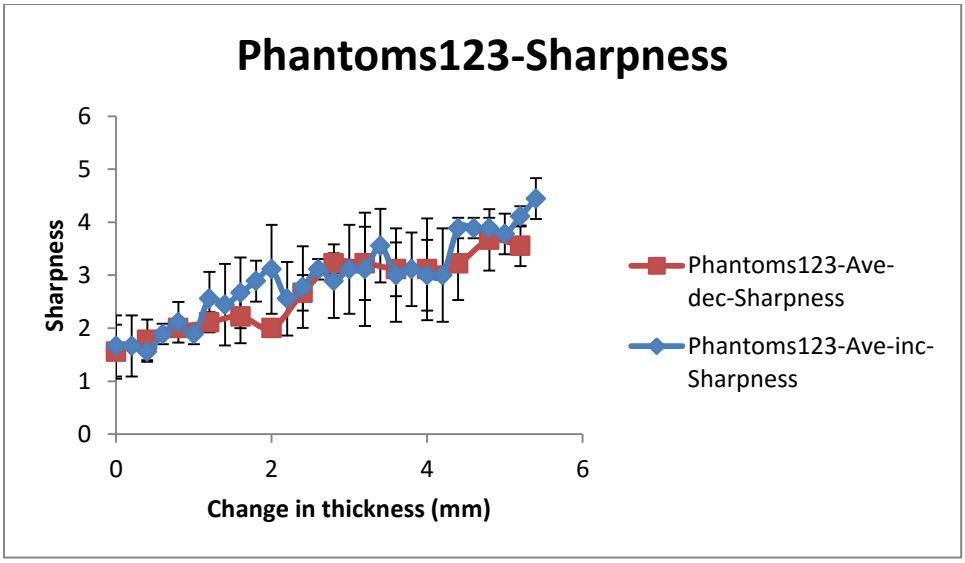

Figure G.6 Average sharpness of the lesions for phantoms 1, 2 and 3

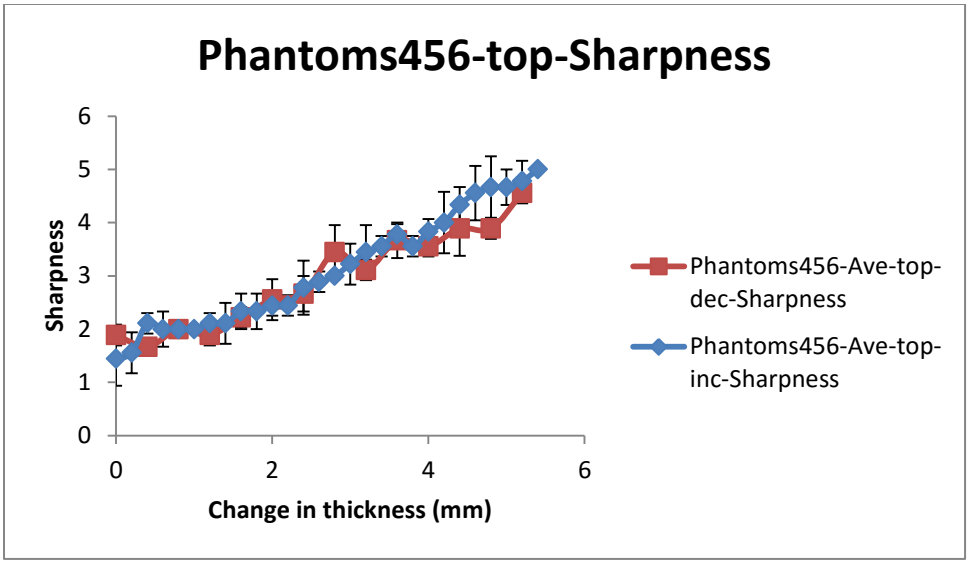

Figure G.7 Average sharpness of the top lesions for phantoms 4, 5 and 6

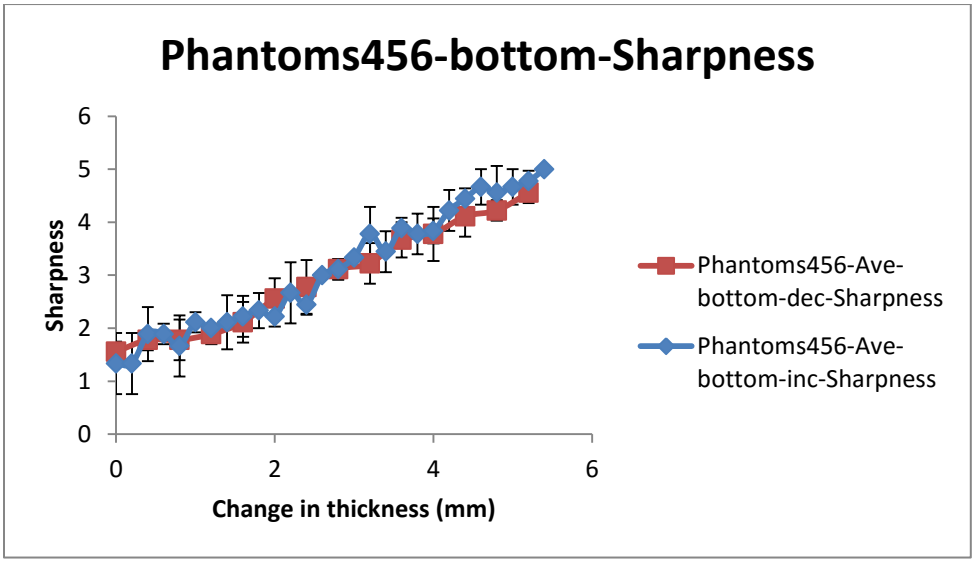

Figure G.8 Average sharpness of the bottom lesions for phantoms 4, 5 and 6

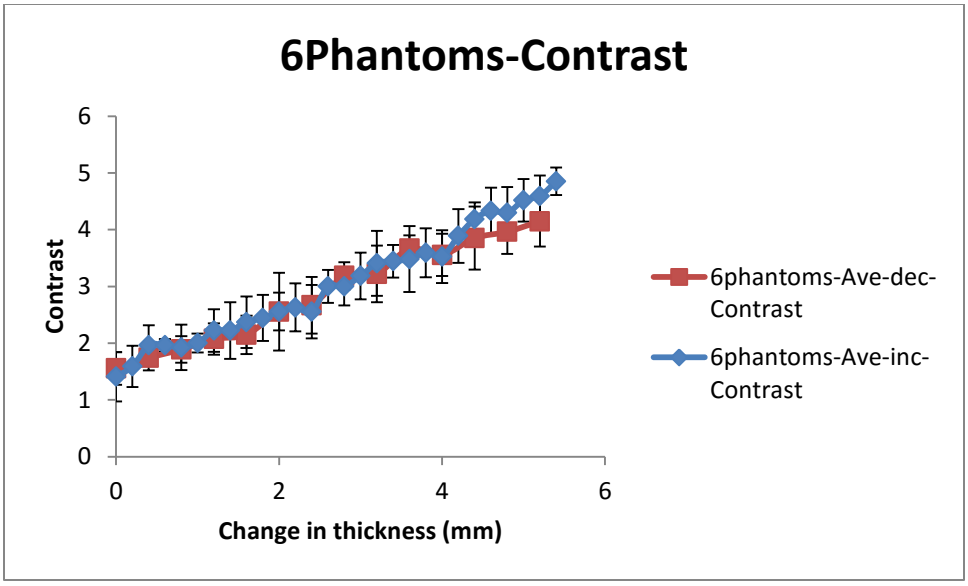

Figure G.9 Average contrast of the lesions for 6 phantoms

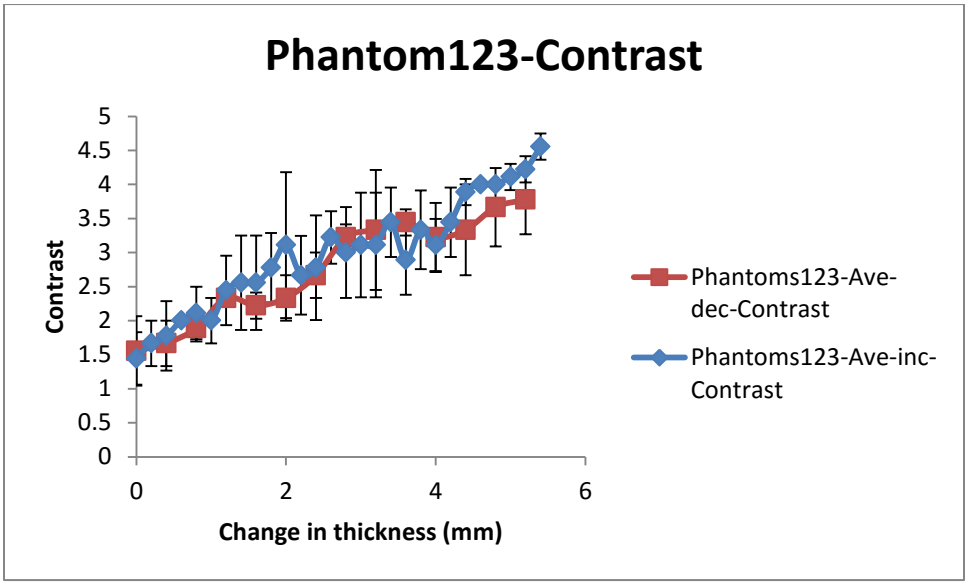

Figure G.10 Average contrast of the lesions for phantoms 1, 2 and 3

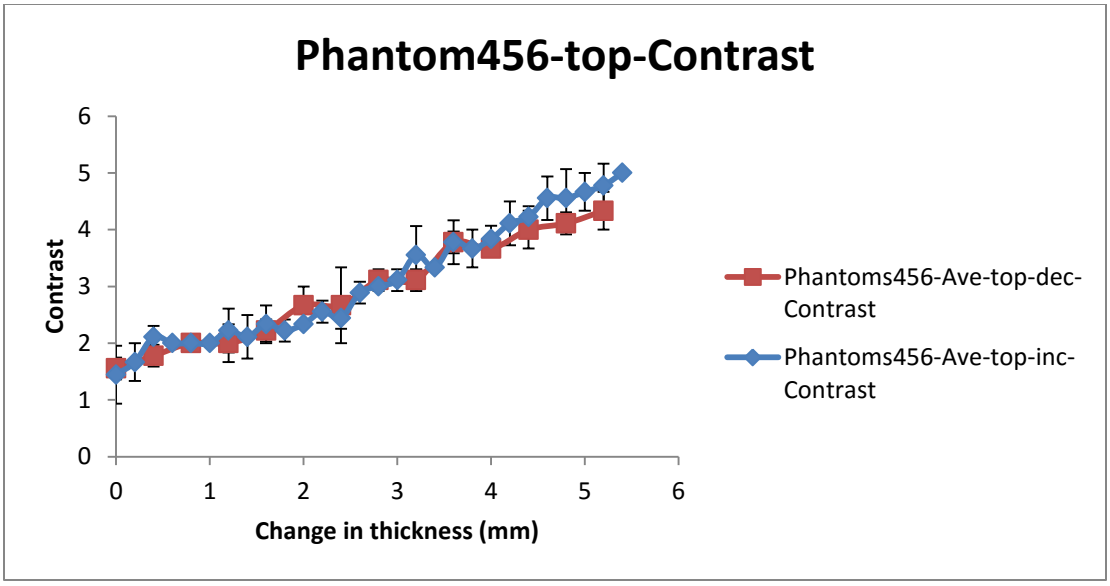

Figure G.11 Average contrast of the top lesions for phantoms 4, 5 and 6

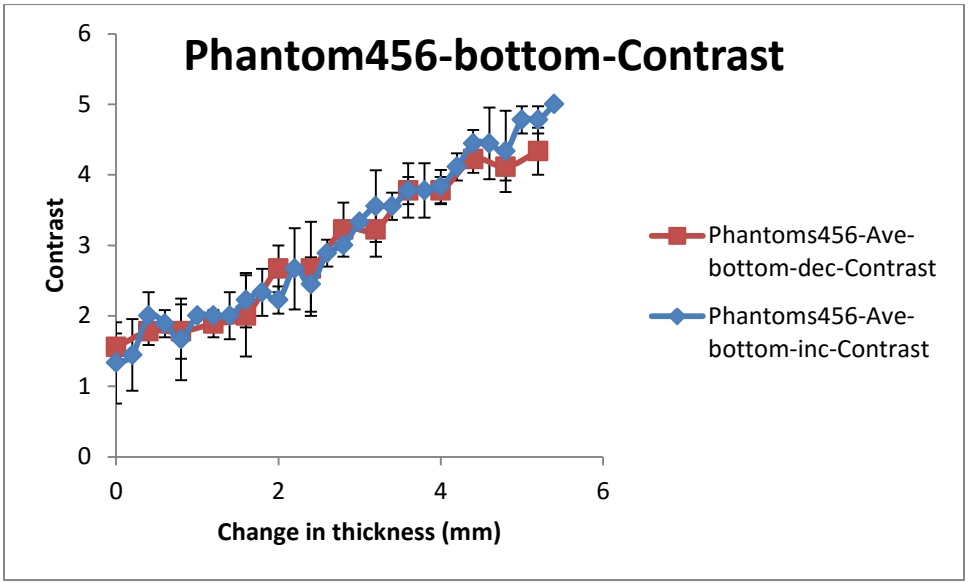

Figure G.12 Average contrast of the bottom lesions for phantoms 4, 5 and 6

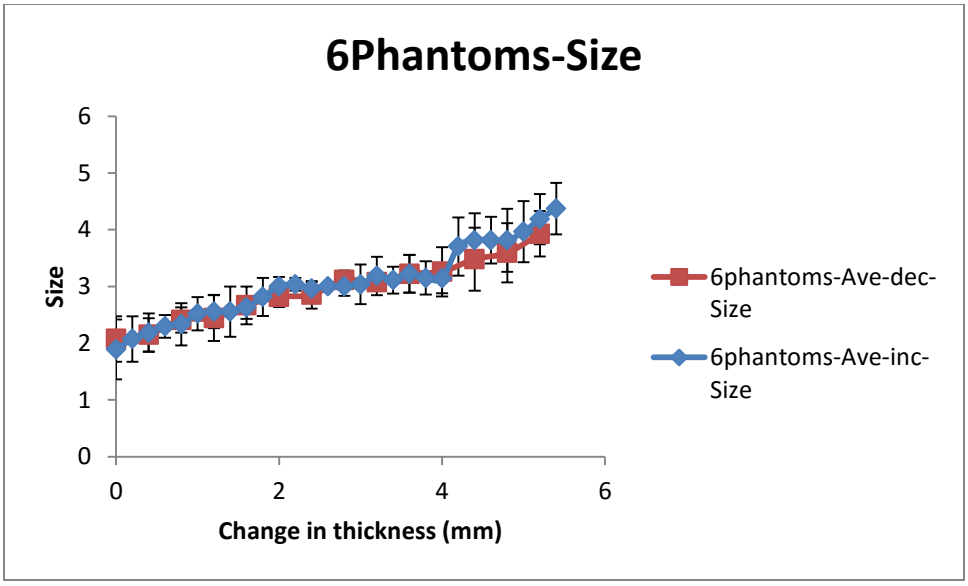

Figure G.13 Average size of the lesions for 6 phantoms

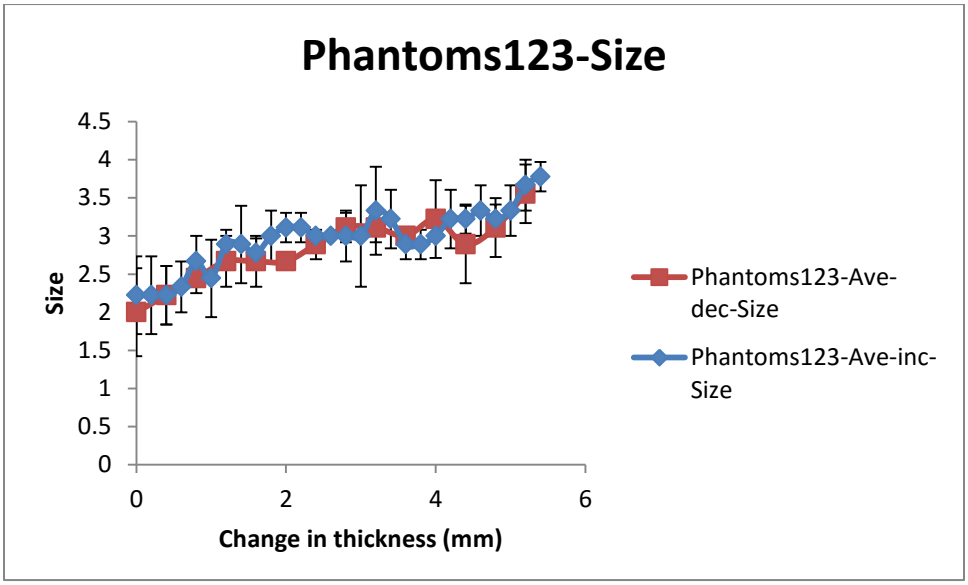

Figure G.14 Average size of the lesions for phantoms 1, 2 and 3

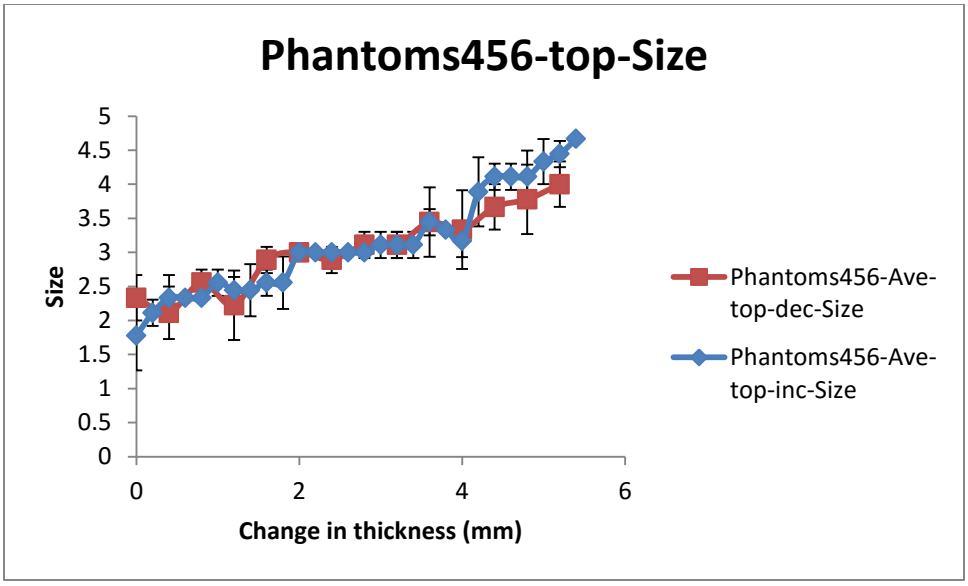

Figure G.15 Average size of the top lesions for phantoms 4, 5 and 6

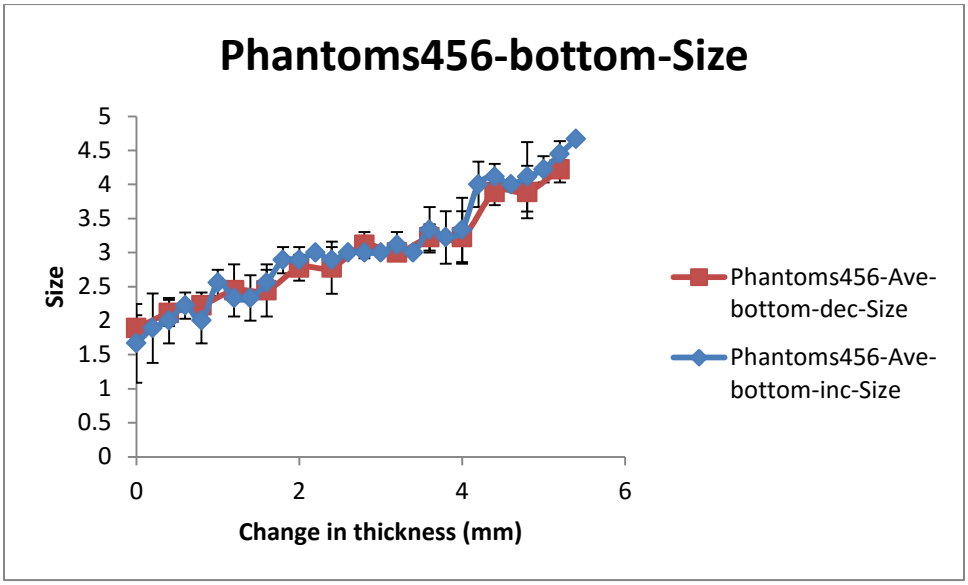

Figure G.16 Average size of the bottom lesions for phantoms 4, 5 and 6

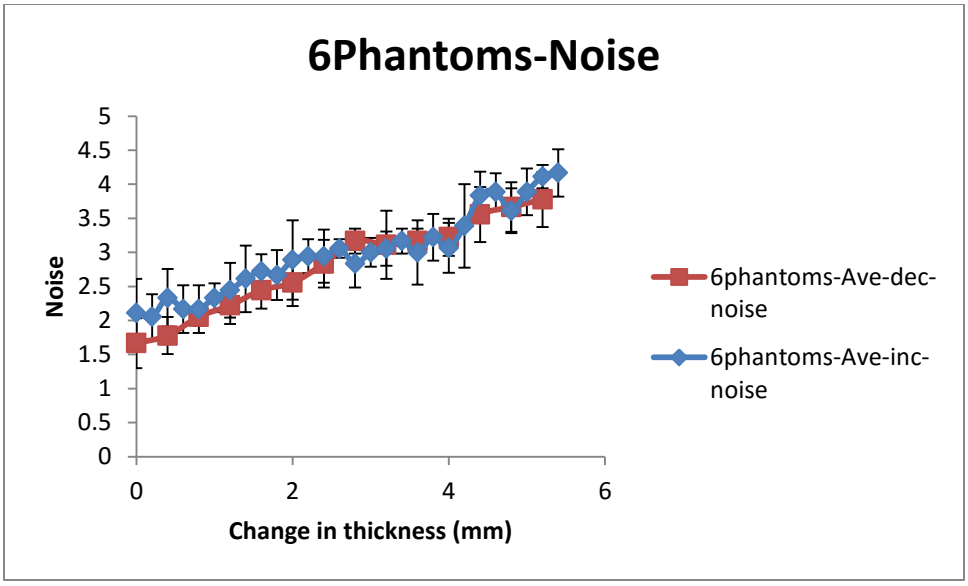

Figure G.17 Average noise for 6 phantoms

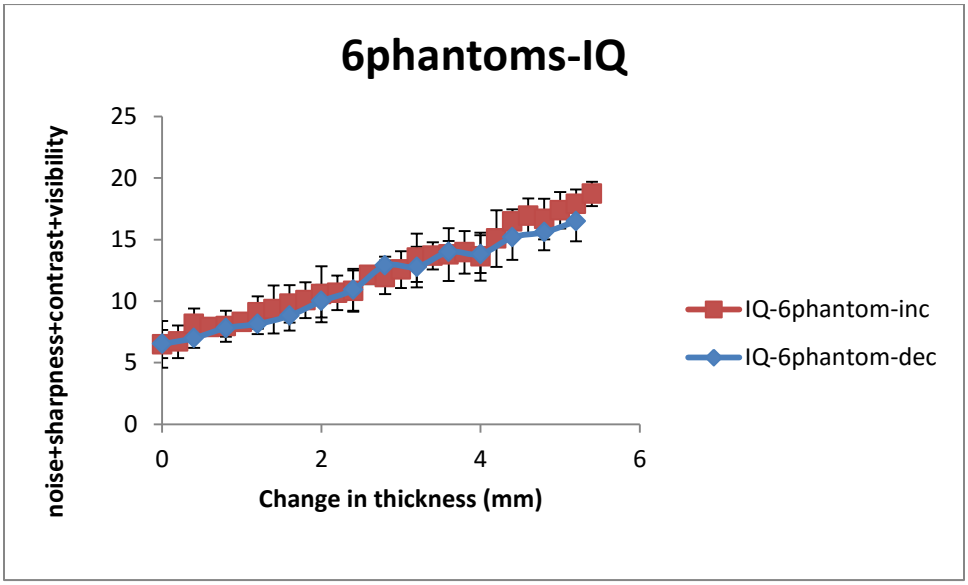

Figure G.18 Average Image Quality (IQ) for 6 phantoms

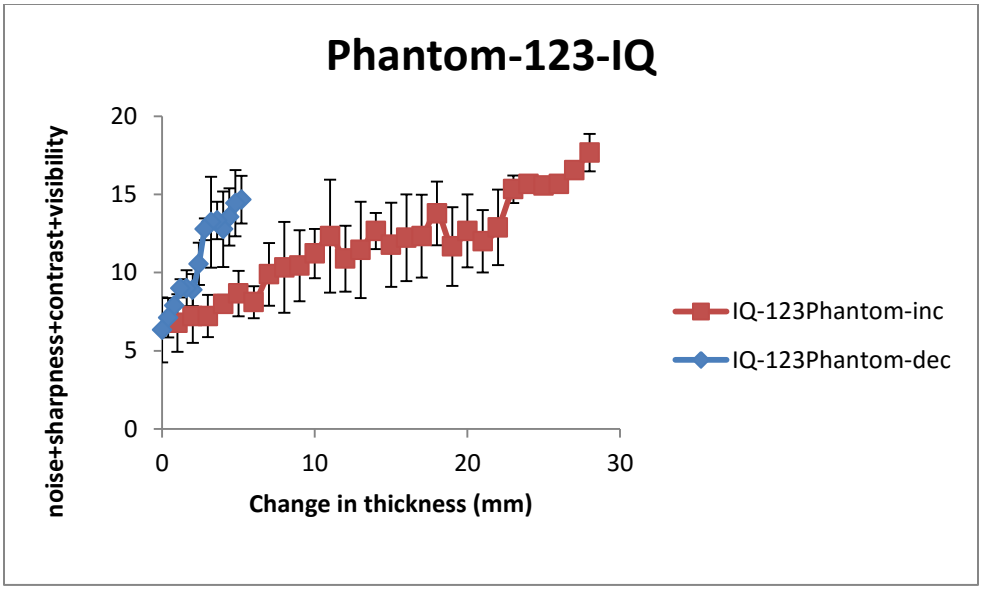

Figure G.19 Average Image Quality (IQ) for phantoms 1, 2 and 3

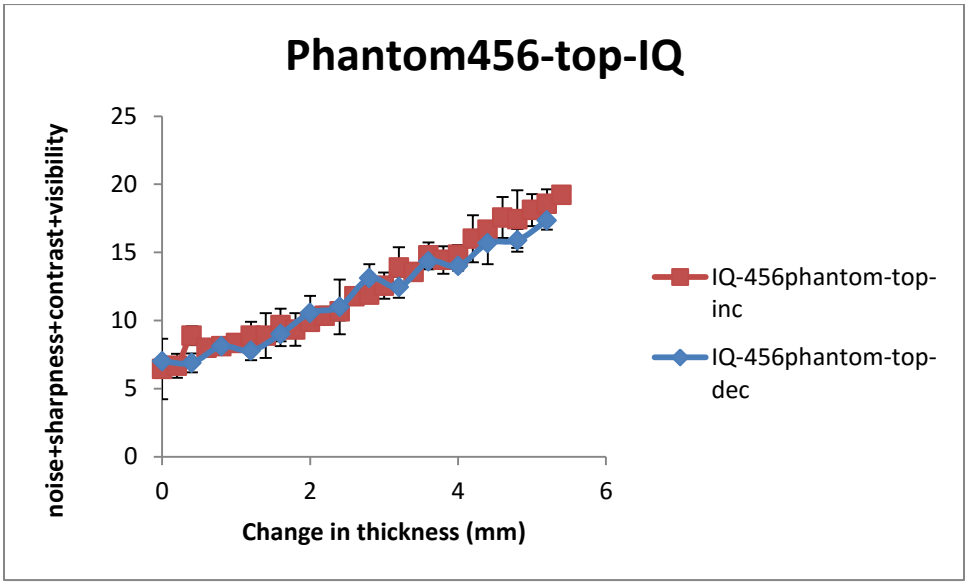

Figure G.20 Average Image Quality (IQ) of the top lesions for phantoms 4, 6 and 6

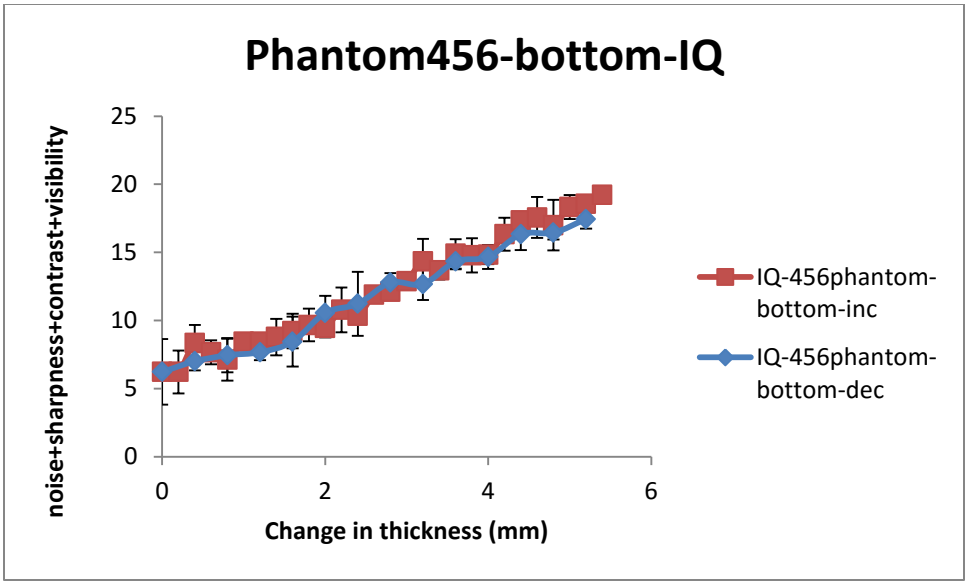

Figure G.21 Average Image Quality (IQ) of the bottom lesions for phantoms 4, 5 and 6

APPENDIX H: INTRACLASS CORRELATION COEFFICIENT

Software	MedCalc 15.6.1
Number of raters (observers or readers)	3
Number of subjects	24 for increased compression force (inc) and 14 for the decreased compression force (dec)
Model of Intraclass Correlation Coefficient (ICC)	The same raters for all subjects. Two-way model.
Type of the test	Consistency and absolute agreement

Table I.1 Software details for intraclass correlation coefficient

Phantoms-Visibility	Consistency	95% confidence Interval	Absolute agreement	95% confidence Interval
Phantom1-inc	0.9274	0.8640 to 0.9640	0.9282	0.8660 to 0.9643
Phantom1-dec	0.9418	0.8573 to 0.9797	0.9438	0.8636 to 0.9804
Phantom2-inc	0.8782	0.7719 to 0.9396	0.8780	0.7728 to 0.9394
Phantom2-dec	0.5781	-0.03422 to 0.8531	0.5931	-0.03286 to 0.8605
Phantom3-inc	0.9008	0.8142 to 0.9508	0.8865	0.7796 to 0.9447
Phantom3-dec	0.9395	0.8516 to 0.9789	0.9428	0.8599 to 0.9801
Phantom4-top-inc	0.9299	0.8687 to 0.9653	0.9313	0.8716 to 0.9659
Phantom4-bottom-inc	0.9598	0.9247 to 0.9801	0.9594	0.9244 to 0.9798
Phantom4-top-dec	0.9157	0.7935 to 0.9707	0.9189	0.8025 to 0.9717
Phantom4-bottom-dec	0.9536	0.8861 to 0.9838	0.9478	0.8712 to 0.9819
Phantom5-top-inc	0.9633	0.9313 to 0.9818	0.9593	0.9217 to 0.9801
Phantom5-bottom-inc	0.9637	0.9321 to 0.9820	0.9628	0.9306 to 0.9815
Phantom5-top-dec	0.9040	0.7647 to 0.9666	0.9079	0.7751 to 0.9679
Phantom5-bottom-dec	0.9276	0.8225 to 0.9748	0.9291	0.8285 to 0.9752
Phantom6-top-inc	0.9793	0.9609 to 0.9899	0.9789	0.9601 to 0.9896
Phantom6-bottom-inc	0.9672	0.9378 to 0.9840	0.9645	0.9320 to 0.9828
Phantom6-top-dec	0.8996	0.7539 to 0.9650	0.9055	0.7669 to 0.9672
Phantom6-bottom-dec	0.9297	0.8276 to 0.9755	0.9321	0.8350 to 0.9763

Table I.2 Intraclass correlation coefficient for the visibility

Phantoms-Sharpness	Consistency	95% confidence Interval	Absolute agreement	95% confidence Interval
Phantom1-inc	0.9251	0.8598 to 0.9629	0.9183	0.8450 to 0.9598
Phantom1-dec	0.9122	0.7848 to 0.9694	0.9172	0.7963 to 0.9712
Phantom2-inc	0.8619	0.7412 to 0.9315	0.8531	0.7256 to 0.9270
Phantom2-dec	0.4658	-0.3096 to 0.8140	0.4814	-0.3328 to 0.8231
Phantom3-inc	0.9073	0.8264 to 0.9541	0.8860	0.7650 to 0.9460
Phantom3-dec	0.9309	0.8307 to 0.9760	0.9246	0.8169 to 0.9736
Phantom4-top-inc	0.9198	0.8498 to 0.9603	0.9215	0.8531 to 0.9610
Phantom4-bottom-inc	0.9581	0.9215 to 0.9792	0.9576	0.9211 to 0.9789
Phantom4-top-dec	0.9163	0.7947 to 0.9708	0.9175	0.8007 to 0.9711
Phantom4-bottom-dec	0.9305	0.8295 to 0.9758	0.9281	0.8270 to 0.9748
Phantom5-top-inc	0.9599	0.9249 to 0.9801	0.9535	0.9076 to 0.9776
Phantom5-bottom-inc	0.9594	0.9239 to 0.9799	0.9573	0.9200 to 0.9789
Phantom5-top-dec	0.9414	0.8563 to 0.9796	0.9414	0.8587 to 0.9795
Phantom5-bottom-dec	0.9245	0.8149 to 0.9737	0.9279	0.8240 to 0.9749
Phantom6-top-inc	0.9717	0.9463 to 0.9861	0.9709	0.9450 to 0.9857
Phantom6-bottom-inc	0.9721	0.9471 to 0.9864	0.9695	0.9412 to 0.9852
Phantom6-top-dec	0.8979	0.7497 to 0.9644	0.8992	0.7563 to 0.9647
Phantom6-bottom-dec	0.9268	0.8205 to 0.9745	0.9299	0.8291 to 0.9756

Table I.3 Intraclass correlation coefficient for the sharpness

Phantoms-Contrast	Consistency	95% confidence Interval	Absolute agreement	95% confidence Interval
Phantom1-inc	0.9108	0.8329 to 0.9558	0.8982	0.8021 to 0.9504
Phantom1-dec	0.8765	0.6972 to 0.9570	0.8820	0.7105 to 0.9590
Phantom2-inc	0.8751	0.7661 to 0.9381	0.8614	0.7367 to 0.9317
Phantom2-dec	0.5383	-0.1318 to 0.8392	0.5493	-0.1304 to 0.8447
Phantom3-inc	0.9121	0.8354 to 0.9564	0.8866	0.7552 to 0.9475
Phantom3-dec	0.9146	0.7907 to 0.9703	0.9074	0.7760 to 0.9675
Phantom4-top-inc	0.9087	0.8291 to 0.9548	0.9113	0.8337 to 0.9561
Phantom4-bottom-inc	0.9572	0.9199 to 0.9788	0.9580	0.9216 to 0.9792
Phantom4-top-dec	0.8793	0.7041 to 0.9580	0.8870	0.7193 to 0.9609
Phantom4-bottom-dec	0.9488	0.8745 to 0.9822	0.9350	0.8266 to 0.9780
Phantom5-top-inc	0.9694	0.9427 to 0.9848	0.9647	0.9300 to 0.9830
Phantom5-bottom-inc	0.9639	0.9324 to 0.9821	0.9630	0.9309 to 0.9816
Phantom5-top-dec	0.9281	0.8236 to 0.9749	0.9238	0.8163 to 0.9733
Phantom5-bottom-dec	0.9262	0.8191 to 0.9743	0.9274	0.8245 to 0.9746
Phantom6-top-inc	0.9718	0.9466 to 0.9862	0.9697	0.9421 to 0.9853
Phantom6-bottom-inc	0.9638	0.9314 to 0.9823	0.9618	0.9275 to 0.9814
Phantom6-top-dec	0.8869	0.7228 to 0.9606	0.8901	0.7328 to 0.9616
Phantom6-bottom-dec	0.9299	0.8281 to 0.9756	0.9305	0.8323 to 0.9757

Table I.4 Intraclass correlation coefficient for contrast

Phantoms-noise	Consistency	95% confidence Interval	Absolute agreement	95% confidence Interval
Phantom1-inc	0.4720	0.01097 to 0.7382	0.4650	0.01563 to 0.7321
Phantom1-dec	0.8465	0.6237 to 0.9465	0.8477	0.6320 to 0.9467
Phantom2-inc	0.8192	0.6613 to 0.9104	0.7865	0.5855 to 0.8959
Phantom2-dec	0.4265	-0.4060 to 0.8003	0.4417	-0.4398 to 0.8099
Phantom3-inc	0.8615	0.7405 to 0.9313	0.7812	0.4550 to 0.9056
Phantom3-dec	0.7939	0.4946 to 0.9282	0.7915	0.4999 to 0.9268
Phantom4-inc	0.7241	0.4832 to 0.8632	0.7185	0.4788 to 0.8595
Phantom4-dec	0.8660	0.6716 to 0.9534	0.8652	0.6757 to 0.9527
Phantom5- inc	0.8481	0.7156 to 0.9247	0.8475	0.7160 to 0.9241
Phantom5- dec	0.9173	0.7973 to 0.9712	0.9219	0.8082 to 0.9729
Phantom6- inc	0.9244	0.8568 to 0.9631	0.9222	0.8534 to 0.9619
Phantom6- dec	0.8927	0.7369 to 0.9626	0.8943	0.7443 to 0.9630

Table I.5 Intraclass correlation coefficient for noise

Phantoms-Size	Consistency	95% confidence Interval	Absolute agreement	95% confidence Interval
Phantom1-inc	0.4798	0.02564 to 0.7421	0.4813	0.02914 to 0.7428
Phantom1-dec	0.5956	0.008587 to 0.8592	0.5806	0.02425 to 0.8506
Phantom2-inc	0.1823	-0.5317 to 0.5946	0.1818	-0.5263 to 0.5935
Phantom2-dec	0.3458	-0.6038 to 0.7722	0.3458	-0.5878 to 0.7714
Phantom3-inc	0.7136	0.4635 to 0.8580	0.7199	0.4718 to 0.8617
Phantom3-dec	0.6321	0.09820 to 0.8719	0.6299	0.1116 to 0.8701
Phantom4-top-inc	0.8513	0.7215 to 0.9263	0.8542	0.7269 to 0.9277
Phantom4-bottom-inc	0.9247	0.8589 to 0.9626	0.9184	0.8456 to 0.9597
Phantom4-top-dec	0.8396	0.6068 to 0.9442	0.7888	0.4658 to 0.9269
Phantom4-bottom-dec	0.8219	0.5634 to 0.9380	0.7983	0.5191 to 0.9288
Phantom5-top-inc	0.8404	0.7011 to 0.9209	0.8272	0.6764 to 0.9143
Phantom5-bottom-inc	0.8540	0.7266 to 0.9276	0.8544	0.7286 to 0.9277
Phantom5-top-dec	0.8433	0.6159 to 0.9454	0.8443	0.6239 to 0.9455
Phantom5-bottom-dec	0.8135	0.5428 to 0.9351	0.7977	0.5201 to 0.9285
Phantom6-top-inc	0.8968	0.8045 to 0.9496	0.8907	0.7932 to 0.9465
Phantom6-bottom-inc	0.8184	0.6559 to 0.9113	0.8217	0.6620 to 0.9129
Phantom6-top-dec	0.5692	-0.05611 to 0.8500	0.5835	-0.05520 to 0.8571
Phantom6-bottom-dec	0.6745	0.2019 to 0.8866	0.6896	0.2146 to 0.8934

Table I.6 Intraclass correlation coefficient for size

APPENDIX I: MAMMOGRAPHY UNIT ADDITIONAL INFORMATION

X-ray tube

X-rays are produced in an X-ray tube. Within the X-ray tube, the main structures involved in generating X-rays are cathodes and anodes. The cathode filament is the negative electrode in the X-ray tube which expels electrons to the target electrode or anode with a positive charge. Most of the energy of the electrons is converted into undesirable heat upon striking the anode. Only a small fraction of the energy produces the X-rays which are generated via interactions of the accelerated electrons emitting from the cathode with the electrons of the target anode. X-rays are generated in two ways: Bremsstrahlung and characteristic (Bushberg, Seibert, Leidholdt, & Boone, 2012) .

In a mammographic X-ray tube, molybdenum (Mo, Z = 42) and rhodium (Rh, Z = 45) as anode materials are utilised. These materials are suitable to produce characteristic radiation for breast imaging (Bushberg, Seibert, Leidholdt, & Boone, 2012).

X-ray production: Bremsstrahlung radiation

Bremsstrahlung or braking radiation is the result of the interaction of high energy electrons with a negative charge and the nucleus of the atoms of the target material which have a positive charge. Due to the coulomb attraction between the opposite charges, an electron decelerates and deviates from its path. This deceleration causes the electron to lose its kinetic energy. Due to the laws of conservation of momentum, the loss of the kinetic energy of the electron is then converted into an X-ray. Figure I.1 illustrates, the X-rays which have been produced from the interactions between the nucleus and the electrons emitting from the cathode (Bushberg, Seibert, Leidholdt, & Boone, 2012).

The energy of the X-ray is dependent upon the influence of the nucleus on the incoming electrons (Cherry & Duxbury, 2009). As Figure I.1 displays, the deviated

electrons closer to the nucleus produce high energy X-rays compared to the ones which are farther and less influenced by the nucleus.

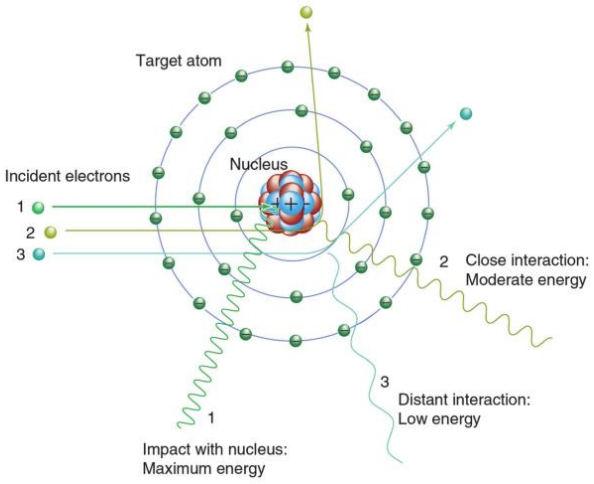

Figure I.1 Bremsstrahlung radiation (Bushberg, Seibert, Leidholdt, & Boone, 2012)

X-ray production: Characteristic radiation

In characteristic radiation, an accelerating incident electron interacts with shell electrons (i.e. K, L, and M). If the energy of the incident electron is greater than the K-shell binding energy, the K-shell electron is removed from its shell. This removal of the K-shell electron leaves a vacancy in that shell. This vacancy is then filled by an electron from one of the higher energy (lower binding energy) shells such as the L-shell (Figure I.2). At the same time, a characteristic X-ray photon is emitted from the atom with an energy level equal to the difference between the binding energies of the two shells (K and L) (Bushberg, Seibert, Leidholdt, & Boone, 2012).

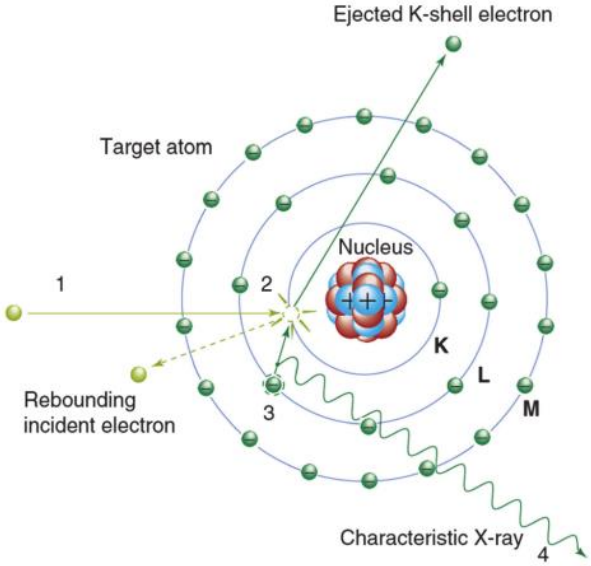

Figure I.2 Characteristics radiation (Bushberg, Seibert, Leidholdt, & Boone, 2012)

Focal spots in mammography

In X-ray tubes typically there are two filaments with different lengths: small and large. Each filament is located in a place called focusing cup. During the imaging procedure, only one of these filaments gets voltage. Depending of the nature of the examination, one of these filaments can be manually or automatically selected for the imaging procedure. Figure I.3 illustrates these focal spot filaments (Bushberg, Seibert, Leidholdt, & Boone, 2012).

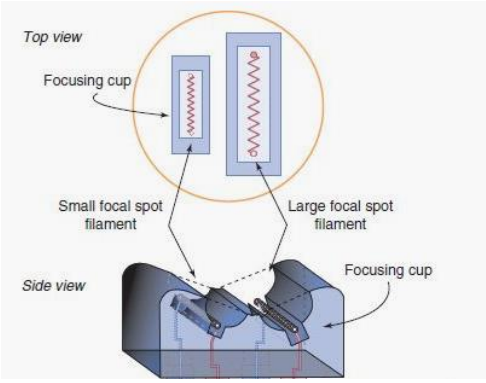

Figure I.3 Small and large focal spot filaments (Bushberg, Seibert, Leidholdt, & Boone, 2012)

In mammography, high resolution mammograms are substantially important in order to detect the lesions and other breast features. Improving the sharpness and reducing the blurring of the image can be influenced by the size of the focal spots. In order to reduce the geometric blurring, the size of the focal spot and the distance between the breast and image detector need to be reduced, the distance between the breast and the focal spot should be kept maximized. It is recommended that the focal spot size should not be greater than 0.3 mm (Paredes, 2007).

A typical mammography unit has two types of focal spots: large and small. A 0.3 mm large focal spot is generally utilised for routine mammography while a 0.1 mm focal spot is used for magnification images (Carlton & Adler, 2012).

Collimator

A collimator is a device which limits the exposure of the X-ray beam to the breast by adjusting the size and shape of the X-ray field. It encloses the area of the radiation in order to prevent exposure of X-rays to other parts of the body. The collimator assembly is attached to the tube housing at the tube port. The rectangular X-ray field is specified by two pairs of the lead shutters (Figure I.4). Typically the collimator can be adjusted by a

light beam reflected from a mirror above the lead shutters (Bushberg, Seibert, Leidholdt, & Boone, 2012).

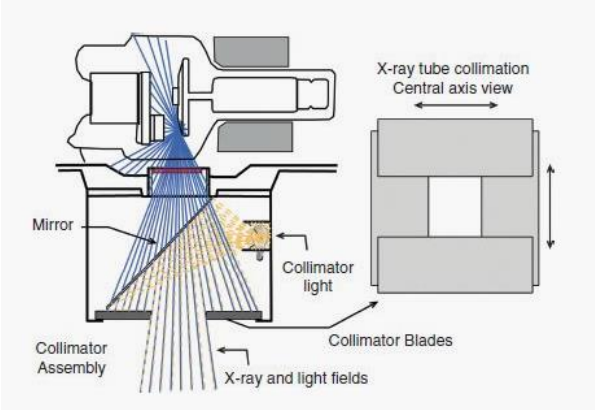

Figure I.4 Collimator in mammography unit (Bushberg, Seibert, Leidholdt, & Boone, 2012)

The misalignment of collimator compared to the detector can generate a vertical white bar artefact in the mammogram as is shown in Figure I.5 (Ayyala, Chorlton, Behrman, Kornguth, & Slanetz, 2008).

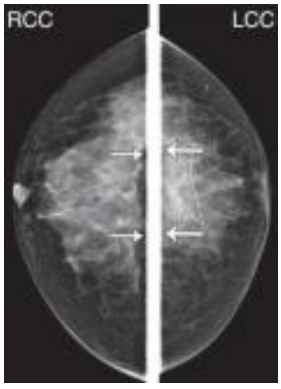

Figure I.5 RCC (a) LCC (b) solid vertical white line (Ayyala, Chorlton, Behrman, Kornguth, & Slanetz, 2008)

Field of View

In FFDM, field of view (FOV) is a parameter which can be defined by the mammographer. This parameter controls the size of the anatomical area to be imaged (Markey, 2013).

The field of view needs to be large enough in order to cover the various breast sizes. The areas of interest can be missed if the FOV is not large enough (Smith, 2003). The following image (Figure I.6) shows the FOV and the pixel size using various detector types.

DETECTOR TYPE	FOV (cm)	PIXEL SIZE (mm)
Indirect TFT	19 × 23	0.10
Indirect TFT	24 × 31	0.10
Direct TFT	18 × 24	0.07
Direct TFT	24 × 29	0.07
CR	18 × 24	0.05
CR	24 × 30	0.05

Figure I.6 FOV and the pixel size using various detectors (Bushberg, Seibert, Leidholdt, & Boone, 2012)

Grid

One of the reasons for the deterioration of the contrast resolution is X-ray scattering from the breast tissue. X-ray scattering can degrade the mammograms and hide the subtle breast features by generating a noisy background. Changes in the background result in a decrease of the contrast, leading to a reduction of contrast to noise ratio (CNR). In order to address this problem, an instrument called anti scatter grid is employed in mammography (Fieselmann, Fischer, Hilal, Dennerlein, Mertelmeier, & Uhlenbrock, 2013).

An anti-scatter grid is typically located between the detector and the patient. The following image (Figure I.7) demonstrates the structure of a grid. As the image shows, a grid comprised of alternating layers of interspace and septa materials. The septa part of the grid is typically made up of lead. The specific alignment of the interspace and septa

materials let the primary radiation beam pass through the grid. It also absorbs the scattered radiation (Bushberg, Seibert, Leidholdt, & Boone, 2012).

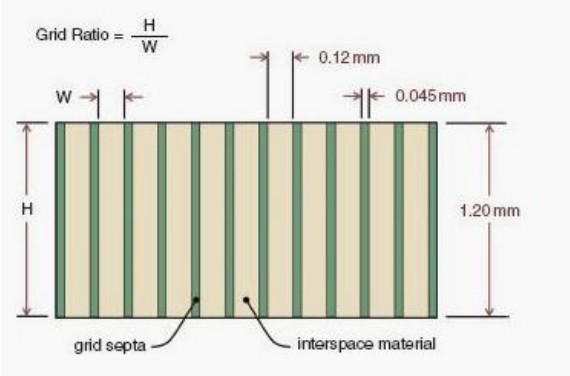

Figure I.7 Anti-scatter grid (Bushberg, Seibert, Leidholdt, & Boone, 2012)

Grid ratio is a parameter to characterize the anti-scatter grid. This parameter is measured by the ratio of the height of the interspace material to its width. The grid ratio is about 5 in mammography which is lower than general diagnostic radiology (Bushberg, Seibert, Leidholdt, & Boone, 2012).

One of the major problems using anti scatter grids is the attenuation of the primary beams as well as the scattered ones. In order to compensate for the lost primary beam, more photons are required thus leading to a higher patient dose (Fieselmann, Fischer, Hilal, Dennerlein, Mertelmeier, & Uhlenbrock, 2013).

Mammographic monitors

The widespread application of FFDM in breast screening and diagnostic purposes requires optimal monitors for displaying the mammograms. Cathode ray tube (CRT) and liquid crystal display (LCD) monitors are used in mammography. CRT monitors have become less desirable because of the following reasons: low luminescence (300 cd/m^2), requiring ambient light, short life expectancy (about 30,000 hours), eye fatigue due to the constant refreshed screen, degraded resolution in some areas of the screen, high heat

output, and heavy weight (about 40 lb [18 kg] each). LCD monitors are coming into favor because of the following advantages: Lightweight (<15 lb [7 kg]), longer life expectancy, uniform resolution due to the use of TFTs, no concern regarding the refresh rates, better resolution and better luminescence (700 cd/m2) (Zuley, et al., 2006).

According to a study by Margarita L. Zuley et al. , The LCD monitors are better for detecting the mass margins and conspicuity, but CRT monitors are better for image noise (Zuley, et al., 2006).The resolution in an LCD monitor typically ranges from 1-5 megapixel (MP), however higher resolution monitors (>9MP) have started being available (Indrajit & Verma, 2009). Since digital mammography requires the highest resolution in order to see the subtle lesions and calcifications, it is highly recommended to use minimum 5MP monitors (Hardy, 2012). The following image (Figure I.8) illustrates a 5 MP diagnostic display for FFDM.

Figure I.8 5MP diagnostic mammography monitors employed in FFDM (MD Publishing Inc., 2012)

Acronyms

2AFC: Two-alternative forced choice

ADC: Analogue to digital convertor

AEC: Automatic Exposure Control

AUC: The area under the ROC curve

CA: Contrast Agent

CAD: Computer-aided diagnosis

CBCT: Cone beam computed tomography

CCD: Charge-coupled device

CMOS: Complementary metal oxide semiconductor

CNR: Contrast to Noise Ratio

CR: Computed radiography

CsI:Tl: Thallium-activated caesium iodide

CT: Computed Tomography

cy/mm: cycles per millimetre (similar to line-pairs/mm)

DCIS: Ductal Carcinoma In Situ

DDR: Direct digital radiography

DEL: Detector Element

DBT: Digital breast tomosynthesis

DICOM: Digital Imaging and Communications in Medicine

DR: Digital radiography

DQE: Detective quantum efficiency

FDA: Food and Drug Administration

FFDM: Full Field Digital Mammography

FTC: Freeze Thaw Cycle

GPa: Giga Pascal

HD: High Density

HU: Hounsfield Unit

IDC: Invasive Ductal Carcinoma

IAEA: International Atomic Energy Agency

ICC: Intraclass Correlation Coefficient

ILC: Invasive Lobular Carcinoma

IP: Image Plate

keV: Kiloelectron volt

kPa: kilo Pascal

LCIS: Lobular Carcinoma In Situ

LD: Low Density

MDCT: Multidetector Computed Tomography

MGD: Mean Glandular Dose

mGy: Milligray

Mo: Molybdenum

MPa: Mega Pascal

MTF: Modulation transfer function

NPS: Noise Power Spectrum

Pa: Pascal

PGMI: Perfect, Good, Moderate, Inadequate

PMT: Photomultiplier Tube

PSP: Photostimulable phosphor

PVAL: Polyvinyl alcohol

Rh: Rhodium

ROC: Receiver operating characteristic

ROI: Region of Interest

RPM: Revolutions Per Minute

sd: Standard deviation

SDNR: Signal Difference to Noise Ratio

SF: Screen film

SNR: Signal to Noise Ratio

SSCT: Single Slice Computed Tomography

TFT: Thin-film transistor

TMM: Tissue-mimicking material

WL: Window Length

WS: Wiener spectra

wt%: weight percent

WW: Window Width

YM: Young's modulus

Glossary

Air Kerma: The sum of kinetic energy of all charged particles liberated per unit mass when X-rays/gamma rays pass through unit mass of air. Kerma stands for Kinetic Energy Released per unit Mass.

Anthropomorphic: Giving a non-human object human characteristics

Attenuation coefficient: The attenuating ability of a medium. Attenuation coefficient or μ is a quantity which indicates how easily an object can be penetrated by an X-ray beam.

DICOM: Digital Imaging and Communications in Medicine is the standard for communicating, viewing, and management of digital medical images.

Echogenicity: The ability of bouncing an echo. In ultrasound imaging, the way the ultrasound wave is bounced to the transducer is called echogenicity. Each tissue has a particular echogenicity. The echogenicity of a diseased organ such as liver can be different than the normal liver.

Exposure latitude: Exposure latitude is the range of exposure factors that will produce an acceptable image.

Fovea centralis: A shallow pit in the centre of the retina that is free of blood vessels and has the highest concentration of cells sensitive to colour and bright light cones. The fovea centralis is the area of most acute vision.

Hydrophilic: Having an affinity for water or water-loving. The compounds which have polar sides in their structures that attract water

Hyperelasticity: This is a model in mechanics which describes the stress-strain behaviour of materials such as rubber.

Image quality figure (IQF): Image quality figure is calculated from the minimum depth and diameter of the air-filled holes in a contrast detailed phantom that the observers can detect. A lower IQF represents better image quality.

Juxtathoracic: The area of the body near the thorax

Line Spread Function: A method to measure the spatial resolution of an imaging system. In this method, a strip of an object (a thin line) is imaged. Since the imaging system is not able to display the line perfectly without adding blurring into the image, the final image will include some degree of blurring. This degree of blurring is represented by line spread function.

Scintillator: A scintillator is a material that produces light when it is exposed to the ionising radiation such as X-rays. Scintillator absorbs the energy of the radiation and re-emits the absorbed energy in the form of light.

Screen film: In screen film radiography, the image receptor consists of the film and one or two intensifying screens which are encased in a cassette. The intensifying screens are made of fluorescent materials such as phosphor. The X-ray energy is absorbed by the intensifying screens and part of it converted to light. The emitted light then exposes the film.

Subdivision surfaces: A method to generate smooth curves/surfaces using a basic mesh such as polygonal through an iterative process.

Telemammography: The secure transfer of mammograms from one location to another.

Uniform Rational B-splines (NURBS): A mathematical model widely used in computer graphics systems for generating and representing curves/surfaces.

References

Acton, A. (2013). *Issues in Applied Physics.* Atlanta, Georgia: ScholarlyEditions.

Aljarrah, A., & Miller, W. (2014). Trends in the distribution of breast cancer over time in the southeast of Scotland and review of the literature. *ecancermedicalscience, 8*.

Allen, E., Hogg, P., Ma, W. K., & Szczepura, K. (2013). Fact or fiction: An analysis of the 10 kVp 'rule' in computed radiography. *Radiography*, 223–227.

Almeida, C. D., Coutinho, C. M., Peixoto, J. E., & Dantas, B. M. (2009). Study of the attenuation coefficient of a breast phantom used in diagnostic radiology. *International Nuclear Atlantic Conference.*

Altair Engineering. (2010). HyperMesh 10.0, User Manual.

American Cancer Society. (2014, January 31). *Breast Cancer Overview.* Retrieved August 19, 2014, from http://www.cancer.org/: http://www.cancer.org/acs/groups/cid/documents/webcontent/003037-pdf.pdf

American Cancer Society. (2014). *Mammograms and Other Breast Imaging Tests* . Retrieved from http://www.cancer.org/: http://www.cancer.org/acs/groups/cid/documents/webcontent/003178-pdf.pdf

AnalyzeDirect. (2010). Analyze 10.0 Essential Training Guide.

Andolina, V., & Lillé, S. (2010). *Mammographic Imaging: A Practical Guide* (Third ed.). Lippincott Williams & Wilkins.

Andolina, V., & Lillé, S. (2011). *Mammographic Imaging: A Practical Guide.* Lippincott Williams & Wilkins.

AR Custom Medical Products. (2007). *Custom Compression Paddles*. Retrieved July 24, 2014, from http://www.arcustommedical.com/: http://www.arcustommedical.com/products.htm

Artinis Medical Systems. (2014). *CDMAM 3.4*. Retrieved from http://www.artinis.com/: http://www.artinis.com/product/cdmam_34

Artinis Medical Systems. (n.d.). *CDMAM 3.4*. Retrieved August 28, 2014, from http://www.artinis.com: http://www.artinis.com/product/cdmam_34

Astley, S. M. (2006). *Digital Mammography: 8th International Workshop, IWDM 2006, Manchester, UK.* Springer.

Ayyala, R. S., Chorlton, M., Behrman, R. H., Kornguth, P. J., & Slanetz, P. J. (2008). Digital Mammographic Artifacts on Full-Field Systems: What Are They and How Do I Fix Them? *RadioGraphics*, 1999-2008.

Azar, F. S., Metaxas, D. N., & Schnall, M. D. (2000). A finite element model of the breast for predicting mechanical deformations during biopsy procedures. *MMBIA*, 38 - 45.

Azar, F. S., Metaxas, D. N., & Schnall, M. D. (2001). A Deformable Finite Element Model of the Breast for Predicting Mechanical Deformations under External Perturbations. *Academic Radiology, 8*(10), 965–975.

Azar, F. S., Metaxas, D. N., & Schnall, M. D. (2002). Methods for modeling and predicting mechanical deformations of the breast under external perturbations. *Medical Image Analysis, 6*, 1–27.

Bajpai, A., & Saini, R. (2005). Preparation and characterization of biocompatible spongy cryogels of poly(vinyl alcohol)–gelatin and study of water sorption behaviour. *Polymer International, 54*(9), 1233-1242.

Baldelli, P., Phelan, N., & Egan, G. (2010). Investigation of the effect of anode/filter materials on the dose and image quality of a digital mammography system based on an amorphous selenium flat panel detector. *The British Journal of Radiology, 83*(988), 290–295.

Bassett, L. W. (2000). Chapter 30F, Imaging the Breast. In R. J. Bast, D. Kufe, & R. Pollock (Eds.), *Holland-Frei Cancer Medicine* (5 ed.). Hamilton, Ontario, Canada: BC Decker.

Bassett, L. W., Jackson, V., Fu, K., & Fu, Y. (2004). *Diagnosis of Diseases of the Breast* (Second ed.). Saunders.

Bast, R. C., Bast, R. C., & Holland, J. F. (2000). *Holland-Frei Cancer Medicine. 5th edition* (5 ed.). B.C. Decker.

Beam, C., Layde, P., & Sullivan, D. (1996, Jan 22). Variability in the interpretation of screening mammograms by US radiologists. Findings from a national sample. *Archives of Internal Medicine, 156*(2), 209-213.

Benchimol, D., Näsström, K., & Shi, X. (2009). Evaluation of automatic exposure control in a direct digital intraoral system. *Dentomaxillofacial Radiology, 38*(6), 407–412.

Bird, R., Wallace, T., & Yankaskas, B. (1992, September). Analysis of cancers missed at screening mammography. *Radiology, 184*(3), 613-617.

Blindell, P., & Hogg, P. (2012). Software for image quality evaluation using a forced choice method. (p. 139). Manchester: United Kingdom Radiological Congress.

Bliznakova, K., Bliznakov, Z., Bravou, V., Kolitsi, Z., & Pallikarakis, N. (2003). A three-dimensional breast software phantom for mammography simulation. *Phys. Med. Biol, 48*, 3699–3719.

Bonakdar, S., Emami, S. H., Shokrgozar, M. A., Farhadi, A., Ahmadi, S. A., & Amanzadeh, A. (2010). Preparation and characterization of polyvinyl alcohol hydrogels crosslinked by biodegradable polyurethane for tissue engineering of cartilage. *Materials Science and Engineering: C, 30*, 636-643.

Boone, J. M., Fewel, T. R., & Jennings, R. J. (1997). Molybdenum, rhodium, and tungsten anode spectral models using interpolating polynomials with application to mammography. *Med. Phys*, 1863-1874.

Boone, J. M., Nelson, T. R., Lindfors, K. K., & Seibert, J. A. (2001). Dedicated Breast CT: Radiation Dose and Image Quality Evaluation. *Radiology, 221*(3), 657-667.

Bor, D., Tükel, S., Olgar, T., & Aydın, E. (2008). Variations in breast doses for an automatic mammography unit. *Diagnostic and Interventional Radiology, 14*, 122-126.

Borg, M., Badr, I., & Royle, G. J. (2011). The use of a figure-of-merit (FOM) for optimisation in digital mammography: a literature review. *Radiation Protection Dosimetry*, 81-88.

Brant, W. E., & Helms, C. A. (2012). Breast Imaging. In *Fundamentals of Diagnostic Radiology* (Fourth ed.). Wolters Kluwer.

Breast Cancer Care. (2014, April 03). *Breast calcifications*. Retrieved August 15, 2014, from http://www.breastcancercare.org.uk/: http://www.breastcancercare.org.uk/breast-cancer-information/breast-awareness/benign-breast-conditions/breast-calcifications

Broeders, M. J., Ten Voorde, M., Veldkamp, W. J., van Engen, R. E., van Landsveld – Verhoeven, C., 't Jong – Gunneman, M. N., et al. (2015). Comparison of a flexible versus a rigid breast compression paddle: pain experience, projected breast area, radiation dose and technical image quality. *European Radiology, 25*(3), 821–829.

Bro-nielsen, M. (1998). Finite Element Modeling in Surgery Simulation. *Proceedings of the IEEE, 86*(3), 490 - 503.

Brooks, L., & Morley, M. (2013, May 14). *Digital Mammography Cancer Detection Rates May Vary*. Retrieved from http://www2.rsna.org/: http://www2.rsna.org/timssnet/media/pressreleases/PDF/pressreleasePDF.cfm?ID=669

Buist, D., Porter, P., Lehman, C., Taplin, S., & White, E. (2004, October 6). Factors contributing to mammography failure in women aged 40-49 years. *Journal of the National Cancer Institute, 96*(19), 1432-1440.

Burgess, A. E., Jacobson, F. L., & Judy, P. F. (2001, April). Human observer detection experiments with mammograms and power-law noise. *Medical Physics, 28*(4), 419-437.

Burrill, J., Dabbagh, Z., Gollub, F., & Hamady, M. (2007, November). Multidetector computed tomographic angiography of the cardiovascular system. *Postgraduate Medical Journal, 83*(985), 698-704.

Bushberg, J. T., Seibert, J. A., Leidholdt, E. M., & Boone, J. M. (2011). 4.4 The Frequency Domain. In *The Essential Physics of Medical Imaging* (pp. Kindle Locations 1816-1987). Philadelphia, PA. USA: Lippincot (Wolters Kluwer Health).

Bushberg, J. T., Seibert, J. A., Leidholdt, E. M., & Boone, J. M. (2011). 4.9 Signal-to-Noise Ratio. In *The Essential Physics Of Medical Imaging* (3 ed., pp. 91-92). London: Lippincott Williams & Wilkins.

Bushberg, J. T., Seibert, J. A., Leidholdt, E. M., & Boone, J. M. (2012). 4.5 Contrast Resolution: Anatomical Noise. In *The Essential Physics of Medical Imaging* (Third ed., p. Kindle Locations 2043). Philadelphia, PA. USA: Lippincot (Wolters Kluwer Health).

Bushberg, J. T., Seibert, J. A., Leidholdt, E. M., & Boone, J. M. (2012). 4.6 Noise Texture: The Noise Power Spectrum. In *The Essential Physics of Medical Imaging* (Third ed., pp. Kindle Locations 2200-2231). Philadelphia, PA. USA: Lippincot (Wolters Kluwer Health).

Bushberg, J. T., Seibert, J. A., Leidholdt, E. M., & Boone, J. M. (2012). 5.1 Analog and Digital representation of data. In *The Essential Physics of Medical Imaging* (p. Kindle Locations 2688). Philadelphia, PA. USA: Lippincot (Wolters Kluwer Health).

Bushberg, J. T., Seibert, J. A., Leidholdt, E. M., & Boone, J. M. (2012). 6.2 X-ray tube: Cathode. In *The Essential Physics of Medical Imaging* (Third ed., pp. kindle locations 4364-4372). Philadelphia, PA. USA: Lippincot (Wolters Kluwer Health).

Bushberg, J. T., Seibert, J. A., Leidholdt, E. M., & Boone, J. M. (2012). 6.2 X-ray Tubes. In *The Essential Physics of Medical Imaging* (pp. Kindle Locations 4342-4417). Philadelphia, PA. USA: Lippincot (Wolters Kluwer Health).

Bushberg, J. T., Seibert, J. A., Leidholdt, E. M., & Boone, J. M. (2012). 6.3 X-ray Tubes . In *The Essential Physics of Medical Imaging* (pp. Kindle Locations 4350-4655). Philadelphia, PA. USA: Lippincot (Wolters Kluwer Health).

Bushberg, J. T., Seibert, J. A., Leidholdt, E. M., & Boone, J. M. (2012). 7.12 Scattered Radiation in Projection Radiographic Imaging. In *The Essential Physics of Medical Imaging* (Third ed., pp. Kindle Locations 5556-5715). Philadelphia, PA. USA: Lippincot (Wolters Kluwer Health).

Bushberg, J. T., Seibert, J. A., Leidholdt, E. M., & Boone, J. M. (2012). 8.5 Digital Mammography. In *The Essential Physics of Medical Imaging* (Third ed., pp. Kindle Locations 6277 - 6513). Philadelphia, PA. USA: Lippincot (Wolters Kluwer Health).

Bushberg, J. T., Seibert, J. A., Leidholdt, E. M., & Boone, J. M. (2012). Computed Tomography. In *The Essential Physics of Medical Imaging* (Third ed., pp. Kindle Locations 7342-7854). Philadelphia, PA. USA: Lippincot (Wolters Kluwer Health).

Bushberg, J. T., Seibert, J. A., Leidholdt, E. M., & Boone, J. M. (2012). *The essential physics of medical imaging* (3 ed.).

Bushberg, J. T., Seibert, J. A., Leidholdt, E. M., & Boone, J. M. (2012). *The Essential Physics of Medical Imaging* (Third ed.). Philadelphia, PA. USA: Lippincot (Wolters Kluwer Health).

Butler, P., Mitchell, A., & Ellis, H. (2007). *Applied Radiological Anatomy for Medical Students.* Cambridge University Press.

Canadian Cancer Society. (2014). *Mammography*. Retrieved July 22, 2014, from http://www.cancer.ca: http://www.cancer.ca/en/cancer-information/diagnosis-and-treatment/tests-and-procedures/mammography

Cancer Research UK. (2014, November). *Breast cancer*. Retrieved from http://publications.cancerresearchuk.org/: http://publications.cancerresearchuk.org/downloads/product/CS_KF_BREAST.pdf

Cancer Research UK. (2014, January 31). *Breast cancer mortality statistics*. Retrieved August 19, 2014, from http://www.cancerresearchuk.org/: http://info.cancerresearchuk.org/cancerstats/types/breast/mortality/uk-breast-cancer-mortality-statistics#sex

Cancer Research UK. (2014, July 30). *Breast cancer tests*. Retrieved August 19, 2014, from http://www.cancerresearchuk.org/:

http://cancerhelp.cancerresearchuk.org/type/breast-cancer/diagnosis/breast-cancer-tests

Cancer Research UK. (2014, July 30). *Mammograms in breast screening*. Retrieved August 19, 2014, from http://www.cancerresearchuk.org: http://www.cancerresearchuk.org/cancer-help/type/breast-cancer/about/screening/mammograms-in-breast-screening

Cancer Research UK. (2014, July 30). *TNM breast cancer staging*. Retrieved August 26, 2014, from http://www.cancerresearchuk.org: http://www.cancerresearchuk.org/cancer-help/type/breast-cancer/treatment/tnm-breast-cancer-staging

cancer.net. (2014). *Breast MRI for the Early Detection of Breast Cancer*. Retrieved from http://www.cancer.net/: http://www.cancer.net/navigating-cancer-care/diagnosing-cancer/tests-and-procedures/breast-mri-early-detection-breast-cancer

Carlton, R., & Adler, A. (2012). *Principles of Radiographic Imaging: An Art and A Science.* Cengage Learning.

Carter, C., & Veale, B. (2014). *Digital Radiography and PACS* (Second ed.). Mobsy.

Cashman, T. J. (2010). NURBS-compatible subdivision surfaces. *NURBS-compatible subdivision surfaces*. University of Cambridge Computer Laboratory.

Centre for Evidence-based Purchasing. (2009, March). Buyer's guide - Multi-slice CT scanners - CEP08007.

Chakraborty, D. P. (2005). Recent advances in observer performance methodology: jackknife free-response ROC (JAFROC). *Radiation protection dosimetry, 114*(1-3), 26-31.

Cherry, P., & Duxbury, A. (2009). *Practical Radiotherapy: Physics and Equipment.* John Wiley & Sons.

Chevalier, M., Leyton, F., Tavares, M. N., Oliveira, M., da Silva, T. A., & Peixoto, J. E. (2012). Image Quality Requirements for Digital Mammography in Breast Cancer Screening. In *Imaging of the Breast - Technical Aspects and Clinical Implication.* Madrid, Spain: InTech.

Chiarelli, A., Edwards, S., Prummel, M., Muradali, D., Majpruz, V., Done SJ, B. P., et al. (2013). Digital compared with screen-film mammography: performance measures in concurrent cohorts within an organized breast screening program. *268*(3), 684-693.

Chida, K., Komatsu, Y., Sai, M., Nakagami, A., Yamada, T., Yamashita, T., et al. (2009). Reduced compression mammography to reduce breast pain. *Clinical Imaging*, 7-10.

Chotas, H. G., Dobbins III, J. T., & Ravin, C. E. (1999). Principles of digital radiography with large-area, electronically readable detectors: a review of the basics. *Radiology*, 595-599.

Chung, J. H., Rajagopal, V., Nielsen, P. M., & Nash, M. P. (2008). A biomechanical model of mammographic compressions. *Biomech Model Mechanobiol*, 43-52.

Chung, J. H., Rajagopal, V., Nielsen, P. M., & Nash, M. P. (2008). Modelling mammographic compression of the breast. *Med Image Comput Comput Assist Interv*, 758-765.

Clark, R. A., Levine, R., & Snedeker, S. (1997). *The Biology of Breast Cancer*. Retrieved 08 16, 2012, from http://envirocancer.cornell.edu/Factsheet/General/fs5.biology.cfm#g

Coombs, N. J., & Boyages, J. (2005). Multifocal and Multicentric Breast Cancer: Does Each Focus Matter? *JOURNAL OF CLINICAL ONCOLOGY, 23*.

Cournane, S., Cannon, L., Browne, J. E., & Fagan, A. J. (2010). Assessment of the accuracy of an ultrasound elastography liver scanning system using a PVA-cryogel phantom with optimal acoustic and mechanical properties. *Physics in Medicine and Biology, 55*, 5965–5983.

Cunha, D., Tomal, A., & Poletti, M. (2012). Optimization of x-ray spectra in digital mammography through Monte Carlo simulations. *Physics in Medicine and Biology, 57*(7), 1919-1935.

Cunningham, I. A. (2000). Applied linear-systems theory. In J. Beutel, H. L. Kundel, & R. L. Metter, *Handbook of medical imaging.* Bellingham, WA: SPIE.

Cush, S. (2007, February). *Routine Quality Control Tests for Full Field Digital Mammography Systems.* National Health Service, NHS Cancer Screening Programmes. Sheffield, England: NHS Cancer Screening Programmes.

DailyMed. (2012, 3). Retrieved from http://dailymed.nlm.nih.gov/: http://dailymed.nlm.nih.gov/dailymed/lookup.cfm?setid=549d38db-d4ed-4708-8f76-7cdaa157063f

Dance, D. R., Skinner, C. L., Young, K. C., Beckett, J. R., & Kotre, C. J. (2000). Additional factors for the estimation of mean glandular breast dose using the UK mammography dosimetry protocol. *Physics in Medicine and Biology*, 3225–3240.

Danziger, K., & Simonsen, J. (2011). *What Are the Different Types of Breast Cancer*. Retrieved August 13, 2012, from http://www.genetichealth.com/brov_types_of_breast_cancer.shtml

Defreitas, K. F., Pellegrino, A., Farbizio, T. A., Janer, R., & Hitzke, G. (2008). *Patent No. US 7319735 B2.* US.

del Palomar, A. P., Calvo, B., Herrero, J., López, J., & Doblaré, M. (2008). A finite element model to accurately predict real deformations of the breast. *Med Eng Phys*, 1089-1097.

del Palomar, A. P., Calvo, B., Herrero, J., López, J., & Doblaré, M. (2008). A finite element model to accurately predict real deformations of the breast. *Medical Engineering & Physics, 30*, 1089–1097.

del Turco, M. R., Mantellini, P., Ciatto, S., Bonardi, R., Martinelli, F., Lazzari, B., et al. (2007). Full-field digital versus screen-film mammography: comparative accuracy in concurrent screening cohorts. *AJR Am J Roentgenol*, 860-866.

Dewerd, L. A., & Kissick, M. (2014). *The Phantoms of Medical and Health Physics.* Madison, USA: Springer.

Dobbins III, J. T. (2000). Image quality metrics for digital systems. In R. L. Metter, J. Beutel, & H. L. Kundel, *Handbook of medical imaging* (Vol. 1, pp. 161-222). Bellingham: SPIE.

Donahue, E. J. (2013). Ultrasound-Guided Breast Biopsy Tissue Sampling: Technique and Breast Ultrasound Characteristics of Benign and Malignant Lesions. In D. S. Francescatti, & M. J. Silverstein, *Breast cancer- A New Era in Management* (p. 144). Springer.

Donga, S., Chu, T., Lee, J., Lan, G., Wua, T., Y.H., Y., et al. (2002). Estimation of mean-glandular dose from monitoring breast entrance skin air kerma using a high sensitivity metal oxide semiconductor field effect transistor (MOSFET) dosimeter system in mammography. *Applied Radiation and Isotopes, 57*(6), 791–799.

Dronkers, D. J., & Hendriks, J. H. (2011). *The practice of mammography: pathology, technique, interpretation, adjunct modalities.* Thieme.

Dustler, M., Andersson, I., Förnvik, D., & Tingberg, A. (2012). The Effect of Breast Positioning on Breast Compression in Mammography: a Pressure Distribution Perspective. *SPIE Medical Imaging, 8313*.

Elkin, E. B., Hudis, C., Begg, C. B., & Schrag, D. (2005). The Effect of Changes in Tumor Size on Breast - Carcinoma Survival in the U.S.: 1975–1999. *Wiley InterScience*, 1149–1157.

ElSharkawy, A. M. (2014). Breast Cancer. In R. A. Al-Naggar, *Principles and Practice of Cancer Prevention and Control.* Foster City, CA, USA: OMICS Group eBooks.

Emanuelli, S., Rizzi, E., Amerio, S., Fasano, C., & Cesarani, F. (2011). Dosimetric and image quality comparison of two digital mammography units with different target/filter combinations: Mo/Mo, Mo/Rh, W/Rh, W/Ag. *Radiologia medica, 116*(2), 310-318.

Eng, J. (2005, July). Receiver operating characteristic analysis: a primer. *Academic radiology, 12*(7), 909-916.

Erkamp, R., Wiggins, P., Skovoroda, A., Emelianov, S., & O'Donnell, M. (1998). *MEASURING THE ELASTIC MODULUS OF SMALL TISSUE SAMPLES.* Retrieved 08 16, 2012, from http://web.eecs.umich.edu/~erkamp/pdfpapers/Paper%201%20-%20measuring.pdf

Espat, A. (2012). *Lumpy or Dense: Your "Breast" Defense*. Retrieved from http://www.mdanderson.org: http://www.mdanderson.org/publications/focused-on-health/issues/2010-october/lumpybreast.html

Exponent Inc. (2010). *Finite Element Analysis for Medical Devices & Biomaterials*. Retrieved from http://www.exponent.com: http://www.exponent.com/finite-element-analysis-for-medical-devices_biomed/

Fawcett, T. (2006). An introduction to ROC analysis. *ScienceDirect*, 861–874.

Ferreira, T. (2012, 4). *Analyze Menu*. Retrieved from http://rsbweb.nih.gov/: http://rsbweb.nih.gov/ij/docs/menus/analyze.html#manager

Fieselmann, A., Fischer, D., Hilal, G., Dennerlein, F., Mertelmeier, T., & Uhlenbrock, D. (2013). Full-field digital mammography with grid-less acquisition and software-based scatter correction: Investigation of dose. *Proceedings of SPIE Medical Imaging 2013: Physics of Medical Imaging, 8668*.

Fischer, U., Baum, F., Obenauer, S., Luftner-Nagel, S., von Heyden, D., Vosshenrich, R., et al. (2002). Comparative study in patients with microcalcifications: full-field digital mammography vs screen-film mammography. *Eur Radiol*, 2679-2683.

Fischmann, A., Siegmann, K. C., Wersebe, A., Claussen, C. D., & Müller-Schimpfle, M. (2005). Comparison of full-field digital mammography and film-screen mammography: image quality and lesion detection. *Br J Radiol*, 312-315.

Fornage, B. D. (2006). Breast cancer. In W. H. Winchester.

Fosbinder, R., & Orth, D. (2011). *Essentials of Radiologic Science.* Lippincott Williams & Wilkins.

Freitas, A. G., Kemp, C., Louveira, M. H., Fujiwara, S. M., & Campos, L. F. (2006). Digital mammography: current view and future applications. *Radiologia Brasileira, 39*.

Fritsch, H., & Kuehnel, W. (2007). *Color Atlas of Human Anatomy, Volume 2* (5 ed., Vol. 2).

Fromageau, J., Brusseau, E., Vray, D., Gimenez, G., & Delachartre, P. (2003). Characterization of PVA cryogel for intravascular ultrasound elasticity imaging. *IEEE transactions on ultrasonics, ferroelectrics, and frequency control, 50*(10), 1318-1324.

Fromageau, J., Gennisson, J., Schmitt, C., Maurice, R., Mongrain, R., & Cloutier, G. (2007). Estimation of polyvinyl alcohol cryogel mechanical properties with four ultrasound elastography methods and comparison with gold standard testings. *IEEE transactions on ultrasonics, ferroelectrics, and frequency control, 54*(3), 498-509.

Gammex Inc. (2014). *"Rachel" Anthropomorphic Breast*. Retrieved August 16, 2014, from http://www.gammex.com: http://www.gammex.com/n-portfolio/productpage.asp?mode=preview&id=303

Gammex Inc. (2014). *Steriotactic breast biopsy phantom*. Retrieved July 25, 2014, from http://www.gammex.com/: http://www.gammex.com/n-portfolio/productpage.asp?id=316

Geddes, D. T. (2007). Inside the Lactating Breast: The Latest Anatomy Research. *J Midwifery Womens Health, 52*(6), 556–563.

Gefena, A., & Dilmoney, B. (2007). Mechanics of the normal woman's breast. *Technology and Health Care, 15*(4), 259-271.

Geller, B., Barlow, W., Ballard-Barbash, R., Ernster, V., Yankaskas, B., Sickles, E., et al. (2002). Use of the American College of Radiology BI-RADS to Report on the Mammographic Evaluation of Women with Signs and Symptoms of Breast Disease. *Radiology*, 536-542.

Gisev, N., Bell, J. S., & Chen, T. F. (2013). Interrater agreement and interrater reliability: key concepts, approaches, and applications. *Research in Social and Administrative Pharmacy, 9*(3), 330-338.

Goel, A., & Pacifici, S. (2014). *PGMI evaluation system*. Retrieved 12 14, 2014, from http://radiopaedia.org: http://radiopaedia.org/articles/pgmi-evaluation-system

Goergen, S. (2009). *Iodine-containing contrast medium (ICCM)*. Retrieved August 3, 2014, from http://www.insideradiology.com.au: http://www.insideradiology.com.au/pages/view.php?T_id=21#.U90l6ONdVyw

Goldberger, J. J., & Ng, J. (2010). *Practical Signal and Image Processing in Clinical Cardiology.* Springer.

Goldman, L. W. (2007). Principles of CT and CT Technology. *Journal of nuclear medicine technology, 35*(3), 115-128.

Goldman, L. W. (2008, June). Principles of CT: Multislice CT. *Journal of nuclear medicine technology, 36*(2), 57-68.

Gupta, S., Webster, T. J., & Sinha, A. (2011). Evolution of PVA gels prepared without crosslinking agents. *Mater Med, 22*, 1763–1772.

Halls, S. B. (2011, March 23). *Breast abnormalities typically discovered by mammogram*. Retrieved August 19, 2014, from http://www.breast-cancer.ca: http://www.breast-cancer.ca/screening/mammogram-abnormalities.htm

Hambly, N. M., McNicholas, M. M., Phelan, N., Hargaden, G. C., O'Doherty, A., & Flanagan, F. L. (2009). Comparison of Digital Mammography and Screen-Film Mammography in Breast Cancer Screening: A Review in the Irish Breast Screening Program. *AJR, 193*(4), 1010-1018.

Hammer, P. E., Sacks, M. S., del Nido, P. J., & Howe, R. D. (2011). Mass-Spring Model for Simulation of Heart Valve Tissue Mechanical Behavior. *Ann Biomed Eng*, 1668-79.

Han, L., Hipwell, J. H., Tanner, C., Taylor, Z., Mertzanidou, T., Cardoso, J., et al. (2012). Development of patient-specific biomechanical models for predicting large breast deformation. *Physics in Medicine and Biology, 57*.

Hardy, K. (2012). Managing Monitors for Digital Mammography. *Radiology Today, 13*(10), 26.

Harish, M. G., Konda, S. D., MacMahon, H., & Newstead, G. M. (2007). Breast Lesions Incidentally Detected with CT:What the General Radiologist Needs to Know. *RadioGraphics*, 37-51.

Hashimoto, I. (2008). *Practical digital mamography.* Thieme.

Hassan, C. M., & Peppas, N. A. (2000). Structure and Applications of Poly(vinyl alcohol) Hydrogels Produced by Conventional Crosslinking or by Freezing/Thawing Methods. *Advances in Polymer Science, 153*, 37-65.

Hassan, C. M., Ward, J., & Peppas, N. A. (2000). Modeling of crystal dissolution of poly(vinyl alcohol) gels produced by freezing/thawing processes. *Polymer*, 6729–6739.

Hauge, I. H., Hogg, P., Connolly, P., McGill, G., & Claire, M. (2012). The readout thickness versus the measured thickness for a range of SFM. *Medical physics, 39*(1), 263-271.

Heddson, B., Rönnow, K., Olsson, M., & Miller, D. (2007). Digital versus screen-film mammography: a retrospective comparison in a population-based screening program. *Eur J Radiol*, 419-425.

Helvie, M. A. (2010). Digital Mammography Imaging: Breast Tomosynthesis and Advanced Applications. *Radiologic clinics of North America, 48*(5), 917-929.

Hendee, W. R. (2013). *Physics of mammography imaging.*

Hendrick, R. E., Pisano, E. D., Averbukh, A., Moran, C., Berns, E. A., Yaffe, M. J., et al. (2010). Comparison of Acquisition Parameters and Breast Dose in Digital Mammography and Screen-Film Mammography in the American College of Radiology Imaging Network Digital Mammographic Imaging Screening Trial. *American Journal of Roentgenology, 194*(2), 362-369.

Henrikson, G. C., Mafee, M. F., Flanders, A. E., Kriz, R. J., & Peyman, G. A. (1987). CT Evaluation of Plastic Intraocular Foreign Bodies. *American journal of neuroradiology, 8*(2), 378-379.

Herrmann, T. (2008). *Computed Radiography and Digital Radiography: A Comparison of Technology, Functionality, Patient Dose, and Image Quality.* Retrieved November 11, 2013, from http://www.eradimaging.com/: http://www.eradimaging.com/site/article.cfm?ID=535#.U9oqhONdVyx

Heywang-Köbrunner, S. H., Hacker, A., & Sedlacek, S. (2011). Advantages and Disadvantages of Mammography Screening. *Breast Care*, 199-207.

Hologic Inc. (2014). *Full-field digital mammography unit -Selenia*. Retrieved July 22, 2014, from http://www.medicalexpo.com: http://www.medicalexpo.com/prod/hologic/full-fields-digital-mammography-units-70711-428957.html

Hologic Inc. (n.d.). User Manual for Selenia Software. Chapter 3- using the patient and patient view screens.

Huda, W., & Slone, R. (2007). *Review of Radiological Imaging:Mammography (Lecture 007)*. Retrieved August 12, 2014, from http://www.uiowa.edu/: http://www.uiowa.edu/hri/courses/physicsOfMedicalImagingReview/lectureTalk007.html

Huda, W., Scalzetti, E. M., & Levin, G. (2000). Technique Factors and Image Quality as Functions of Patient Weight at Abdominal CT. *Radiology, 217*(2).

Imaginis Corporation. (2010, December). *Mammogram report*. Retrieved August 26, 2014, from http://www.imaginis.com/: http://www.imaginis.com/mammography/mammogram-report-1

Imaginis Corporation. (2014). *Diagnostic Mammography*. Retrieved August 15, 2014, from http://www.imaginis.com: http://www.imaginis.com/mammography/diagnostic-mammography-2

Indrajit, I. K., & Verma, B. S. (2009). Monitor diplays in radology: part 2. *The Indian Journal of Radiology & Imaging*, 94-98.

International Atomic Energy Agency. (2013). *Mammography (radiography of the breast)*. Retrieved August 26, 2014, from https://rpop.iaea.org: https://rpop.iaea.org/rpop/rpop/content/informationfor/healthprofessionals/1_radiology/mammography/mammography-technique.htm

International Atomic Energy Agency. (2013). *Mammography Screening*. Retrieved from https://rpop.iaea.org: https://rpop.iaea.org/RPOP/RPoP/Content/InformationFor/HealthProfessionals/1_Radiology/Mammography/MammographyScreen.htm

Jarrousse, O. (2011). *Modified Mass-Spring System for Physically Based Deformation Modeling*. Retrieved from http://www.ibt.kit.edu/: http://www.ibt.kit.edu/download/PRJ_2011-02-10_O_Jarrousse.pdf

Jiang, S., Liu, S., & Feng, W. (2011). PVA hydrogel properties for biomedical application. *Journal of the Mechanical Behavior of Biomedical Materials, 4*(7), 1228-1233.

Johns, P., & Yaffe, M. (1987). X-ray characterisation of normal and neoplastic breast tissues. *Physics in Medicine and Biology, 32*(6), 675-95.

Johnson, J. O., & Robins, J. M. (2012). CT Imaging: Radiation Risk Reduction—Real-Life Experience in a Metropolitan Outpatient Imaging Network. *American College of Radiology, 9*(11), 808-813.

Jones, D. W., Hogg, P., & Seeram, E. (2013). *Practical SPECT/CT in Nuclear Medicine.* Springer.

Joy, J. E., Penhoet, E. E., & Petitti, D. B. (2005). *Saving Women's Lives: Strategies for Improving Breast Cancer Detection and Diagnosis.* Washington, D.C.: National Academies Press.

Kaabi, F. A., Bariki, N. A., & Janeczek, J. (2013). Variation of the Breast Mean Glandular Doses According to Breast Thicknesses. *In World Congress on Medical Physics and Biomedical Engineering, 39*, 1125-1127.

Kalender, W. (2011). *Computed Tomography.* Publicis.

Kalender, W. (2011). *Computed Tomography Fundamentals, System Technology, Image Quality, Applications* (Third ed.). Publicis.

Kaplan, D., & Glass, L. (1995). Understanding Nonlinear Dynamics. *Springer, 19*.

Karahaliou, A. N., Arikidis, N. S., Skiadopoulos, S. G., Panayiotakis, G. S., & Costaridou, L. I. (2012). Computerized Image Analysis of Mammographic Microcalcifications: Diagnosis and Prognosis. In N. Uchiyama (Ed.), *Mammography - Recent Advances* (pp. 321-340). InTech.

Kayar, R., Civelek, S., Cobanoglu, M., Gungor, O., Catal, H., & Emiroglu, M. (2011). Five Methods of Breast Volume Measurement: A Comparative Study of Measurements of Specimen Volume in 30 Mastectomy Cases. *Breast Cancer: Basic and Clinical Research*(5), 43–52.

Kempston, M. P., Mainprize, J. G., & Yaffe, M. J. (2006). *Digital Mammography, 8th International Workshop.* Springer-Verlag Berlin Heidelberg.

Kharine, A., Manohar, S., Seeton, R., Kolkman, R. G., Bolt, R. A., Steenbergen, W., et al. (2006). Poly(vinyl alcohol) gels for use as tissue phantoms in photoacoustic mammography. *Physics in Medicine and Biology, 48*, 357-370.

Kim, S., Lee, G., Lee, S., Park, S., Pyo, H., & Cho, J. (1999). Body fat measurement in computed tomography image. *Biomedical sciences instrumentation, 35*, 303-308.

Kimme-Smith, C. (1999). New Digital Mammography Systems May Require Different X-ray Spectra and, Therefore, More General Normalized Glandular Dose Values. *Radiology, 213*(1), 7-10.

King, D. M., Moran, C. M., McNamara, J. D., Fagan, A. J., & Browne, J. E. (2011). Development of a vessel-mimicking material for use in anatomically realistic Doppler flow phantoms. *Ultrasound in medicine & biology, 37*(5), 813-826.

Kolb, T. M., Lichy, J., & Newhouse, J. H. (2002). Comparison of the performance of screening mammography, physical examination, and breast US and evaluation of factors that influence them: an analysis of 27,825 patient evaluations. *Radiology*, 165-175.

Korf, A., Herbst, C., & Rae, W. (2009). The relationship between compression force, image quality and radiation dose in mammography. *South African Journal of Radiology, 13*.

Krouskop, T. A., Wheeler, T. M., Kallel, F., Garra, B. S., & Timothy, H. (1998). Elastic Moduli of Breast and Prostate Tissues under Compression. *Ultrasonic imaging, 20*(4), 260-274.

Krupinski, E. (2010). Current perspectives in medical image perception. *Attention, Perception, & Psychophysics, 75*(5), 1205-1217.

Krupinski, E. (2010). Perceptual factor in reading medical images. In E. Samei, & E. Krupinski, *The handbook of Medical Image Perception and Techniques* (p. 82).

Krupinski, E., & Borah, J. (n.d.). *Eye Tracking Helps Improve Accuracy in Radiology*. Retrieved July 30, 2014, from http://www.photonics.com/: http://www.photonics.com/Article.aspx?AID=43855

Kyoto Kagaku. (n.d.). *Breast Ultrasound Examination Phantom "BREAST FAN"*. Retrieved August 19, 2014, from http://www.kyotokagaku.com: http://www.kyotokagaku.com/products/detail03/pdf/us-6_catalog.pdf

Lai, C. J., Shaw, C. C., Chen, L., Altunbas, M. C., Liu, X., Han, T., et al. (2007). Visibility of microcalcification in cone beam breast CT − Effects of x-ray tube voltage and radiation dose. *National Institute of Health Medical Physics, 34*(7), 2995-3004.

Lança, L., & Silva, A. (2009). Digital radiography detectors – A technical overview: Part 2. *Radiography, 15*(2), 134–138.

Lança, L., & Silva, A. (2013). *Digital Imaging Systems for plain Radiography.* Springer.

Lazos, D., Kolisti, Z., & Pallikarakis, N. (2000). A software data generator for radiographic imaging investigations. *IEEE Transactions on Infirmation Technology in Biomedicine, 4*(1), 76-79.

Li, C. M., Segars, W. P., Lo, J. Y., Veress, A. I., Boone, J. M., & Dobbins III, J. T. (2008). Three-Dimensional Computer Generated Breast Phantom Based on Empirical Data. *Proceedings of SPIE, 6913*, 691314-1.

Li, X., & Samei, E. (2010). Logistical issues in designing perception experiments. In E. Samei, & E. Krupinski (Eds.), *The Handbook of Medical Image Perception and Techniques* (pp. 177-186). Cambridge: Cambridge University Press.

Ljungberg, M., Strand, S.-E., & King, M. A. (2013). *Monte Carlo Calculations in Nuclear Medicine.* Boca Raton, FL: CRC Press.

Lozinsky, V. I., & Plieva, F. M. (1998). Poly(vinyl alcohol) cryogels employed as matrices for cell immobilization. 3. Overview of recent research and developments. *enzyme microb. technology.*, 227–242.

Maddox, T. G. (2002). *Adverse Reactions to Contrast Material: Recognition, Prevention, and Treatment*. Retrieved August 3, 2014, from http://www.aafp.org/afp: http://www.aafp.org/afp/2002/1001/p1229.html

Madjar, H., & Mendelson, E. B. (2011). *Practice of Breast Ultrasound: Techniques, Findings, Differential Diagnosis* (Second ed.). Thieme.

Manning, D. J., Ethell, S. C., & Donovan, T. (2004). Detection or decision errors? Missed lung cancer from the posteroanterior chest radiograph. *The British journal of radiology, 77*(915), 231-235.

Markey, M. K. (2013). *Physics of mammographic imaging.* CRC press.

Marshall University. (2009, 10). *Breast Cancer – General Information*. Retrieved 08 16, 2012, from www.marshall.edu: http://www.marshall.edu/wpmu/wcenter/breast-and-cervical-cancer/breast-cancer-general-information/

Martin, A. (2008, February). *Adrian's FWHM V1.1 code documentation*. Retrieved August 26, 2014, from http://rsbweb.nih.gov/: http://rsbweb.nih.gov/ij/plugins/fwhm/

Mathers, N., Fox, N., & Amanda, H. (2009). *Surveys and Questionnaires*. Retrieved from http://www.rds-yh.nihr.ac.uk/: http://www.rds-yh.nihr.ac.uk/wp-content/uploads/2013/05/12_Surveys_and_Questionnaires_Revision_2009.pdf

Mawdsley, G., Tyson, A., Peressotti, C., Jong, R., & Yaffe, M. (2009). Accurate estimation of compressed breast thickness in mammography. *Medical physics, 36*(2), 577-586.

Mayo Clinic. (2015). *Ultrasound-guided breast biopsy*. Retrieved from http://www.mayoclinic.org: http://www.mayoclinic.org/tests-procedures/breast-biopsy/multimedia/ultrasound-guided-breast-biopsy/img-20007415

Mazumdar, M. D. (n.d.). *ANATOMY OF THE FEMALE BREAST.* Retrieved August 17, 2012, from http://www.breastcancertreatment.in/breast_anatomy.htm

McCormack, V. A., & dos Santos, S. (2006). Breast density and parenchymal patterns as markers of breast cancer risk: a meta-analysis. *Cancer Epidemiology Biomarkers & Prevention, 15*(6), 1159-1169.

McCullagh, J. B., Baldelli, P., & Phelan, N. (2010). Measured Dose versus Organ Dose Performance in Digital Mammography Systems. In J. Martí, A. Oliver, J. Freixenet, & R. Martí (Eds.), *Digital Mammography: Lecture Notes In Computer Science* (Vol. 6136, pp. 86-91). Springer.

McCullagh, J. B., Baldelli, P., & Phelan, N. (2011). Clinical dose performance of full field digital mammography in a breast screening programme. *British Journal of Radiology, 84*(1007), 1027–1033.

MD Publishing Inc. (2012). *Product Showroom: Mammography*. Retrieved July 22, 2014, from http://medicaldealer.com: http://medicaldealer.com/sony-5mp-diagnostic-display/

MedCalc . (2015). Retrieved from https://www.medcalc.org/: https://www.medcalc.org/

Medical Services Advisory Committee . (2008). *Digital mammography for breast cancer screening, surveillance and diagnosis.* Medical Services Advisory Committee . Sydney, Australia: Commonwealth of Australia.

Mehrabian, H., & Samani, A. (2009). Constrained hyperelastic parameters reconstruction of PVA (Polyvinyl) Alcohol) phantom undergoing large deformation. *SPIE, 7261*.

Mello-Thoms, C., Trieu, P., & Brennan, P. (2014). Going on with false beliefs: What if satisfaction of search was really suppression of recognition? *Spie Digital Library, 9037*.

Mercer, C. E., Hogg, P., Cassidy, S., & Denton, E. R. (2013). Does an increase in compression force really improve visual image quality in mammography? – An initial investigation. *Radiography*, 363–365.

Mercer, C. E., Hogg, P., Szczepura, K., & Denton, E. R. (2013). Practitioner compression force variation in mammography: A 6-year study. *Radiology*, 200–206.

Millon, L. E., Mohammadi, H., & Wan, W. K. (2006). Anisotropic Polyvinyl Alcohol Hydrogel for Cardiovascular Applications. *Journal of Biomedical Materials Research Part B: Applied Biomaterials, 79*(2), 305-311.

National Breast Cancer Foundation. (2012). *Breast Anatomy*. Retrieved 08 15, 2014, from http://www.nationalbreastcancer.org/: http://www.nationalbreastcancer.org/breast-anatomy

National Cancer Institute. (2014, March 28). *Breast Cancer Screening*. Retrieved August 19, 2014, from http://www.cancer.gov: http://www.cancer.gov/cancertopics/pdq/screening/breast/Patient/page3

NHS. (2014). *http://www.nhs.uk*. Retrieved from Breast cancer (female): http://www.nhs.uk/Conditions/Cancer-of-the-breast-female/Pages/Introduction.aspx

NHS Breast Screening Programme. (2000). *QUALITY ASSURANCE GUIDELINES*. Retrieved from http://www.cancerscreening.nhs.uk: http://www.cancerscreening.nhs.uk/breastscreen/publications/nhsbsp30.pdf

NHSBSP. (2006). *ACCEPTABILITY TO WOMEN OF FULL FIELD DIRECT DIGITAL MAMMOGRAPHY*. Retrieved from http://www.cancerscreening.nhs.uk/: http://www.cancerscreening.nhs.uk/breastscreen/publications/nhsbsp-equipment-report-0603.pdf

Nicholson, B. T., LoRusso, A. P., Smolkin, M., Bovbjerg, V. E., Petroni, G. R., & Harvey, J. A. (2006). Accuracy of assigned BI-RADS breast density category definitions. *Acad Radiol*, 1143-1149.

Noel, A., & Thibault, F. (2004). Digital detectors for mammography: the technical challenges. *European Radiology*, 1990–1998.

O'Leary, D., & Al Maskari, M. Z. (2013). Pain in mammography: where and why does it arise? *BREAST CANCER RESEARCH, 15*.

Oberhofer, N., & Bolzano. (2011). Comparison of new digital mammography systems: physical characterisation and image quality evaluation. *ECR* , (pp. 1-22).

Oberhofer, N., Fracchetti, A., Nassivera, E., Valentini, A., & Moroder, E. (2010). Comparison of Two Novel FFDM Systems with Different a-Se Detector Technology: Physical Characterization and Phantom Contrast Detail Evaluation in Clinical Conditions. *Digital Mammography, 6136*, 459-466.

Obuchowski, N. A. (2004, April). How Many Observers Are Needed in Clinical Studies of Medical Imaging? *American Journal of Roentgenology, 182*(4), 867-869.

O'Leary, D., Grant, T., & Rainford, L. (2011). Image quality and compression force: the forgotten link in optimisation of digital mammography? *Breast Cancer Research, 13 Suppl 1*, 10.

Oliveira, L. J., & Lança, C. (2011, March). *Radiological imaging in digital systems: the effect of exposure parameters in diagnostic quality and patient dose.* Retrieved August 26, 2014, from Universidade de Aveiro - RIA Statistics: http://hdl.handle.net/10773/3950

Otani, T. (2013, April 4). *New Compression Paddle Reduces Pain in Mammography*. Retrieved January 15, 2014, from http://techon.nikkeibp.co.jp: http://techon.nikkeibp.co.jp/english/NEWS_EN/20130404/274926/

Pan, X., Sidky, E. Y., & Vannier, M. (2009). Why do commercial CT scanners still employ traditional, filtered back-projection for image reconstruction? *Inverse problems, 25*(12).

Paredes, E. S. (2007). *Atlas of mammography* (Third ed.). Lippincott Williams & Wilkins.

Patete, P., Iacono, M. I., Spadea, M. F., Trecate, G., Vergnaghi, D., Mainardi, L. T., et al. (2013). A multi-tissue mass-spring model for computer assisted breast surgery. *Med Eng Phys*, 47-53.

Peppas, N. A. (1976). Crystallization of polyvinyl alcohol-water films by slow dehydration. *European Polymer Journal*, 495–498.

Peppas, N. A., & Scott, J. E. (1992). Journal of Controlled Release. *Controlled release from poly (vinyl alcohol) gels prepared by freezing-thawing processes, 18*(2), 95-100.

Peppas, N. A., & Stauffer, S. R. (1991). Reinforced uncrosslinked poly (vinyl alcohol) gels produced by cyclic freezing-thawing processes: a short review. *Journal of Controlled Release*, 305-310.

Perry, N., Broeders, M., De Wolf, C., Törnberg, S., Holland, R., & Von Karsa, L. (2013). European guidelines for quality assurance in breast cancer screening and diagnosis - Fourth edition - Supplements.

Philips. (1999). *Back to CT basics: Why 100 kVp?* Retrieved from http://clinical.netforum.healthcare.philips.com/: http://clinical.netforum.healthcare.philips.com/global/Explore/White-Papers/CT/Back-to-CT-basics-Why-100-kVp-

Pisano, E. D., & Yaffe, M. J. (2005). Digital Mammography. *Radiology*, 353–362.

Pisano, E. D., Hendrick, R. E., Yaffe, M. J., Baum, J. K., Acharyya, S., B., C. J., et al. (2008). Diagnostic Accuracy of Digital versus Film Mammography: Exploratory Analysis of Selected Population Subgroups in DMIST. *Radiology, 246*(2), 376–383.

Pope, T. L., Read, M. E., Medsker, T., Buschi, A. J., & Brenbridge, A. N. (1984). Breast skin thickness: normal range and causes of thickening shown on film-screen mammography. *J Can Assoc Radiol*, 365-368.

Poulos, A., & McLean, D. (2004). The application of breast compression in mammography: a new perspective. *Radiology*, 131–137.

Poulos, A., McLean, D., Rickard, M., & Heard, R. (2003). Breast compression in mammography: how much is enough? *Australas Radiol*, 121-126.

Price, B. D., Gibson, A. P., Tan, L. T., & Royle, G. J. (2010). An elastically compressible phantom material with mechanical and x-ray attenuation properties equivalent to breast tissue. *Physics in Medicine and Biology, 55*, 1177-1188.

Prionas, N. D., Lindfors, K. K., Ray, S., Huang, S.-Y., Beckett, L. A., Monsky, W. L., et al. (2010). Contrast-enhanced Dedicated Breast CT: Initial Clinical Experience. *Radiology, 256*(3), 714-723.

Public Health England. (2014). *NHS Breast Cancer Screening Programme*. Retrieved July 21, 2014, from http://cancerscreening.nhs.uk/: http://cancerscreening.nhs.uk/breastscreen/digital-mammography.html

Puretec Industrial Water. (2012). *Is It Safe To Drink Deionized Water*. Retrieved August 3, 2014, from http://puretecwater.com: http://puretecwater.com/safe-to-drink-deionized-water.html

Qureshi, G. U., & Samera, A. (2009). Mammographic density – a useful biomarker for breast cancer risk in epidemiologic studies. *Norsk Epidemiologi*, 59-68.

Rajendran, P. T., Krishnapillai, V., Tamanang, S., & Chelliah, K. K. (2012). Comparison of Image Quality Criteria between Digital Storage Phosphor Plate in Mammography and Full-Field Digital Mammography in the Detection of Breast Cancer. *Malaysian Journal of Medical Sciences, 19*(1), 52–59.

Ranger, N. T., Lo, J. Y., & Samei, E. (2010). A technique optimization protocol and the potential for dose reduction in digital mammography. *Medical Physics, 37*(3), 962–969.

Ricchiardi, R., Auriemma, F., & de Rosa, C. (2005). Structure and Properties of Poly(vinyl alcohol) Hydrogels obtained by Freeze/Thaw techniques. *Macromol. Symp*, 49-63.

Robson, K. J. (2010). Advances in mammographic imaging. *The British Journal of Radiology, 83*(988), 273-275.

Rossmann, K. (1969). Point spread-function, line spread-function, and modulation transfer function: tools for the study of imaging. *Radiology*, 257-272.

Ruiter, N. V., Stotzka, R., Gemmeke, H., Reichenbach, J., & Kaiser, W. (2002). Automatic image matching for breast cancer diagnostics by a 3d deformation of the mamma. *Biomed. Tech*, 644–647.

Ru-yin, M., & Dang-sheng, X. (2008). Synthesis and properties of physically crosslinked poly (vinyl alcohol) hydrogels. *Journal of China University of Mining and Technology, 18*(2), 271-274.

Sabih, D.-e., Sabih, A., Sabih, Q., & Khan, A. N. (2011). Image perception and interpretation of abnormalities; can we believe our eyes? Can we do something about it? *Insights into Imaging, 2*(1), 47-55.

Saha, G. B. (2013). *Physics and Radiobiology of Nuclear Medicine.* Springer.

Samani, A., & Plewes, D. (2004). A method to measure the hyperelastic parameters of ex vivo breast tissue samples. *Phys. Med. Biol, 49*, 4395–4405.

Samani, A., Bishop, J., Yaffe, M. J., & Plewes, D. B. (2001). Biomechanical 3-D finite element modeling of the human breast using MRI data. *Medical Imaging, IEEE Transactions on, 20*, 271 - 279.

Samani, A., Zubovits, J., & Plewes, D. (2007). Elastic moduli of normal and pathological human breast tissues: an inversion-technique-based investigation of 169 samples. *Physics in Medicine and Biology, 52*(6), 1565-1576.

Samei, E. (2003). Performance of Digital Radiographic Detectors: Quantification and Assessment methods. *RSNA*, 37-47.

Samei, E., & Krupinski, E. (2010). Medical image perception. In E. Samei, & E. Krupinski (Eds.), *The Handbook of Medical Image Perception and Techniques* (pp. 1-6). Cambridge: Cambridge University Press.

Samei, E., & Li, X. (2010). Logistical issues in designing perception experiments. In E. Samei, & E. Krupinski (Eds.), *The handbook of Medical Image Perception and Techniques* (pp. 177-186). Cambridge, England: Cambridge University Press.

Samei, E., Dobbins III, J. T., Lo, J. Y., & Tornai, M. P. (2005). *Radiology Protection Dosimetry*, 220-229.

Sardanelli, F., Zandrino, F., Imperiale, A., Bonaldo, E., Quartini, M. G., & Cogorno, N. (2000). Breast Biphasic Compression versus Standard Monophasic Compression in X-ray Mammography. *Radiology, 217*(2).

Sarvazyan, A. (1993). Shear acoustic properties of soft biological tissues in medical diagnostics. *The Journal of the Acoustical Society of America, 93*(4), 2329-2330.

Saunders, R. S., & Samei, E. (2008). The effect of breast compression on mass conspicuity in digital mammography. *Medical Physics*, 4464-4473.

Schaefer-Prokop, C., & Prokop, M. (1997, March). Digital radiography of the chest: Comparison of the selenium detector with other imaging systems. *Medicamundi, 41*(1).

Sechopoulos, L. (2014). Patient dose. In S. G. Ingrid Reiser, *Tomosynthesis Imaging* (p. 52). CRS Press.

Segars, P., & Tsui, B. M. (2009). MCAT to XCAT: The Evolution of 4-D Computerized Phantoms for Imaging Research. *Proceedings of the IEEE, 97*, 1954-1968.

Silva, F. A., Souza, L. F., Salmon, C. E., & Souza, D. N. (2010, August 23). Breast phantom with silicone implant for evaluation in conventional mammography. *JOURNAL OF APPLIED CLINICAL MEDICAL PHYSICS, 12*(1).

Skaane, P., Hofvind, S., & Skjennald, A. (2007). Randomized trial of screen-film versus full-field digital mammography with soft-copy reading in population-based screening program: follow-up and final results of Oslo II study. *Radiology*, 708-717.

Smith, A. (2003). *Fundamentals of Digital Mammography: Physics, Technology and Practical Considerations*. Retrieved from http://lraxray.com/: http://lraxray.com/Media/Fundamentals%20of%20DM.pdf

Smith, A. (2008). *Fundamentals of Breast Tomosynthesis*. Retrieved from http://www.hologic.com/: http://www.hologic.com/sites/default/files/Fundamentals%20of%20Breast%20Tomosynthesis_WP-00007.pdf

Smith, A. (2014). *The Principles of Contrast Mammography*. Retrieved from http://www.hologic.com: http://www.hologic.com/sites/default/files/Principles%20of%20Contrast.pdf

Smith, N. B., & Webb, A. (2010). *Introduction to Medical Imaging Physics, Engineering and Clinical Applications.* Cambridge university press.

Smith, S. W. (1997). Special Imaging Techniques. In S. W. Smith, *The Scientist and Engineer's Guide to Digital Signal Processing.* California technical.

Sprawls, P. (1995). *http://www.sprawls.org*. Retrieved from Mammography Physics and Technology for effective clinical imaging: http://www.sprawls.org/resources/MAMMO/module.htm#12

Sprawls, P. (1995). *Image Noise*. Retrieved 7 23, 2014, from http://www.sprawls.org: http://www.sprawls.org/ppmi2/NOISE/

Sprawls, P. (1995). *Iodine and Barium Contrast Media*. Retrieved September 22, 2014, from http://www.sprawls.org/: http://www.sprawls.org/ppmi2/XRAYCON/#Iodine and Barium Contrast Media

Sprawls, P. (1995). *Radiation Quantities and Units*. Retrieved 7 23, 2014, from http://www.sprawls.org: http://www.sprawls.org/resources/RADQU/#Air KERMA

Stangl, E. (2013, September 29). *Theory and Practice of Trying to Combine Just Anything*. Retrieved 1 15, 2014, from http://elkement.wordpress.com: http://elkement.wordpress.com/2013/09/29/may-the-force-field-be-with-you-primer-on-quantum-mechanics-and-why-we-need-quantum-field-theory/

Stauffer, S. R., & Peppas, N. A. (1992). Poly(vinyl alcohol) hydrogels prepared by freezing-thawing cyclic processing. *Polymer, 33*(18), 3932 - 3936.

Stewart, M. L., Smith, L. M., & Hall, N. (2011). A numerical investigation of breast compression: a computer-aided design approach for prescribing boundary conditions. *IEEE Trans Biomed Eng, 58*(10), 2876-2884.

Surry, K. J., & Peters, T. M. (2001). A PVA-C Brain Phantom Derived from a High Quality 3D MR Data Set. *Lecture Notes in Computer Science, 2208/2001*, 1149-1150.

Surry, K. J., Austin, H. J., Fenster, A., & Peters, T. M. (2004). Poly(vinyl alcohol), cryogel phantoms for use in ultrasound and MR imaging. *Physics in Medicine and Biology, 49*, 5529-5546.

Suryanarayanan, S., Karellas, A., Vedantham, S., Ved, H., Baker, S., & D'Orsi, C. (2002). Flat-panel digital mammography system: contrast-detail comparison between screen-film radiographs and hard-copy images. *Radiology*, 801-807.

Svahn, T. M., & Tingberg, A. (2014). Observer experiments with tomosynthesis. In S. G. Ingrid Reiser, *Tomosynthesis Imaging* (pp. 161-163). CRC Press.

Tanner, C., Hipwell, J. H., & Hawkes, D. J. (2008). Statistical Deformation Models of Breast Compressions from Biomechanical Simulations. *Lecture Notes in Computer Science, 5116*, 426-432.

Tanner, C., Schnabel, J., Smith, A. C., Sonoda, L., Hill, D., & Hawkes, D. (2002). The Comparison of Biomechanical Breast Models: Initial Results.

The Collaboration for NDT Education. (2012). *Transmitted Intensity and Linear Attenuation Coefficient*. (Iowa State University) Retrieved August 26, 2014, from http://www.ndt-ed.org: http://www.ndt-ed.org/EducationResources/CommunityCollege/Radiography/Physics/attenuationCoef.htm

Thomas, S. J. (1999). Relative electron density calibration of the CT scanners for radiotherapy treatment planning. *The British journal of Radiology, 72*, 781-786.

Toennies, K. D. (2012). *Guide to Medical Image Analysis: Methods and Algorithms.* Springer.

Tourassi, G. (2010). Receiver operating characteristic analysis: basic concepts and practical aplicatons. In E. K. Ehsan Samei, *The handbook of Medical Image Perception and Techniques* (p. 167).

Tugwell, J., Everton, C., Kingma, A., Oomkens, D., Pereira, G., Pimentinha, D., et al. (2014). Increasing source to image distance for AP pelvis imaging – Impact on radiation dose and image quality. *Radiology*.

University of Guelph. (2002, August 29). *Standard Operating Procedures for Using Ethanol (Ethyl Alcohol 95%) at Laminar Flow Benches.* Retrieved August 16, 2012, from http://www.uoguelph.ca/plant/resource/pdf_sops/Ethanol_procedure.pdf

University of Texas. (2014). *High-resolution X-ray CT*. Retrieved from http://www.ctlab.geo.utexas.edu/: http://www.ctlab.geo.utexas.edu/overview/

University of the West of England. (2010). *X-ray contrast media made clear*. Retrieved September 22, 2014, from http://hsc.uwe.ac.uk/: http://hsc.uwe.ac.uk/idis2/contrast_agents/cm%20zip/contrastmedia_schering.pdf

Unlu, M. Z., Krol, A., Coman, I. L., Mandel, J. A., Baum, K. G., Lee, W., et al. (2005). Deformable model for 3D intramodal nonrigid breast image registration with fiducial skin markers. *Medical Imaging, 5747*, 1528-1534.

Upstate medical university. (2011). *CT Radiographic Techniques*. Retrieved from http://www.upstate.edu: http://www.upstate.edu/radiology/education/rsna/ct/technique/

Varjonen, M., Pamilo, M., Hokka, P., Hokkanen, R., & Strömmer, P. (2007). Breast positioning system for full field digital mammography and digital breast tomosynthesis system. *SPIE medical imaging*.

Veenland, J. F., Grashuis, J. L., van der Meer, F., Beckers, A. L., & Gelsema, E. S. (1996). Estimation of fractal dimension in radiographs. *Medical Physics, 23*(4), 585–594.

Verlet, L. (1967). Computer experiments on classical fluids. *Phys Rev, 159*, 98–103.

Vigeland, E., Klaasen, H., Klingen, T. A., Hofvind, S., & Skaane, P. (2008). Full-field digital mammography compared to screen film mammography in the prevalent round of a population-based screening programme: the Vestfold County Study. *Eur Radiol*, 183-191.

Wan, W. K., Campbell, G., Zhang, Z. F., Hui, A. J., & Boughner, D. R. (2002, February 27). Optimizing the Tensile Properties of Polyvinyl Alcohol Hydrogel for the Construction of a Bioprosthetic Heart Valve Stent. *Wiley Periodicals, Inc.*, pp. 854-861.

Wang, C.-L., Wang, C.-M., Chan, Y.-K., Wang, S., & Liou, M.-R. (2011). Image Quality Fig. Evaluator Used in Radiography Based on Contrast-Detail Phantom. *IEEE 3rd International Conference*, 431-435.

Wang, Y., Xiong, Y., & Xu, K. (2006). A Mass-Spring Model for Surface Mesh Deformation Based on Shape Matching. *GRAPHITE '06*, 375-380.

Weisstein, E. W. (2013, July 29). *Full Width at Half Maximum*. Retrieved August 19, 2014, from http://mathworld.wolfram.com/: http://mathworld.wolfram.com/FullWidthatHalfMaximum.html

Wellman, P. S. (1999). Tactile Imaging. PhD Thesis. Harvard.

Whitman, G. J., & Haygood, T. M. (2013). *Digital Mammography: A Practical Approach.* (G. J. Whitman, & T. M. Haygood, Eds.) Cambridge, England: Cambridge University Press.

Willcox, P. J., Howie, D. W., Schmidt-Rohr, K., Hoagland, D. A., Gido, S. P., Pudjijanto, S., et al. (1999). Microstructure of Poly(vinyl alcohol) Hydrogels Produced by Freeze/Thaw Cycling. *Journal of Polymer Science*, 3438–3454.

Williams, M. B., Krupinski, E. A., Strauss, K. J., III, W. K., Rzeszotarski, M. S., Applegate, K., et al. (2007). Digital Radiography Image Quality: Image Acquisition. *American College of Radiology*, 371-388.

Winchester, D. P., & Winchester, D. J. (2006). *Breast Cancer* (Second ed.). Hamilton, Ontario: BC Decker.

Wolfe, J. N. (1976). Breast patterns as an index of risk for developing breast cancer. *AJR*, 1130-1137.

Wu, B., Heidelberg, A., & Boland, J. J. (2005). Mechanical properties of ultrahigh-strength gold nanowires. *Nature Materials, 4*(7), 525 - 529.

Yaffe, M. J. (2008). Mammographic density. Measurement of mammographic density. *Breast Cancer Research*, 209.

Yaffe, M. J. (2010). Basic Physics of Digital Mammography. In U. Bick, & F. Diekmann, *Digital Mammography* (pp. 1-12). London: Springer.

Yaffe, M. J. (2010). Detectors for Digital Mammography. In U. Bick, & F. Diekmann, *Digital Mammography* (pp. 13-32). Londoon: Springer.

Yaffe, M. J. (2010). Detectors for Digital Mammography. In U. Bick, & F. Diekmann, *Digital Mammography.* Springer.

Yaffe, M. J., & Mainprize, J. G. (2011). Risk of radiation-induced breast cancer from mammographic screening. *Radiology*, 98-105.

Yan, Z., Gu, L., Huang, P., Lv, S., Yu, X., & Kong, X. (2007). Soft Tissue Deformation Simulation in Virtual Surgery using Nonlinear Finite Element Method.

Yang, K., Burkett Jr, G., & Boone, J. (2014). A breast-specific, negligible-dose scatter correction technique for dedicated cone beam breast CT: a physics-based approach to improve Hounsfield Unit accuracy. *Physics in medicine and biology, 59*(21), 6487–6505.

Yip, W. M., Pang, S. Y., Yim, W. S., & Kwok, C. S. (2001). ROC curve analysis of lesion detectability on phantoms: comparison of digital spot mammography with conventional spot mammography. *Br J Radiol*.

Yu, P. (2000, November 27). *Anatomy of the Breast*. Retrieved 08 19, 2014, from http://ylb1.bol.ucla.edu: http://ylb1.bol.ucla.edu/anatomy.htm

Zhang, D., Li, X., & Liua, B. (2012). X-ray spectral measurements for tungsten-anode from 20 to 49 kVp on a digital breast tomosynthesis system. *Medical physics, 39*(6), 3493-3500.

Zhang, J., Roa, D., Sehga, V. l., He, Q., & Al-Ghazi, M. (2011). Comprehensive clinical implementation of a 16-slice Brilliance Big Bore CT Simulator in a radiation oncology department. *MedicaMundi, 55*(1).

Zhang, S., Gu, L., Liang, W., Zhang, J., & Qian, F. (2006). Real-Time Virtual Surgery Simulation Employing MM-Model and Adaptive Spatial Hash. *Lecture Notes in Computer Science*, 666-675.

Zuley, M. L. (2010). Perceptual issues in reading mammograms. In E. K. Ehsan Samei, *The Handbook of Medical Image Perception and Techniques* (pp. 364-379). Cambridge: Cambridge University Press.

Zuley, M. L., Willison, K. M., Bonaccio, E., Miller, D. P., Leong, D. L., Seifert, P. J., et al. (2006). Full-Field Digital Mammography on LCD Versus CRT Monitors. *American Journal of Roentgenology*, 1492-1498.